Non-Thermal Emission From Jets of Massive Protostars

Willice Odhiambo Obonyo

Department of Physics and Astronomy

University of Leeds

A thesis submitted for the degree of

Doctor of Philosophy

March 2020

Acknowledgements

First and foremost, my gratitude goes to God, the Almighty Father, for granting me this rare opportunity, and for the wisdom, peace of mind, good health and strength to conduct the research.

Many thanks to Stuart, a great mentor, a patient and supportive advisor whose door was always opened. You allowed me to experiment, make mistakes and learn. I still wonder how you never got tired of reading my many drafts of write-ups, sometimes giving me feedback earlier than I expected. You are a blessing, Stuart.

To Melvin, I cant thank you enough. Besides your many challenging questions during supervision meetings, your project, DARA (Development in Africa through Radio Astronomy) financed my studies and upkeep in the UK. Special thanks to you and the DARA project. A big thank you also goes to Trish for her support.

Julian, without your hydrodynamics code, this thesis is incomplete. Your advice on the use and understanding of the code were invaluable. Thank you very much.

To all my colleagues, past and present, as well as other staff members, thank you very much for the constant support and encouragements. Simon Purser, my unofficial fourth supervisor and football captain, accept my deepest thanks and appreciation. I know I asked you very many questions during my first year of PhD.

Finally, to my family, you were always by my side, encouraging me and providing fun moments. It is difficult to express the deep love I have for you. Carol, I cannot thank you enough for taking good care of the family while I was away. Min Awil, your prayers and wise counsel kept me going. Wuon Awil, thank you for the support and constant encouragement. Lucas Obonyo Junior, Adushe Manuar, thank you for the friendship, humorous conversations, and prayers. Brent and

Oliver, thanks for the exciting video conversations. Many thanks and God bless you all.

Abstract

This thesis details the outcome of a study of non-thermal radio emission from a sample of massive protostellar jets. The jets are ionized and can interact with magnetic fields within their vicinity to generate non-thermal emission. A search for the emission was conducted on a sample of fifteen massive protostars, observed using the JVLA at 1.5 GHz in 2015. Emission from the objects was characterised based on their spectral indices and spectral index maps, generated from their 1.5 GHz (L-band) data, and previous observations at 6.0 GHz (C-band) and 44.0 GHz (Q-band). 40% of the jets have characteristic non-thermal lobes, associated with synchrotron emission, especially sources of higher bolometric luminosity. All the cores, on the other hand, were found to be thermal, driving out material at rates that lie in the range 3×10^{-7} to $7 \times 10^{-6}\,\mathrm{M_{\odot}yr^{-1}}$.

Spectral energy distributions (SEDs) and spectral index maps of some of the protostellar jets displayed evidence of variability. As a result, four protostellar jets, previously observed in 2012 at C-band were identified and re-observed in 2018, at the same frequency, to study their variability property. Two of the protostars, S255 NIRS3 and W3 IRS5, displayed significant flux and positional variabilities respectively. S255 NIRS3 was in outburst while W3 IRS5 manifested clear proper motions and precession.

Lastly, some of the observable properties of the protostellar cores were used in simulating their features. Numerical calculations of their hydrodynamic properties were performed, followed by computation of their spectra using a ray-tracing code. Examples of the properties that were used to initiate the hydrodynamic simulations include; mass-loss rates, velocities and opening angles. The radio emission of the cores were generally found to be stable unless the input parameters were varied. Indeed, a change in the velocities and mass-loss rates of the thermal jets led to a corresponding change in their fluxes.

Abbreviations

ARWEN	Astrophysical Research With Enhanced Numerics
CGS	centimetre-gram-second system
CASA	Common Astronomy Software Application
FWHM	Full Width Half Maximum
GMC	Giant Molecular Cloud
HH	Herbig-Haro
HMPO	High Mass Protostellar Object
HPBW	Half Power Beamwidth
IMF	Initial Mass Function
IRDC	Infrared Dark Cloud
JVLA	Karl G. Jansky Very Large Array
LOFAR	Low Frequency ARray
MHD	Magneto-hydrodynamics
MSX	Midcourse Space eXperiment
MYSO	Massive Young Stellar Object
NIR	Near-Infrared
NRAO	National Radio Astronomy Observatory
RMS	Red MSX Source (survey)
SED	Spectral Energy Distribution
SMH	Smooth Particle Hydrodynamcis
SNR	Signal-to-Noise Ratio
UCHII	Ultra compact HII region
UKIDSS	UKIRT Infrared Deep Sky Survey
UKIRT	United Kingdom Infrared Telescope
WFCAM	Wide Field Camera
ZAMS	Zero Age Main Sequence

Contents

List of Figures

Chapter 1

Introduction

A look at the sky on a clear night brings to light a spectacular view of stars, planets, nebulae and clusters of stars. These objects are the building blocks of our universe. A closer look at the stars divulge some of their properties which can be used to classify them e.g. brightness, colour and size. The differences in stellar masses, for example, provide an opportunity to categorise them into two broad classes namely massive stars and low-mass stars. The boundary mass of the two categories is a mass equivalent to eight times the mass of the sun ($8\,M_\odot$). A main-sequence star whose mass $M > 8\,M_\odot$ (or bolometric luminosity $L > 5000\,L_\odot$) at solar metallicity (Carroll & Ostlie 2006, Caratti o Garatti *et al.* 2017) is classified as a massive star.

Massive stars differ from their low mass counterparts on two accounts; one, they undergo Type II supernova at death and two, they produce energetic UV radiation that can ionize their ambient HI gas to form HII regions at birth. Their high mass and stronger gravity can provide enough temperature and pressure that is needed to fuse heavy elements (Clayton, 1983). The stars, therefore, can be described as the main energisers, chemical enrichers and sources of turbulence in the universe (Oey & Clarke, 2009). Indeed, they inject large amounts of energy as well as synthesised chemicals to the interstellar medium as they die, during the supernovae phase.

The stars have significant impacts in astrophysics. First, their strong radiation pressure can influence star and planet formation within their surroundings (Kennicutt, 2005). Also, the mechanical energy of their jets and supernova may either

trigger star formation (Prialnik, 2000) or inhibit it by disrupting a nearby molecular core. In the larger scale, they influence structure, evolution and luminosity of galaxies as they convert galaxies' gas into stars. The objects also influence the chemistry of their environment by heating dust particles around them, prompting evaporation of ice on the dust surfaces. Despite the aforementioned benefits, their formation processes are still unclear (Beuther *et al.*, 2007a).

The slow growth in the understanding of their formation is due to several factors. They are rare compared to sun-like stars. For instance, the ratio of $20\,M_\odot$ to $1\,M_\odot$ stars is $\sim 1 : 100,000$ and that of a $100\,M_\odot : 1\,M_\odot$ stars is $\sim 1 : 1,000,000$ in the Milky Way (Massey, 2003), a clear sign of their scarcity. Apart from their rarity, they are typically far away from us and are heavily obscured by clouds of dense ambient gas and dust. This limits the ability to study them observationally, especially at shorter wavelengths of the electromagnetic spectrum. The stars, due to their high mass, burn their fuel faster hence have short evolutionary phases, limiting the number of samples per evolutionary stage needed to achieve statistical significance. Finally, they are mostly born in binaries and higher multiples complicating the estimation of their intrinsic quantities e.g. luminosities (Zinnecker & Yorke, 2007).

1.1 Star Formation Sites

1.1.1 Molecular Clouds

Star formation takes place within the cold and dense parts of the interstellar medium (ISM) called molecular clouds (Larson, 1994). The clouds are complex environments comprising dense clumps, dust and ionized regions called HII regions. Such environments are ubiquitous in the observable universe with thousands found within our Galaxy (Scoville & Solomon, 1975) e.g. the G305 star-forming complex shown in Figure 1.1 (Hindson *et al.*, 2013). Most of the clouds display evidence of ongoing star formation except in a few cases e.g. the Pipe Nebula (Forbrich *et al.*, 2009).

Molecular clouds are transient, self-gravitating, turbulent, magnetic and compressible (Blitz & Williams 1999, Larson 1994). Their lifespans, masses, number

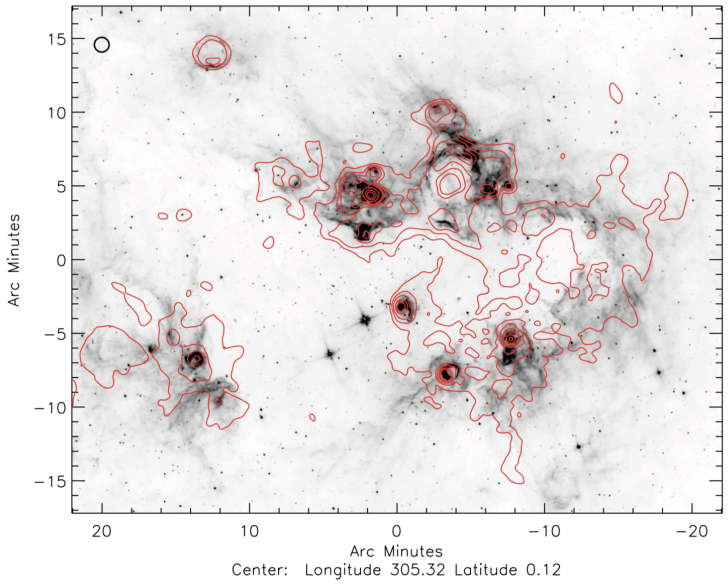

Figure 1.1: 5.8 μm GLIMPSE image and 5.5 GHz radio emission contours (shown in red) of the star forming complex G305 (Hindson *et al.*, 2013).

densities and temperatures are $\sim 10-40$ Myrs (Murray 2011, Lada & Kylafis 1991 & Larson 1994), $M \sim 10 - 10^6\,\mathrm{M}_\odot$, $n \sim 10^2 - 10^4\,\mathrm{cm}^{-3}$ and T $\sim 5 - 300$ K respectively. These physical properties, however, change within dynamical timescales (Larson, 1994) due to tidal and radiation disruptions.

Molecular clouds are semi virial (Solomon *et al.*, 1987) even though they show evidence of turbulent interiors and rotating cores (Goodman *et al.*, 1993). Kinematic study of the clouds by Larson (1981) shows that their internal velocity dispersions σ_v correlate with their sizes R and masses M as shown in equation 1.1. Where $p = 0.5 \pm 0.1$ and $q = 0.25$ for clouds within our Galaxy.

$$\begin{aligned} \sigma_v &\propto R^p \\ \sigma_v &\propto M^q(M_\odot) \end{aligned} \tag{1.1}$$

Being semi virial, the ratio of gravitational potential energy of the clouds to twice their total kinetic energy is ~ 1 (see Figure 1.2) and $\frac{GM^2}{R} \sim M\sigma_v^2$, where G is the gravitational constant and M is the cloud mass. This means that the clouds

are gravitationally bound and tend to have masses that are much larger than their Jeans masses, M_J (Larson 1981). According to Figure 1.2, for example, clouds with sizes larger than 1 pc have masses $M \gtrsim M_J$. It is clear, therefore, that molecular clouds of comparable masses share similar properties, σ_v, R and $N(H_2)$, and may have related formation and evolution mechanisms.

1.1.2 Giant Molecular Clouds

Molecular clouds are subdivided into diffuse molecular clouds (also called Cirrus; Blitz & Williams 1999), the Bok globules (Clemens & Barvainis, 1988) and the giant molecular clouds (GMC). Massive star formation takes place within the giant molecular clouds. The GMCs are characterised by high number densities $\sim 100\,\mathrm{cm}^{-3}$, low temperatures $\sim 10 - 20\,\mathrm{K}$, high masses $\sim 10^4 - 10^7\,\mathrm{M}_\odot$ and extensive sizes $\sim 50 - 200\,\mathrm{pc}$ (Miura *et al.* 2012, Zinnecker & Yorke 2007). A good example of a GMC is the nearby star forming region, Orion, located $\sim 410\,\mathrm{pc}$ (Reid *et al.*, 2009) away from the Sun. The Bok globules are isolated, small and dense molecular clouds whose average sizes $\sim 0.3\,\mathrm{pc}$. They are seen as silhouettes against bright background stars or emission nebula. Their sizes and masses are comparable to those of cores within the GMCs, i.e., $M \gtrsim 100\,\mathrm{M}_\odot$. They show evidence of star formation activities since they harbour newly forming stars (Smith, 2004). The Cirrus, on the other hand, are extended, diffuse and filamentary clouds with low number densities, $n \sim 30\,\mathrm{cm}^{-3}$ (Gillmon & Shull, 2006), and masses, $M \leq 100\,\mathrm{M}_\odot$. They are mainly observed at the high latitudes since lower latitudes are dominated by the globules and GMCs which outshine them.

Formation of the GMCs can be explained using either of the two models namely; 'bottom-up' and 'top-down' (McKee & Ostriker, 2007). In the bottom-up model, smaller clouds undergo multiple inelastic collisions that coalescence and form a larger cloud of higher density and mass. The pitfall with the bottom-up process is that it takes a longer period to form a GMC compared to observational estimates, $\sim 10^7 - 10^8$ years (Kwan 1979, Blitz & Shu 1980). Kwan (1979), for example, estimates that it takes more than 2×10^8 years for a $10^5\,\mathrm{M}_\odot$ cloud to form through this model. Top-down model, on the other hand, occurs due to large-scale instabilities within the diffuse ISM. The model was proposed to take

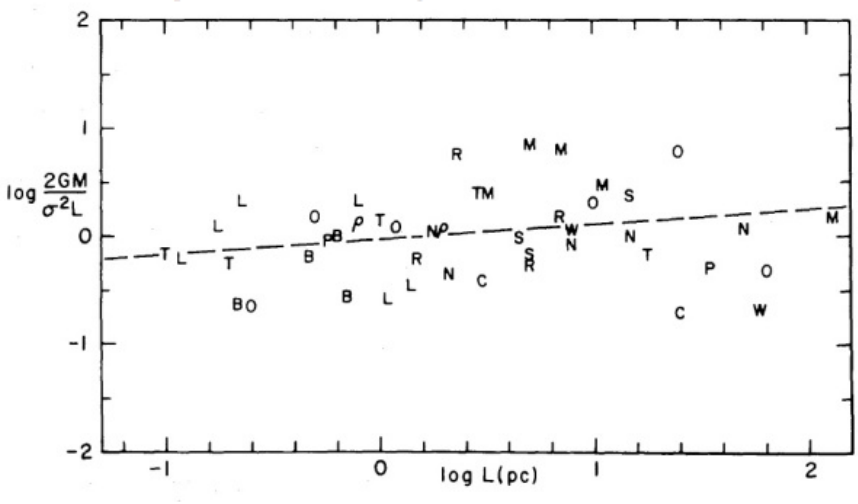

Figure 1.2: An illustration showing how the virial ratio, $\frac{2GM}{\sigma^2 L}$, of clouds varies with their sizes, L, i.e., $\frac{2GM}{\sigma^2 L} = 0.92L^{0.14}$. The sizes are in parsec, masses in solar mass and velocity dispersion in km s^{-1} (Larson, 1981).

care of the long formation periods in the bottom-up mechanism. In the model, atomic or molecular gas flows from larger scales and settles within a smaller region. The large scale instabilities are brought about by changes in magnetic field strength (Parker instability) and self-gravitation within the clouds (McKee & Ostriker, 2007). According to Parker instability, interstellar gas, frozen in magnetic field lines, slide along the lines to the lowest potential zones until they form denser and larger molecular clouds, giving rise to GMCs whose formation timescales are comparable to observations. The mechanism also accounts for the presence of excess atomic hydrogen in the clouds (Blitz & Shu, 1980). Finally, self gravitation instabilities, also called Jeans instabilities, build up the GMCs as clouds of different masses attract. Besides 'bottom-up' and 'top-down' formation mechanisms, large scale colliding flows (Heitsch *et al.*, 2005) where streams of supersonic atomic gas collide and compress isothermally may lead to higher density zones which are conducive for the formation of molecular gas.

Giant molecular clouds have substructures called clumps, the over-dense regions where most of their mass reside. The clumps are considered the building blocks of the GMCs. Observations show that the clumps harbour young OB stars

(Blitz, 1979), implying that they are the locations of star formation. A clump may disintegrate into more dense and compact regions called cores. This means that a single clump can harbour one or more cores, making them the precursor of either an isolated massive star, a binary system or a star cluster. Some properties of the clumps which may form massive stars include; masses that lie in the range $\sim 100\,\mathrm{M}_\odot - 1000\,\mathrm{M}_\odot$, number densities $\rho \sim 10^5 \mathrm{cm}^{-3}$, temperatures $T \sim \sim 10 - 20\mathrm{K}$ and typical sizes $\mathrm{r} \sim 0.5\,\mathrm{pc}$ (Tan *et al.*, 2014). Table 1.1 summarises the physical properties of GMCs, clumps and cores.

Star formation sites are associated with dense molecular gas, collisions due to accretion or outflows, ionization by protostars, and presence of dust particles. These features can be traced by carbon sulfide molecules, ammonia molecules, methanol and OH masers, water masers, free-free emission, synchrotron emission and dust continuum emission. For example, carbon sulfide lines CS $\mathrm{J} = 7 \rightarrow 6$, CS $J = 5 \rightarrow 4$ (Knez *et al.*, 2002), ammonia molecules (Smith, 2004) and water masers (Knez *et al.*, 2002) trace clouds of number densities $n \sim 2.8 \times 10^7\,\mathrm{cm}^{-3}$, $n \sim 8.9 \times 10^6\,\mathrm{cm}^{-3}$, $n \sim 10^8\,\mathrm{cm}^{-3}$ and $n \gtrsim 10^{10}\,\mathrm{cm}^{-3}$ respectively. Besides, water masers and class I (Cragg *et al.*, 1992) methanol masers are indicators of collision while class II (Fontani *et al.*, 2010) methanol masers are associated with radiation.

1.2 Star Formation

The formation of stars is a complex process. It takes place within clouds that span a wide range of mass and size (Shu *et al.*, 1987). The end products of the processes

Table 1.1: A table showing a summary of properties of GMC, their clumps and cores (Zinnecker & Yorke, 2007)

Property	GMC	Clump	Core
Mean radius (pc)	50-200	2	0.08
Number density $\mathrm{n(H_2)\,cm^{-3}}$	100	10^3	10^5
Mass ($\mathrm{M}_\odot$)	10^5	10^3	10^2
Linewidths ($\mathrm{km\,s^{-1}}$)	7	2	0.3
Average temperature (K)	15	10	10

are equally diverse, ranging from stars whose masses are just enough to trigger thermonuclear fusion at the core, i.e., $M \gtrsim 0.08\,\mathrm{M}_\odot$ (Hayashi & Nakano, 1963) to extremely massive counterparts e.g. R136a1 ($M \simeq 315 \pm 50\,\mathrm{M}_\odot$; Crowther *et al.* 2016). This makes the origin of the different stellar masses one of the fundamental questions in star formation. The range in mass can be due to fragmentation of clumps into cores of different masses. Alternatively, it may result from a process that halts accumulation of mass by a protostellar core e.g. radiation pressure (Shu *et al.*, 1987). It is not clear if the formation mechanism for such a broad spectrum of stellar masses is common but the clouds that form massive stars (early B and O type stars) seem to be warmer, i.e., $> 20\,\mathrm{K}$ (Solomon *et al.*, 1985).

Furthermore, the stellar initial mass function (IMF), which quantifies the distribution of masses of stars at birth (see Figure 1.3), suggests a bimodal star formation process (Shu *et al.*, 1987). Some IMF plots show evidence of two maxima (Drass *et al.*, 2016); at the substellar regime, i.e., $M \sim 0.025\,\mathrm{M}_\odot$ and the low mass regime, i.e., $M \sim 0.25\,\mathrm{M}_\odot$, exhibiting the existence of different populations whose formation processes may be distinct. On the contrary, there is a clear match between stellar IMF and prestellar core mass function (Motte *et al.*, 1998), suggesting that the final masses attained by stars are perhaps set at the time when the cores are being formed or even earlier.

Clearly, there are fundamental similarities and differences between low and high mass stars. Some of the differences include; non-identical birthplaces, dissimilar evolutionary paths and distinct nature of death. Despite the differences, the models that explain the formation of both low (Larson, 1969) and high mass (Hosokawa & Omukai, 2008) stars begin with the collapse of a prestellar core. For a molecular cloud to collapse, it must have a minimum mass called the Jeans' mass, $\mathrm{M_J}$. The Jeans' mass for a cloud of number density ρ, particle mass m and temperature T is given mathematically as:

$$M_J = \left(\frac{5kT}{Gm}\right)^{\frac{3}{2}} \left(\frac{3}{4\pi\rho}\right)^{\frac{1}{2}} \mathrm{M}_\odot \tag{1.2}$$

where G and k are gravitational and Boltzmann's constants respectively. This is a simplified case of $\mathrm{M_J}$ given that only gas pressure is considered. Other forms of pressure, present in a molecular cloud, that can oppose gravity include magnetic,

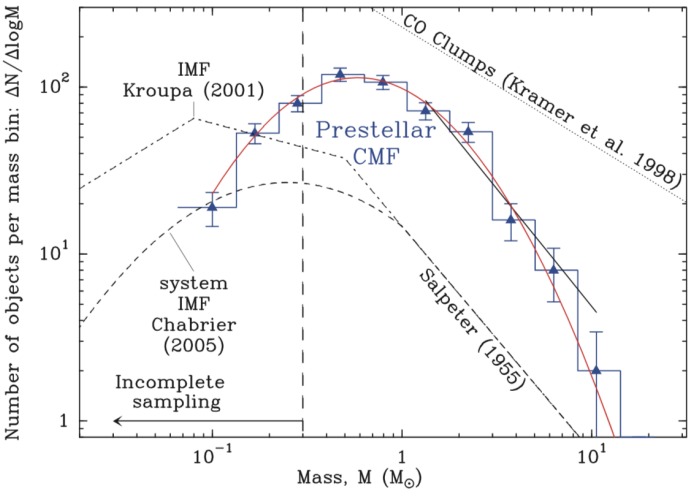

Figure 1.3: A plot showing initial mass function and prestellar core mass function (André *et al.*, 2013). The shapes are comparable.

turbulence and rotational pressure. Any isothermal collapse under the influence of gravity of a cloud takes place within a period of time called the free fall time t_{ff}, given as:

$$t_{ff} = \left(\frac{3\pi}{32G\rho}\right)^{\frac{1}{2}} = 3.4 \times 10^{7} n^{-\frac{1}{2}} \text{ years} \tag{1.3}$$

where ρ and n are the mass and number densities of the cloud in $\mathrm{kg\,m^{-3}}$ and $\mathrm{cm^{-3}}$ respectively. As an illustration, clumps and cores of number densities $\sim 100\,\mathrm{cm^{-3}}$, $10^3\,\mathrm{cm^{-3}}$ and $10^5\,\mathrm{cm^{-3}}$ will have free fall timescales of ~ 3.4 Myrs, 1.0 Myrs and 0.1 Myrs respectively.

The core of a protostar undergoes contraction as it forms. This contraction is accompanied by energy changes which the core radiates away within a timescale called the Kelvin Helmholtz time, t_{KH}. The time taken to radiate away all the energy from an object of mass M, radius R and luminosity L after contraction is given by equation 1.4:

$$t_{KH} = \frac{GM^2}{RL} \tag{1.4}$$

In low mass stars, t_{KH} is higher than t_{ff} (see Figure 1.4), implying that accretion ends before the start of hydrogen burning. As a collapsing core radiates energy, it

contracts within the Kelvin - Helmholz period and joins the main sequence when the core is hot enough. On the contrary, $t_{KH} < t_{ff}$ in high mass stars, as a result, their protostars evolve to the main sequence while still accreting material. An effect of this property is the obscuration of young high mass stars by the dusty in-falling clouds.

1.2.1 Low Mass Star Formation

The formation of low mass stars is relatively well studied compared to that of high mass stars. Certainly, their relative abundance and the avalanche of data from recent observations have led to this. Despite known fundamental differences between low and high mass stars, the knowledge gathered from low mass star formation may provide some insight into the study of high mass star formation.

Models that explain the formation of low mass stars have evolved over the years, however, nearly all the models begin with the collapse of an unstable molecular cloud. In a model by Larson (1969), an optically thin spherical cloud collapses isothermally (Gaustad, 1963). The collapse is accompanied by compressional heat which is conducted away by dust grains within the optically thin cloud (Bhandare *et al.*, 2018). A collapsing cloud forms into a core, its interior, and an envelope. At any given time, the density ρ of the core is relatively constant while that of the envelope changes with the radius r, i.e., $\rho \propto r^{-2}$ (see Figure 1.5). Shu (1977) noted that the gravitational stability of the cores changes as they evolve, classifying them as sub-critical when their masses are lower than the Bonnor-Ebert mass (Bonnor 1956, Ebert 1955) and super-critical otherwise. A super-critical core is prone to collapse due to its gravity.

As a cloud collapses, the density and opacity of the interior grow with time until radiative cooling becomes ineffective. Further compression of the core is largely adiabatic, as a result, the temperature and pressure of the core halt any additional collapse. The core then approaches hydrostatic equilibrium as its temperature rises to 2000 K, when hydrogen molecules dissociate to atomic hydrogen. The dissociation is endothermic and the temperature of the core remains relatively constant as more material piles up around it. Gravity due to the increased mass overcomes the pressure and the core collapses a second time. This second

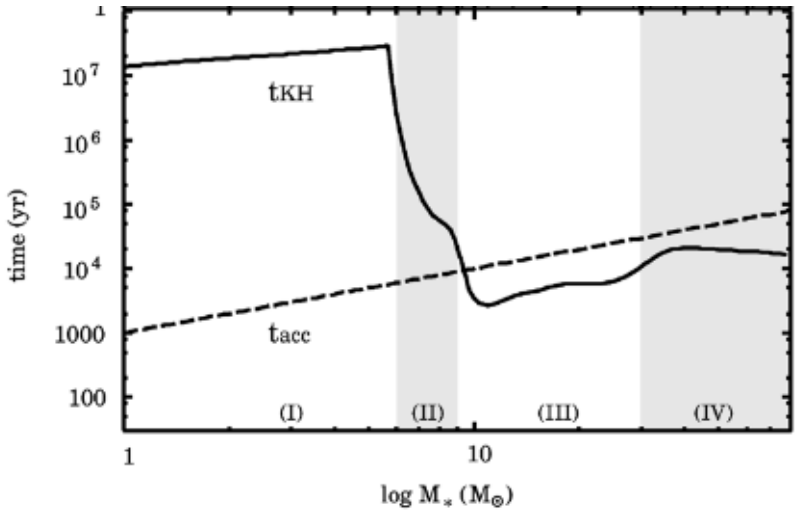

Figure 1.4: An illustration showing how Kelvin-Helmholtz time (t_{KH}) and accretion time t_{acc} vary with mass. The four roman numbers represent four evolutionary phases: (I) adiabatic accretion, (II) swelling, (III) Kelvin-Helmholtz contraction, and (IV) main-sequence accretion phases (Hosokawa *et al.*, 2010).

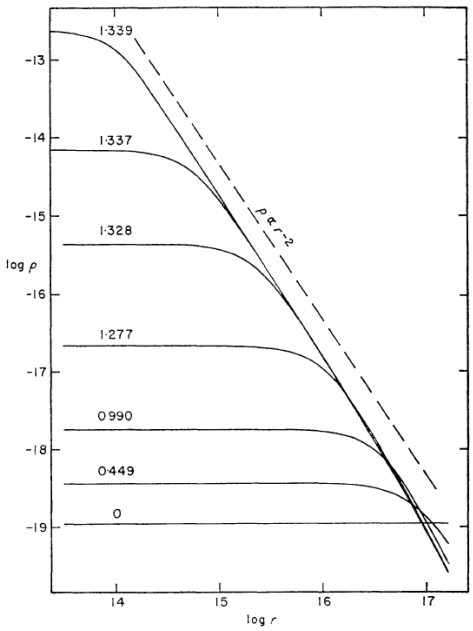

Figure 1.5: Left: A plot showing how density distribution within a collapsing cloud varies with time (Larson, 1969). The times on the plots are in units of 10^{13} s.

collapse generates a denser and more opaque core whose temperature increases up to 10^4 K. The difference in temperature and density between the core and the surrounding region occasions the formation of convective zones and radiating shocks (Shu, 1977) respectively. These shocks eventually disappear as the protostar radiates heat convectionally, giving way for the collapse of the whole cloud towards the core to form a protostar.

The nature of collapse outlined, and detailed in Shu *et al.* (1987) and Shu (1977), can be described as 'inside out', meaning that the interior falls before the envelope of the cloud. Densities of the different regions of the collapsing cloud can be approximated as $\rho \sim c_{eff}^2/2\pi G r^2$, where c_{eff} is the effective sound speed. The inside thus collapses before the outer parts since free fall time $t_{ff} \propto \frac{1}{\sqrt{\rho}}$, implying that the dense innermost part collapses faster than the outer parts. Other models, e.g. Hartmann *et al.* (1996), considered a molecular cloud whose morphology is cylindrical. The core of the resultant protostar collapses spherically, producing some of the observed features e.g. cavities in the in-falling envelopes and a mini-disk. A more recent model by Tomisaka (2002) included rotation and magnetic fields on a collapsing cloud, replicating observable characteristics like a central dense core, an accretion disk and an outflow.

Theoretical as well as observational studies of low mass star formation have made numerous advances and it is now clear that the process takes place in stages as shown in Figure 1.6. It begins with the collapse of a molecular cloud and ends when a dusty natal cloud is cleared by the outflows and radiation pressure from the protostar. The collapse is also accompanied by the formation of a disk around the protostar as well as an outflow that drives out material back to the ambient medium. After a given period, a protostar and a residual circumstellar disk, where planets are formed, is what remains.

The different evolutionary stages provide a framework of classifying low mass protostars (Gao & Lou 2017, Schulz 2012). The earliest stage is class 0, characterised by a dense envelope. The majority of the mass of a protostar is accreted at this stage in a quasi-spherical manner and via a small disc. The protostar then evolves to a class I source where it accretes at a slower rate. This source is characterised by a remnant envelope and a larger circumstellar disk. The class I source advances to a class II object. At this stage, the envelope is missing, exposing an

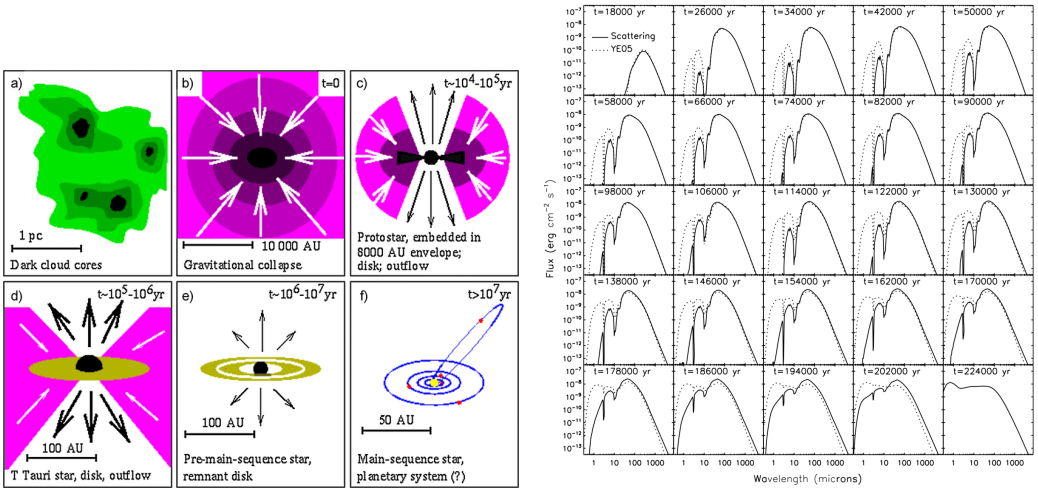

Figure 1.6: Left: A model illustration how low mass stars are formed (Hogerheijde 1998, Shu *et al.* 1987). Right: Changes in SED of a low mass protostar with time (Dunham *et al.*, 2010).

accretion disc that is characterised by excess infrared emission. The final stage of evolution is known as class III. This stage is characterised by a fully photo-evaporated disk and a star that is free from circumstellar material (see Figure 1.6). This classification layout makes use of accretion rates of the sources, and some protostellar features e.g. episodic accretion may lead to misclassification (Gramajo *et al.*, 2014).

1.2.2 Massive Star Formation

The processes involved in the formation of massive stars are still actively debated. Whether they form like their low mass counterparts or not is yet to be fully established. Compared to low mass sources, they are relatively rare, have shorter lifetimes, form in complex environments and have larger distances, complicating a deeper understanding of their formation mechanisms. Some of the main unresolved challenges in massive star formation are i) how the extreme radiation pressure from the central protostar can either escape or be overcome by in-falling material and ii) why massive protostellar cores do not fragment during collapse.

1.2.2.1 Radiation Pressure Problem

Theoretically, a particle of mass m and dust opacity κ at a distance r from the centre of a protostar of mass M and luminosity L will only be accreted by the protostar if the force of gravity per unit mass $f_{grav} = \frac{GM}{r^2}$ is greater than the outward radiative force $f_{rad} = \frac{\kappa L}{4\pi r^2 c}$ (Krumholz, 2015), i.e.,:

$$\frac{L}{M} < \frac{4\pi G c}{\kappa} = 2500 \left(\frac{\kappa}{5\mathrm{cm}^2/\mathrm{g}} \right)^{-1} \frac{\mathrm{L}_\odot}{\mathrm{M}_\odot} \tag{1.5}$$

In spherical collapse, it is estimated that any protostar of mass $M \gtrsim 20\mathrm{M}_\odot$ has $\frac{L}{M} > \frac{4\pi G c}{\kappa} = 2500 \frac{\mathrm{L}_\odot}{\mathrm{M}_\odot}$ implying that $M \simeq 20\,\mathrm{M}_\odot$ is the maximum mass limit. Of course, the value of the estimate depends on the abundance of dust grains in the cloud hence a higher estimate of $40\,\mathrm{M}_\odot$ by Kahn (1974). Yorke & Sonnhalter (2002) made use of a rotating molecular cloud in their simulation and realised a mass limit of $43\,\mathrm{M}_\odot$, part of which was accreted via an accretion disk. Recent work by Kuiper *et al.* (2010) considered accretion of material through circumstellar disks, generating a star of mass $M = 137.2\ \mathrm{M}_\odot$ from a core of mass $M = 480\ \mathrm{M}_\odot$ in their simulation. The question then is do massive stars have disks and are jets the evidence of their existence? This question was partly answered by Kraus *et al.* (2010) when they imaged a disk around a massive young stellar object, however, more MYSOs with disks are needed to support this accretion mechanism.

Observations, as well as simulations, suggest that massive protostars could accrete matter via accretion disks although their radiation pressure is so extreme that it can disrupt or blow away any tenuous disks. This implies that very high accretion rates and an outlet through which part of the radiation pressure escapes are needed. Indeed the simulation by Banerjee & Pudritz (2007) points to higher accretion rates in massive protostars, i.e., $M_{acc} > 10^{-3}\,\mathrm{M}_\odot\mathrm{yr}^{-1}$. Both Banerjee & Pudritz (2007) and Kuiper *et al.* (2014) also showed that part of the accreted materials get excreted through their jets. The jets form cavities through which part of the radiation pressure escapes with minimal interaction with the protostellar accretion disk.

1.2.2.2 Fragmentation Problem

The typical temperatures and number densities of GMCs are; T$\sim$ $10 - 20\,\mathrm{K}$ and n $\sim 10^3 - 10^5\,\mathrm{cm}^{-3}$ respectively, implying that clumps and cores within the GMCs should have masses that lie in the range $0.5 \lesssim \mathrm{M} \lesssim 2\,\mathrm{M}_\odot$. The collapse of a massive core, therefore, should be accompanied by fragmentation as the cloud tends to form objects whose masses are comparable to the Jeans mass (Krumholz, 2015):

$$M_J = \frac{\pi}{6}\frac{c_s^3}{\sqrt{G^3\rho}} = 0.5\left(\frac{T}{10\,\mathrm{K}}\right)^{\frac{3}{2}}\left(\frac{n}{10^4\,\mathrm{cm}^{-3}}\right)^{\frac{1}{2}}\mathrm{M}_\odot \tag{1.6}$$

Fragmentation of a collapsing massive core can be inhibited by the rise in temperature due to in-fall (Krumholz *et al.*, 2005). Clouds of higher temperatures are associated with higher Jeans masses (see illustration in Figure 1.7). Clearly, the actual process that leads to the formation of a massive star is still debatable. Whether they form from the collapse of massive cores, merger of low mass protostars or accumulation of mass by low mass cores is unclear.

In summary, the radiation pressure problem, core fragmentation and other challenges, encountered in the study of massive star formation, can be circumnavigated in many ways e.g. disk-fed accretion, high accretion rates (Kuiper *et al.*, 2010) and a rise in temperature of a collapsing core. The other factors that may affect massive star formation are ionization feedback (Xu *et al.*, 2019) and stellar winds.

1.2.3 Models of Massive Star Formation

Three models; core accretion (also known as monolithic collapse), competitive accretion and mergers & collisions (Zinnecker & Yorke, 2007) were proposed to explain how massive stars form.

1.2.3.1 Core Accretion (Monolithic Collapse) Model

This is a scaled-up version of low mass star formation. In the model, also known as the gravo-turbulent method, a cloud fragments hierarchically under the influence of its turbulence, magnetic field and gravity. This process can lead to the

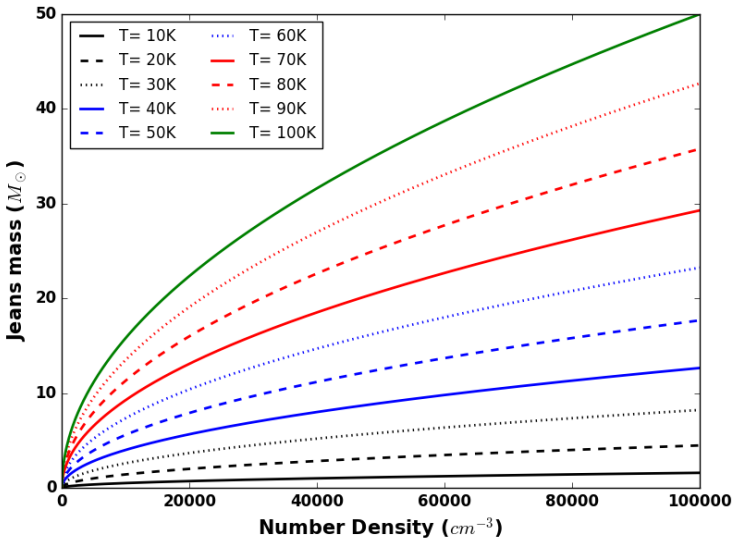

Figure 1.7: Variation of Jeans mass with number density of molecular clouds at different temperatures made using equation 1.2.

formation of a high mass core (Ballesteros-Paredes *et al.*, 2007) which cannot undergo any further considerable disintegration. The core can then collapse under its gravity, forming a massive star. Ordinarily, a collapsing cloud undergoes a significant change in angular momentum. To conserve the momentum, the cloud material concentrates around the equatorial region before eventually spreading out to form an accretion disk that is oriented approximately perpendicular to the protostar's rotation axis (Larson 1978, Sicilia-Aguilar *et al.* 2013). This model can be used to explain the formation of the high mass stars which are found in relatively isolated environments.

The main characteristic of the core accretion model is localised accretion activities (He *et al.*, 2016). In the model, a protostar can only accumulate materials from the core that harbours it, i.e., localised accretion field. The final mass of a star is thus largely controlled by the mass of the core. Inclusion of other factors like the magnetic field of a cloud can result in more massive cores and corresponding stars. Kuiper *et al.* (2010), for example, modelled a star of mass $M \sim 140\,\mathrm{M}_\odot$ by introducing magnetic fields and feedback in their simulation. Another concept

that was introduced in the model by McKee & Tan (2003) is turbulence and high accretion rate, of up to $\dot{M} \geq 1.1 \times 10^{-3}\,\mathrm{M}_{\odot}\,\mathrm{yr}^{-1}$. The high rates are linked with higher infalling pressure, capable of overcoming radiation pressure. In a more recent simulation of massive star formation, Hosokawa *et al.* (2010) revealed that high accretion rates, i.e., $\dot{M} > 10^{-4}\,\mathrm{M}_{\odot}\,\mathrm{yr}^{-1}$, result in a protostellar phase where the envelope of the accreting core is swollen. The envelope of the swollen core shields in-falling matter against pressure from the protostar, allowing further accretion until a massive star is formed. The 'puffed up' gas becomes the reservoir of the protostar. Presence of accretion disks around some massive protostars (Carrasco-González *et al.*, 2012) and the close similarity between core and stellar initial mass functions (Alves *et al.*, 2007) supports this model.

1.2.3.2 Competitive Accretion

In competitive accretion (Bonnell *et al.*, 1997), a star's final mass is connected with the size of its protostellar core and its location in a protocluster. This accretion model favours the massive cores that are located at the densest parts of a protocluster, usually the centre of its potential well. Gravitational collapse of a dense cloud gives rise to a protocluster that is buried in a gas reservoir. It actuates accretion of matter from the reservoir using its combined potential as illustrated in Figure 1.8. Once the gas that is accreted by a protocluster is within the reach of its stars, they compete for it, effectively causing massive cores at the centre of the potential well to accrete more (He *et al.*, 2016). This model effectively explains why high mass stars have masses that are significantly higher than the Jeans' masses of their molecular clouds.

To explain the accretion mechanisms responsible for the high masses observed, three possibilities were proposed namely; Bondi accretion, gravitational focusing and mass segregation. Mass segregation impels massive cores to be together creating a high potential well for accretion, which together with Bondi accretion enhances the accumulation of matter (Bonnell *et al.*, 2001). In the Bondi accretion model, a core of Bondi radius R, would move about a gas of density ρ with velocity v to accrete mass at a rate $\dot{M} = 4\pi R^2 \rho v$. These mechanisms are normally accompanied by gravitational focusing which intensifies collection of mass due to

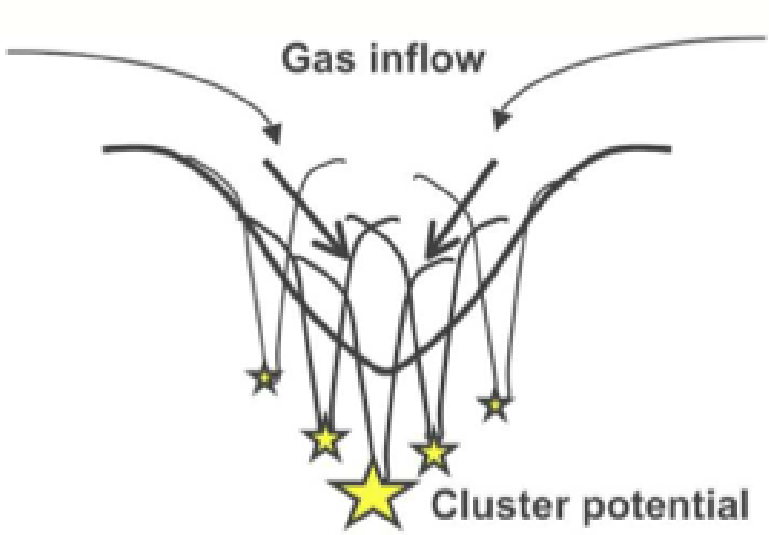

Figure 1.8: An illustration of the competitive accretion process. Highest potential zone accretes more mass (Krumholz & Bonnell, 2009)

large cross-sections of massive cores $\sigma_{grav} = \pi R_{min}^2 \left(1 + \frac{2GM}{V_{inf}^2 R_{min}}\right)$. Here R_{min} is distance of closest approach of particles and V_{inf} is the relative velocity at infinity.

1.2.3.3 Mergers and Collisions

In this model, stars of a cluster of a high stellar density can collide and merge into a massive star. Stars within a cluster of stellar density $\gtrsim 10^3\,\mathrm{stars\,pc^{-3}}$ have the potential of merging into a massive star. The timescales of the collisions, however, depend on the stellar densities of the cluster as shown in Figure 1.9 (Bonnell & Bate, 2002). The densities needed for shorter collisional timescales have never been observed in Galactic clusters, seeing that the current highest estimate is $\sim 10^6\,\mathrm{stars\,pc^{-3}}$ (Megeath *et al.*, 2005) in W3 IRS5. The difficulty in mergers can be reduced by the presence of gas around the stars which have the potential of increasing the effective collision cross-section (Mannings *et al.*, 2000) in clusters of lower stellar densities. Besides, binary stars in a cluster of a lower stellar density e.g. $\sim 10^6\,\mathrm{stars\,pc^{-3}}$ can tighten as they accrete mass until they collide and merge (Bonnell & Bate, 2005). Despite the challenges surrounding

this theory of massive star formation, it may be the model that is responsible for the formation of the very massive stars e.g. R136a1 ($M \simeq 315 \pm 50\,\mathrm{M}_{\odot}$; Crowther *et al.* 2016)

1.2.4 Evolutionary Stages in High Mass Star Formation

Star formation is a gradual process that takes place in stages. Massive protostars, for example, spend a considerable part of their life ($\gtrsim 10\%$) embedded in natal molecular clouds, as a result, it is possible to categorise their formation into evolutionary stages (van der Tak, 2004). Infrared dark cloud (IRDC), defined as extinction features against the bright Galactic mid-infrared background, harbour compact cores that represent the earliest stage of massive star formation (Rathborne *et al.*, 2010). The cores may be classified as 'active' or 'quiescent' based on their star formation activities (Chambers *et al.*, 2009). Quiescent cores are starless while their active counterparts are star-forming (Chambers *et al.* 2009, Battersby *et al.* 2017). Active cores are characterised by an excess infrared emission at $4.5\,\mu$m (Cyganowski *et al.*, 2008), a tracer of shocked gas. The active cores are also known as high mass protostellar objects (HMPOs), described as point-like infrared sources of bolometric luminosity $L_{bol} \gtrsim 10^3\,\mathrm{L}_{\odot}$.

Some protostellar condensations of the IRDCs, e.g. IRDC 18223-3, drive molecular outflows and show evidence of inflow via a disk (Fallscheer *et al.*, 2009). The accretion heats up the objects, giving rise to hot and dense molecular cores known as the hot molecular cores (Shimonishi *et al.*, 2016). These cores are characterised by small sizes $\lesssim 0.1\,\mathrm{pc}$, high densities $\geq 10^6\,\mathrm{cm}^{-3}$ and temperatures $\gtrsim 100\,\mathrm{K}$ (van der Tak, 2004). Continued accretion by the hot molecular cores occasion heating of their environment until UV photons, responsible for ionizing gas, induce ultracompact HII regions (UCHII) around them. The UCHII regions are ionised bubbles which are small in size $\lesssim 0.1\,\mathrm{pc}$, dense $n \gtrsim 10^4\,\mathrm{cm}^{-3}$ and bright $\sim 10^5\,\mathrm{L}_{\odot}$ (Jin *et al.* 2016, Beuther *et al.* 2007c). Accretion stops at the UCHII region phase. The region then expands until an optically visible star is exposed. Normally, the star reaches the main sequence while at this stage. An illustration showing the earliest stage of evolution is shown in Figure 1.10.

The age of the different phases cannot be estimated accurately since they

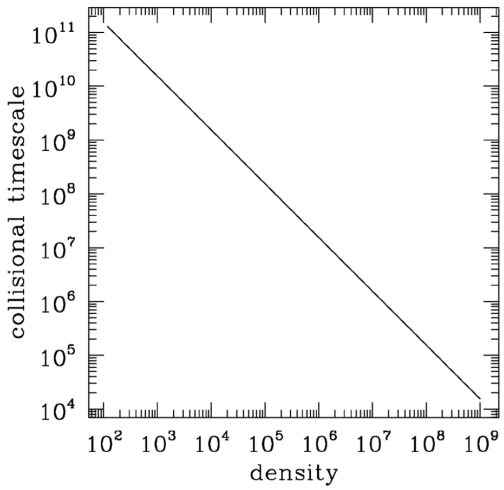

Figure 1.9: A plot showing the relationship between stellar density of a cluster and the collisional timescales of its stars (Bonnell & Bate, 2002).

evolve quickly and occur one after another. Besides, the stars are normally born in clusters where multiple phases are present at once. This, coupled with the fact that they are embedded in their mother clouds, complicates the estimation. A rough estimate, however, puts the ages of hot molecular cores at $t \sim 10^3 - 10^4$ years (Millar & Hatchell, 1997) and those of UCHII regions as $\sim 10^4 - 10^5$ years (de Pree *et al.* 1995, Smith 2004) meaning that they form almost concurrently.

1.3 Jets and Outflows

1.3.1 Introduction

Any astrophysical object that is accreting matter, rotating and has magnetic fields, ejects materials in the form of a bipolar outflow or a collimated jet (Bally, 2016). Examples of the astrophysical objects that drive jets include protostars, planetary nebulae, accreting neutron stars e.g. SS433 and active galactic nuclei. The morphologies of the jets are similar irrespective of the source, however, their outflow speeds and sizes show significant differences.

Jets and outflows are ubiquitous in protostars of all masses. Their discovery

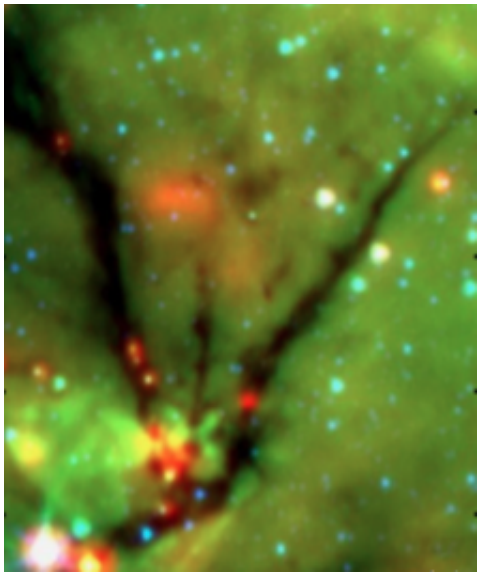

Figure 1.10: A three colour (blue: 3.6 μm, green: 8 μm, and red: 24 μm) image of IRDC, the filamentary structure seen in black. The red/yellow points represent young stars within the clouds while the blue points are foreground stars. (Peretto & Fuller, 2010).

in the protostars, in the early 1980s (Snell *et al.* 1980, Rodriguez *et al.* 1980), revealed a new model of star formation where both infall and ejections coexist (Frank *et al.*, 2014), replacing a model that was purely associated with infall (Huang 1957). Indeed, it was later realised that ejections stem from infall via accretion disks (Pudritz *et al.* 2007, Hartigan *et al.* 1995b). The jets are therefore indicators of disk-fed accretion (Reipurth & Bally, 2001), tracers of accretion history (Kuiper *et al.*, 2015) and pointers of stellar birthplaces. The jets also provide a vent through which part of the high radiation pressure from a forming protostar is released (Kuiper *et al.* 2014, Banerjee & Pudritz 2007). Another fundamental role played by the jets and outflows is the removal of excess angular momentum from a protostar to its ambient medium, giving room for further accretion (Anglada *et al.*, 2018). Jets and outflows can also be used to categorise evolutionary stages of the MYSOs (Beuther & Shepherd, 2005).

Jets are detectable at different wavelengths of the electromagnetic spectrum e.g. at the X-ray (Favata *et al.*, 2002), optical, infrared (Zinnecker & McCaugh-

rean, 1997) and radio (Anglada, 1995) wavelengths. They can be categorised according to the wavelength at which they are detected e.g. radio jets are detectable in the radio wavelengths. Some jets are detectable in more than one wavelength e.g. HH1-2 (see Figure 1.11). In the optical and near-infrared, they are characterised by Herbig-Haro (HH) objects (Reipurth & Heathcote, 1997) and molecular hydrogen emission-line objects (MHOs; Davis *et al.* 2010, Wolf-Chase *et al.* 2017) which are tracers of supersonic shock waves (Bally, 2016).

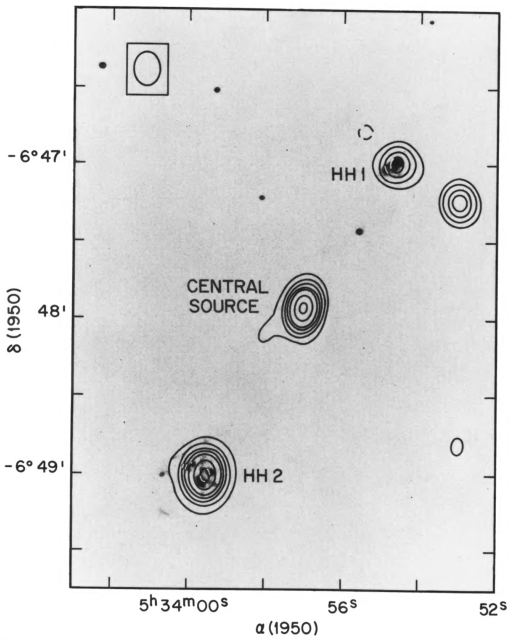

Figure 1.11: Optical map, shown in grey (Herbig & Jones, 1981) and contours of radio continuum emission (Pravdo *et al.*, 1985) of HH1 and HH2 field.

Jets and outflows are composed of molecular, atomic and ionised particles (Cabrit 2002). Molecular outflows, associated with the youngest protostars (age $\sim 10^4$ yrs), are poorly collimated and slow-moving ($v \leq 10\,\mathrm{km\,s^{-1}}$), however, their interiors are characterised by warm and fast-moving ($v > 10 - 100\,\mathrm{km\,s^{-1}}$) gas (Gueth & Guilloteau 1999, Bachiller & Tafalla 1999, Cabrit *et al.* 2011). Morphological differences between the molecular outflows and ionized jets may provide hints about their origin and driving mechanisms. The highly collimated ionized jets are either magnetically (Blandford & Payne 1982, Shu *et al.* 1994a)

or radiatively (Frank & Mellema, 1996) driven, and their particles are believed to originate from any of the three locations; the stellar surface, the inner edge of a disk or the extended region of a disk (Cabrit, 2007). The poorly collimated molecular outflows, on the other hand, are entrained (Klaassen *et al.*, 2013) by the collimated jets through; ploughing of the molecular gas by jet heads, mixing of jet particles with ambient molecular gas due to hydrodynamic instabilities, and deflection of in-falling particles due to rotation of a protostar (Arce *et al.*, 2007). The driving mechanism of the outflows gives them their wide-angle morphology. Atomic jets, driven by more evolved protostars where accretion activities have subsided (Smith, 2004), may also be magnetically driven (Frank *et al.*, 2014). These jets are weak but highly collimated compared to molecular jets.

1.3.2 Roles of Protostellar Jets

Formation of stars takes place within dusty and obscured environments, hindering direct observation of the process at shorter wavelengths. However, at the longer wavelengths, protostellar jets emit radio waves that penetrate the dust, revealing the signatures of accretion and accurate locations of protostellar cores. Owing to the connection between protostellar ejections and accretion (Pudritz *et al.*, 2007), jets can be used to estimate accretion rates. In addition, the objects can be observed at different epochs to study their precession and proper motions (Rodríguez *et al.*, 2010). With the advent of the low radio frequency instruments e.g. LOFAR, it is now possible to estimate the emission measure of most of the sources, including the ones whose free-free turn-over frequencies lie in the low-frequency regime (Coughlan *et al.*, 2017).

Jets and outflows also have an astrochemical impact. They influence the chemical composition of their environments by dragging gases of higher metallicities from a protostellar neighbourhood to the ambient cloud. Other chemicals may also be generated through collision-induced dissociation at the jet shocks. The jets also inject energy and momentum into the clouds (Bally *et al.*, 2007). Finally, the flow of their particles creates cavities through which more materials are swept away, influencing the shape of their environments (Dionatos & Güdel, 2017). Such cavities deprive the forming protostars of gas reservoirs and influence

their upper mass limit (Wang *et al.*, 2010).

1.3.3 Properties of Jets

1.3.3.1 Size and Proper Motion

Protostellar jets exhibit a wide range of sizes spanning ~ 0.1 pc to a few parsecs across (Mundt & Ray, 1994). The sizes can be used to estimate their kinematic ages if velocities of propagation v_j are known. v_j can be calculated from the proper motion of a jet knot or approximated using equation 1.7 (Panoglou *et al.*, 2012), where r_o is the ejection radius and M_* is the mass of the protostar. Typical velocities of the jets are approximated to lie in the range $100 \leq v_j \leq 1000\,\mathrm{km\,s^{-1}}$.

$$v_j \simeq 100 \left(\frac{\mathrm{r_o}}{1\,\mathrm{AU}}\right)^{-\frac{1}{2}} \left(\frac{\mathrm{M_*}}{0.5\mathrm{M_\odot}}\right)^{\frac{1}{2}} \mathrm{km\,s^{-1}} \tag{1.7}$$

If a jet is observed at different epochs, separated by a few years, it is possible to estimate the proper motion of its core as well as resolved jet lobes. The movement of the core can provide information about the displacement of its protostar with respect to neighbouring objects (Anglada *et al.*, 2018) while the proper motion of the lobes tells about the velocity of jet materials. Some observations have captured the ejection of jet lobes from the core, permitting a rough estimate of the launch velocity (Marti *et al.* 1995, Martí *et al.* 1998). In the study by Marti *et al.* (1995), inner knots have lower velocities compared to outer lobes, demonstrating that they get accelerated as they flow away from the core. However, jet lobes also seem to decelerate with time (Anglada *et al.*, 2018) as earlier estimates of lobe velocities by Marti *et al.* (1995), $V_j \sim 600{-}1400\,\mathrm{km\,s^{-1}}$, are higher than Heathcote *et al.* (1998)'s estimates for the same lobes, $V_j \sim$300 - 500 $\mathrm{km\,s^{-1}}$.

1.3.3.2 Opening Angles

Jet materials are understood to be launched through conical openings (Reynolds, 1986) whose angular sizes θ_o are approximated to be a few tens of degrees (Moscadelli *et al.*, 2016). On the contrary, the sizes of HH objects and MHOs which are located farther away from the launch radius display smaller cross-sections that are expected from narrower jets, suggesting that the sources are

re-collimated along the jet. The jets channel out a combination of molecular, atomic and ionised gas, from which the mass of materials flowing through them can be inferred. The mass of ionized matter passing through radio jets in a year is estimated to lie in the range $10^{-9} \leq M \leq 10^{-5}\,\mathrm{M}_{\odot}$ (Konigl & Pudritz 2000, Purser *et al.* 2016), but may vary based on the mass of the core. These estimates are approximately an order of magnitude lower than values derived from molecular outflows, suggesting that radio jets are only partially ionised, i.e, $\sim 1 - 10\,\%$ (Bacciotti *et al.* 1995, Hartigan *et al.* 1994).

1.3.3.3 Rotation and Precession

Reports indicate that ejections from protostars may be rotating about the outflow axis, especially at the early stages of formation (Launhardt *et al.* 2009, Chrysostomou *et al.* 2008). As transporters of angular momentum, the rotation of ejections provides a mechanism through which the momentum is taken away from the vicinity of the central object. Besides rotation, there is evidence of precession in a considerable number of protostellar jets e.g. IRAS13484 − 6100 (Purser *et al.*, 2018) and IRAS 16547 − 4247 (see Figure 1.12; Rodríguez *et al.* 2008), another avenue through which angular momentum is transported away from a protostar. Precession may also be a pointer to binarity or presence of a wobbling accretion disk (Sheikhnezami & Fendt, 2015).

1.3.3.4 Variability

Some protostellar cores show moderate (Martí *et al.*, 1998) and, in some instances, extreme (Cesaroni *et al.*, 2018) variation in flux. Moderate changes are within 10-20 % (Reipurth 1990, Herbig 1966) of an object's flux while in extreme cases, also known as outbursts, the change is higher, i.e., $> 25\,\%$ (Choi *et al.*, 2014). An example of a plot showing how the flux of a protostar, NGC2071 IRS3, vary with the epoch of observation is shown in Figure 1.13. Changes in the flux of a protostellar core are attributed to fluctuations in accretion rates (see equation 1.8). M_*, R_* and $\dot{M}$, in equation 1.8, are the mass, radius and accretion rate of the protostar respectively.

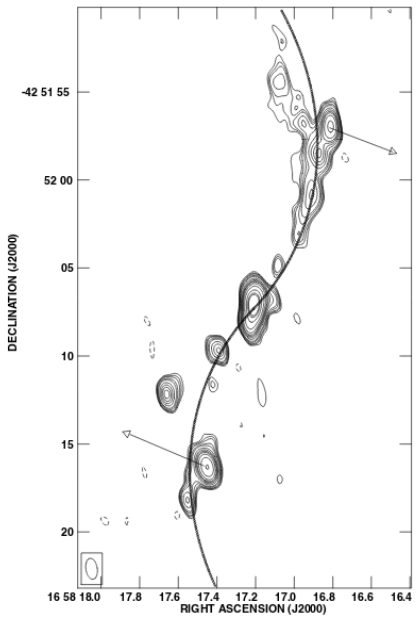

Figure 1.12: VLA image of IRAS 16547 − 4247, a precessing jet, at 8.46 GHz (Rodríguez *et al.*, 2008).

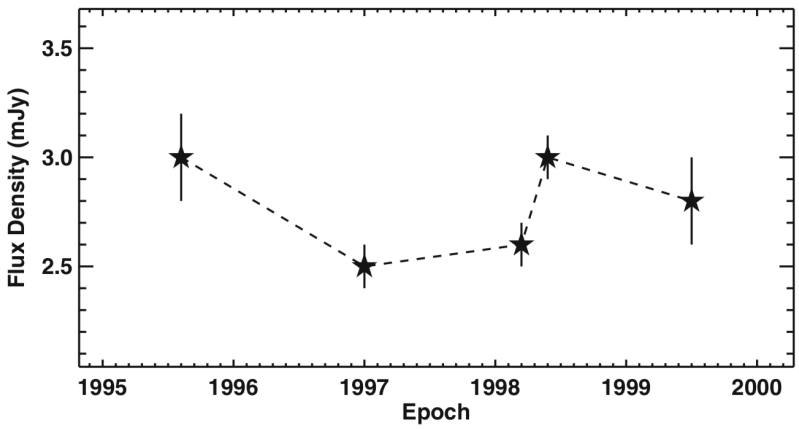

Figure 1.13: Variations of 3.6 cm flux of NGC2071 IRS3 between the years 1995 and 2000 (Anglada *et al.*, 2018).

$$L_{acc} \simeq \frac{GM_*\dot{M}}{R_*} \tag{1.8}$$

Flux outbursts are also known as FU Orionis phenomenon. They only occur within a short period of protostellar evolution. As already mentioned, they are characterised by brightening of protostars and are considered a reflection of an increase in the mass accretion rate through a circumstellar disk. The occurrence dates back to the year 1937 when a protostar named FU Ori (Hoffleit, 1939) went into an outburst. Other known FU Orionis stars are; V 1057 Cygni (Gieseking, 1973), V 1647 Orionis (Walter *et al.*, 2004) and V 1515 Cyg (Herbig, 1977), all of which are low mass stars. Protostars in outburst manifest IR excess emission, change of spectral type to F or G supergiants in the optical and M supergiant in the IR (Hartmann & Kenyon, 1996), strong Balmer absorption lines, broadened spectral lines and P-Cygni profiles at Hα (Bastian & Mundt, 1985). The outbursts are characterised by sharper rise, longer decay periods and are expected to repeat after a period of about 10^4 years in T-Tauri stars (Hartmann & Kenyon 1996, Herbig 1977).

Flux variabilities are attributed to accretion activities, yet the mechanisms responsible for the outbursts are not well-known (Hartmann & Kenyon, 1985). One of the mechanisms proposed is thermal instability. An increase in the flux of accreted materials from the outer to the inner part of a disk heats it (Bell & Lin, 1994), ionizing hydrogen gas in the disk. The ionized gas, as well as sublimation of dust particles that are responsible for extinction (Turner *et al.* 1997, Hartmann & Kenyon 1985), activates a rise in the flux of the disk. Other mechanisms that can cause an increase in accretion rates and reproduce some of the observed properties of FU Ori stars (Hartmann & Kenyon, 1996) are gravitational instabilities and magnetohydrodynamic (MHD) turbulence (Armitage *et al.*, 2001). A gravitationally unstable accretion disk (Liu *et al.* 2016, Vorobyov & Basu 2005), for example, can fragment into clumps which are then accreted episodically. In radio jets, a rise in the flux of thermal cores is directly related to the number density of ionized particles. Given the link between accretion and ejection in protostars (Stepanovs & Fendt 2016, Konigl & Pudritz 2000), higher accretion rates should

correspond to a rise in the amount of materials ejected, thus brighter jets.

Until recently, the FU Orionis phenomenon was largely observed in low mass protostars. However, the latest reports of outbursts in two 20 $M_\odot$ MYSOs, S255 NIRS 3 (Caratti o Garatti *et al.*, 2017) and V723 Carinae (Tapia *et al.*, 2015), suggests that it may equally be common in high mass protostars. Other variable MYSOs are; NGC 6334I (Hunter *et al.*, 2017) and V645 Cygni (Clarke *et al.*, 2006).

1.3.3.5 Radio Emission From Jets

Protostellar jets can radiate continuum, radio recombination line (RRL) and maser emission at centimetre wavelengths (Rosero *et al.* 2016, Jiménez-Serra *et al.* 2011, Burns 2018). Both line and continuum emission are essential in understanding star formation models. Line emission, just like the other radio emissions, penetrates the dusty envelopes of forming protostars, divulging information about their kinematics. However, the low sensitivity of the current instruments and the weak nature of the emission has complicated its detection in radio jets, especially at lower frequencies.

Centimetre radio continuum radiation can be classified as thermal or non-thermal emission. Thermal and non-thermal emission, also known as free-free and synchrotron emission are due to the acceleration of charged particles by electric and magnetic fields respectively (Rybicki & Lightman, 1979). The emissions are distinguishable by their characteristic slopes in a flux density versus frequency plot, in logarithmic scales. The slope of the plot, also known as the spectral index can be used to characterise continuum emission. Spectral index α_ν of thermal emission is ≥ -0.1 while the index of non-thermal radiation $\alpha_\nu < -0.1$. Thermal emission whose spectral index is -0.1 is further classified as optically thin while one whose index is ≥ 0 is said to be optically thick. Models (Wright & Barlow 1975, Reynolds 1986) indicate that the flux density of radio continuum emission and the frequency of emission are related by equation 1.9.

$$S_\nu \propto \nu^{\alpha_\nu} \tag{1.9}$$

Emission from ionized spherical winds has a characteristic spectral index of 0.6

(Wright & Barlow 1975, Reynolds 1986). Ionized winds are said to be spherical if they move at a constant velocity, are isothermal, have a constant ionization fraction and their density varies with the radius of flow r according to equation 1.10, where r_o is the launch radius of the winds. The major axes of thermal jets also exhibit a decrease with frequency of observation as $\theta_\nu \propto \nu^{\alpha-1.3}$ (Reynolds, 1986).

$$\rho \propto \left(\frac{r}{r_o}\right)^{-2} \tag{1.10}$$

Most protostellar jets radiate thermal emission whose spectral indices are moderately positive, i.e., $0.1 \leq \alpha \leq 1.0$ (Anglada *et al.*, 2018). The average spectral index of thermal emission, expected from the cores of protostellar jets, is 0.5 (Rosero *et al.*, 2016). A few young stellar objects e.g. IRS 5 (Feigelson *et al.*, 1998) are known to be dominated by synchrotron emission. In this example, however, the orientation of the YSO is approximately 0° to our line of sight, i.e., its pole is facing the earth and the emission could be from its jet lobes. T Tauri stars also display strong magnetic activities and non-thermal properties (del Valle & Romero, 2011).

1.3.4 Models of Protostellar Jets

It is clear, from observations, that protostars of all masses drive out well-collimated jets. However, the mechanisms responsible for ejection, acceleration and collimation of the jet materials are not well known. There are two mechanisms, magnetic (Shu *et al.* 1994a, Pudritz & Norman 1983) and radiative (Frank & Mellema, 1996), that are currently used to explain how protostellar jets are driven (see illustration in Figure 1.14). Examples of magnetically and radiatively driven jets are HH 80-81 (Carrasco-González *et al.*, 2010) and W75N B (Carrasco-González *et al.*, 2015) respectively.

High mass stars, however, are not expected to have the magnetic field strengths seen in low mass counterparts (Shultz *et al.*, 2015) since they have radiative envelopes. This conundrum may be overcome through a star formation model by Hosokawa & Omukai (2009), where a massive protostellar core of mass $10\,\mathrm{M}_\odot \leq M \leq 30\,\mathrm{M}_\odot$, accreting mass at a high rate, $> 10^{-4}\,\mathrm{M}_\odot\mathrm{yr}^{-1}$, goes through a phase where its envelope is swollen and convective, and therefore capable of generating

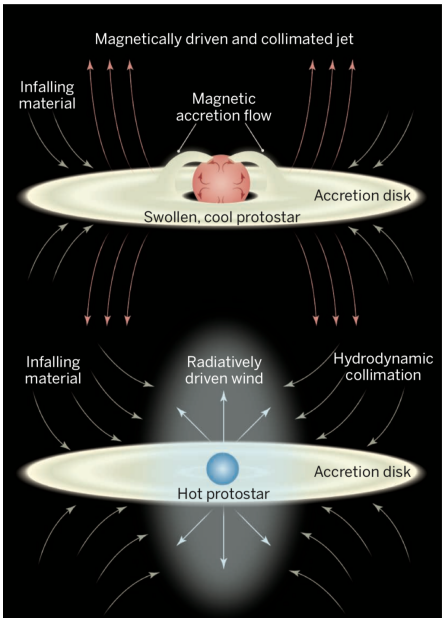

Figure 1.14: Illustrations showing how protostellar jets are magnetically and radiatively driven (Hoare, 2015).

magnetic fields.

1.3.4.1 Radiatively driven jets

Radiatively driven jets are launched due to radiation pressure and collimated when protostellar wind bubbles interact with the ambient medium. The collapse of protostellar cores is accompanied by rotation to conserve angular momentum. The rotation occasions toroidal distribution of material around the protostars. As protostellar winds collide with the toroidally distributed matter, a collimated and pressure confined prolate-like bubble is formed (Frank & Mellema 1996, Konigl 1982, Koo & McKee 1992).

Launch of the materials takes place at the poles of the shell through a nozzle similar to a de Laval nozzle. The collimated winds undergo converging conical flow, colliding adiabatically, and giving rise to high pressure at the poles (Canto *et al.*, 1988). The pressure at the poles can launch jet materials at high velocities. This model has two shortcomings; heat dissipation through the high-density materials and an unstable nozzle (Frank & Mellema, 1996).

1.3.4.2 Magnetically Driven Jets

Today, two models describe how MHD jets are driven, i.e., X- and disk- wind. In an X-wind model, both the central core of a YSO and its accretion disk are magnetised while in the disk wind, only the disk requires the presence of magnetic fields.

X-Wind Model: In an X-wind jet model, jet materials are ejected from an X-region that is located on the inner part of a protostellar disk (Shu *et al.*, 1994a). This region is an interface between the magnetosphere of the protostar and the magnetic field of its accretion disk. It is formed when magnetic field lines of a strongly magnetised protostar thread its partially conducting accretion disk; in effect, interacting with the disk's shielding surface current and magnetic field. Protostellar field lines can only slip into the disk's inner part where it co-rotates with the protostar. Any particles to the interior of the X region are funnelled to the star while those to the outer part are ejected off the disk in a magneto-centrifugal manner (see Figure 1.15).

Disk-Wind Model: This model, originally proposed by Blandford & Payne (1982) to describe how galactic jets are driven was later modified by Pudritz & Norman (1983) to explain jet driving mechanisms in protostars. According to the model, if a protostellar disk has poloidal magnetic field lines, threading it at an angle $\theta < 60^o$ to the surface of the disk, then disk winds can be launched magneto-centrifugally from its surface (Smith 2004, Blandford & Payne 1982). Such winds begin to form when a protostar is in a position to ionize the inner part of its accretion disk, also known as the disk core region (Pudritz & Norman, 1983). Rotation of the protostar aids twisting of the magnetic field lines, leading to the formation of a helical field pattern that is capable of collimating the jet.

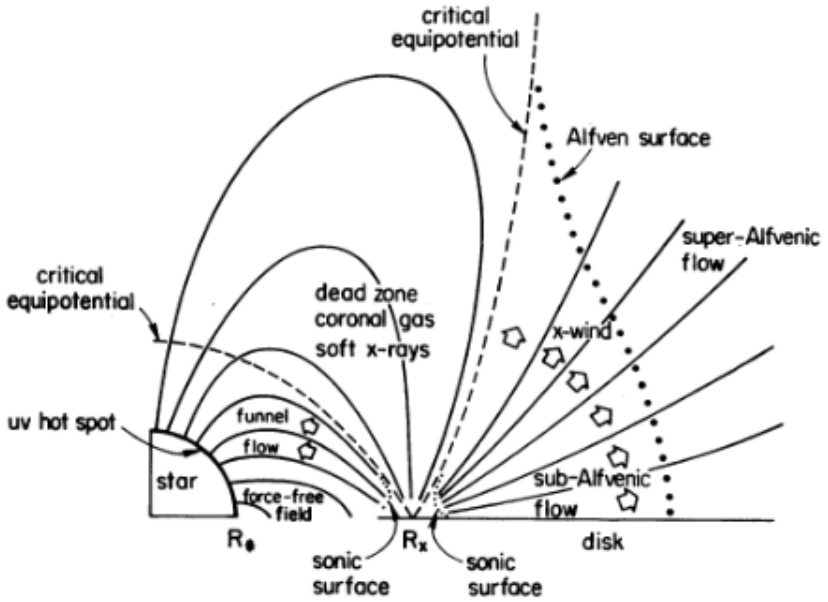

Figure 1.15: An illustration of X-wind model by Shu *et al.* (1994a) showing the location of X region and its distance from the star R_x.

1.4 Instruments and Techniques of Radio Astronomy

The detection of radio emission from the centre of the Milky Way by Jansky (1933) opened a window of observing the universe at radio wavelengths. Since then, better radio telescopes, with expanded frequencies of observation, improved sensitivities and higher resolutions have been developed (Wilson, 2011). Indeed, the baseline and sensitivity of the next generation of telescopes, e.g. the Square Kilometre Array (SKA; Keane 2018) and the next-generation VLA (ngVLA; McKinnon *et al.* 2019) will greatly improve the capabilities of their precursors. For example, the SKA will have a baseline that extends across the African continent and an effective collection area of one square kilometre after completion.

A radio telescope can image as a single-dish or an array of antennas called an interferometer. Interferometers have higher resolutions, defined by their maximum baselines (Thompson *et al.*, 2001), unlike in single-dish telescopes where the maximum resolution is set by the diameter of the dish. As a result, this study

was conducted using data from the Jansky Very Large Array (JVLA; Perley *et al.* 2011), a sensitive and a high-resolution interferometer. The JVLA has movable antennas and is re-configurable in four principal arrays; A, B, C and D. Its A-configuration has the longest baseline, b=36.4 km, capable of resolving some of the jets of the distant protostars.

The functioning of an interferometer involves two steps; collecting signals from an astronomical object through its antenna and matching them through a correlator. The correlator matches the signal to generate power values (Thompson *et al.*, 1986) by multiplying and integrating voltages received by the antennae. Cross-correlation of signals, say $v_i(t)$ and $v_j(t)$, from two antennae, i and j respectively, can be written as $X_{ij}(\tau) = v_i(t)v_j(t+\tau)$, where τ is the time delay due to antenna separation (D'Addario, 1982). The working principle of an interferometer can be illustrated using the simplest radio interferometer, a pair of antenna separated by a distance d, normally represented by a vector called the baseline $\vec{b}$ (see Figure 1.16). Plane waves from a distant object arrive at the two antennas at different times causing a path difference (phase) due to the time delay (Condon & Ransom, 2016). The path length between the signals is given as $c\tau = \vec{b}.\hat{s}$, where $\hat{s}$ is a unit vector in the direction of the source and c is the speed of the wave. The phase difference (ϕ) can also be written in terms of the wavelength of the incident radiation λ and path length $\vec{b}.\hat{s}$ using equation 1.11 or 1.12, out of which interferometric quantities called visibilities can be calculated. Visibility is a measure of variations in interference pattern (fringes), giving information about the brightness and location of the source of the radio wave. Mathematically, the visibility, V_{ij}, due to two antennas i and j, can be represented by equation 1.13 where I_ν is the brightness of the source at the frequency of observation ν.

$$\phi = \frac{\vec{b}.\hat{s}}{\lambda} \tag{1.11}$$

$$\phi = e^{-2\pi i \frac{\vec{b}.\hat{s}}{\lambda}} \tag{1.12}$$

$$V_{ij} = I_\nu e^{-2\pi i \frac{\vec{b}.\hat{s}}{\lambda}} \tag{1.13}$$

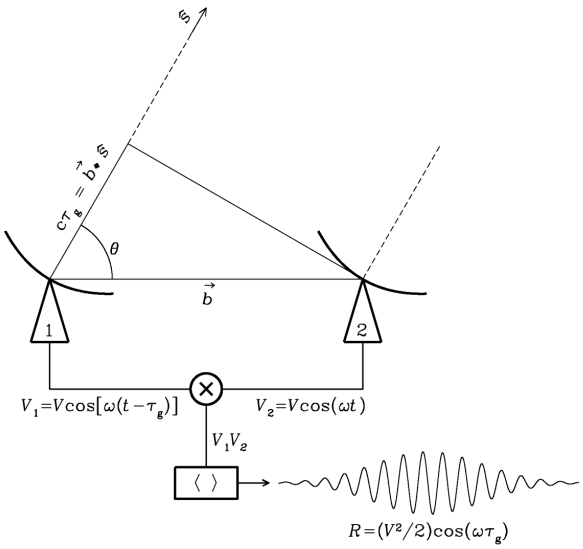

Figure 1.16: An illustration of a two element interferometer and how correlator multiplies signals (Thompson *et al.*, 1986).

Conventionally, interferometric elements are represented in a Cartesian coordinate system with axes (u, v, w), where u and v axes are in the east-west and north-south directions while w is an up-down axis. If an interferometer lies on a plane, which is normally assumed to be the case, then $w = 0$. Corresponding to the interferometric (u,v,w) coordinate system is a target's sky coordinate system whose axes are denoted by $(l, m, \sqrt{1-l^2-m^2})$, with l and m axes in east-west and north-south directions as well, while $\sqrt{1-l^2-m^2}$ is an up-down counterpart.

The baseline vector $\vec{b}$, in units of wavelength λ and the unit vector in the direction of the source $\hat{s}$ can be written in terms of the coordinate systems of an interferometer and a target, i.e., $\frac{\vec{b}}{\lambda}(u, v, w)$ and $\hat{s}(l, m, \sqrt{1-l^2-m^2})$ respectively, to yield equation 1.14. The visibility V_{ij} due to a single baseline and time delay is given by equations 1.15 while the equations describing the sum of visibilities

are 1.16 and 1.17.

$$\begin{aligned} \frac{\vec{b}.\hat{s}}{\lambda} &= (u,v,w).(l,m,\sqrt{1-l^2-m^2}) \\ \frac{\vec{b}.\hat{s}}{\lambda} &= (ul+vm+w\sqrt{1-l^2-m^2}) \end{aligned} \tag{1.14}$$

$$\begin{aligned} V_{ij} &= I_\nu e^{-2\pi i \frac{\vec{b}.\hat{s}}{\lambda}} \\ V_{ij} &= I_\nu e^{-2\pi i(ul+vm+w\sqrt{1-l^2-m^2})} \end{aligned} \tag{1.15}$$

$$V = \Sigma V_{ij} = \Sigma I_\nu e^{-2\pi i(ul+vm+w\sqrt{1-l^2-m^2})} \tag{1.16}$$

$$V(u,v) = \int\int I(l,m) e^{-i2\pi(ul+vm)} dldm \tag{1.17}$$

Seeing that the visibility is related to the brightness of the source of incident signals as shown in equation 1.17, i.e., a $u-v$ plane; the visibilities are a 2-dimensional Fourier transform of the sky brightness $I_\nu(l,m)$, and it is possible to recover sky brightness from the visibilities. The sky brightness $I_\nu(l,m)$ can, therefore, be recovered from the visibilities $V(u,v)$ through performing an inverse Fourier transform on the visibilities (see equation 1.18).

$$I_\nu(l,m) = \int\int V(u,v) e^{i2\pi(ul+vm)} dudv \tag{1.18}$$

Interferometers cannot fill in the entire Fourier domain that corresponds to a true sky image. They only sample part of the sky, with a single baseline only sampling a single spot on the sky unless rotated. Thus, imaging the sky and recovering its brightness $I_\nu(l,m)$ is influenced by the distribution of the visibilities on the $u-v$ plane (also known as sampling the $u-v$ plane). The distribution of the visibilities on the $u-v$ plane is directly related to the amount of information they give about the sky. Each visibility has information about the phase and magnitude of the sky's spatial frequencies. Ideally, recovery of every part of the

observed sky requires a $u-v$ plane that is totally filled with the visibilities. This is not the case as radio telescope arrays only sample part of the sky, giving rise to sampled u-v planes. Sampling of the $u-v$ plane has a function that convolves with the visibility function, giving rise to a dirty map $I'_\nu(l,m)$ of the observed sky, represented mathematically by equation 1.19.

$$I'(l,m) = \int\int S(u,v)V(u,v)e^{i2\pi(ul+vm)}dudv \tag{1.19}$$

Here, S(u,v) is the sampling function of the visibilities on a u-v plane. S(u,v) is assigned a value of one where V(u,v) is present and zero otherwise.

The dirty map, equation 1.19, is the inverse Fourier transform of a product of the sampling function S(u,v) and the visibility function V(u,v). It is equivalent to the convolution of the point spread function or synthesised beam $b(l,m)$ and the sky brightness $I_\nu(l,m)$, i.e., $I'_\nu = b(l,m) \circledast I_\nu(l,m)$, where $b(l,m) = \int\int S(u,v)e^{-i2\pi(u+v)}dudv$. The convolution theorem of Fourier transforms allows us to disentangle the sampling effect to recover a model of the sky brightness $I_\nu(l,m)$.

1.5 Thesis Outline

Jets are indirect indicators of accretion disks, and their presence points to disk-fed accretion in protostars. Their driving mechanisms are still debatable, especially in massive protostars, however, simulations of magnetically driven jets can reproduce observable features of the protostars. This thesis, therefore, investigates the radio properties of a sample of massive protostellar jets, using a combination of observations and modelling, specifically to establish the prevalence of non-thermal emission in massive protostars. The thesis is subdivided into five chapters. Chapter 1 details a review of the relevant literature. In Chapter 2, the results of a search for the non-thermal (synchrotron) radio emission from a sample of massive protostars as well as the procedures used in conducting the search are presented. The emission was characterised as thermal or non-thermal based on spectral index maps and spectral energy distribution (SEDs) of the sources. During the study of the sample, some of the protostars displayed evidence of vari-

ability, as a result, the property was explored in a sample of four protostars (see Chapter 3). Both flux and positional variabilities were considered. In Chapter 4, the procedure and results of numerical hydrodynamics simulations of ionized jets are presented. Typical values of observable quantities were used to initialise the simulations. Fluxes of the simulated jets were also calculated using a ray-tracing code. Finally, in Chapter 5 the conclusions and possible areas of future work, drawn from the study, are presented.

Chapter 2

Non-Thermal Emission From Massive Protostars

2.1 Introduction

Any interaction between a moving charged particle and magnetic field causes radial acceleration (Rybicki & Lightman, 1979). For non-relativistic particles, the radiation emitted due to the interaction is called cyclotron emission and the frequency of emission is equivalent to the frequency of gyration of the particles around the field. Relativistic particles, on the other hand, produce synchrotron emission (Condon & Ransom, 2016), characterised by a broad spectrum, high intensity, both circular and linear polarisation and high collimation (Winick & Doniach, 1980).

Synchrotron radiation is ubiquitous in astronomy and is significant in pointing out the presence of magnetic fields and relativistic charged particles. It is usually referred to as non-thermal emission, i.e., radiation whose characteristics are not influenced by the temperature of the source. However, it is significant to note that there are other non-thermal emissions, e.g., stimulated emission and emission from Compton scattering. Examples of astrophysical sources that emit synchrotron radiation include; active galactic nuclei (AGNs), stars, protostars (Girart *et al.*, 2009) and even planets, e.g., Jupiter. The processes involved in generating the emission are unique to the objects. In Jupiter, for example, the

emission is due to an interaction between its relativistic charged particles, accelerated adiabatically (Kollmann *et al.*, 2018) and magnetic fields, generated via the dynamo effect (Russell, 1993).

Protostars are known to emit synchrotron radiation irrespective of their masses (Lee *et al.*, 2018) or stages of evolution (Girart *et al.* 2009, Carrasco-González *et al.* 2010). Nonetheless, the details of how magnetic fields and relativistic charged particles are generated by protostars are not yet clear. A model for generating magnetic fields in a protostar was proposed by Latif & Schleicher (2016). In the model, the field is generated via fluctuations in protostellar plasma and amplified through the dynamo effect. This model is effective in low mass protostars whose envelopes are convective and can generate strong magnetic fields via the dynamo effect. High mass protostars, on the other hand, have high surface temperatures and radiative envelopes (Hoare, 2015), a difficulty which may be solved through the star formation model by Hosokawa & Omukai (2009) where a massive protostar goes through a swollen and convective phase as it evolves.

The mechanism responsible for accelerating the charged jet particles to relativistic levels is known as first-order Fermi acceleration or diffusive shock acceleration (Bell 1978, Blandford & Eichler 1987). This mechanism takes place in collisionless shocks where energy is only dissipated through wave-particle interaction and not particle-particle collision. The shocks enhance acceleration by amplifying magnetic fields through compression, current-driven instabilities and turbulence (Ji *et al.*, 2016). Actual acceleration of a charged particle occurs as it crosses a shock-front through gain of energy. The energy of a particle after crossing a shock-front downstream and back is given by equation 2.1 (Bell, 1978), where E_k is the initial energy of the particle upstream, v_{k1} is the velocity with which the particle crosses the shock from upstream to downstream and θ_{k1} is the angle between the direction of motion of the particle and the normal of the shock-front. v_{k2} and θ_{k2} are the return velocities and angles upstream.

$$E_{k+1} = E_k \frac{1 + v_{k1}(u_1 - u_2)\cos\theta_{k1}/c^2}{1 + v_{k2}(u_1 - u_2)\cos\theta_{k2}/c^2} \tag{2.1}$$

Two conditions are necessary for the acceleration of the charged particles to relativistic velocities; (i) a mechanism that constrains the particles to cross the

shocks repeatedly and (ii) particles whose energies are higher than the thermal energy of the shock. Movement of a shock through a jet cavity or the interstellar medium is accompanied by disturbance of jet plasma which can cause magnetic turbulence. As the turbulence dissipates downstream, it can scatter any energetic charged particles to bounce back upstream at larger gyroradii, capable of crossing the shocks. This process can repeat several times until relativistic energies are achieved.

Spectral indices are a key element in determining the presence of synchrotron emission in protostellar jets, for example, the spectral index analysis of HH 80-81 (Rodríguez-Kamenetzky *et al.* 2017, Vig *et al.* 2018) and the triple radio source in the Serpens star-forming region (Rodríguez-Kamenetzky *et al.*, 2016). Ionised thermal jets have spectral indices ~ 0.6 (Reynolds, 1986), but as shown by Brooks *et al.* (2007) and Vig *et al.* (2018) the terminal shocks in the jet can be non-thermal. Vig *et al.* (2018) demonstrated the value of studying the spectral index for non-thermal emission at lower radio frequencies by using the radio flux of non-thermal lobes to derive equipartition magnetic fields. A more spectacular example of a non-thermal jet was reported by Carrasco-González *et al.* (2010), where polarized synchrotron emission was seen in an extended jet arising from the MYSO GGD27 and showed magnetic field lines parallel to the jet's outflow axis (see Figure 2.1). This jet does show a thermal inner region, however. Indeed, of the three components of a protostar, i.e., the central object, the disk and the jet, non-thermal emission is largely expected from the jets and, in some low mass cases, the central object (White *et al.*, 1992). In massive protostars, the envelopes of the central objects are dusty (McKee & Chakrabarti, 2005), capable of absorbing the energetic electrons which are responsible for generating the emission. The jets of both low and high mass protostars are thus the major emitters of non-thermal radiation (Carrasco-González *et al.* 2013, López-Cámara & Raga 2010, Velusamy *et al.* 2007).

Motivated by the need to establish the prevalence of non-thermal emission in jets of massive protostars, a sample of MYSOs were observed at L-band (frequency range 1-2 GHz and central frequency ν =1.5 GHz) where synchrotron emission is dominant and easily detectable. Previous C- and Q-band observations by Purser (2017) were also used in the study. The C-and Q-band observations were of

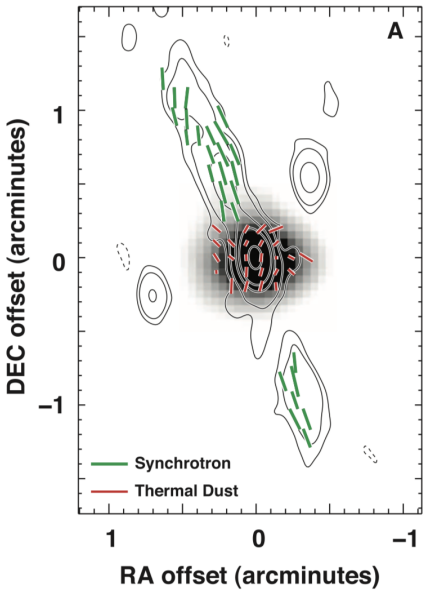

Figure 2.1: HH 80-81 field showing its 850 μm dust emission and 6 cm continuum emission as a grey map and grey contours respectively. The green and red bars represent the directions of magnetic fields, inferred from synchrotron- and dust-polarisations respectively (Carrasco-González *et al.*, 2010).

bandwidths 2 GHz and 8 GHz, centred at 6 GHz and 44 GHz, respectively.

2.2 Sample Selection

Fifteen objects, listed in Table 2.1, were selected from a sample of 63 MYSOs that were previously observed in C-band at 6 GHz using the NRAO's [1] Jansky Very Large Array (JVLA) telescope (Purser, 2017). These objects were the brightest in the C-band sample and had the highest likelihood of being detected in L-band at 1.5 GHz. All of the fifteen objects were chosen from the RMS catalogue [2] (Lumsden *et al.*, 2013). The sample spans a wide range of bolometric luminosities ($2,600 \leq L_{bol} \leq 44,620\,L_{\odot}$) and infrared colours ($4 \lesssim \frac{F_{21\mu m}}{F_{8\mu m}} \lesssim 22$), suggesting that they represent different evolutionary stages. A plot of known infrared dark clouds, MYSOs and HII regions, shown on the e-MERLIN Legacy programme web

[1] National Radio Astronomy Observatory
[2] http://rms.leeds.ac.uk/cgi-bin/public/RMS_DATABASE.cgi

page[1], clearly shows an evolutionary pattern (see Figure 2.2). The trend manifests the shift in the peak of the spectral energy distribution (SED) of MYSOs towards shorter wavelengths as they evolve towards the main sequence (Molinari *et al.*, 2008). The plot, however, cannot be used to distinguish between YSO and HII-regions since their infrared properties overlap. An alternative plot, that may be effective in selecting MYSOs is the radio- versus bolometric- luminosity graph, assuming that collisional ionization is the only mode of ionization in both low and high mass protostars.

Finally, the distances to the sources were considered during the selection and only the sources at a distance $d \lesssim 7\,\mathrm{kpc}$ from the Sun were selected. Given the typical sizes of MYSO jets which lie in the range $\sim 0.1\,\mathrm{pc}$ to $2.4\,\mathrm{pc}$ (Mundt & Ray, 1994), it is only possible to resolve some of the lobes within the jets at the frequency of observation and telescope configuration (i.e resolution of $1''.2$) if they are nearby.

2.3 Observations and Data Reduction

2.3.1 Observation

The 15 objects were observed on the 8^{th}, 19^{th} and 22^{nd} of August 2015 using the JVLA in the A configuration array under project code 15A-218. All the observations were done using the telescope's 27 antennae at a resolution θ_{HPBW} of $\sim 1''.2$. Both continuum and maser emission were observed. Four OH maser lines of rest frequencies 1612 MHz, 1665 MHz, 1667 MHz and 1720 MHz (Wright, 2001) were observed at a spectral resolution of 1 MHz to assist in the phase-only self-calibration of the data. Continuum data were observed in sixteen spectral windows (SPW), each of bandwidth 64 MHz. The spectral windows were further subdivided into 64 channels, each of width 1 MHz to ease the flagging procedure and control the spread of RFI (radio-frequency interference) across the observed frequencies. The sources observed at L-band were also observed at C-band in 2012 and some of them at Q- band in 2014/15 (Purser, 2017) using the JVLA's A configuration. Synthesised beams of C- and Q-bands are typically $0.''33$ and

[1] http://www.e-merlin.ac.uk/legacy/proposals/e-MERLIN_Legacy_MassiveSF.pdf

Table 2.1: Table showing object names, pointing centres, distance from the Sun and bolometric luminosities as taken from the Urquhart *et al.* (2011) catalogue. Local rms noise levels of the maps and properties of their restoring beams (size in arcsec and position angle in degrees) at L-band are also shown. The types of self-calibration that were performed on the images are represented by P for phase-calibration and A for amplitude calibration. The numbers before P denotes the number of cycles of phase self-calibration.

RMS Name	Common Name	RA (J2000)	Dec (J2000)	d (kpc)	L_{Bol} ($L_{\odot}$)	Field rms (μJy/beam)	Beam size maj ($''$) × min ($''$)	Beam PA (^{o})	Self-Cal
G083.7071+03.2817	-	$20^h33^m36.51^s$	$+45°35'44.0''$	1.4	3900	25	1.45 × 1.13	83.0	–
G094.2615-00.4116	IRAS 21307+5049	$21^h32^m30.59^s$	$+51°02'16.0''$	5.2	9000	33	1.47 × 1.09	82.3	P/A
G094.4637-00.8043	IRAS 21334+5039	$21^h35^m09.14^s$	$+50°53'08.9''$	4.9	21000	25	1.47 × 1.11	82.6	P/A
G094.6028-01.7966	V645Cyg	$21^h39^m58.25^s$	$+50°14'20.9''$	4.0	43000	24	1.49 × 1.13	83.1	P
G103.8744+01.8558	IRAS 22134+5834	$22^h15^m08.97^s$	$+58°49'07.3''$	1.6	6800	23	1.53 × 1.08	78.2	3P/A
G108.5955+00.4935C	IRAS 22506+5944	$22^h52^m38.09^s$	$+60°01'01.1''$	4.3	3000	17	1.30 × 1.10	-26.7	–
G110.0931-00.0641	IRAS 23033+5951	$23^h05^m25.16^s$	$+60°08'15.4''$	4.3	11850	18	1.31 × 1.16	-19.8	–
G111.2552-00.7702	IRAS 23139+5939	$23^h16^m10.40^s$	$+59°55'28.2''$	3.5	9870	18	1.39 × 1.20	-22.9	–
G111.5671+00.7517	NGC 7538 IRS 9	$23^h14^m01.76^s$	$+61°27'19.9''$	2.7	44620	29	1.32 × 1.22	-17.9	–
G114.0835+02.8568	IRAS 23262+6401	$23^h28^m27.76^s$	$+64°17'38.5''$	4.2	7130	20	1.33 × 1.06	-13.5	2P/A
G126.7144-00.8220	S187 IR	$01^h23^m33.17^s$	$+61°48'48.2''$	0.7	2600	20	1.47 × 1.06	-25.1	P/A
G136.3833+02.2666	IRAS 02461+6147	$02^h50^m08.57^s$	$+61°59'52.1''$	3.2	7800	40	1.50 × 1.15	-05.1	–
G138.2957+01.5552	AFGL 402d	$03^h01^m31.32^s$	$+60°29'13.2''$	2.9	17000	25	1.45 × 1.12	25.8	–
G139.9091+00.1969A	AFGL 437s	$03^h07^m24.52^s$	$+58°30'43.3''$	3.2	11000	25	1.29 × 1.06	21.2	–
G141.9996+01.8202	AFGL 490	$03^h27^m38.76^s$	$+58°47'00.1''$	0.8	5500	28	1.30 × 1.06	27.4	P

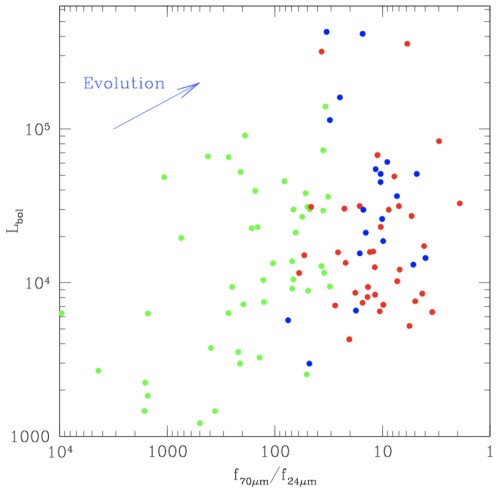

Figure 2.2: A plot showing the distribution of the different phases of massive protostars on an infrared colour versus a bolometric luminosity plot. The green, blue and red points represent the infrared dark cloud (IRDC), hypercompact HII region and the MYSOs that drive jets respectively.

0.″04 respectively. Noise levels in the C- and Q-band maps lie in the range $\sim 6.5-10\,\mu$Jy and $\sim 35-60\,\mu$Jy at full $uv-$range i.e 13-800 kλ and 100-5300 kλ respectively.

The average duration of the individual scans for the flux calibrator, phase calibrators and targets were $\sim$ 7 minutes, 2 minutes and between 3-7 minutes respectively. The phase calibrators were used to correct for instrumental and atmospheric effects on the phases and flux densities of the science sources. Each of the science objects had a total integration time of $\sim 30-40$ minutes. Table 2.2 shows the calibrators and their fluxes at L-band. All the calibrators are point-like at L-band (see Figures 2.3 and 2.4).

2.3.2 Calibration and Imaging

Calibration and imaging were done using NRAO's CASA (Common Astronomy Software Applications; McMullin *et al.* 2007). Image reconstruction was done using the CASA task CLEAN in the multi-frequency synthesis (`mfs`) mode. CLEAN components of the fields were identified from defined regions, specified by clean masks. The masking was done hierarchically with the brightest objects in the

Table 2.2: Calibrators, their fluxes at L-band and the corresponding objects that they were used to calibrate.

Calibrator	Type	RA (J2000)	DEC (J2000)	Flux (Jy)	Calibrated Objects
3C286	Flux	$13^h31^m08.29^s$	$+30°30'33.0''$	14.91±0.05	G083.7071+03.2817
					G094.2615-00.4116
					G094.4637-00.8043
					G094.6028-01.7966
					G103.8744+01.8558
3C48	Flux	$01^h37^m41.30^s$	$+33°09'35.1''$	16.7±0.1	G108.5955+00.4935C
					G110.0931-00.0641
					G111.2552-00.7702
					G111.5671+00.7517
					G114.0835+02.8568
					G126.7144-00.8220
					G136.3833+02.2666
					G138.2957+01.5552
					G139.9091+00.1969A
					G141.9996+01.8202
J0019 + 7327	Phase	$00^h19^m45.78^s$	$+73°27'30.0''$	0.610±0.004	G114.0835+02.8568
J0102 + 5824	Phase	$01^h02^m45.76^s$	$+58°24'11.1''$	2.181±0.008	G126.7144-00.8220
					G136.3833+02.2666
J0303 + 4716	Phase	$03^h03^m35.24^s$	$+47°16'16.3''$	2.058±0.002	G138.2957+01.5552
					G139.9091+00.1969A
					G141.9996+01.8202
J2023 + 5427	Phase	$20^h23^m55.84^s$	$+54°27'35.8''$	0.884±0.001	G083.7071+03.2817
J2148 + 6107	Phase	$21^h48^m16.05^s$	$+61°07'05.8''$	1.923±0.004	G103.8744+01.8558
					G108.5955+00.4935C
					G110.0931-00.0641
					G111.2552-00.7702
					G111.5671+00.7517
J2202 + 4216	Phase	$22^h02^m43.29^s$	$+42°16'40.0''$	2.615±0.002	G094.2615-00.4116
					G094.4637-00.8043
					G094.6028-01.7966

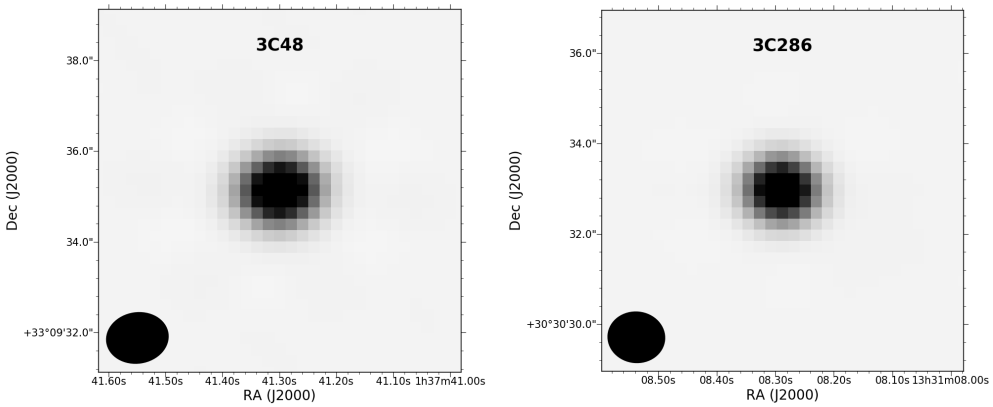

Figure 2.3: Images of flux calibrators at L-band

field masked first. If an object or a nearby source was bright enough, notably a signal-to-noise (SNR) $\gtrsim$10 (Brogan *et al.*, 2018), then a phase-only self-calibration (Pearson & Readhead, 1984) of between 1-3 iterations was carried out until a much smaller phase scatter was achieved, i.e., minimal variations in phase vs time plot are realised. Qualities of some of the images were further improved by performing an amplitude self-calibration on them, especially if the dynamic range of an image was higher than 1000 (Brogan *et al.*, 2018).

While CLEANing the data, the *uv* visibilities for most of the objects were weighted using Briggs weighting with a robustness parameter of 0.5 (Briggs, 1995), resulting in synthesised beams with an average size $1.4'' \times 1.1''$. In some circumstances, where a source was faint or highly affected by a diffuse and bright emission, other appropriate robustness parameters were adopted. Briggs weighting of robustness $r = 0$ provides a balance between resolution and sensitivity. A weighting of robustness parameter of 2, also known as natural weighting, gives equal weights to all samples. This weighting results in a higher sensitivity since the lower spatial frequencies are normally well sampled compared to higher spatial frequencies. Uniform weighting which corresponds to a Briggs weighting of robustness parameter -2, on the other hand, gives equal weights to all the frequencies leading to a higher resolution but lower sensitivity.

The rms noise levels of the cleaned maps of full $uv-$ coverage, $\sim 2 - 220\,\mathrm{k}\lambda$, lie in the range $18 - 40\,\mu$Jy with objects close to bright and extended sources

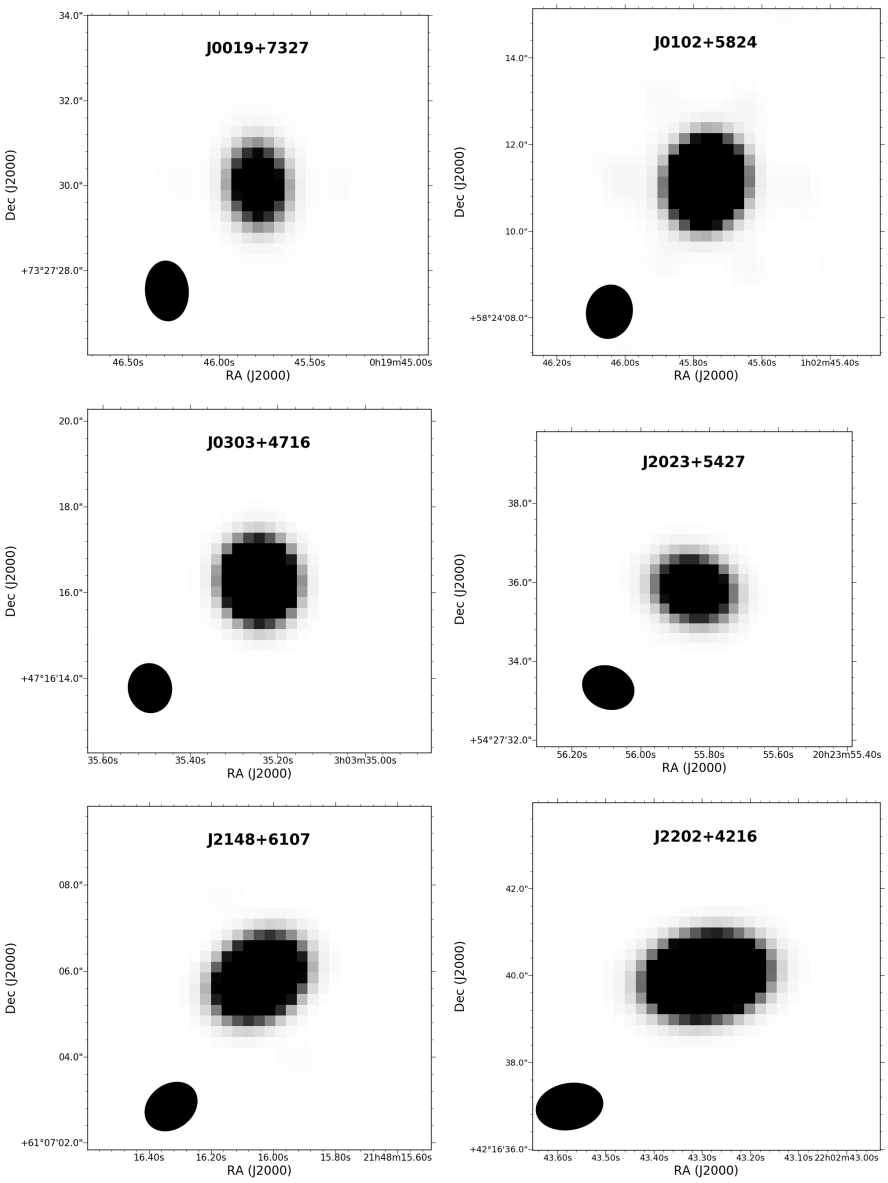

Figure 2.4: Images of the phase calibrators at L-band.

having higher rms noise. A list of the objects, local rms noise and properties of synthesised beams is shown in Table 2.1.

2.4 Infrared Emission

Massive protostars are embedded in natal clouds containing dust particles. The particles can be distributed into various geometries by jets and outflows, creating cavities and shells within the clouds. Light from the embedded sources can then scatter off the dust, at NIR wavelengths, tracing their structure. The jets also have shocks that radiate molecular hydrogen emission at the infrared, i.e 2.12 μm. As a result, infrared images were relied upon to provide helpful hints for the presence of protostellar outflows and jets.

Most of the infrared images used in the study were generated by the Wide Field Camera (WFCAM; Casali *et al.* 2007) of the United Kingdom Infrared Telescope (UKIRT; Lawrence *et al.* 2007) as part of the UKIDSS Galactic Plane Survey (Lucas *et al.*, 2008). UKIRT is a 3.8-m telescope whose typical angular resolution is $\sim$0.8$''$ (Lucas *et al.*, 2008). WFCAM has a pixel scale of 0.4$''$ and observes at five IR wavebands; Z, Y, J, H and K of wavelength range 0.83$-$2.37 μm. However, only three of the bands; J, H and K of central wavelengths 1.2483 μm, 1.6313 μm and 2.2010 μm respectively (Hewett *et al.*, 2006) were used in the study since they are the bands which are least affected by dust. Besides, 2MASS (Two Micron All Sky Survey) images of some of the objects were inspected, especially if their declinations are above the region of the sky covered by UKIDSS i.e $\delta > 60^o$, even though the images are of a lower resolution (i.e a pixel size of 2$''$) and sensitivity (Skrutskie *et al.*, 2006). Also used were findings from H_2 emission observations of the MYSOs e.g. Navarete *et al.* (2015), Wolf-Chase *et al.* (2017), Varricatt *et al.* (2010) and Davis *et al.* (1998).

GLIMPSE's mid-infrared band, centred at 4.5μm, detects the excess 4.5μm emission besides radiation from dust. The extended emission is a tracer of ionized gas and shocked molecular gas (H_2 and CO), a feature that was used to identify a class of MYSOs described as the extended green objects (EGO; Cyganowski *et al.* 2008). These objects, characterised by shocked molecular outflows, are thought to be massive protostars which are still embedded in infalling envelopes

(Cyganowski *et al.*, 2008).

2.5 Results and Discussion

2.5.1 L-Band Results

L-band images of all the sources are shown in Figure 2.5. Positions, fluxes, sizes and position angles of all their components are presented in Table 2.3. The components can be classified as cores or lobes. A core is detectable in the near/mid infrared, brighter at higher radio frequencies, e.g. Q-band, and is likely to be located between lobes, if the components show a linear orientation. Lobes, on the other hand, are seen a few arc-seconds away from the cores, aligned in the direction of the outflow cavities. Thermal lobes are detectable at higher frequencies while non-thermal lobes are more prominent at lower radio frequencies.

The L-band images display a variety of morphologies ranging from emission that comes from cores with radio lobes and partially resolved cores to point-like counterparts. G094.4637, G094.6028, G111.5671, G114.0835, G138.2957 and G141.9996 have radio lobes, suggesting that they harbour cores that drive the jets. G110.0931, on the other hand, is resolved, displaying an extended and jet-like structure but does not have radio lobes at L-band. However, it encloses multiple components at higher resolution, in C-band. Some of the components may be lobes. Other sources whose L-band emission encloses multiple components at the higher resolution, in C-band, are G094.2615, G094.4637 and G139.9091. Four sources; G083.7071-A, G108.5955C, G111.2552 and G139.9091 are partially resolved while three; G103.8744-A, G114.0835-A and G126.7144 are point-like.

The cores of all the protostars were detected at L-band except for G103.8744, G136.3833 and G138.2957. None of the detections in the field of G103.8744 appear to be its core; they are all located a few arcseconds away from the position of the IR source. G136.3833's field has a bright source that is approximately $6''$ to the west of its IR emission. This radio source does not manifest an explicit association with the MYSO. G138.2957, on the other hand, has two non-thermal lobes that are approximately $2''$ apart. Each of the lobes is located $\sim 1''$ away from the position of the core (see Figure 2.5). All the L- and C-band emission

have a positional match that agree within $\sim 0.3''$. However, NIR positions, taken from 2MASS, show slight offsets from the radio emission, perhaps because the emission is from a section of an outflow cavity that is further away from the source and is less obscured. In some cases, no radio emission coincides with the NIR position, e.g. in G103.8744, where the peaks of the radio source are positioned a few arcseconds away from the peak of the IR emission.

The flux densities and peak fluxes of the sources that lie within a radius of 5-10$''$ from the MYSOs' position were estimated by enclosing a box or a polygon around a source. Uncertainties on the fluxes were calculated by averaging fluxes from five different locations of a source's field which were devoid of emission, estimated using a box of the same size. An additional error, approximated at 10% of a source's flux density was incorporated, in quadrature, to include the uncertainty associated with calibration of absolute flux. Besides the use of an enclosing polygon to estimate the flux of a radio source, other techniques e.g the use of CASA task `imfit` or measuring the integrated flux enclosed by a 3σ contour are normally employed. The results from `imfit` and 3σ contours were compared with the enclosing box method and found to be consistent, i.e., agree within their uncertainties, however, the values of the box techniques show an average difference of 10% with the measurements from the other techniques (see Figure 2.6). The results also show that measuring fluxes from 3σ contours generally underestimates the fluxes of the sources.

Sizes of the sources θ_S were calculated as $\theta_S = \sqrt{\theta^2_{FWHM} - \theta^2_B}$, where θ_S is the deconvolved size of the source, θ_{FWHM} is the full width at half maximum of a source's flux distribution and θ_B is the full width at half maximum of the beam. The sizes were all found to be smaller than the largest angular size of the observation $\theta_{LAS} = 36''$. Table 2.3 lists the the sizes and their position angles, estimated by inspection. A source's radio emission was considered real if its peak flux is at least three times higher than the root mean square noise in the field (i.e at least 3σ detection). Sources were considered resolved if their structures are extended with respect to the beam (i.e larger than the beam) otherwise they are compact.

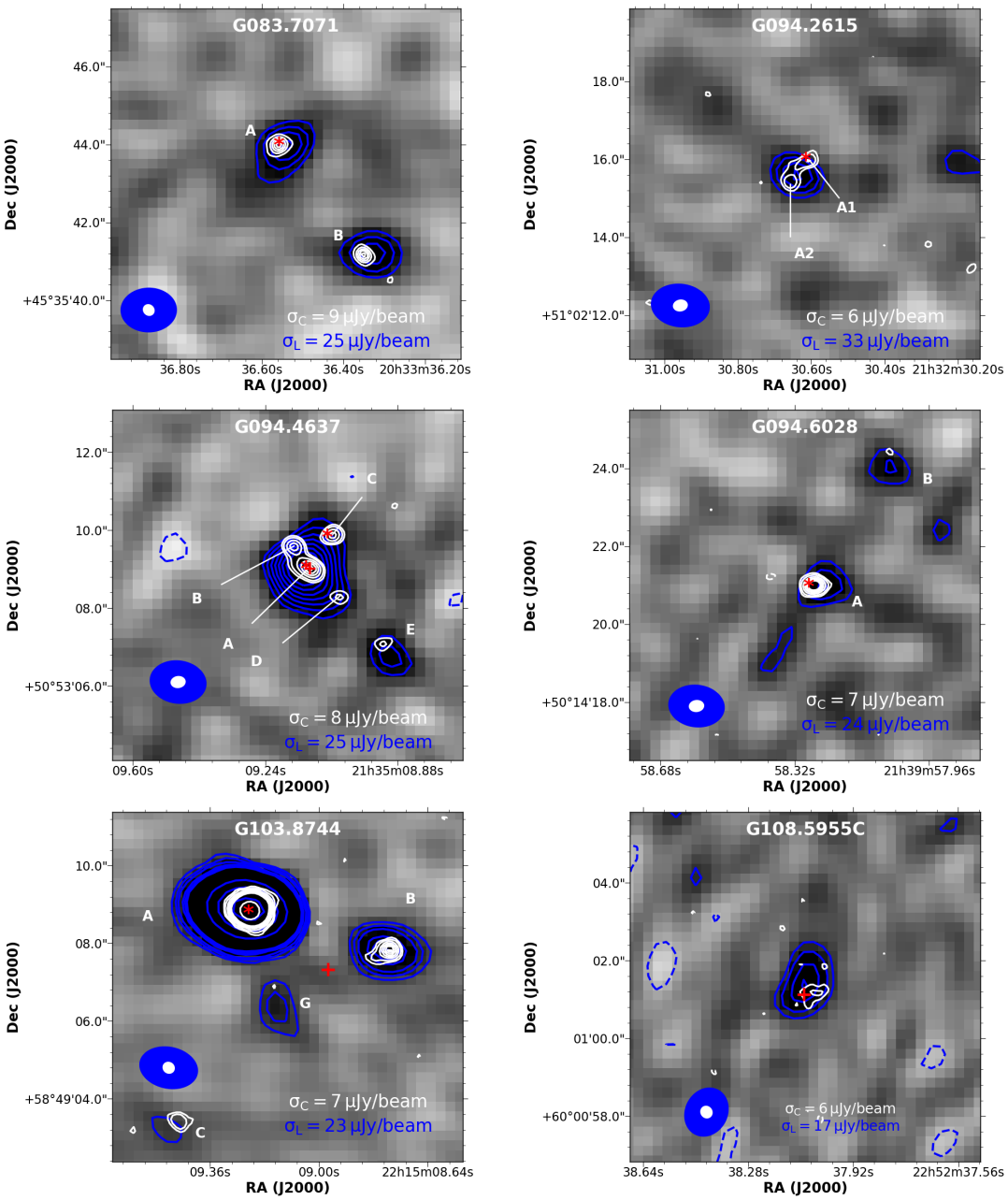

Figure 2.5: L-band maps of the sources together with their L- and C-band contours of levels -3σ(dashed), 3σ, 4σ, 5σ,... and -3σ(dashed), 3σ, 5σ, 9σ, 13σ, 17σ, 21σ,... shown in blue and white colours respectively. All the cores were detected at L- band except for G138.2957 and G136.3833, both of which were detected at C-band. The red asterisks show the Q-band locations of the MYSOs' cores. The locations agree with the positions of the IR emission from the MYSOs within 1″. IR locations of MYSOs whose Q-band positions are unavailable are indicated with a plus sign. Synthesised beams for both L- and C- (Purser et al. 2020 in prep) bands are shown on the lower left corner of each frame.

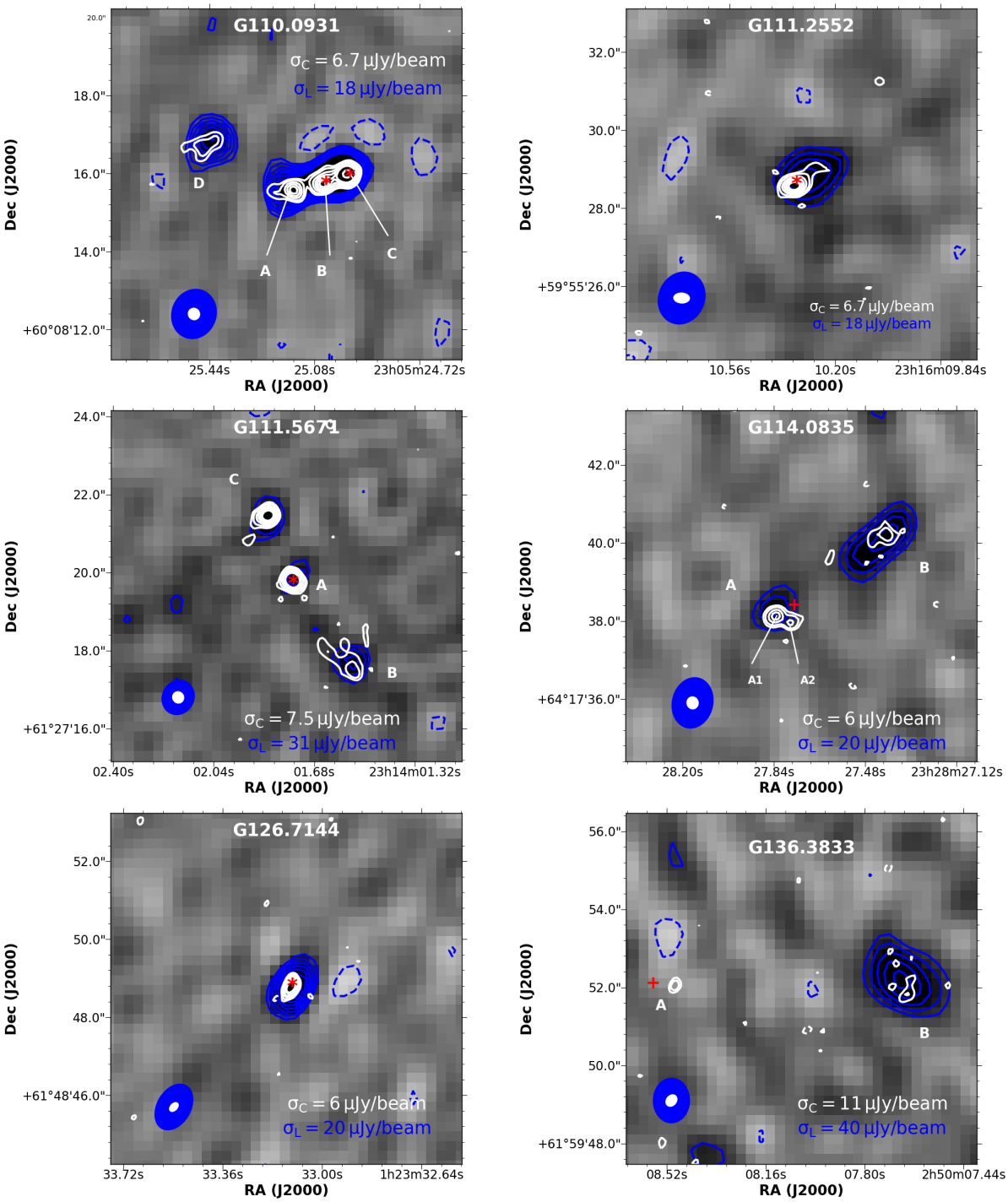

Figure 2.5: continued.

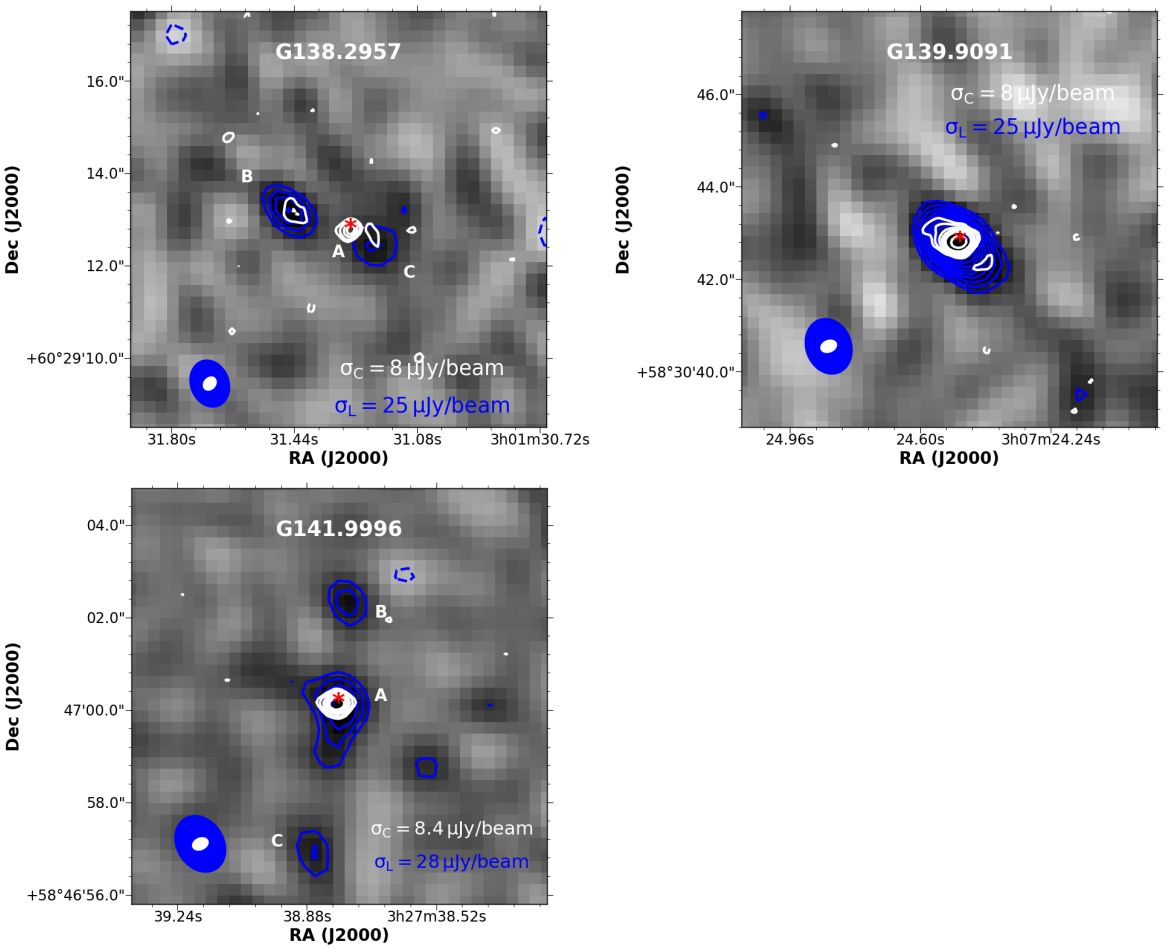

Figure 2.5: continued.

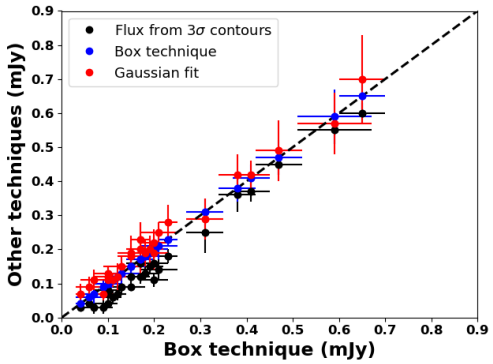

Figure 2.6: Comparing the measured fluxes of the sources and the techniques used in estimating the fluxes. The black, blue and red dots represent fluxes derived from 3σ contours, enclosed boxes and gaussian fits respectively.

Table 2.3: The position, flux density, peak intensity, size and position angle of emission from the components of the MYSOs at L-band. Sources whose sizes are not shown are point-like at the resolution of 1.2″. Any other sources that are located near a MYSO and are likely to be associated with it are also listed. The source naming scheme is adopted from Purser et al. 2020 (in prep) for consistency.

Object Name	RA (J2000)	DEC (J2000)	Integrated Flux (mJy)	Peak flux (mJy/beam)	Deconvolved Source Size $\theta_{\rm maj}('') \times \theta_{\rm min}('')$	Source Position Angle (^{o})
G083.7071-A	$20^h33^m36.56^s$	$+45°35'43.9''$	0.17 ± 0.02	0.13 ± 0.02	$2.4 \pm 0.2 \times 1.6 \pm 0.3$	130 ± 10
G083.7071-B	$20^h33^m36.34^s$	$+45°35'41.1''$	0.09 ± 0.02	0.09 ± 0.03	–	–
G094.2615(A1+A2)	$21^h32^m30.61^s$	$+51°02'15.8''$	0.11 ± 0.02	0.13 ± 0.03	$2.0 \pm 0.3 \times 1.1 \pm 0.2$	48 ± 7
G094.4637(A + B + C + D)	$21^h35^m09.13^s$	$+50°53'09.1''$	0.38 ± 0.04	0.27 ± 0.03	$1.8 \pm 0.4 \times 1.6 \pm 0.4$	–
G094.4637-E	$21^h35^m08.91^s$	$+50°53'07.0''$	0.03 ± 0.01	0.04 ± 0.02	–	–
G094.6028-A	$21^h39^m58.27^s$	$+50°14'20.9''$	0.08 ± 0.02	0.12 ± 0.02	–	–
G094.6028-B	$21^h39^m58.07^s$	$+50°14'24.0''$	0.07 ± 0.02	0.10 ± 0.02	–	–
G103.8744-A	$22^h15^m09.25^s$	$+58°49'08.8''$	2.21 ± 0.10	1.90 ± 0.05	$3.3 \pm 0.3 \times 2.3 \pm 0.2$	70 ± 15
G103.8744-B	$22^h15^m08.79^s$	$+58°49'07.8''$	0.17 ± 0.02	0.23 ± 0.02	$2.3 \pm 0.2 \times 1.3 \pm 0.2$	63 ± 16
G103.8744-G	$22^h15^m09.16^s$	$+58°49'06.6''$	0.09 ± 0.03	0.15 ± 0.02	–	–
G108.5955C	$22^h52^m38.06^s$	$+60°01'01.1''$	0.20 ± 0.03	0.16 ± 0.02	$1.9 \pm 0.4 \times 1.1 \pm 0.3$	160 ± 20
G110.0931	$23^h05^m25.04^s$	$+60°08'15.8''$	0.59 ± 0.08	0.38 ± 0.04	$2.6 \pm 0.3 \times 1.2 \pm 0.2$	108 ± 8
G110.0931-D	$23^h05^m25.43^s$	$+60°08'16.9''$	0.19 ± 0.03	0.17 ± 0.03	–	–
G111.2552	$23^h16^m10.34^s$	$+59°55'28.6''$	0.16 ± 0.03	0.12 ± 0.02	$1.7 \pm 0.5 \times 1.1 \pm 0.4$	121 ± 11
G111.5671-A	$23^h14^m01.76^s$	$+61°27'19.8''$	0.12 ± 0.03	0.17 ± 0.02	–	–
G111.5671-B	$23^h14^m01.54^s$	$+61°27'17.5''$	0.20 ± 0.03	0.17 ± 0.03	–	–
G111.5671-C	$23^h14^m01.85^s$	$+61°27'21.4''$	0.18 ± 0.03	0.18 ± 0.03	–	–
G114.0835-A	$23^h28^m27.82^s$	$+64°17'38.1''$	0.10 ± 0.03	0.10 ± 0.01	–	–
G114.0835-B	$23^h28^m27.40^s$	$+64°17'40.2''$	0.21 ± 0.04	0.13 ± 0.02	$2.5 \pm 0.4 \times 1.2 \pm 0.3$	135 ± 8
G126.7144	$01^h23^m33.11^s$	$+61°48'48.8''$	0.47 ± 0.05	0.56 ± 0.03	$2.0 \pm 0.2 \times 1.2 \pm 0.3$	140 ± 15
G136.3833-A	$02^h50^m08.49^s$	$+61°59'52.1''$	< 0.01	< 0.12	–	–
G136.3833-B	$02^h50^m07.68^s$	$+61°59'52.2''$	0.65 ± 0.05	0.29 ± 0.01	$1.6 \pm 0.4 \times 0.8 \pm 0.3$	60 ± 12
G138.2957-A	$03^h01^m31.28^s$	$+060°29'12.8''$	< 0.06	< 0.06	–	–
G138.2957-B	$03^h01^m31.45^s$	$+060°29'13.2''$	0.13 ± 0.04	0.16 ± 0.02	$1.5 \pm 0.2 \times 0.8 \pm 0.2$	48 ± 8
G138.2957-C	$03^h01^m31.20^s$	$+060°29'12.4''$	0.10 ± 0.03	0.12 ± 0.02	–	–
G139.9091	$03^h07^m24.49^s$	$+58°30'42.8''$	0.41 ± 0.04	0.34 ± 0.02	$2.5 \pm 0.3 \times 1.5 \pm 0.2$	50 ± 8
G141.9996-A	$03^h27^m38.76^s$	$+58°47'00.2''$	0.31 ± 0.04	0.18 ± 0.02	$2.3 \pm 0.5 \times 1.6 \pm 0.3$	180 ± 21
G141.9996-B	$03^h27^m38.77^s$	$+58°47'02.3''$	0.06 ± 0.03	0.12 ± 0.02	–	–
G141.9996-C	$03^h27^m38.86^s$	$+58°46'57.0''$	0.07 ± 0.03	0.11 ± 0.02	–	–

Table 2.4: Flux densities of the objects at different frequencies together with their spectral indices. The L-and C-band fluxes, shown, are from images of a similar range of uv-distance (in λ). The Q-band fluxes were taken from Purser et al. 2020 (in prep). For fluxes taken from the literature, the reference is shown in brackets. Separable components of the MYSOs are also included in the table. The class tells us whether an L-band emission traces a core or a lobe. Known HII regions, assumed to be sources that have stopped driving jets, are also indicated in the table.

Object	Integrated Flux (mJy)				Spectral Index			Class
	1.5 GHz	5.8 GHz	44.0 GHz	Other (Ref)	α_{LC}	α_{CQ}	α_{LQ}	
G083.7071-A	0.17 ± 0.02	0.22 ± 0.02	0.68 ± 0.06	–	0.19 ± 0.11	0.56 ± 0.06	0.44 ± 0.10	Core
G083.7071-B	0.09 ± 0.02	0.20 ± 0.02	–	–	0.60 ± 0.13	–	–	Core
G094.2615(A1+A2)	0.11 ± 0.03	0.10 ± 0.02	0.24 ± 0.08		-0.07 ± 0.25	0.44 ± 0.20	0.23 ± 0.18	Core/Lobe
G094.4637(A+B+C+D)	0.38 ± 0.04	0.52 ± 0.05	1.89 ± 0.08		0.23 ± 0.12	0.64 ± 0.05	0.53 ± 0.09	Core(s) + lobe(s)
G094.4637-E	0.03 ± 0.01	0.04 ± 0.02	–	–	0.21 ± 0.45	–	–	Lobe
G094.6028-A	0.08 ± 0.02	0.32 ± 0.03	0.62 ± 0.07	(a)	1.04 ± 0.20	0.32 ± 0.09	0.44 ± 0.15	Core
G094.6028-B	0.07 ± 0.02	< 0.04	–		< -0.42	–	–	Lobe
G103.8744-A	2.21 ± 0.10	3.52 ± 0.04	1.56 ± 0.34	(f)	0.39 ± 0.05	-0.25 ± 0.06	–	HII-region
G103.8744-B	0.17 ± 0.02	0.25 ± 0.06	< 0.11	–	0.29 ± 0.20	–	–	Unknown
G103.8744-C	< 0.06	0.09 ± 0.02	–	–	> 0.30	–	–	Unknown
G103.8744-G	0.09 ± 0.03	< 0.05	–	–	< -0.44	–	–	Lobe
G108.5955C	0.20 ± 0.03	0.26 ± 0.04	–	–	0.20 ± 0.16	–	–	Unknown
G110.0931(A+B+C)	0.59 ± 0.08	0.95 ± 0.13	1.03 ± 0.20	(b)	0.36 ± 0.14	0.05 ± 0.07	0.17 ± 0.07	Core + lobe(s)
G110.0931-A	–	0.22 ± 0.02	–	(b)	–	-0.14 ± 1.49	–	Lobe
G110.0931-B	–	0.31 ± 0.02	0.62 ± 0.15	(b)	–	0.33 ± 0.14	–	Core
G110.0931-C	–	0.49 ± 0.01	0.38 ± 0.11	(b)	–	-0.11 ± 0.07	–	Unknown
G110.0931-D	0.19 ± 0.03	0.17 ± 0.02	–	–	-0.08 ± 0.15	–	–	HII-region
G111.2552	0.16 ± 0.03	0.36 ± 0.04	0.35 ± 0.07	(c)	0.61 ± 0.16	0.73 ± 0.08	0.67 ± 0.04	Core
G111.5671-A	0.12 ± 0.03	0.42 ± 0.08	2.46 ± 0.10	(d)	0.94 ± 0.23	0.79 ± 0.14	0.84 ± 0.09	Core
G111.5671-B	0.20 ± 0.03	< 0.09	–	–	< -0.60			Lobe
G111.5671-C	0.18 ± 0.03	0.40 ± 0.09	–	–	0.60 ± 0.21	–	–	Lobe
G114.0835-A	0.10 ± 0.03	0.17 ± 0.03	–	–	0.40 ± 0.20	–	–	Core
G114.0835-B	0.21 ± 0.04	0.12 ± 0.02	–	–	-0.42 ± 0.19	–	–	Lobe
G126.7144	0.47 ± 0.05	1.28 ± 0.05	6.86 ± 0.24	–	0.75 ± 0.08	0.83 ± 0.02	0.82 ± 0.02	Core
G136.3833-A	< 0.01	0.04 ± 0.01	0.47 ± 0.09	–	> 1.04	1.22 ± 0.16	> 1.20	Core
G136.3833-B	0.65 ± 0.05	0.26 ± 0.02	< 0.14	–	-0.68 ± 0.08	< -0.31	< -0.49	Unknown
G138.2957(A+B+C)	0.23 ± 0.05	0.27 ± 0.05	0.55 ± 0.09	(e)	0.12 ± 0.15	0.35 ± 0.09	0.28 ± 0.06	Core + lobes
G138.2957-B	0.13 ± 0.04	–	–	–	–	–	–	Lobe
G138.2957-C	0.10 ± 0.03	–	–	–	–	–	–	Lobe
G139.9091	0.41 ± 0.04	0.74 ± 0.07	1.39 ± 0.14	–	0.44 ± 0.10	0.31 ± 0.07	0.36 ± 0.04	Core
G141.9996-A	0.31 ± 0.04	0.37 ± 0.04	1.04 ± 0.14	–	0.13 ± 0.13	0.51 ± 0.09	0.37 ± 0.12	Core
G141.9996-B	0.06 ± 0.03	<0.03	–	–	< -0.51	–	–	Lobe
G141.9996-C	0.07 ± 0.03	<0.03	–	–	< -0.63	–	–	Lobe

[a] Di Francesco *et al.* (1997) [b] Rodríguez *et al.* (2012b) [c] Trinidad *et al.* (2006) [d] Sandell *et al.* (2005) [e] Carral *et al.* (1999) [f] Wang *et al.* (2016)

2.5.2 Spectral Indices and Maps of the Sources

Spectral indexing provides a means of classifying radio emitters as either thermal ($\alpha \geq -0.1$) or non-thermal ($\alpha < -0.1$) e.g Rodríguez-Kamenetzky *et al.* (2017), Vig *et al.* (2018). However, it is difficult to distinguish between optically thin thermal emission and non-thermal emission if the value of the spectral index is closer to -0.1 and the uncertainties are large. Non-thermal emission is thus claimed with certainty only when $\alpha << -0.1$ and the uncertainty on the index does not allow for overlap with -0.1.

The integrated fluxes of the sources at L-, C- and Q-bands, together with any others available in the literature, were used to estimate their indices even though data collection was not contemporaneous and MYSOs may be variable e.g. S255 NIRS 3 (Cesaroni *et al.*, 2018). Moreover, the observations are of different resolutions and are clearly sensitive to different spatial scales. To ensure the accuracy of the method, both L- and C- band data were re-imaged using a common range of $uv-$wavelength i.e 15-200 kλ, to use emission from comparable spatial scales in estimating the spectral indices of the sources. Nonetheless, a full range of $uv-$wavelength was used in Q-band even though it traces a different spatial scale as the overlap between its uv-coverage and 15-200 kλ is insufficient. Further caution was exercised by estimating L- and C-band fluxes from a similar enclosing box, regardless of the morphology of a source, to provide uniformity by measuring the fluxes from the same region of the sky.

A high-resolution observation at Q-band can result in missing flux (van der Tak & Menten, 2005), but at the same time dust emission contributes about 43$\pm$11 % (Purser, 2017) of the flux at Q-band. For example, the flux of G111.5671 at 44 GHz (Purser et al. 2020 in prep), observed using the VLA's A configuration is lower than the C-configuration flux (van der Tak & Menten, 2005) by 18%. Thus, the quantities of free-free emission at Q-band, essential for estimating the spectral indices, are unknown and some of the indices may have large uncertainties. However, the indices are used since the SEDs of most of the cores, shown in Figure 2.7, do not show strong evidence of unexpected behaviour.

The indices were estimated to be equivalent to the slopes of the lines of best fit of a plot of the logarithm of flux density and frequency of an object, generated

by minimising chi-squares (shown in Figure 2.7). In cases where a source's flux density could not be estimated (i.e too faint to detect), an upper limit, evaluated as three times its field rms (i.e 3× rms), was set as its peak flux. An upper limit on the integrated flux of such a source was estimated from a polygon whose size is similar to that of the source at a frequency where it is detected. Some sources are extended at L-band but are resolved into multiple cores and lobes e.g G094.4637 or a core and a lobe, e.g G094.2615, in the higher resolution C- and Q-bands. For the extended sources, the flux at L-band and the sum of the fluxes of the components in the higher resolution observations were used to estimate the index. If a source was only detected at one frequency, a limit on the index was calculated. Table 2.4 shows a list of the objects, their spectral indices and the fluxes used in estimating the indices. Details of the components incorporated in the calculation of the spectral indices of L-band sources are indicated in Table 2.4.

Spectral index maps of the MYSOs were generated from L- and C- band images using CASA task `immath`, in `spix` mode, to display the distribution of the indices across a source. The maps used are of $uv-$wavelength range 15-200 kλ. Only pixels whose values are more than 3σ in both L- and C-bands were used in creating the maps. The re-imaged C-band maps show varied morphologies, some of which are comparable to L-band emission e.g. G110.0931 while others are not e.g. G111.2552 and G108.5955 (see Figure 2.8). Uncertainty in the spectral index of a given pixel on the map was approximated by assuming that the error on the flux of each cell is equivalent to the rms of the field. This error was propagated while calculating the spectral index of the corresponding L- and C-band pixels. The maps and the corresponding errors are shown in Figure 2.8. Whereas the beams of L- and C-band maps that were used in generating the spectral index maps are largely similar, a few maps were generated from C-band images of smaller beams. The smaller C-band beams can result in slightly lower fluxes at C-band and more negative spectral indices on the pixels of non-thermal sources.

2.5.2.1 Spectral Indices of the Cores

The L-Q band spectral indices α_{LQ} show that all the detected cores are thermal radio emitters ($\alpha > -0.1$). To decipher the nature of the objects further, their L-, C- and Q-band fluxes, among others from the literature, were used to compare their spectral indices as derived from L- to C- bands α_{LC} with those from C- to Q- bands α_{CQ}. Table 2.4 shows three possibilities: α_{LC} that is lower than α_{CQ} e.g. G094.2615, G094.4637 and G141.9996; α_{LC} that is higher than α_{CQ} e.g. G110.0931 and G094.6028-A and α_{LC} which is comparable to α_{CQ} e.g. G139.9091 and G126.7144.

Sources whose $\alpha_{LC} < \alpha_{CQ}$ have overall spectral indices that are flattened by L-band fluxes. This may be due to steepening of α_{CQ} by dust emission at Q-band or contribution of non-thermal emission at L-band. Purser (2017) estimated that dust emission is, on average, $\sim 43\pm11\,\%$ of the total emission at 44 GHz, capable of steepening the C-Q band slope, however, the values of α_{CQ} are $\sim +0.6$, consistent with thermal jets.

Spectra of sources whose α_{LC} are higher than α_{CQ} exhibit an HII region-like feature due to the apparent turnovers of their SEDs. In G110.0931, this can be attributed to the loss of flux at Q band where one of its components (A) was not detected. Finally, sources whose α_{LC} are comparable with α_{CQ} seem to have thermal cores that are separated from the lobes (e.g. in G111.5671-A) or cores with no clear lobes (e.g. in G111.2552 and G126.7144). In conclusion, L-Q band spectral indices (α_{LQ}) of the MYSOs are largely positive ($\alpha > 0$) and the radiation from what one can consider a central component of a MYSO is also primarily thermal, making it a substantial radio emitter at higher frequencies. The average α_{LC}, α_{CQ} and α_{LQ} of the sources are 0.42 ± 0.34, 0.43 ± 0.33 and 0.42 ± 0.27 confirming that the cores are thermal.

2.5.2.2 Spectral Indices of Lobes

Four sources, G094.6028, G103.8744, G111.5671 and G141.9996, have non-thermal lobes of spectral indices $\alpha \leq -0.42$. The lobes were detected at L- but not C-band. G138.2957 has non-thermal lobes of spectral indices -0.46 ± 0.31 and -0.38 ± 0.33 to the east and west of its thermal core respectively (see Figure 2.8).

Two sources; G114.0835 and G136.3833 have nearby non-thermal sources that are aligned with the orientation of NIR emission in their fields. G094.4637 has a thermal lobe whose L- and C-band emissions are displaced in the direction of the outflow. It also has a component, D, that is non-thermal. Besides the lobes, two sources; G094.2615 and G108.5955 show tentative indications of non-thermal emission to the south-east and east of their cores, respectively.

These findings suggest that six of the sources, equivalent to 40 %, have non-thermal lobes which indicate the presence of magnetic fields. It is, however, not clear if the magnetic fields are generated in the surrounding interstellar medium or by the protostars themselves. The non-thermal emission, present on an object's spectral index map, is mainly seen further away from the central source, confirming that the central sources are thermal while the jet lobes are not.

2.5.2.3 Magnetic Field Strength of the Jet Lobes

Owing to the *minimum energy requirement* for synchrotron radiation (Longair, 2011), it is possible to set limits on the magnetic field strength and the energy required by the relativistic particles of a radio lobe to emit synchrotron emission of a given flux and energy spectrum. The luminosity L_ν of a synchrotron source at a given frequency ν has a known correlation with the energy spectrum of its relativistic electrons and magnetic flux density $\vec{B}$. Given that the radio luminosity of a synchrotron source of volume V can be produced when a large flux of electrons interact with a weak magnetic field and vice versa, identifying the dominant form of energy in such a source is not straightforward. However, in between the extreme options of a strong magnetic field and dominant particle energy is a total minimum energy requirement (Ainsworth, 2016).

The total energy W_{total}, in Joules, of a synchrotron source can be approximated from equation 2.2, where $\eta \simeq 40$ (Beck & Krause, 2005) in strong shocks is the ratio of proton to electron population, V is volume of the source, μ_o is permeability of free space and $G(\alpha)$ is a quantity that is defined by the spectral index, minimum frequency and maximum frequency of the observation (see equation 2.3). In equation 2.3, $a(p)$ is given by equation 2.4 (Ainsworth, 2016) and $p = 1 - 2\alpha$. Minimizing equation 2.2 with respect to magnetic field B gives the

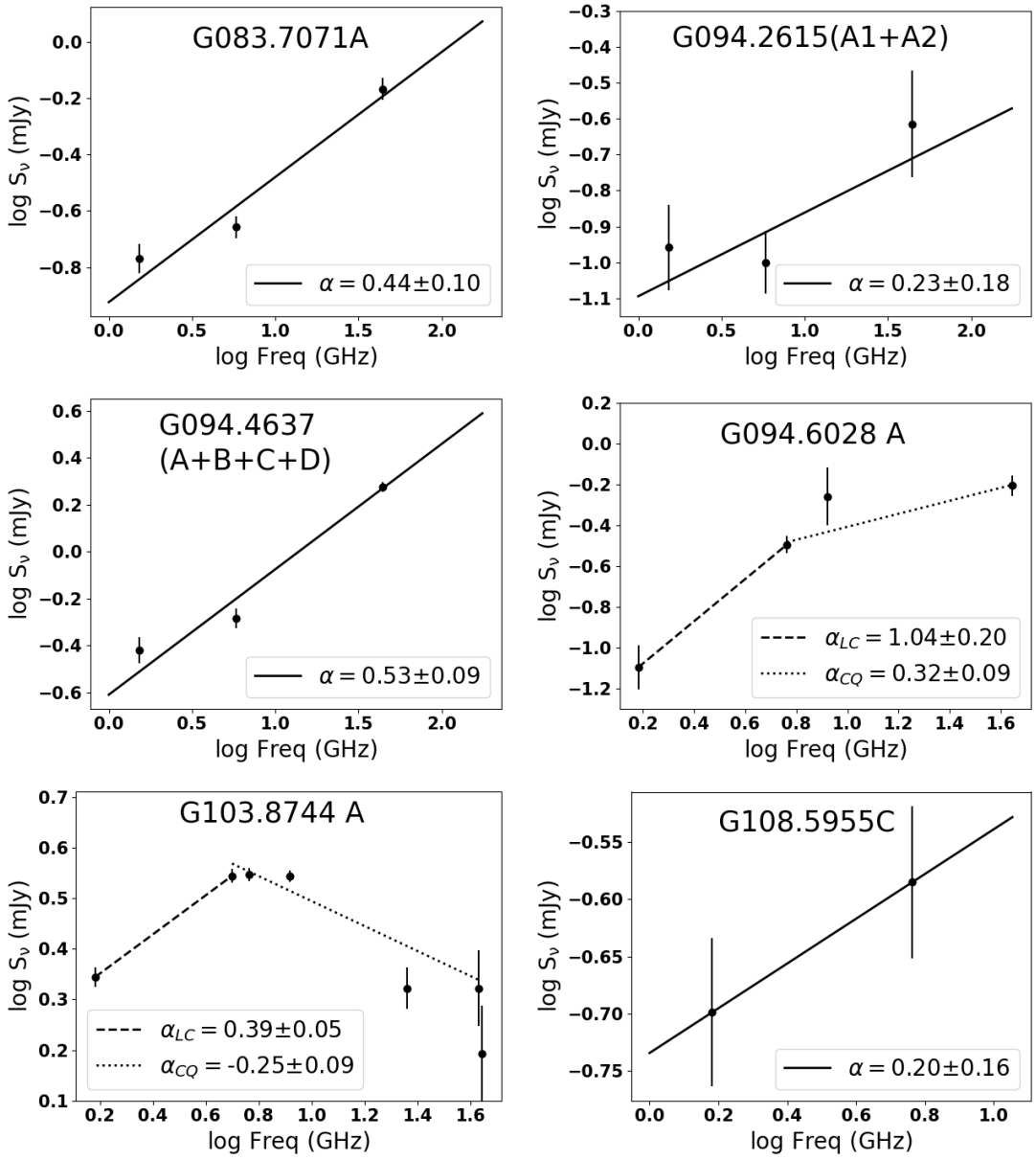

Figure 2.7: A plot showing how the flux densities of the L-band cores vary with frequency. The core of G103.8744 was not detected and the spectrum of a HII-region that is closest to its location was used. In some sources, additional data, available in the literature and listed in Table 2.4, were used in estimating their indices. The red data points represent values that were considered to be too low or high due to variability and were not used in the fit.

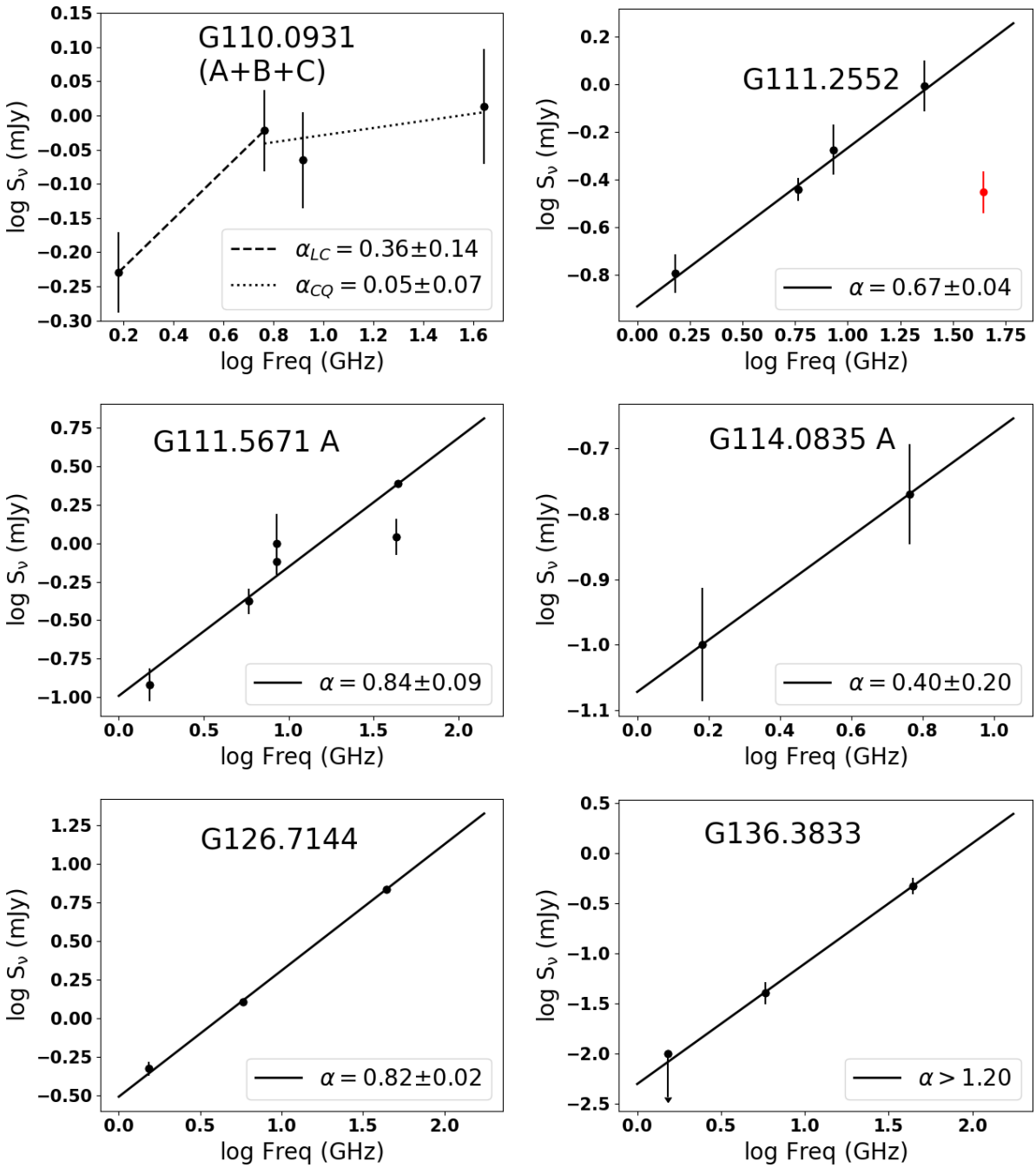

Figure 2.7: continued.

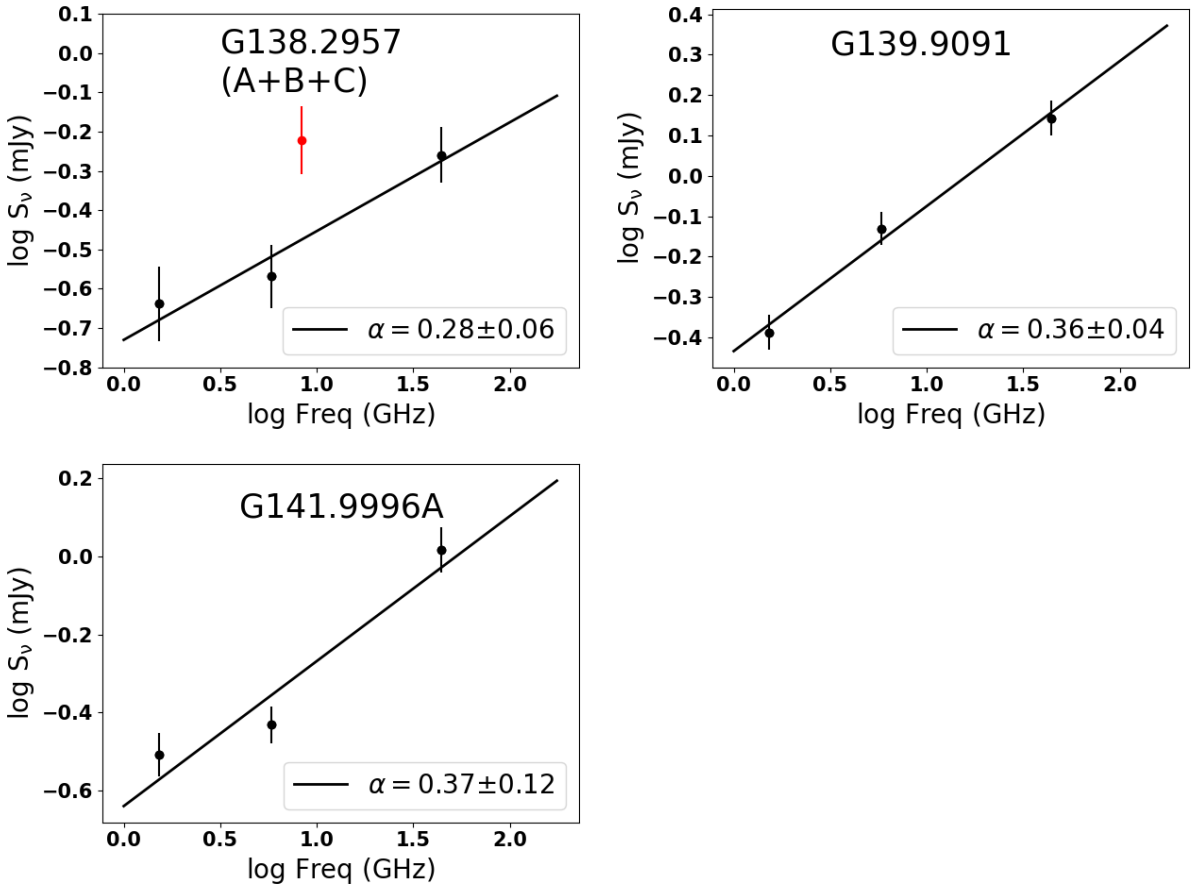

Figure 2.7: continued.

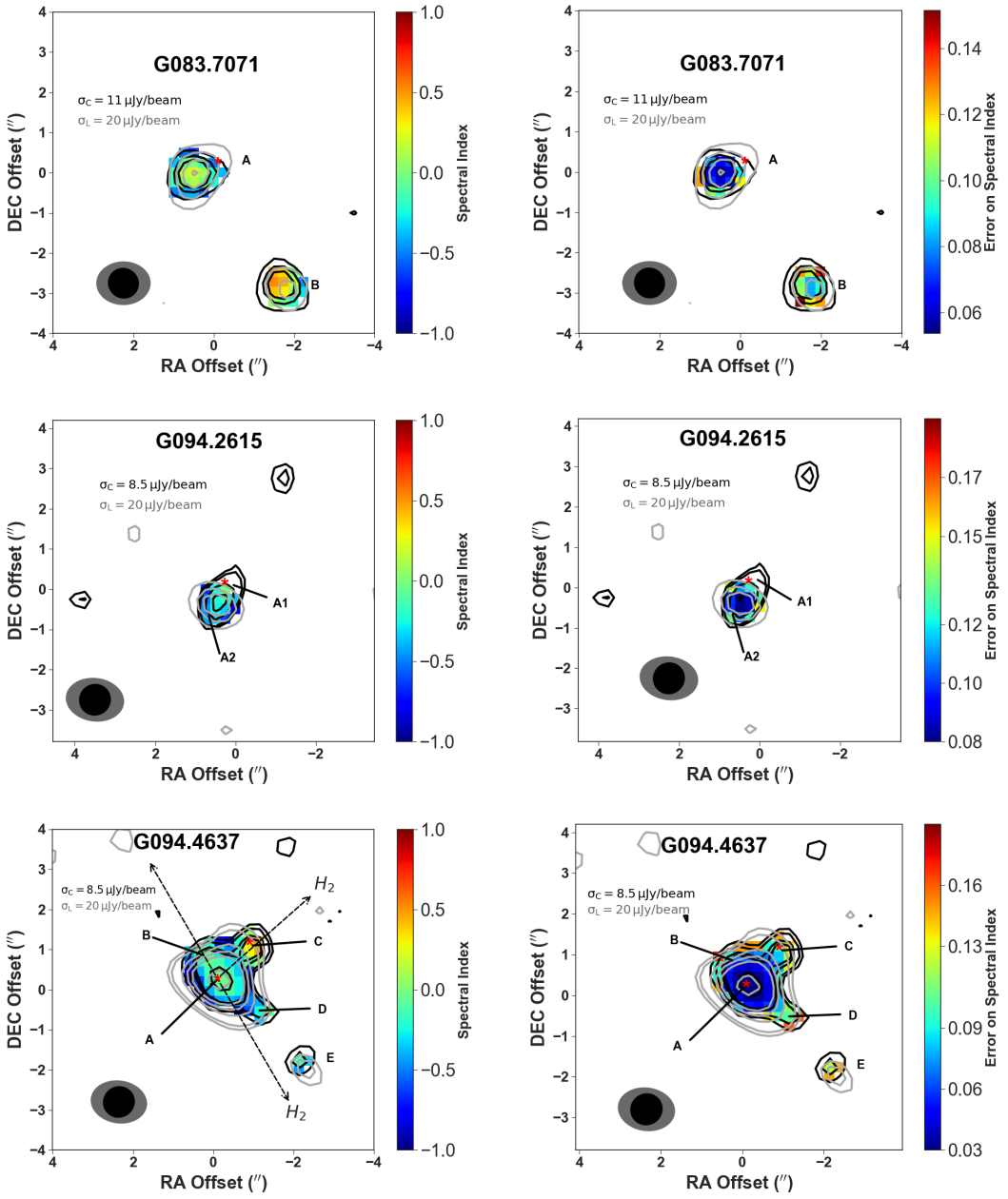

Figure 2.8: Spectral index maps of the sources shown on the left panels and their corresponding error maps on the right. L- and C-band contours of levels $3, 5, 7\sigma, \ldots$ and $3, 7, 11, 15\sigma, \ldots$ are overlaid in grey and black colours respectively. The maps were generated from L- and C-band maps of similar uv-wave coverage (i.e $15 - 200\,\mathrm{k}\lambda$). Colour-scales show L-C band spectral indices α_{LC} of the sources and corresponding errors. Locations of sources that lie within the L-band emission are indicated by their names. The dashed lines are the approximate directions of known emissions that are associated with outflows. Asterisk and plus symbols are the Q-band and IR locations of the MYSO cores. The synthesised beams are shown in the lower left corner.

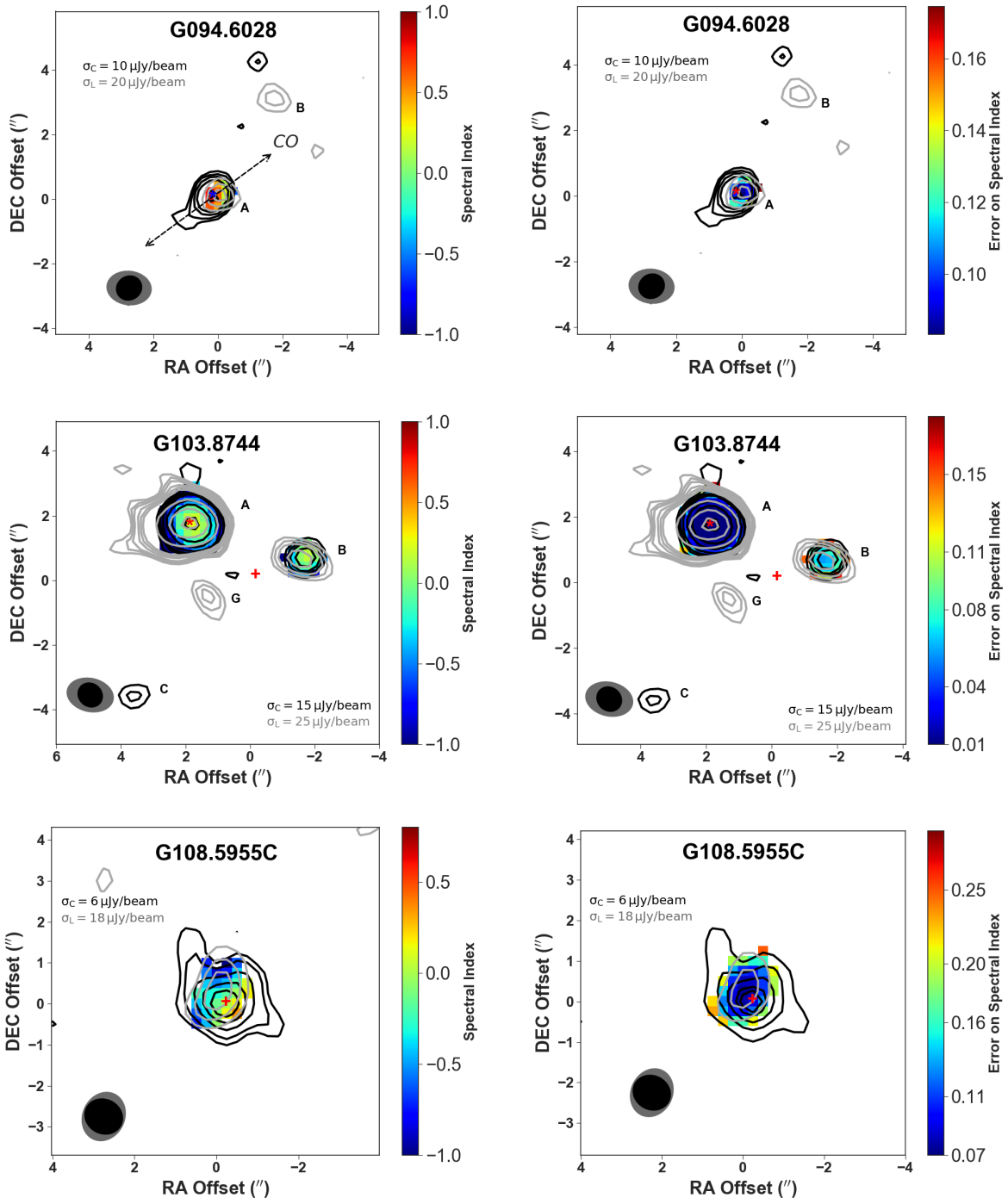

Figure 2.8: continued.

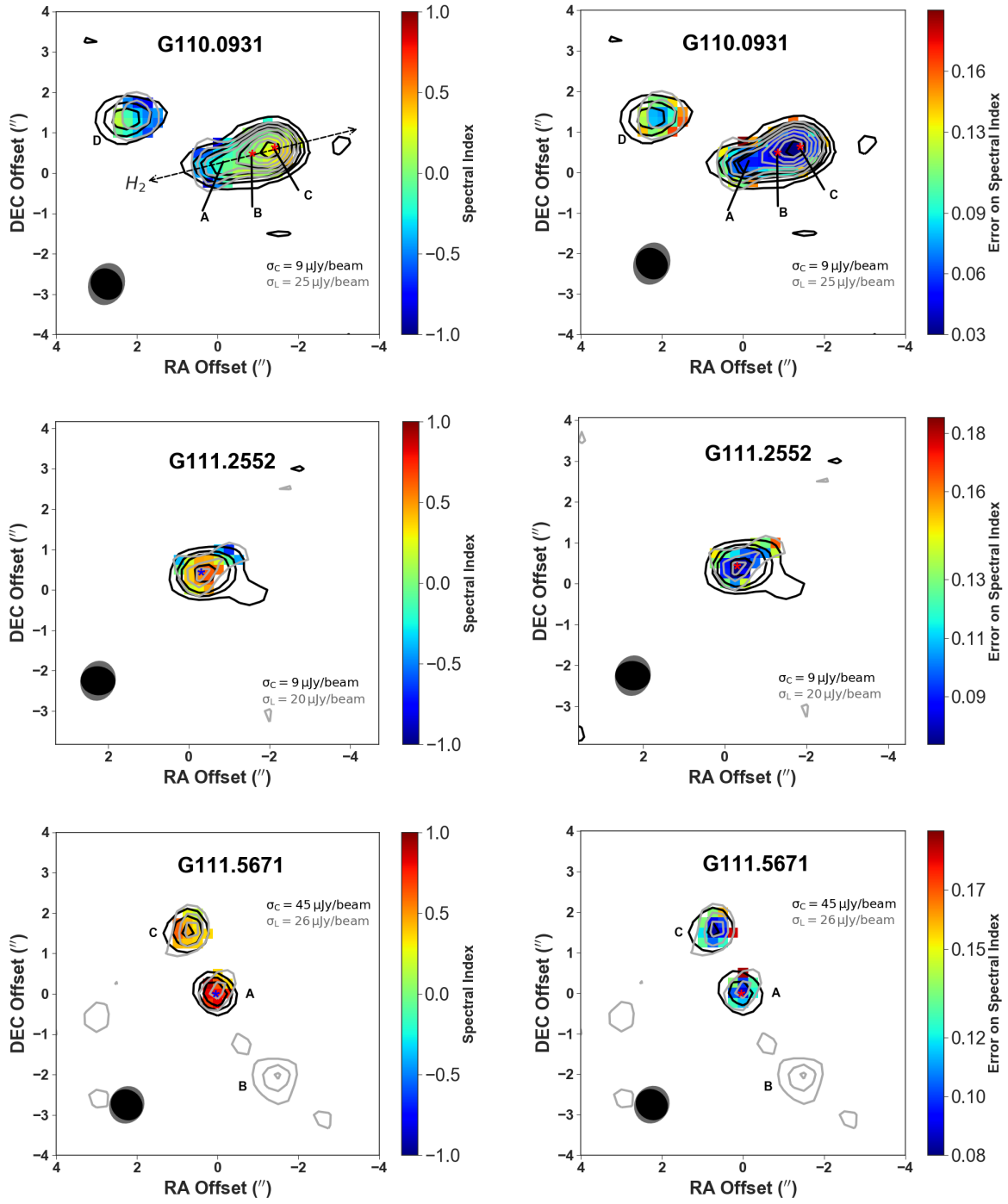

Figure 2.8: continued.

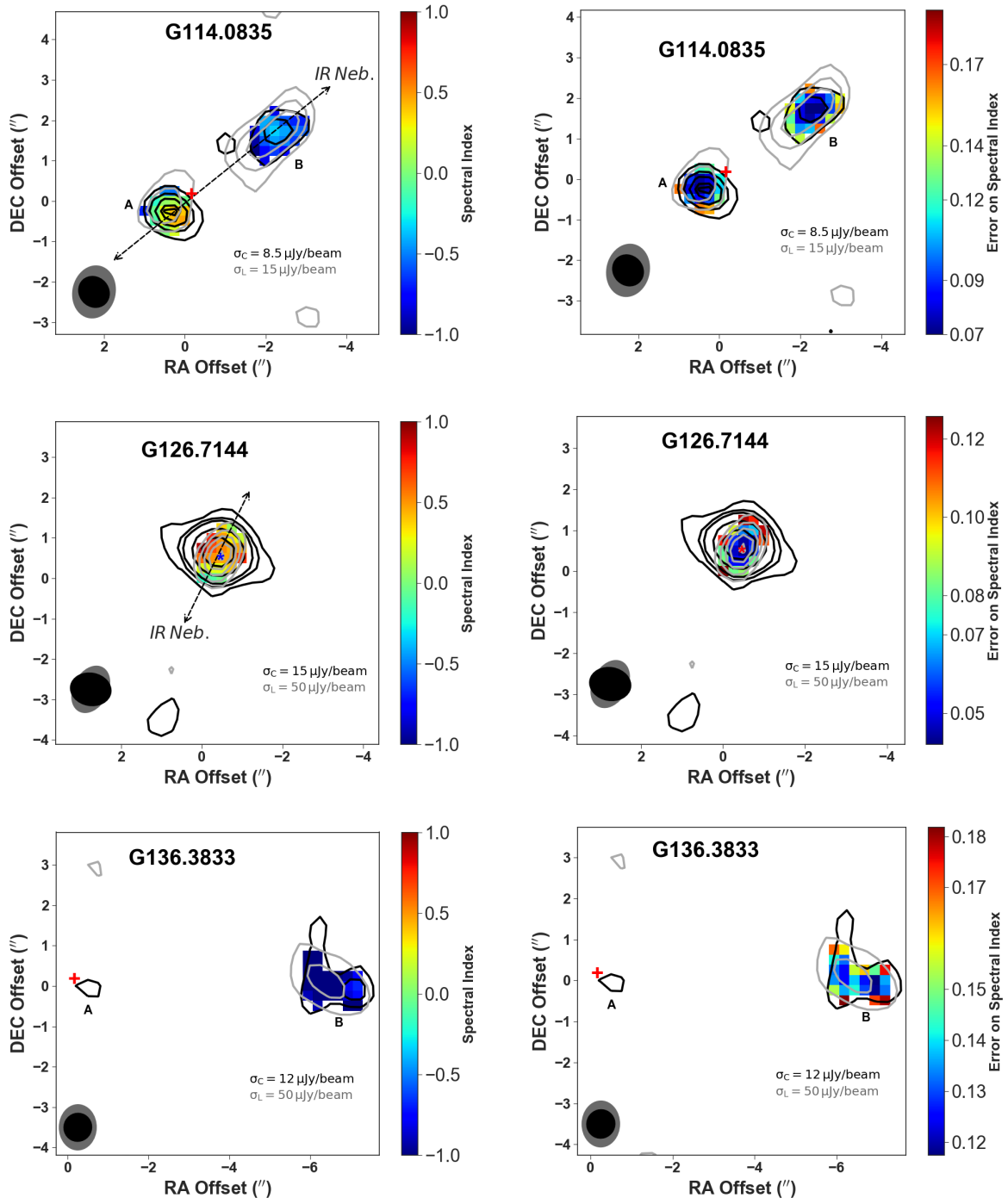

Figure 2.8: continued.

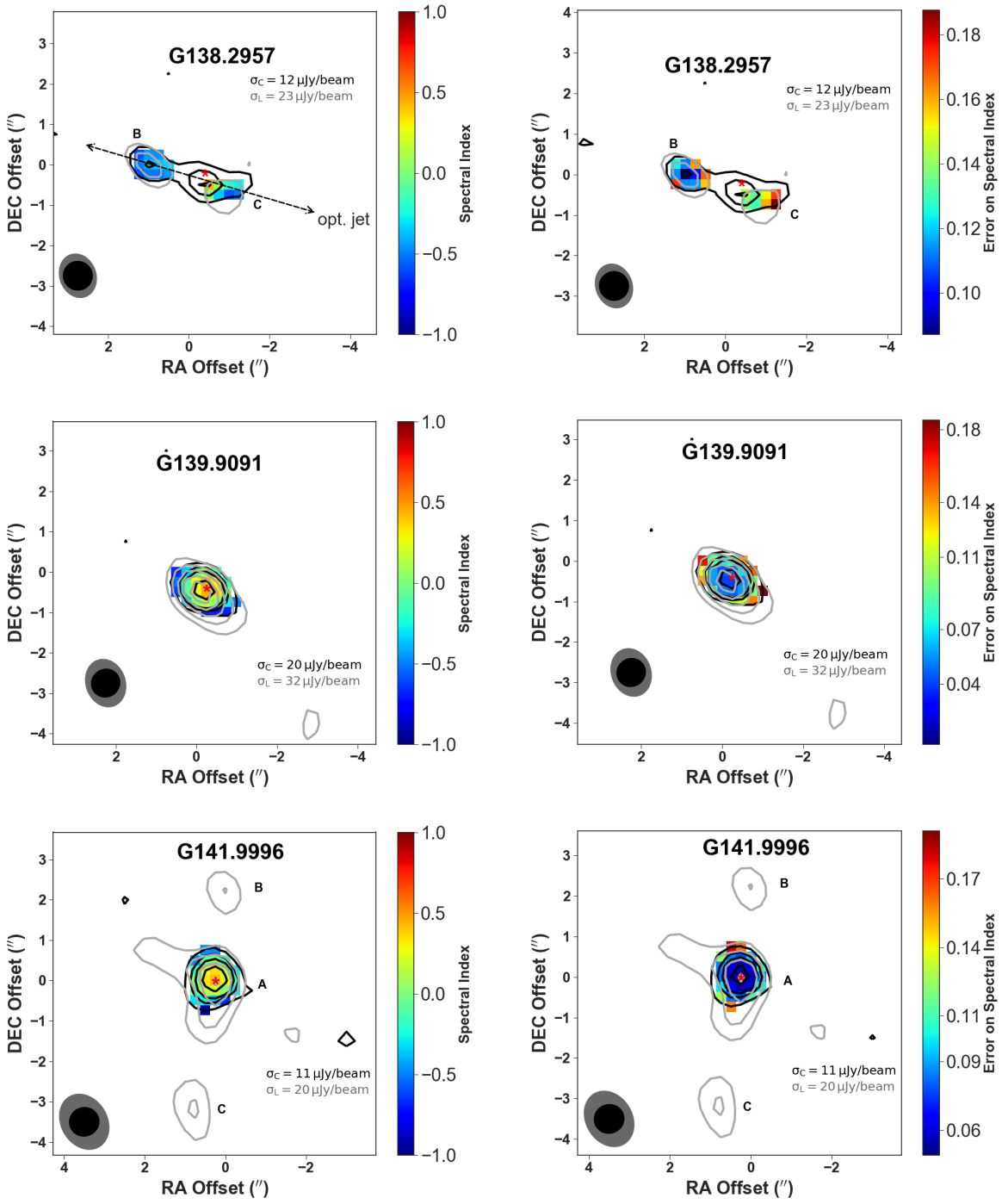

Figure 2.8: continued.

minimum energy W_{min} in Joules and corresponding B, B_{min} in Tesla, shown in equations 2.5 and 2.6 respectively.

$$W_{total} = G(\alpha)\eta L_\nu B^{-\frac{3}{2}} + V\frac{B^2}{2\mu_o} \tag{2.2}$$

$$\begin{aligned} G(\alpha) = & \frac{1}{a(p)(p-2)}[\nu_{min}^{-(p-2)/2} - \nu_{max}^{-(p-2)/2}]\nu^{(p-1)/2} \\ & \times \frac{(7.4126\times10^{-19})^{-(p-2)}}{2.344\times10^{-25}}(1.253\times10^{37})^{-(p-1)/2} \end{aligned} \tag{2.3}$$

$$a(p) = \frac{\sqrt{\pi}}{2}\frac{\Gamma(\frac{p}{4}+\frac{19}{12})\Gamma(\frac{p}{4}-\frac{1}{12})\Gamma(\frac{p}{4}+\frac{5}{4})}{(p+1)\Gamma(\frac{p}{4}+\frac{7}{4})} \tag{2.4}$$

$$W_{min} = \frac{7}{6\mu_o}(Vf)^{3/7}\Big[\frac{3\mu_0}{2}G(\alpha)\eta L_\nu\Big]^{4/7} \tag{2.5}$$

$$B_{min} = \Big[\frac{3\mu_0}{2}\frac{G(\alpha)\eta L_\nu}{Vf}\Big]^{2/7} \tag{2.6}$$

Equations 2.5 and 2.6 were used to estimate the minimum energies and magnetic fields of the non-thermal lobes, assuming that they occupy spherical volumes whose radii are equivalent to the average value of their semi-major and semi-minor radii. Lobes whose sizes could not be measured directly were assigned the size of their deconvolving beams. f in equations 2.5 and 2.6 is known as a filling factor, a fraction of the volume that contains the synchrotron emitter. It was assumed to be 0.5 (Ainsworth *et al.*, 2014). The average values of the minimum energies and magnetic fields, estimated from the spectral indices and flux densities of the lobes at 1.5 GHz, were found to be $\simeq 5.07\times10^{41}$ ergs and $\simeq 0.57\pm0.07$ mG respectively. Minimum energies of the sample range from 1.2×10^{40} ergs to 1.5×10^{42} ergs, two orders of magnitude difference. Magnetic fields, on the other hand, are more similar i.e 0.40 mG $\leq B_{min} \leq$0.64 mG and approximately two to three times higher

than the field in HH 80-81 (Carrasco-González *et al.*, 2010), a difference that can be attributed to uncertainties in objects' distances, assumed volumes and fluxes as well as the use of upper limits of four of the indices. The analysis of Zeeman splitting of OH maser emission, from massive star forming regions, shows that the B-fields of the regions lie in the range $0.1 \leq B \leq 10$ mG (Fish *et al.*, 2003) i.e in agreement with the estimates.

2.5.3 Nature of the Cores and Their Radio Luminosity at L-Band

The nature of the cores and their L-band emission were examined further by exploring the distribution of the cores on a bolometric-colour plot and the relationship between bolometric- and radio- luminosities at L-band.

2.5.3.1 Relationship Between Infrared Colour and Bolometric Luminosity

The infrared colour of young stellar objects is likely to be related to their evolution as they become bluer with age. A plot of mid-infrared colour versus bolometric luminosity of the sample, shown in Figure 2.9, suggests that MYSOs of higher bolometric luminosities are more likely to have lobes compared to their lower luminosity counterparts, especially at lower values of $\frac{F_{21\mu m}}{F_{8\mu m}}$. Whether this property of the jets is related to their evolution or driving power is not clear. However, the radio luminosity of a jet is correlated with its bolometric luminosity and force (Anglada *et al.*, 2015), implying that sources with higher bolometric luminosity are likely to have more powerful lobes that are easily detectable in the radio compared to sources of lower luminosity.

2.5.3.2 Relationship Between L-Band Radio Luminosity and Bolometric Luminosity

The radio luminosities of thermal radio jets show a correlation with bolometric luminosities. Different studies find that the slope of the correlation lies in the range $0.6 - 0.9$, in a log-log plot. Cabrit & Bertout (1992) and Anglada (1995)

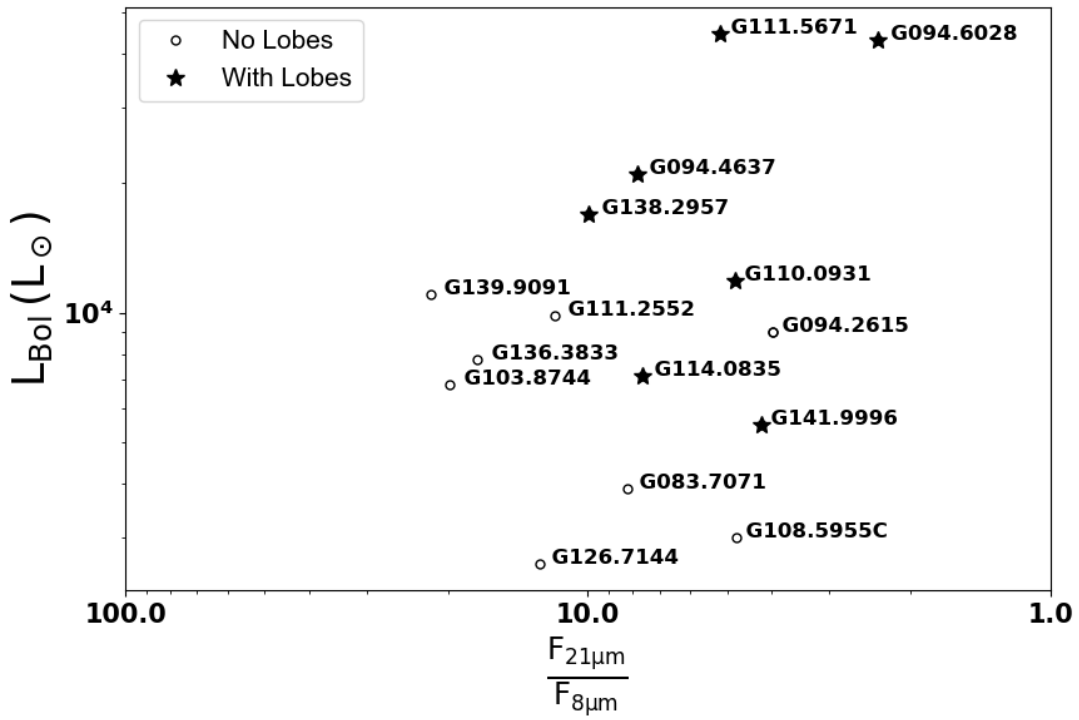

Figure 2.9: An illustration showing how mid-IR colour of MYSOs varies with bolometric luminosity.

estimated it as 0.8 and 0.6 respectively. Recently, Shirley *et al.* (2007) found the slope to be ∼0.9 and 0.7 at 5 GHz and 8.3 GHz respectively, in low mass stars. At L-band, the slope was found to be 0.64 ± 0.03. This slope is for all the objects on the plot shown in Figure 2.10, consisting of cores of L-band sources and thermal radio jets taken from the literature. Fluxes of the sources from the literature were scaled to L-band frequency using a spectral index of 0.6. High mass sources in the plot show a slope of $\sim 0.57 \pm 0.15$, consistent with the lower end of the previous estimates i.e $\sim$ 0.6-0.9. Despite the presence of non-thermal emission at L-band, the cores are largely thermal, manifesting the properties of free-free emitters and showing no significant effect on the slope. The lower slope of high mass sources may be due to a smaller range of luminosity and uncertainties in their distances and fluxes. Clearly, the slopes are comparable to Anglada *et al.* (2018) who derived an empirical equation relating the two quantities at 8.3 GHz, for objects of bolometric luminosities $\sim 1 L_{\odot} \leq L_{bol} \leq 10^6\, L_{\odot}$ (see equation 2.7):

$$\left(\frac{S_{\nu} d^2}{mJy\, kpc^2}\right) = 10^{-1.90 \pm 0.07} \left(\frac{L_{bol}}{L_{\odot}}\right)^{0.59 \pm 0.03} \tag{2.7}$$

The slopes, as seen in Figure 2.10, demonstrates the similarity between low and high mass protstellar jets, owing to the comparable radio-bolometric luminosity correlations, implying that they have a common ionization, and perhaps driving mechanism.

2.5.4 Derived Properties of the Radio Jets

Quantities such as the jets' mass-loss rates, injection radius and opening angles can be estimated from the fluxes and angular sizes of their cores. Fluxes and angular sizes of the cores at L-band, together with their spectral indices, were used to calculate some of these properties in accordance with the Reynolds (1986) model.

2.5.4.1 Mass Loss Rate

Reynolds (1986) modelled free-free emission from an ionised jet. The model can be used to calculate the mass loss rate through the jet if its ionization fraction,

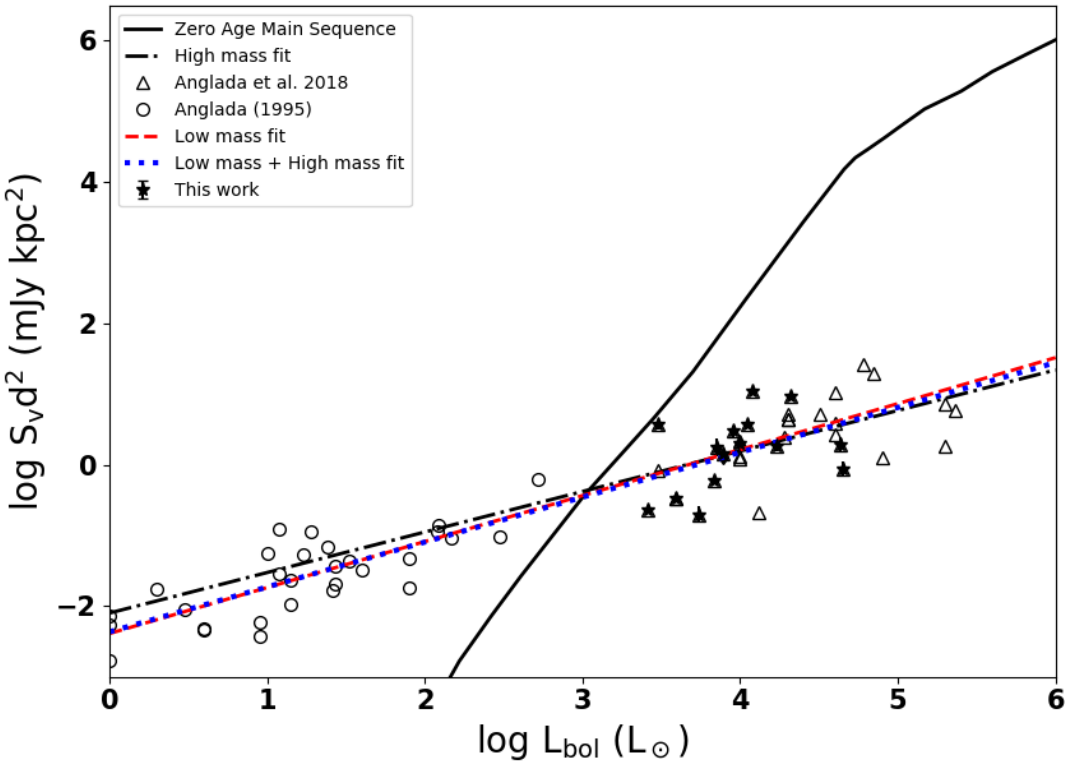

Figure 2.10: Relationship between L-band radio luminosity and bolometric luminosity for thermal radio sources. The asterisks represent the MYSOs under study while the empty circles and triangles represent the cores of low and high mass jets from Anglada (1995) and Anglada *et al.* (2018) respectively.

electron temperature, terminal velocity and an inclination angle to the line of sight are known. The model estimates the mass loss rate through a conical jet of pure hydrogen, electron temperature $T_e = 10^4$ K and inclination angle $i = 90^o$, in units of $10^{-6}\mathrm{M}_\odot\mathrm{yr}^{-1}$, to be:

$$\dot{M}_{-6} = 0.938 v_t x_o^{-1} \left(\frac{\mu}{m_p}\right) S_{mJy}^{0.75} \upsilon_o^{-0.75\alpha} d_{kpc}^{1.5} \upsilon_m^{0.75\alpha-0.45} \theta_o^{0.75} F^{-0.75} \tag{2.8}$$

where α, μ, m_p, v_t, x_o, S_{mJy}, υ_o, υ_m, d_{kpc} and θ_o are the derived spectral index, mean particle mass per hydrogen atom, proton mass, terminal velocity of the jet in 10^3 km/s, ionization fraction, observed flux density in mJy, frequency of observation (here L-band) in units of 10 GHz, turn-over frequency in units of 10 GHz, object's distance in kpc and the opening angle (in radians given as $\theta_o = 2\tan^{-1}(\frac{\theta_{min}}{\theta_{maj}})$, Eisloffel *et al.* 2000) respectively. F is a quantity that depends on the opacity and spectral index of a jet given as (Reynolds, 1986):

$$F \equiv F(q_\tau, \alpha) = \frac{2.1^2}{q_\tau(\alpha - 2)(\alpha + 0.1)} \tag{2.9}$$

where q_τ is a quantity that describes how opacity varies along the jet. F was calculated using the parameters of a standard spherical jet model if the spectral index of a source lies in the range $0.4 \leq \alpha \leq 0.8$ and standard collimated model if $0 < \alpha < 0.4$. q_τ was taken to be -3 if $0.4 \leq \alpha \leq 0.8$ and -2 for $0 < \alpha < 0.4$. The ionization fraction of MYSO jets is determined by collisions within the jets (Bacciotti 2002, Hartigan *et al.* 1994, Bacciotti & Eislöffel 1999) and perhaps ionising radiation from the central source. Typical values of jet ionization fraction x_o are ~ 0.02 to 0.4 (Bacciotti 2002, Bacciotti & Eislöffel 1999), a quantity that varies along a jet in accordance with recombination models. The maximum value of ionization fraction in the literature ($x_o = 0.4$) was used in the calculation of mass loss rate in this work as all the YSOs considered here are massive and are expected to have more powerful jets that are better collisional ionisers. The terminal velocity of jet materials (or simply jet velocity) was estimated from its range i.e. ~ 270 km/s in low-mass stars to ~ 1000 km/s in high-mass stars (Anglada *et al.*, 2015). The average velocity of optical jets is ~ 750 km/s (Mundt & Ray, 1994), a value comparable to Jiménez-Serra *et al.* (2011) and

Martí *et al.* (1998) estimates of $\sim 500\,\mathrm{km/s}$ in Cepheus A HW2 and HH 80-81 respectively. Whereas the average velocity in optical jets is $\sim 750\,\mathrm{km/s}$, a value of $v_t = 500\,\mathrm{km/s}$, estimated via proper motion of a radio jet (Martí *et al.*, 1998) was adopted as a reasonable approximation of the sample's jets' terminal velocity, in calculating the mass loss rate. A turn-over frequency of 50 GHz was assumed as the value is generally expected to be higher than 40 GHz (Anglada *et al.*, 2018). Finally, a semi-opening angle of $31°\pm3$, the average semi-opening angle for nine sources whose angles were calculated directly, was adopted for sources whose angles could not be estimated from $\theta_o = 2\tan^{-1}(\frac{\theta_{min}}{\theta_{maj}})$. The range of the calculated semi-opening angles, $25-35°$, is comparable to the estimate by Moscadelli *et al.* (2016) i.e $20° \pm 5°$.

The sample's mass loss rates $\dot{M}$ lie in the range $\sim 2.8 \pm 0.6 \times 10^{-7}$ to $6.6 \pm 0.9 \times 10^{-6}\,\mathrm{M_\odot yr^{-1}}$ (see Figure 2.11), typical of rates from MYSOs (Poetzel *et al.* 1993, Mundt & Ray 1994, Purser *et al.* 2016) and $\sim 10^2 - 10^3$ times higher than low mass counterparts. Mass loss rates of the MYSOs were found to be related to their bolometric luminosity by the equation $\dot{M} \simeq 10^{-7.5\pm0.9} L_{bol}^{0.4\pm0.2}$. Although low mass YSOs are expected to have lower mass loss rates ($\sim 10^{-10} - 10^{-8}\,\mathrm{M_\odot yr^{-1}}$; Hartigan *et al.* 1995a, Konigl & Pudritz 2000, Mundt & Ray 1994), some of them have rates that are comparable with high mass ones, in effect implying that distinguishing such jets from high mass ones (Ceccarelli *et al.*, 1997) is not straightforward.

2.5.4.2 Accretion Rate

Stellar jet outflows are considered to be closely related to accretion inflows (Pudritz *et al.*, 2007), therefore it is reasonable to estimate accretion rates of YSOs from their mass-loss rates. Hartigan *et al.* (1995b) empirically established a correlation between accretion and ejection rates of low mass stars where they demonstrated that $8 \times 10^{-5} \leq \frac{\dot{M}}{\dot{M}_{acc}} \leq 0.4$ with an average value of 0.01. Matt & Pudritz (2005) also modelled MHD jets and found that the stellar angular momentum problem in YSOs can only be solved if jet outflow rates are $\sim 10\%$ of accretion rates although the magnetic field strength can influence the ratio. This value lies within Hartigan *et al.* (1995b)'s range, albeit a factor of 10 above the average.

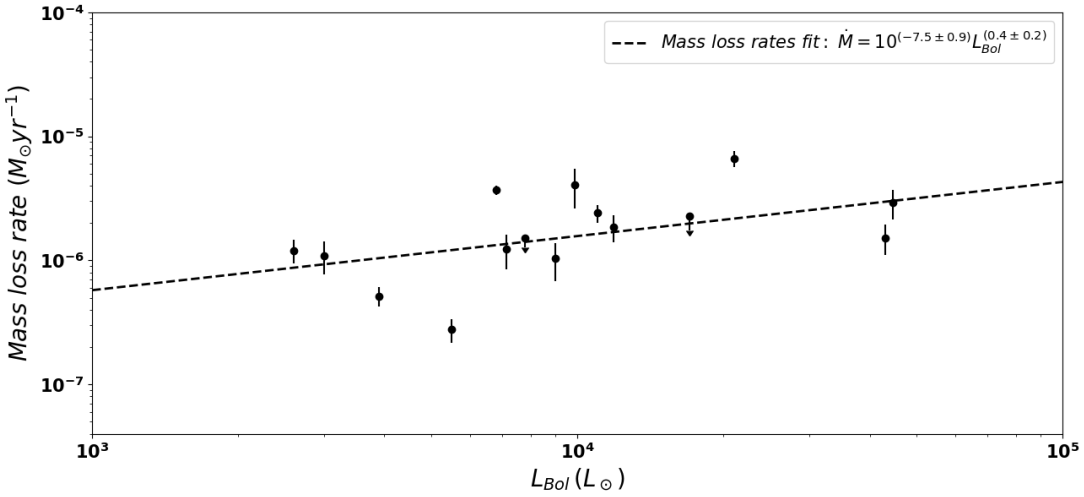

Figure 2.11: A plot showing how mass loss rates of the sources vary with their bolometric luminosity.

The average value of $\frac{\dot{M}}{\dot{M}_{acc}} \sim 0.01$ in Hartigan *et al.* (1995b)'s work was therefore used in estimating accretion rates resulting in $\dot{\mathrm{M}}_{\mathrm{acc}} \sim 10^{-4.6\pm0.3} - 10^{-3.2\pm0.2}\,\mathrm{M}_\odot\mathrm{yr}^{-1}$ which is consistent with high rates theoretically expected from the sources i.e $\sim 10^{-4} - 10^{-3}\,\mathrm{M}_\odot\mathrm{yr}^{-1}$ (McKee & Tan 2002). The accretion rate of one of the sources, G094.6028, $1.5 \pm 0.4 \times 10^{-4}\ \mathrm{M}_\odot\mathrm{yr}^{-1}$ was found to be comparable to $\sim 1.2 \pm 0.06 \times 10^{-4}\ \mathrm{M}_\odot\mathrm{yr}^{-1}$ (Pomohaci *et al.*, 2017), derived using hydrogen Brγ spectral lines.

2.5.4.3 Ejection Radius

The ejection radius of protostellar jets cannot be observed directly due to the low resolution of current instruments. However, it is possible to estimate the quantity, in units of 10^{15} cm, using equation 2.10 (Reynolds, 1986), assuming that a jet has a temperature of 10^4 K and is inclined at an angle of 90^o to our line of sight. In the equation, the symbols have their usual meaning, as described in section 2.5.4.1.

$$r_{15} = 0.56 S_{mJy}^{0.5} \upsilon_o^{-0.5\alpha} \theta_o^{-0.5} \upsilon_m^{0.5\alpha-1} d_{kpc} T^{-0.5} F^{-0.5} \tag{2.10}$$

The ejection radii of the sources range from 5.1×10^{13} cm to 1.5×10^{15} cm, with

an average value of $\sim 5 \pm 3 \times 10^{14}$ cm. It shows a correlation with the bolometric luminosity of the sources (see equation 2.11).

$$\left(\frac{r}{cm}\right) = 10^{12.1 \pm 0.8} \left(\frac{L_{bol}}{L_{\odot}}\right)^{0.6 \pm 0.2} \tag{2.11}$$

2.6 Discussion of Individual Objects

2.6.1 G083.7071

Two sources, A and B were detected in the field (see Figure 2.12). Source A whose spectral index α =0.44±0.10 is the MYSO. The L-band emission of A is elongated, perhaps signifying the presence of a jet. Apart from the MYSO, source B, located $\sim$ 3.5″ to the SW of A was also detected in the field. This source was detected in UKIDSS's IR K band just like A but not at Q-band where the rms noise $\sim 29\,\mu$Jy/beam. It is a thermal radio source of L-C spectral index $\alpha_{LC} \sim 0.60 \pm 0.13$, perhaps another MYSO.

2.6.2 G094.2615

G094.2615 is made up of two sources, A1 and A2 (Purser et al 2020 in prep), clearly seen in the C-band map of high resolution (see Figure 2.5). Its L-C band spectral index is lower than that of C-Q band which could be due to non-thermal contribution at L even though the overall spectral index shows that it is thermal i.e $\alpha_{\nu} = 0.23 \pm 0.18$. A1 was detected at both C- and Q bands giving it a C-Q spectral index of 0.47±0.24, consistent with the MYSO core. UKIDSS map of the field (Figure 2.13) shows emission that is largely aligned in a SE-NW direction similar to that of C-band. The UKIDSS emission, 2.12 μm H_2 line emission (Wolf-Chase *et al.* 2017, Varricatt *et al.* 2010) and CO molecular outflow (Fontani *et al.*, 2004) all point to a source that drives a jet in a SE-NW direction. There is also NIR emission to the west of the MYSO but its source is unclear.

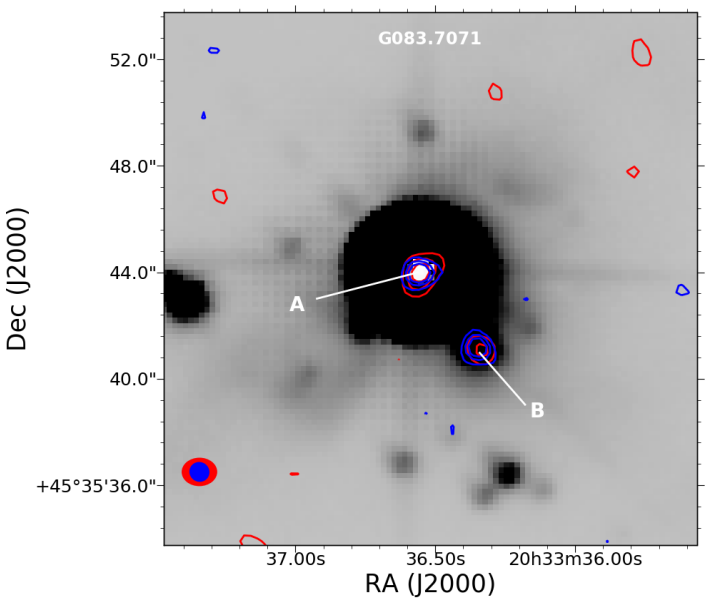

Figure 2.12: UKIDSS K band IR image of the field with L- and C-band contours shown in red and blue lines respectively.

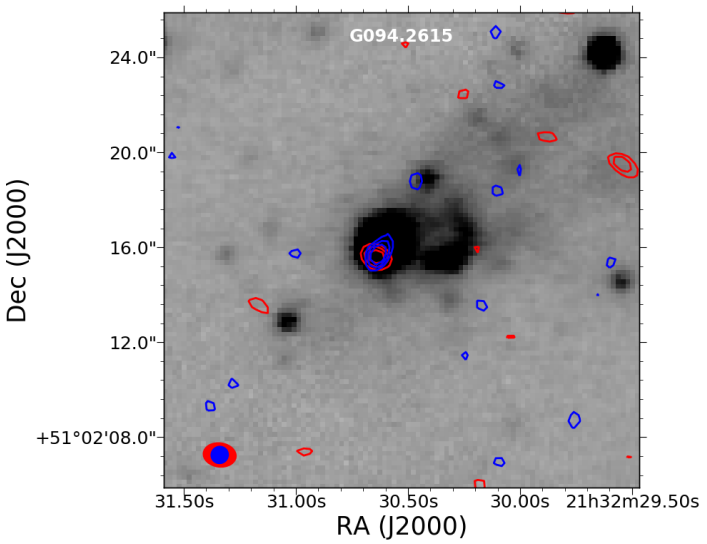

Figure 2.13: G094.2615 UKIDSS K band map with L- and C- band contours shown in red and blue lines respectively.

2.6.3 G094.4637

Two sources, G094.4637 (A+B+C+D) and a lobe (source E), of spectral indices 0.53±0.09 and 0.21±0.45 respectively were detected at L-band. The spectral index of G094.4637 (A+B+C+D) suggests that it is thermal but one of its components, D, shows non-thermal property (Figure 2.8). Lobe E is aligned with components A, B and D in such a way that they exhibit a central thermal core and associated jet lobes. Its C- and L-band emission are slightly offset in a NE-SW direction, similar to that of the outflow, consequently giving it a non-thermal nature towards the SW where the L-band emission is stronger and a thermal characteristic towards the NE. The displacement of its L-band emission is consistent with that of a jet originating from A and directed towards E.

Of the four sources, only A appears to be the core given its proximity to the IR source. Again, it is the only source in the group that was detected at Q-band (Purser, 2017) where it splits into two thermal sources, A and A2 of C-Q band spectral indices 0.39±0.12 and >1.47±0.17, suggesting that it is a binary and A or A2 drives the jet. The morphology of L-band emission, as well as the alignment of the sources in C-band, suggests the presence of a jet. The results of Smith & Fischer (1992) and Navarete *et al.* (2015) indicate the presence of multiple jets. Navarete *et al.* (2015), for example, detected a monopolar and two bipolar outflows in the field. Two of their outflows, 2a and 3a, have position angles that are comparable to the position angles of D and C from the location of the IR source i.e $\sim 210^o$ and 330^o respectively. Despite the evidence of multiple outflows in the field, the driving sources are not clear from both L- and C-band emission. Source C, detected at Q-band (Purser, 2017) may also be a thermal core. Its C-Q band spectral index is $\alpha_{CQ} \sim 0.86 \pm 0.05$. The source is located at a position angle of $\sim -30^o$ from A and is aligned with the main K-band NIR emission (Figure 2.14) hence is a potential thermal core. A 12.5 μm image of the field also display two sources [1], possibly A and C, aligned in a SE-NW direction, confirming that there are two cores.

[1] http : //rms.leeds.ac.uk/cgibin/public/RMS_DATABASE.cgi

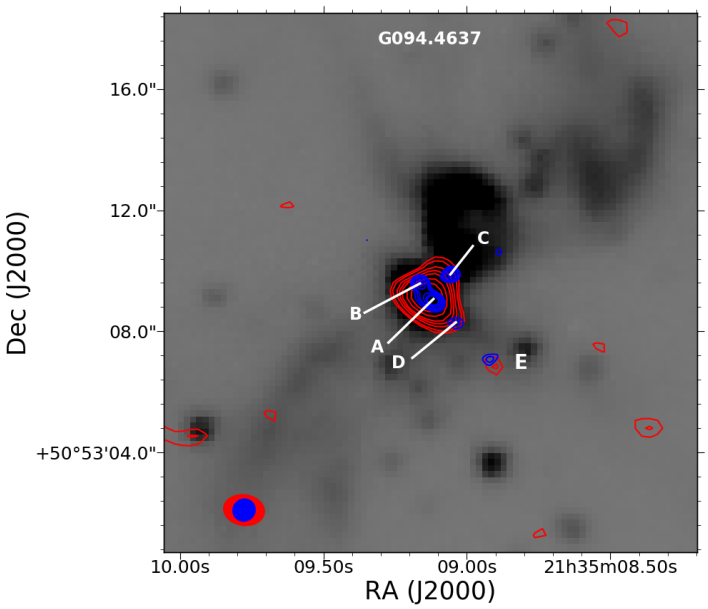

Figure 2.14: G094.4637 UIST map together with L- and C- band contours shown in red and blue respectively. Both L- and C- band contours start from 3σ and increase in steps of 2σ and 4σ respectively.

2.6.4 G094.6028

G094.6028, also known as V645 Cyg, has a thermal radio core of spectral index 0.44 ± 0.15. The source, named A is a known variable protostar of spectral type ∼O7 - O9 (Cohen, 1977). Earlier observation of the source by Di Francesco *et al.* (1997) at 8.3 GHz registered a higher flux, perhaps confirming its variability (Clarke *et al.*, 2006). Apart from the MYSO, a nearby source, B, of flux density 0.07 ± 0.02 mJy was also detected $\sim 4''$ away to the NW at L- but not C-band. It appears to be a non-thermal lobe of spectral index < -0.42. The MYSO is known to emit Brγ, accrete material, drive a bipolar CO outflow and harbour a circumstellar disk (Eisner *et al.* 2015, Hamann & Persson 1989, Clarke *et al.* 2006, Schulz *et al.* 1989).

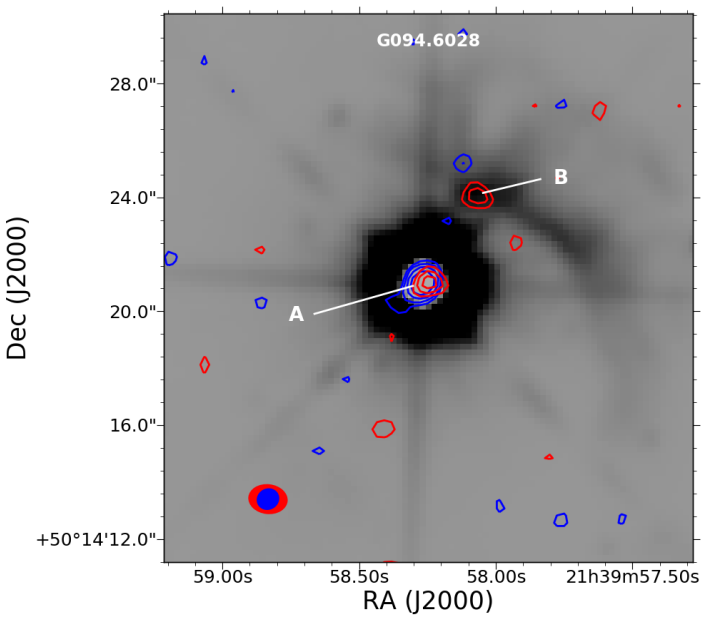

Figure 2.15: G094.6028 UKIDSS K band map with L (3,4,5 σ) - and C(3,5, 9,15 σ)- band contours shown in red and blue continuous lines respectively.

2.6.5 G103.8744

G103.8744 is associated with the IRAS source 22134+5834. It has seven radio sources in its field, three of which are within a radius of $\sim 3''$ from the location of the IR source (white asterisk in Figure 2.16). Both A and B are thermal and are close to the location of the MYSO but their SEDs suggest that they are HII-regions (see Figure 2.17; SED of G103.8744-B). Indeed, A is a known ultra-compact HII-region (Wang *et al.*, 2016) whose turn-over frequency seems to lie between 5 and 8.3 GHz (see Figure 2.7). B has a weaker but more compact IR emission, suggesting that it is a core, perhaps a low mass YSO or an obscured massive protostar. Source G, on the other hand, was not detected at C-band where the rms noise is $\sim$15 μJy/beam, implying that it is a non-thermal radio source of spectral index $\alpha < -0.44$.

Seeing that B has an IR counterpart and sources B, D, E, F and G are all aligned in a SE-NW direction, reminiscent of jet lobes, B could be the jet driver. Wang *et al.* (2016) imaged the source at radio frequencies but could not separate the MYSO from the HII region. They estimated a combined flux for the sources

as 2.1±0.2 mJy, 3.5±0.11 mJy and 2.9±0.70 mJy at 1.3 cm, 6.0 cm and 20 cm respectively. These fluxes were also used in generating the SED of source A as it is the dominant emitter in the field. A map of H_2 line emission at 2.12μm does not reveal any clear evidence of shocks or photo-dissociation locations (Kumar *et al.*, 2002), however its $C^{18}O$ (J = 1 − 0) map displays an outflow (Dobashi & Uehara, 2001) in a direction similar to that of the IR emission i.e a position angle PA∼45^o.

2.6.6 G108.5955C

L- and C- band emission of G108.5955C show different morphologies. Its L-C band spectral index $\alpha_{LC} = 0.20 \pm 0.16$ shows that it is thermal but the spectral index map displays evidence of non-thermal emission on the eastern part. Both Wu *et al.* (2009) and Xu & Wang (2010) detected molecular outflows in the field, however, the 2.12 μm H_2 line map (Wolf-Chase *et al.*, 2017) does not show any evidence of knots which may be associated with the source.

2.6.7 G110.0931

G110.0931's field contains two L-band sources, the MYSO and source D (see Figure 2.5), whose L-C band spectral indices are 0.36 ± 0.14 and -0.08 ± 0.15 respectively. The MYSO encompasses three sources; A, B and C of spectral indices α_ν = -0.14±1.49, 0.33±0.14 and -0.11±0.07 respectively (Rodríguez *et al.* 2012b, Purser 2017).

Unlike B and C, A was not detected at Q-band (Purser, 2017) consequently giving G110.0931 the overall HII region-like spectrum. The detection of sources B and C at Q-band suggests that they could be cores, however, only B is detected by NOEMA[1] at 1.3mm (Bosco et al. 2019 in prep), whereas it is expected that any core at this evolutionary stage should be detectable in the mm. Overall it seems likely, therefore, that B is the core and A and C are jet lobes. Source D, detected on the eastern part of G110.0931 was not detected at Q-band where the field rms is ~ 0.044 mJy/beam, setting a limit on its spectral index as $\alpha \leq -0.12$,

[1]NOrthern Extended Millimeter Array

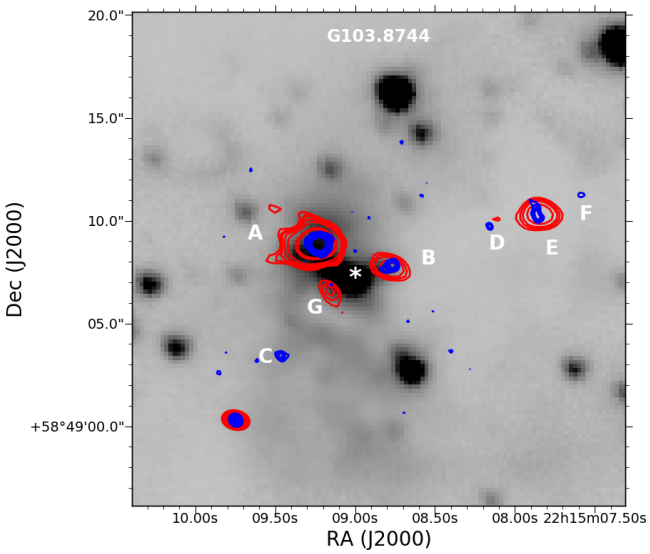

Figure 2.16: UKIDSS K band image of G103.8744 field with L- and C- band contours shown in red and blue lines respectively. The contour levels both start at 3σ. C-band ones increase in steps of 4σ while L-band in steps of 2σ.

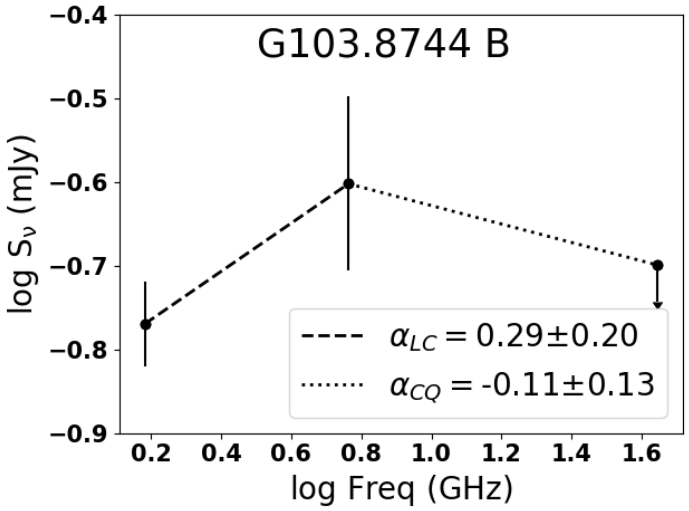

Figure 2.17: SED of G103.8744-B.

suggesting that it may be an optically thin HII region. This source does not show any clear association with G110.0931 which is approximately 3.3″ away from it.

Navarete *et al.* (2015) detected a bipolar outflow that is aligned in a direction similar to that of both L- and C- band emission. 2MASS IR- emission as well as the IR K-band continuum emission shown in Navarete *et al.* (2015) are also oriented in the same direction. Lu *et al.* (2014) detected $NH_3(1,1)$ emission that is aligned in a direction perpendicular to the jet and passing through the location of the central source, B. The orientation of $NH_3(1,1)$ emission, which is a tracer of dense molecular gas (Levshakov *et al.*, 2013) and that of the molecular line at 2.12 μm suggests that the source may be a disk-jet system. Finally, source C has higher radio flux compared to A, perhaps an indicator of an E-W density gradient.

2.6.8 G111.2552

G111.2552, also known as I23139 (Trinidad *et al.*, 2006) is a thermal radio source of spectral index $\alpha \sim 0.67 \pm 0.04$. Its L- and C-band emission are largely aligned in a SE-NW direction (see Figure 2.8). Its Q-band flux appears to be lower than expected (see Figure 2.7) when compared to estimates from Trinidad *et al.* (2006) i.e a flux density of 0.98±0.24 mJy and 0.53±0.13 mJy at 23 GHz and 8.5 GHz respectively. Furthermore, Trinidad *et al.* (2006) detected a nearby source of flux density 0.22±0.07 mJy, approximately 0.5″ to the south, at 8.5 GHz, which they suppose is I23139's companion. Finally, molecular outflows (Wouterloot *et al.*, 1989) and water maser emission (Tofani *et al.* 1995; Trinidad *et al.* 2006), detected in the field, suggests presence of outflow activity (De Buizer *et al.*, 2005).

2.6.9 G111.5671

Three sources, A, B and C were detected in the field at L-band (see Figure 2.18). Source A, also known as NGC 7538 IRS9 (Mitchell & Hasegawa, 1991) seems to be the core of G111.5671 while B and C, located $\sim$ 2.8″ and 1.7″ away to the SW and NE of the core respectively are its lobes. L-C spectral indices (α_{LC}) of B and C are < -0.6 and 0.60 ± 0.21 suggesting that B is a non-thermal source while C is thermal. Also, B seems to be more diffuse, bow-shaped and extended

towards A as seen in the C-band image of higher resolution, suggesting that it is a bow shock.

A has a flux density of 1.00±0.44 mJy, 0.76±0.15 mJy (Sandell *et al.*, 2005) and < 0.51 mJy (Rengarajan & Ho, 1996) at 4.86 GHz, 8.46 GHz and 15 GHz respectively. van der Tak & Menten (2005) used both C and A configurations of the VLA to estimate its flux density at 43 GHz, obtaining 2.9 ± 0.3 mJy and 1.1 ± 0.3 mJy respectively. The fluxes give it a spectral index $\alpha = 0.84 \pm 0.09$. The three sources were previously detected by Sánchez-Monge *et al.* (2008) as a single source at 1.3 cm. The source, aligned in a NE-SW direction has a spectral index of $> +0.1$. They also detected another source to the SW of A, B and C whose spectral index is > -1.2. The orientation of the sources suggests the presence of a jet in a NE-SW direction.

Both a highly collimated HCO^+ outflow observed by Sandell *et al.* (2005) and 2.12 μm H_2 emission by Davis *et al.* (1998) are aligned in a NE-SW direction, similar to the alignment of the radio sources. An offshoot of the IR emission that is directed towards the south is also seen in both 2MASS and Sandell *et al.* (2005)'s map. This emission is in the same direction as a CO outflow (Sandell *et al.* 2005, Davis *et al.* 1998), perhaps implying the presence of two outflow drivers. Furthermore, the CO J = 2 − 1 observed by Mitchell & Hasegawa (1991) shows a blue outflow lobe that is aligned in a NE - SW direction and a red one in the SE-NW.

2.6.10 G114.0835

Two sources, A and B were detected at L-band (see Figure 2.19). B is a non-thermal source of spectral index $\alpha \sim -0.42 \pm 0.19$ while A is a thermal source whose spectral index is 0.40±0.20. A high-resolution image of A at C-band reveals two partially resolved sources, A1 and A2, that are oriented in a NE-SW direction. The two sources (Figure 2.5) are likely to be thermal. It is not clear if A and B are associated but B is elongated in the direction of IR emission in the field (Navarete *et al.* 2015, Skrutskie *et al.* 2006) signifying the likelihood of the presence of a jet. Also, A and B are aligned in the direction of IR emission.

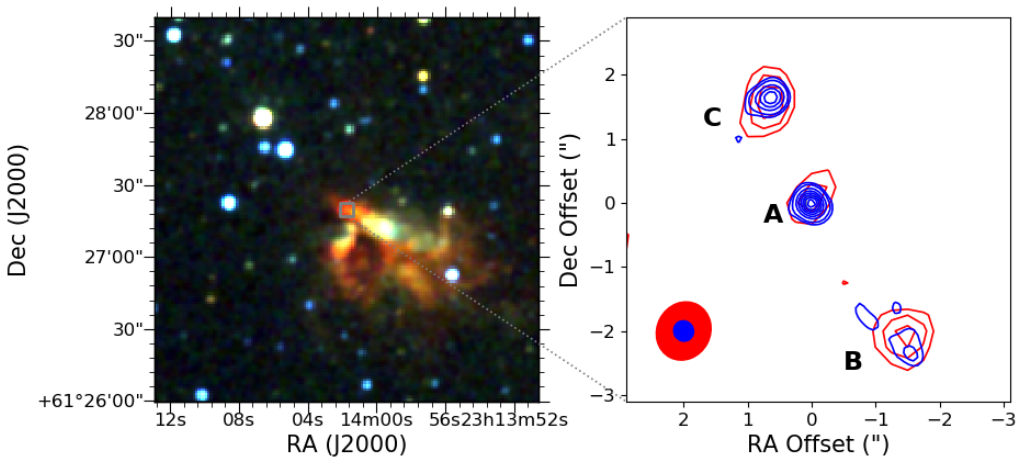

Figure 2.18: Left panel: 2MASS Near IR colour image (R,G,B colour-scale of K,H,J bands) of G111.5671's field. Right: L- and C- band contours of G111.5671, shown in red and blue lines respectively. The contour levels both start at 3σ. C-band ones increase in steps of 4σ while L-band in steps of 1σ.

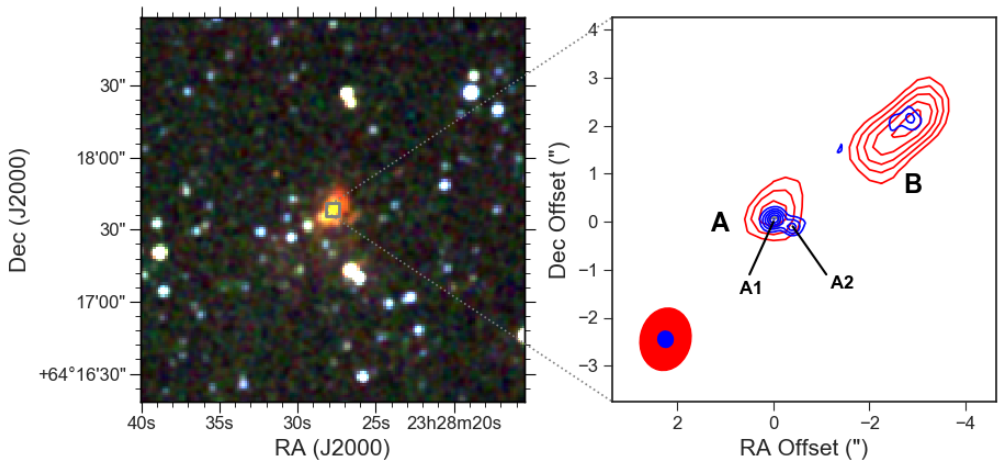

Figure 2.19: Left panel: 2MASS Near IR colour image (R,G,B colour-scale of K,H,J bands) of G114.0835 field. Right: L- and C- band contours of the MYSO, shown in red and blue lines respectively. The contour levels both start at 3σ. C-band ones increase in steps of 4σ while L-band in steps of 2σ.

2.6.11 G126.7114

G126.7114 is a thermal source of spectral index $\alpha = 0.82 \pm 0.02$. Its L-band and C-band emission are largely aligned in a SE-NW direction. Apart from G126.7114, a weak source (4σ detection) of flux density 0.08±0.02 was also detected at C-band, approximately 4.5″ away to the SE at ($\alpha = 01^h23^m33.29^s; \delta = +061°48^m44.7^s$). NIR K-band emission (Jiang *et al.* 2001; Navarete *et al.* 2015) of the source is aligned in a direction similar to that of L- and C-bands suggesting the presence of a SE-NW outflow. Navarete *et al.* (2015) also detected knots that are typical of a bipolar jet with a similar orientation i.e at a position angle PA$\sim 160^o$. Moreover, Jiang *et al.* (2001) detected a polarization disk that is oriented in a direction perpendicular to that of the outflow, suggesting a disk-jet case.

2.6.12 G136.3833

G136.3833-A was detected at both C- and Q- but not L-band where the field rms is $\sim 50\,\mu$Jy/beam. It is a thermal radio source whose C-Q band spectral index α_{CQ} is $\sim 1.22 \pm 0.11$. A non-thermal source, B of spectral index $\alpha_{LC} = -0.68 \pm 0.08$, was detected approximately 6″ to the west of A at L-band. The source whose position angle is 60 ± 12^o at L-band is elliptical at L- but irregular at C-band. The IR nebula in the field is oriented in an east-west direction (Skrutskie *et al.*, 2006), just like the alignment of sources A and B (see Figure 2.20). Both A and B have 2MASS counterparts at K-band and B may, therefore, be a non-thermal lobe or a star.

2.6.13 G138.2957

G138.2957, also known as AFGL 4029 (Ray *et al.*, 1990) displays an extended morphology at the C-band map of uv-range 15-200 kλ but splits into B and C at L-band. Both B and C are non-thermal lobes whose flux densities at L-band are 0.13±0.04 mJy and 0.10±0.03 mJy respectively. Polygons whose sizes are equivalent to the size of the sources at L-band were used to estimate their fluxes at C- band. The fluxes of B and C were approximated to be 0.07±0.02 mJy and 0.06±0.02 mJy respectively, at C-band, giving them spectral indices of -0.46±0.31

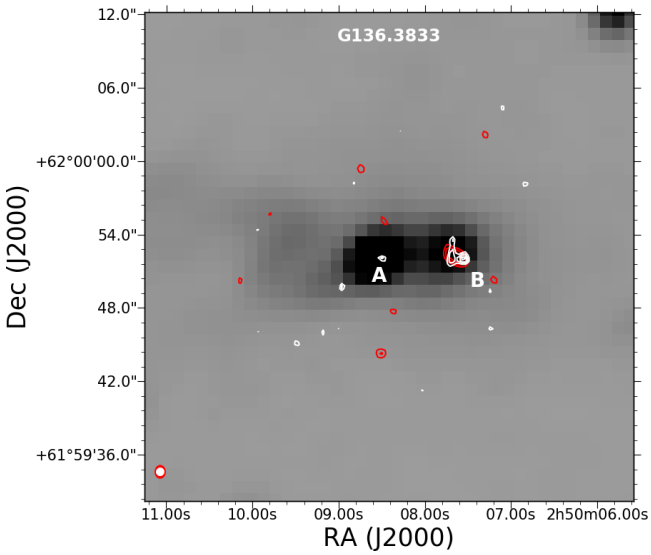

Figure 2.20: 2MASS Ks-band map of G136.3833 field and over-plots of L- and C-band contours shown in red and white lines respectively.

and -0.38±0.33 respectively. Its spectral index map also displays evidence of non-thermal emission, with some pixels having a non-thermal index of -0.6±0.2. The central core of the source was not detected at L-band. It appears to be located at the position of the peak emission at C-band (Figure 2.8). A polygon that is equivalent to the C-band contour of level 7 (80μJy/beam), which encloses the peak emission, was used in estimating the flux density of the core at C-band as 0.09±0.01 mJy. A similar polygon was used at L-band, approximating its peak flux at the frequency as <0.06 mJy. The fluxes suggest that the source has a thermal core of spectral index α >0.69.

G138.2957 is known to drive an optical jet (Ray *et al.*, 1990) whose position angle is comparable to that of C-band emission ($\sim 75^o$). Navarete *et al.* (2015) also mapped a bipolar outflow of position angle PA $\sim$ 90 degrees which appears to be associated with it. Kurtz *et al.* (1994) and Carral *et al.* (1999) observed the source using VLA's B and D configurations respectively, estimating its flux density at 3.6 cm to be $\sim$ 2.1 mJy and 0.60 $\pm$ 0.12 mJy, perhaps signifying variability.

2.6.14 G139.9091A

G139.9091A, also known as GL437S (Kumar Dewangan & Anandarao, 2010) is a thermal radio source of spectral index $\alpha = 0.36 \pm 0.04$. It has a position angle of $\sim 50 \pm 8^{o}$, similar to the orientation of de Wit *et al.* (2009)'s mid-infrared emission. Similarly, Manjarrez *et al.* (2012) imaged it using archival data from JVLA's B,C and D configurations at 3.6 cm and 2 cm getting a comparable position angle i.e $\sim 60^{o}$. Its flux density at 3.6 cm and 2 cm are 1.5±0.4 mJy and < 2 mJy respectively. Both infrared (Figure 2.21) and CO (Gomez *et al.*, 1992) emission of the field are aligned in a N-S direction, however, its 2.12 μm map (Davis *et al.*, 1998) does not show evidence of outflow.

Apart from G139.9091A, an optically thin HII region of spectral index -0.11 ± 0.02, also identified as AFGL 437W (Manjarrez *et al.*, 2012), was detected to the NW of A. It has flux densities of 19.0±0.5 mJy and 16.3 ±0.4 mJy at L- and C-bands respectively.

2.6.15 G141.9996

G141.9996, also known as AFGL 490 (Davis *et al.*, 1998) is an extended source that is largely elongated in a N-S direction. Two lobes, B and C, of flux densities 0.06±0.03 mJy and 0.07±0.03 mJy respectively were detected at L- but not at C-band. The L-C spectral indices of B and C are $\alpha_{LC} < -0.51$ and < -0.63 respectively, suggesting that they are non-thermal lobes. The core, A, is thermal and is elongated in a direction that is similar to the alignment of A, B and C i.e PA $\sim 180°$. Both CO outflow (Mitchell *et al.* 1995) and 2.12 μm emission (Davis *et al.* 1998, Navarete *et al.* 2015) maps of the field are oriented in a NE-SW direction. However CS J = 2 → 1 emission of the source has a position-angle of -45^{o} (Schreyer *et al.*, 2002).

In addition, an optically thin source of spectral index -0.06±0.16 was detected approximately 13″ away, at both bands. The source, located to the west of G141.9996, at α(J2000) $\sim 03^{h}27^{m}37.07^{s}$ δ(J2000) $\sim +058°46^{m}59.4^{s}$, has flux densities of 0.12±0.03 mJy and 0.11±0.02 mJy at L- and C-bands respectively.

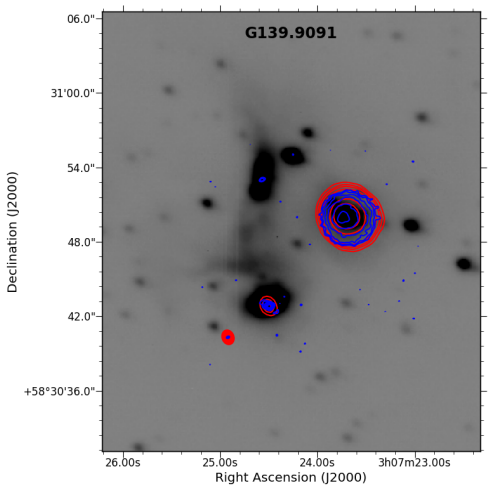

Figure 2.21: UKIDSS K band map of G139.9091A field and over-plots of L- and C-band contours shown in red and blue lines respectively.

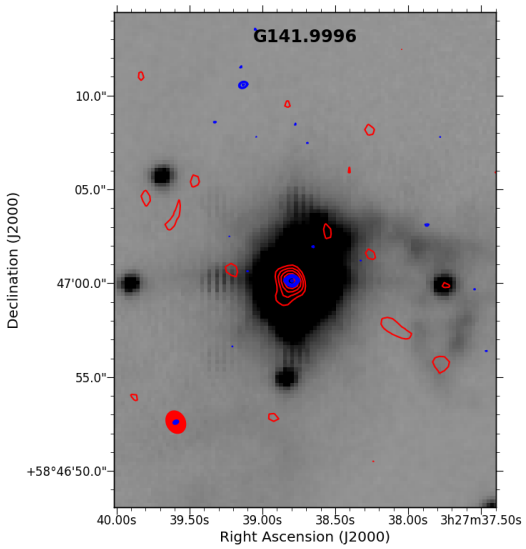

Figure 2.22: UKIDSS J band image of G141.9996 shown in grey together with L- and C-band contours in red and blue respectively.

2.7 Conclusions

At least forty per cent of the objects studied show evidence of non-thermal emission. Six of the sources; G094.6028, G103.8744, G111.5671, G114.0835, G138.2957 and G141.9996, have non-thermal radio lobes, implying that massive stars form via disk-fed accretion, just like their low mass counterparts. Clearly, non-thermal lobes were not detected in a significant fraction of the jets which complicates the interpretation of their driving mechanisms. However, with the rms of the L-band observation, $\sim$25 mJy/beam, it is likely that their lobes were too weak to detect at the sensitivity of the observation. For example, the average value of the upper limit of a detection in the L-band observation, estimated as 3$\times$rms, is 0.075 mJy, a value comparable with the integrated fluxes of some of the lobes. Therefore, any lobes with lower intensities were undetectable, perhaps that is why sources of higher bolometric luminosities showed a higher likelihood of having lobes compared to lower luminosity counterparts. Again, the presence non-thermal lobes in both low and intermediate mass protostars (Rodríguez-Kamenetzky *et al.*, 2016) suggest that the lobes are ubiquitous in protostars of all masses.

The detection of non-thermal lobes in some of the jets is also a clear indicator of the presence of synchrotron emission in the objects, in effect, implying the existence of magnetic fields and charged relativistic particles. This finding suggests that magnetic fields play a significant role in the jets, perhaps in driving them (Blandford & Payne 1982, Shu *et al.* 1994b), although a thermal jet can interact with the ambient magnetic field to generate non-thermal emission. Certainly, the similarity between the alignment of the non-thermal lobes and the orientation of the IR outflow cavities, in most of the jets, strongly support the presence of jet magnetic fields. A previous study of 46 MYSOs by Purser *et al.* (2016) also detected non-thermal lobes in 50% of the objects, emphasising the significance of magnetic fields in massive protostellar jets.

The driving sources, also known as cores, were all found to be thermal. Their average spectral index is $\sim 0.42 \pm 0.27$, similar to the index of ionized winds, i.e. α =0.6. They drive out mass at rates that lie in the range $\sim 3 \times 10^{-7} \lesssim \dot{M} \lesssim 7 \times 10^{-6}\,M_{\odot}yr^{-1}$, approximately $10^2 - 10^3$ times higher than their low mass

counterparts. On the other hand, when the radio luminosities of the jets were plotted against the bolometric luminosities of their protostars, they were found to scale in a manner similar to low mass protostellar jets. Again, supporting a tight similarity between low and high mass protostellar jets.

Chapter 3

Multi-Epoch Study of Massive Protostars

3.1 Introduction

Multi-epoch study of astrophysical objects is crucial in identifying any changes that they display. Massive protostellar jets, for example, W75N B (Carrasco-González *et al.*, 2015), have shown evidence of changes in both size and shape. Indeed protostars are known to manifest variability in many ways (Marti *et al.* 1995, Zwintz 2008). They show displacement through tidal interactions with their neighbours (Paron *et al.*, 2016) and jet proper motions. Knowledge of variability of the objects can thus be instrumental in identifying their driving sources and associated knots with minimal ambiguity (Caratti o Garatti *et al.*, 2009). The rates at which their jets accelerate and/or decelerate can also be estimated from the proper motion of their knots.

Unlike in massive protostars where flux variability has been observed in a few sources, ∼20% to 30% of low-mass protostars are estimated to manifest evidence of variability (Choi *et al.*, 2014), some of which may be associated with jet activities. About $20 - 50\%$ of the variable low-mass protostars experience mild changes (Choi *et al.*, 2014), attributed to an increase in their magnetic activities. However, flux variability in protostars is largely linked to accretion activities (Contreras Peña *et al.*, 2017). Indeed, some studies attribute flux variabilities to

periods of accretion burst (Zhu *et al.* 2009, Vorobyov & Basu 2006, Zhu *et al.* 2009) that occur within relatively stable rates of inflows. Such accretion activities should manifest through their jets as outflows are tightly linked to inflow activities. A piece of possible evidence for accretion burst in massive protostars is the discrepancy between the observed and theoretical estimates of their accretion rates (Purser *et al.* 2016, Krumholz *et al.* 2009). Intervals of high accretion rates, in the form of bursts, could be responsible for their formation.

Massive protostars can experience the rare but intense outbursts of radio emission. The phenomenon was reported in two 20 $M_{\odot}$ MYSOs, S255 NIRS 3 (Caratti o Garatti *et al.*, 2017) and V723 Carinae (Tapia *et al.*, 2015). Other known variable MYSOs are; NGC 6334I (Hunter *et al.*, 2017) and V645 Cygni (Clarke *et al.*, 2006). Such observations are relatively rare in massive stars and there is considerable scope for a large scale survey. However, the number of objects of interest vis-a-vis the available instruments does not allow for systematic monitoring over long periods, only permitting sporadic multi-epoch observations (Teixeira *et al.* 2018, Thomas *et al.* 2013, Marti *et al.* 1995) of long baselines. In view of the mentioned significance of multi-epoch observations, a sample of four massive protostars, previously observed in 2012 was re-observed in March 2018 to search for and study variability in jets of massive protostars.

3.2 Observation and Data

3.2.1 Source Selection

Eleven objects were selected from a C-band survey that was conducted by Purser (2017) in 2012, however, only four of the objects, G133.7150 + 01.2155, G173.4839 +02.4317, G192.6005 − 00.0479 and G196.4542 − 01.6777, were observed. These sources, spatially resolved at C-band, were identified for re-observation at the same frequency band in 2018 to search for evidence of positional variability. The time difference between the two observations, approximately five and a half years, allowed for detection of displacements within the jets at their distances i.e 2.0−5.5 kpc. For example, a jet located within a distance d=2.0−5.0 kpc, driving out mass at a typical velocity v=500 km s^{-1} (Marti *et al.* 1995; Curiel *et al.* 2006)

should manifest an angular shift of θ_s $\sim$0.12$-$0.3″, detectable between the two epochs. Calculations from astrometric precision of an image, $\sim \frac{FWHM}{SNR}$ (Walker 1997, Monet *et al.* 2010), show that a 1σ shift of 0.03″ should also be detectable for components with a SNR=10. The difference in the epochs also provides an opportunity for a search for evidence for flux variability and precession, features that were noted by Purser (2017). The thermal cores were also selected for observation at 22.2 GHz to allow for a more accurate estimate of their free-free SEDs, free from effects of dust and non-thermal emission. Table 3.1 shows a list of the sources and some of their properties.

3.2.2 VLA Observation

The four objects were observed on the 29$^{\text{th}}$ of March 2018 using NRAO's JVLA telescope in A configuration at 6 GHz. Two of them, G192.6005 $-$ 00.0479 and G196.4542 $-$ 01.6777, were observed again on the 05$^{\text{th}}$ of May 2018 at 22.2 GHz to allow for estimation of spectral indices. The observations, done under the project code 18A-158, are of angular resolutions, 0.33″ and 0.089″; bandwidths, 4 and 8 GHz; and integration times, $\sim$ 20 minutes and 30 minutes at 6 GHz and 22.2 GHz respectively. A list showing the observed sources and the calibrators used in scaling their fluxes and phases at 6.0 and 22.2 GHz is shown in table 3.2. The same set of calibrators were used in the 2012 observation to minimise calibration errors. Some of the physical properties of the calibrators, at the frequencies of observations, are also shown in the table.

Calibration and imaging were done using the NRAO's data reduction software, CASA (Common Astronomy Software Applications; McMullin *et al.* 2007). C-band images were created using Briggs (Briggs, 1995) weighting of robustness 0.5,

Table 3.1: A table listing RMS source names, positions, bolometric luminosities and distances. The last column shows the references for the adopted distances.

Source	RA(J2000)	DEC(J2000)	L_{bol}	Distance	
			($L_\odot$)	(kpc)	Reference
G133.7150 + 01.2155	$02^h25'40.77''$	$+62°05'52.4''$	140000	2.0	Hachisuka *et al.* 2006
G173.4839 + 02.4317	$05^h39'09.92''$	$+35°45'17.2''$	2900	1.8	Snell *et al.* 1990
G192.6005 $-$ 00.0479	$06^h12'54.01''$	$+17°59'23.1''$	45000	1.8	Burns *et al.* 2016
G196.4542 $-$ 01.6777	$06^h14'37.06''$	$+13°49'36.4''$	94000	5.3	Honma *et al.* 2007

Table 3.2: Calibrators and the sources that they were used to calibrate. Fluxes for both the flux and phase calibrators, together with the angular sizes of phase calibrators are shown in the table. − means that a source is point-like. 3C48 is a single source of angular size, $0.35 \pm 0.01''$ by $0.19 \pm 0.01''$ at 6.0 GHz. It splits into two sources at 22.2 GHz. P shows that phase-only self-calibration was performed on the objects. The number before P indicates the number of iterations of the calibration.

Source	Calibrators						Self-cal
	Flux Cal	S_ν (mJy)	Phase Cal	S_ν (mJy)	Size ($''\times''$)	PA	
		At 6.0 GHz					
G133.7150 + 01.2155	3C48	4450±50	J0228+6721	1280±5	–	–	–
G173.4839 + 02.4317	3C48	4450±50	J0555+3948	3980±10	$0.05 \pm 0.01 \times 0.05 \pm 0.01$	170 ± 30	2P
G192.6005 − 00.0479	3C48	4450±50	J0559+2353	251±1	$0.05 \pm 0.01 \times 0.04 \pm 0.01$	160 ± 10	P
G196.4542 − 01.6777	3C48	4450±50	J0559+2353	251±1	$0.05 \pm 0.01 \times 0.04 \pm 0.01$	160 ± 10	P
		At 22.2 GHz					
G192.6005 − 00.0479	3C48	1130±50	J0559+2353	193±1	–	–	p
G196.4542 − 01.6777	3C48	1130±50	J0559+2353	193±1	–	–	P

except in G133.7150 + 01.2155, where robustness was set at -1 due to the presence of diffuse emission of its field. In K-band, imaging of G192.6005 − 00.0479 and G196.4542 − 01.6777 was done with robustness parameters of 0.0 and 0.5 respectively. G192.6005 − 00.0479 was in outburst and its field was affected by strong side-lobes which were suppressed by the Briggs weighting of robustness 0.0. The HPBW of the synthesised beams, used in deconvolving the dirty maps at both C- and K- bands, are shown in Table 3.3. Some of the images were generated after self-calibration of their visibilities, either once or twice, to improve their signal to noise ratios (see section 2.3.2 for details). Phase-only self-calibration was performed on the images to improve their dynamic range. The resultant images have rms noise values shown in Table 3.3.

The average rms noise for three fields at 6 GHz is 6 μJy/beam, however, in G133.7150+01.2155's field, the rms is higher i.e 21 μJy/beam due to the presence of diffuse emission in its field. At 22.2 GHz, the rms noise is slightly higher than the rms noise at 6 GHz i.e an average value of 10 μJy/beam. To check on the effectiveness of the calibration process, the calibrators were imaged and inspected, especially phase calibrators (see Figure 3.1). All the phase calibrators are point-like at both frequencies, demonstrating the success of the process. The flux calibrator, on the other hand, is resolved into two sources at 22.2 GHz.

Table 3.3: Wavelength, synthesised beam, position angle and field rms of the observations.

Source	Synthesised beams					
	$\nu = 6$ GHz			$\nu = 22.2$ GHz		
	$\theta_{maj} \times \theta_{min}$ ($''$)	PA ($^\circ$)	rms(μJy/beam)	$\theta_{maj} \times \theta_{min}$ ($''$)	PA ($^\circ$)	rms(μJy/beam)
G133.7150 + 01.2155	0.29×0.19	-64.12	21	–	–	–
G173.4839 + 02.4317	0.29×0.26	-21.29	6	–	–	–
G192.6005 − 00.0479	0.29×0.27	15.08	6	0.10×0.09	-51.23	9.5
G196.4542 − 01.6777	0.29×0.27	4.30	6	0.13×0.10	76.45	11

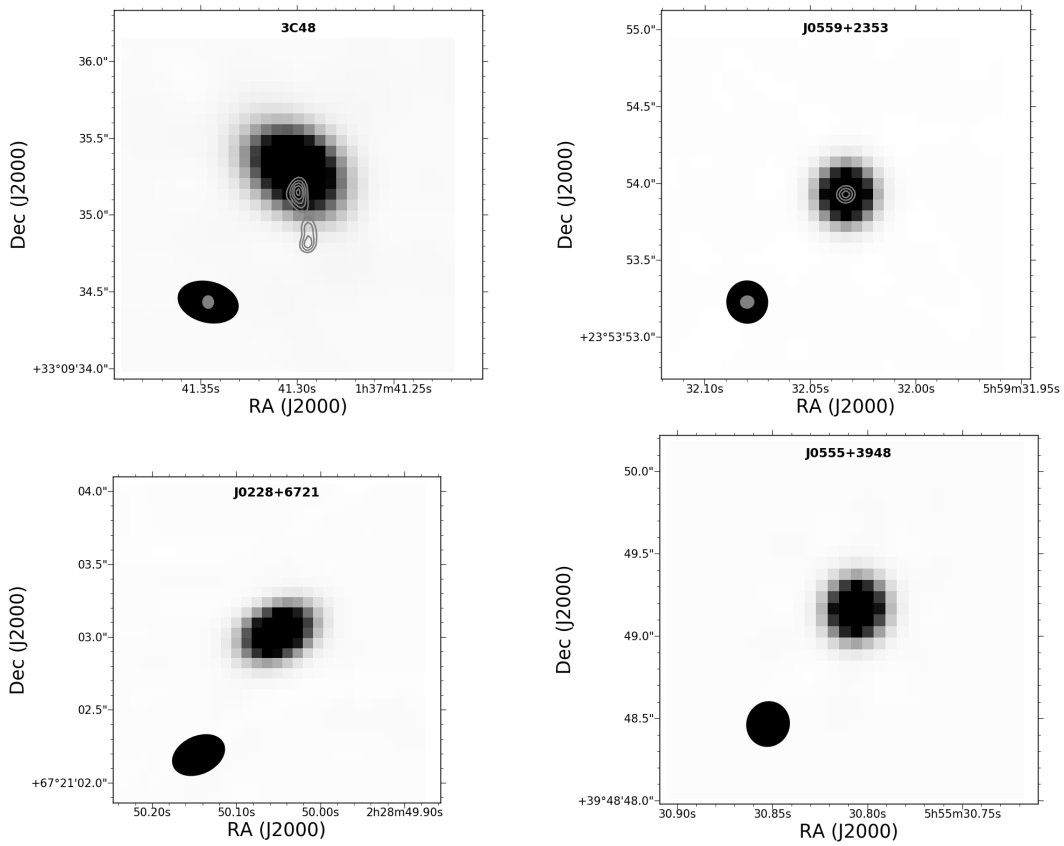

Figure 3.1: Grey-scale and contour images of the flux and phase calibrators. The grey maps represent 6.0 GHz emission while the contours are for 22.2 GHz.

3.3 Results

3.3.1 Continuum Emission

All the sources were detected at the frequencies of the observations, four at 6 GHz and two of them at 22.2 GHz. At 6 GHz, all the fields of the objects display evidence of multiple radio sources. Eleven were detected in the field of G133.7150+01.215, three in G173.4839+02.4317, nine in 192.6005-00.0479 and four sources in G196.4542-01.6777. In some cases, the 6 GHz emission manifested elongated morphology, enclosing multiple components within it e.g in G196.4542-01.6777. G192.6005-00.0479 and G196.4542-01.6777, observed at both 6 GHz and 22.2 GHz, have radio sources that were detected at both frequencies. Four sources were detected within the field of G192.6005-00.0479 and one in G196.4542-01.6777's field at both frequencies. These sources show more compact structures at 22.2 GHz compared to 6 GHz, even though their emission at 22.2 GHz also manifests extended features. In all the sources, the extended features have major axes θ_{maj} that are smaller than the largest angular sizes θ_{LAS} of the observations. Typically, θ_{maj} of the sources $\lesssim 2''$ at 6 GHz and $\lesssim 1''$ at 22.2 GHz while $\theta_{LAS} = 3.6''$ and $2.4''$ at 6 GHz and at 22.2 GHz respectively.

Besides the continuum emission, methanol and water maser emission of frequencies 6.7 GHz and 22.2 GHz respectively, were also observed to aid in the calibration of the data. The emission were detected in fields of both G133.7150+01.215 and G173.4839+02.4317, however, no detections were registered in the fields of G192.6005-00.0479 and G196.4542-01.6777 where the rms noise estimates are 0.6 mJy and 0.4 mJy respectively.

Fluxes, sizes and positions of the sources were estimated using the CASA task `imfit` except for the unresolved sources whose sizes could not be deconvolved. Besides the uncertainties by `imfit`, additional errors, added in quadrature, were included to take care of the errors due to calibration of the fluxes and positional accuracy of the observations. The uncertainties due to calibration of the fluxes were estimated to be 10% of a source's flux. Likewise, a typical value of the positional accuracy of the JVLA, estimated as 10% of the HPBW of a synthesised beam, was used.

3.3.2 Radio Sources

3.3.2.1 G133.7150+01.215

G133.7150+01.2155 is located in the W3 IRS5 high-mass star-forming region (see Figure 3.2). This region is known to harbour compact radio sources, three of which have mid-IR counterparts (van der Tak *et al.*, 2005). All the radio sources detected in van der Tak *et al.* (2005) and Purser (2017) were detected at 6 GHz except Q10 (Purser, 2017). The labelling in van der Tak *et al.* (2005) and Purser (2017) were adopted here. Table 3.4 lists all the sources detected above 3σ.

Table 3.4: Peak intensities, flux densities, deconvolved angular sizes and position angles of the sources detected within the field of G133.7150+01.215 at C-band in 2018. − means that the source is a point source or its emission is elongated and irregular such that its actual size and orientation is not clear.

Source	Peak flux (mJy/beam)	Sν (mJy)	Major Axis (arcsecs)	Minor Axis (arcsecs)	PA (deg)
C1	0.18±0.03	0.25±0.06	0.35±0.03	0.22±0.02	30±10
Q2+Q3+Q6	1.55±0.05	0.66±0.04	–	–	–
Q4	0.25±0.03	0.24±0.15	–	–	–
Q4b	0.24±0.04	0.59±0.07	0.36±0.09	0.17±0.09	41±25
Q5+Q7	0.96±0.13	3.26±0.57	1.2±0.1	0.36±0.04	20±10
K8	0.98 ±0.09	1.11±0.19	–	–	–
Q9	0.16±0.02	0.11±0.03	–	–	–
Q8	0.77±0.11	0.93±0.22	–	–	–

van der Tak *et al.* (2005) established shifts in the positions of some of the radio sources, translating to an average transverse velocity of 116 km s^{-1}, an estimate comparable to the proper motion of K8 by Wilson *et al.* (2003). They also observed that the position angles (PAs) of the shifts are different, implying that the jet is undergoing precession. Comparing the locations of some of the radio sources in 2012 (Purser, 2017) with their positions in 2018 confirms that they are moving away from Q5, perhaps the core of the jet (see Table 3.5). Indeed Q5 has a mid-IR counterpart and its position, at Q-band, in both van der Tak *et al.* (2005) and Purser (2017) only manifests a marginal offset of 0.040″±0.006 after a period of sixteen years. Moreover, the spectral indices of C1, K8, Q7, Q8 and Q9 are negative, implying that they are non-thermal lobes (Purser, 2017) while

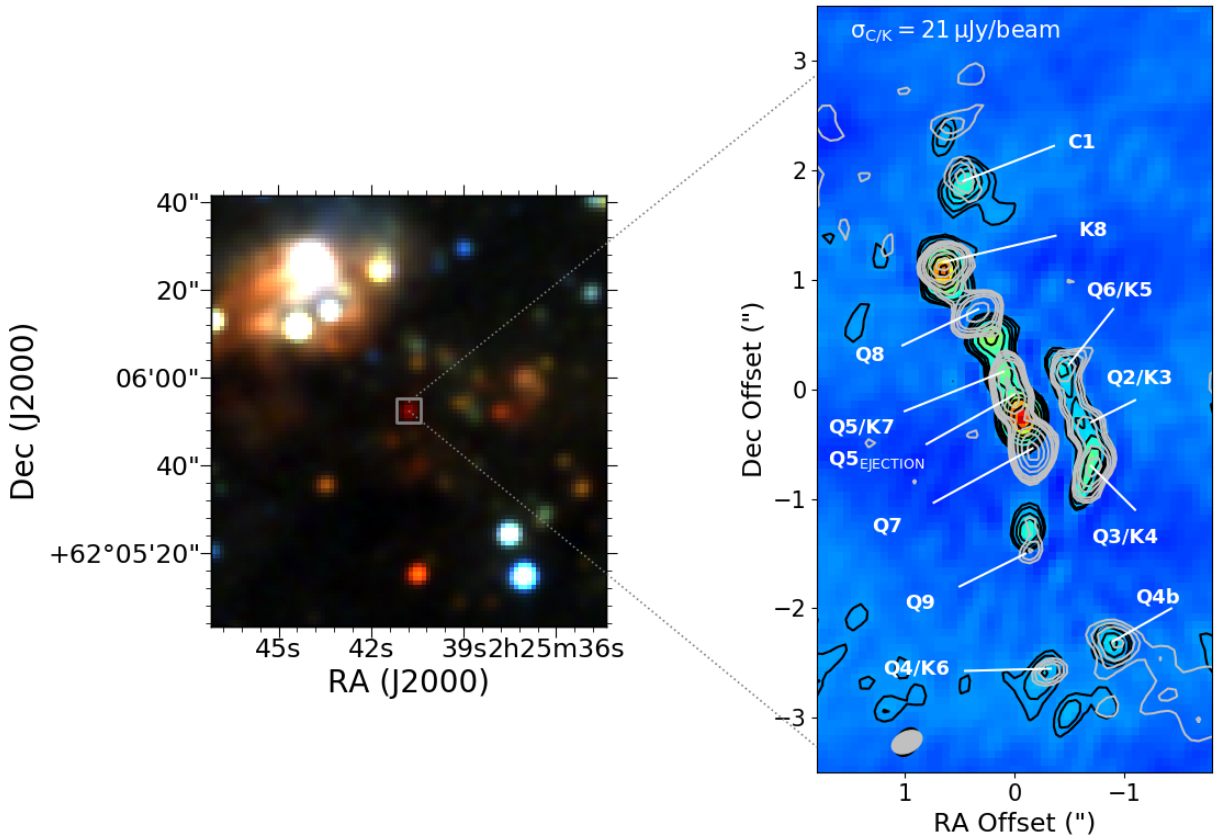

Figure 3.2: Left: 2MASS RGB image of the field of G133.7150+01.215. Right: The silver contours show positions and morphologies of the radio sources in the 2018 observation. Features of the radio sources in 2012 are also added, i.e the colour map and black contours, to show how they changed within the period. The contour levels are 3, 5, 7, 11, 15, 25, 37, 48 and 70σ in both the 2012 and 2018 maps. The letters used in the naming of the radio sources correspond to the frequency band of their detection.

that of Q5 is thermal. Q4b also has a negative spectral index and may be one of the lobes. Q4, on the other hand, appears to be a lobe but it has a mid-IR counterpart and its spectral index (Purser, 2017) shows that it is thermal. Besides the sources in van der Tak *et al.* (2005) and Purser (2017), a new source, denoted as $Q5_{\rm Ejection}$, was detected in the 2018 observation. This source seems to be a new ejection from the core of the jet.

Knowledge of positional variability in G133.7150+01.2155 can be used to estimate the proper motions of its lobes. The time gap of 1971.25 days permitted considerable angular displacements of the lobes, ranging from θ_s =0.″08 to θ_s =0.″31 as shown in Table 3.5. With the recent estimate of the distance to the object, d = 2.3±0.2 kpc (Navarete *et al.*, 2019), the lower limits of the proper motions of the lobes, calculated on the assumption that the axis of the jet is 90° to the line of sight, lie in the range; $v \sim 170\pm70\,\mathrm{km\,s^{-1}}$ for $\theta_s = 0.08''\pm0.01$ and $\sim 650\pm50\,\mathrm{km\,s^{-1}}$ for $\theta_s = 0.31''\pm0.02$. Figure 3.3 shows that the inner lobes have higher proper motions compared to the outer lobes. The inner lobes also depict an acceleration, especially near the core. Further out, the velocities drop to lower values, implying that the lobes get decelerated at the later stages of jet evolution, either due to a drop in the energy of its particles or as a result of interaction with ambient material. The average value of the proper motions of the lobes, therefore, is $\sim$390±90 km s^{-1}. However, considering only the first three lobes, least affected by surroundings or loss of energy, gives an average value of $540\pm50\,\mathrm{km\,s^{-1}}$. Indeed, K8, Q9 and C1 seem most affected by the impact of the ambient medium. These objects also display the least displacement. For example, K8, detected in three epochs, van der Tak *et al.* (2005), Purser (2017) and this observation, shows a relatively stable position, i.e an overall angular displacement $\theta_s < 0.1''$.

The distribution of C1, Q4, Q7, Q8, Q9 and K8 on the sky creates a pattern that is point-symmetric about Q5. This, coupled with the directions of motion of C1, Q8, Q7 and Q9 suggests the presence of a precessing jet (Purser, 2017). A simple model, similar to the one described in Eisloffel *et al.* (1996), was adopted in assessing the nature of the precession. In this model, the path of a jet head follows a conical spiral whose projection on the plane of the sky is a sinusoid. If the angle between the axis of precession and the line of sight is perpendicular, then the model can be described mathematically by equation 3.1, where x and

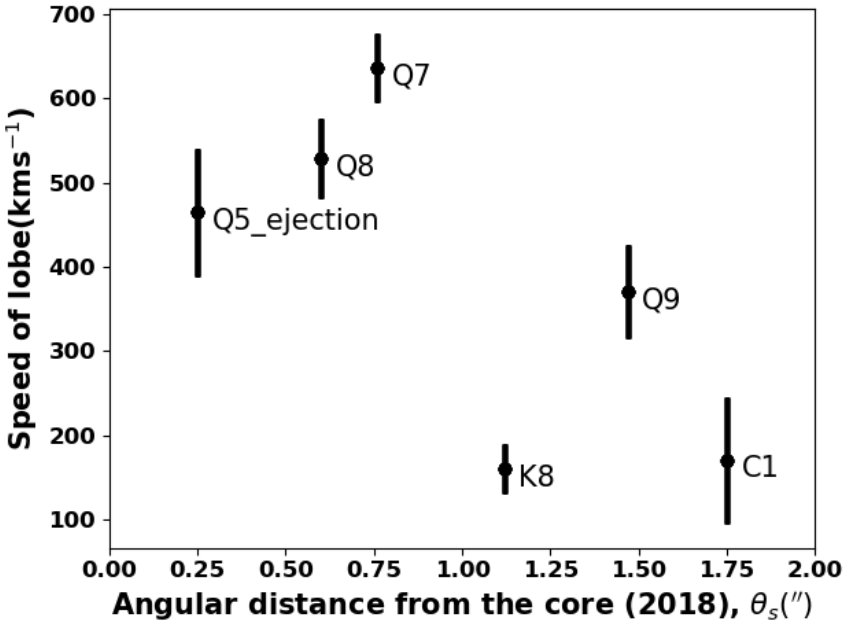

Figure 3.3: Proper motions of the different lobes of G133.7150+01.215.

y are the axial and radial displacements of the jet head from the location of the driving source respectively. ϕ is the position angle of the jet, v is the velocity of the jet, α is the precession angle, t is the time of evolution of the jet and p is the period of precession.

$$\begin{pmatrix} x \\ y \end{pmatrix} = \begin{pmatrix} \sin\phi & -\cos\phi \\ \cos\phi & -\sin\phi \end{pmatrix} \begin{pmatrix} vt\cos\alpha \\ vt\sin\alpha\sin\left(\frac{2\pi}{p}t\right). \end{pmatrix} \tag{3.1}$$

This simple model does not consider the angle of inclination of the jet to the plane of the sky and any variations in velocity along a jet, seen in G133.7150 +01.215, implying that the velocities are lower limits. A constant velocity of $500\,\mathrm{km\,s^{-1}}$ and an inclination angle of 90° were therefore adopted in the calculations. The model, shown in Figure 3.4, was obtained for a position angle $\phi = 72° \pm 5$, a period $p = 40 \pm 3$ years and a precession angle $\alpha = 10° \pm 2$, quantities that are comparable to estimates by Purser (2017) except the precession angle. The model, fit by inspection (Eisloffel *et al.*, 1996), seems to agree with the positions of the lobes and the directions of the displacement vectors despite

its simplicity.

van der Tak *et al.* (2005) noted a difference between the fluxes they derived and estimates from Tieftrunk *et al.* (1997), in some of the radio sources e.g Q5 and K8, suggesting flux variability. The flux densities of the radio sources, in 2012, were compared with the fluxes in 2018 to identify the sources that experience flux variability. K8 and Q7, the brightest lobes, also manifest the greatest change in flux (see Figure 3.5), pointing to recombination and/or diffusion process following an impact between the jet and its ambient medium. This form of variability, associated with radio lobes, does not seem to have a direct relation to accretion activities.

Radio sources Q2, Q3 and Q6, present in the field, do not seem to be associated with the MYSO. Their alignment and morphology of emission depict Q2 as a thermal jet, with Q3 and Q6 as its lobes, however, their spectral indices, 0.16±0.13, 0.76±0.10 and 0.58±0.20 (Purser, 2017) respectively, suggest that they may be thermal cores. Purser (2017) classified Q3 as a jet with lobes and both Q2 and Q6 as jet candidates. Of the three radio sources, only Q3 which has a mid-IR counterpart may be a core.

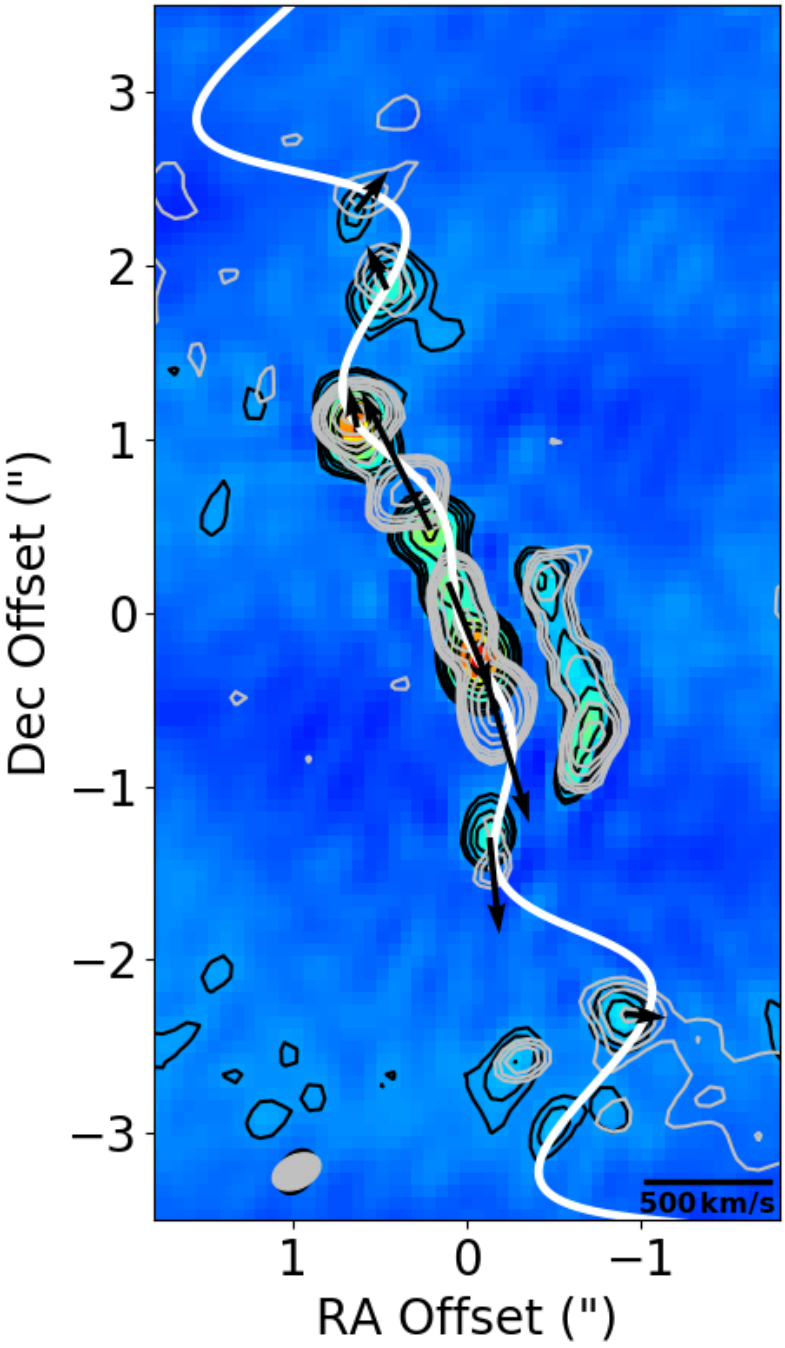

Figure 3.4: Precession model plotted over C-band contours of G133.7150+01.215 in white. Also included are the vectors of the proper motions which are shown as black arrows.

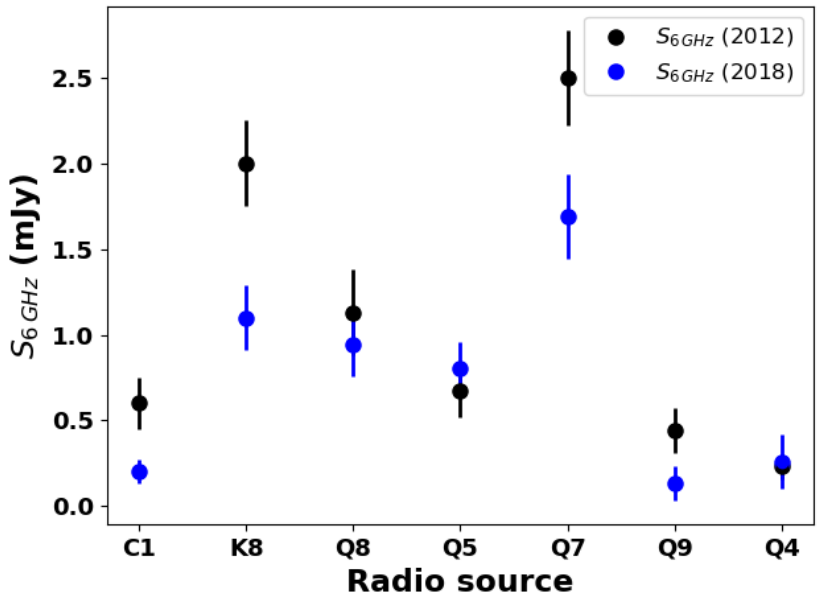

Figure 3.5: Flux densities of the radio sources that are associated with G133.7150 +01.215. Blue data points represent the fluxes of the sources in 2018 while black points represent their peak fluxes in 2012 (Purser, 2017).

Table 3.5: Displaced radio sources, their locations in 2012 and 2018, and displacements, in arc seconds, and position angles of their proper motion.

Source	Position in 2012		Position in 2018		offset	PA of PM
	RA(J2000)	Dec(J2000)	RA(J2000)	Dec(J2000)	($''$)	(deg)
C1	02:25:40.835±0.002	+062:05:54.276±0.016	02:25:40.840±0.003	+62:05:54.353±0.025	0.08±0.03	24±22
$Q5_{EJ}$	02:25:40.783±0.002	+062:05:52.542±0.007	02:25:40.771±0.002	+062:05:52.328±0.031	0.23±0.04	200±7
K8	02:25:40.861±0.001	+062:05:53.452±0.007	02:25:40.861±0.002	+062:05:53.531±0.013	0.08±0.01	5±12
Q7	02:25:40.760±0.001	+062:05:52.139±0.006	02:25:40.746±0.001	+062:05:51.840±0.017	0.31±0.02	198±5
Q8	02:25:40.800±0.001	+062:05:52.874±0.012	02:25:40.817±0.002	+062:05:53.107±0.014	0.26±0.02	27±5
Q9	02:25:40.749 ± 0.001	+062:05:51.109±0.022	02:25:40.750±0.002	+062:05:50.926±0.017	0.18±0.03	178±5

3.3.2.2 G173.4839+02.4317

Two radio sources, A1 and A2, detected by Purser (2017) in 2012, were detected in 2018 (see Figure 3.6). A third source, A3, located to the east of A1, was also detected at 5σ. A1 and A2 manifest a slight increase in flux, however, their positions have not changed significantly. For example, the peak and integrated flux of A1 are 0.11±0.02 and 0.22±0.04 mJy while in 2012 the peak and integrated flux were 0.15±0.02 and 0.16±0.03 mJy respectively. The fluxes of A1 and A2 imply constancy given the large and overlapping uncertainties. Uncertainties in the fluxes include errors due to calibrations, estimated at 10% of the flux and added in quadrature. Identifying the nature of the sources is not straightforward from the limited available information, however, their relative stability in position and flux, low reddening seen in the 2MASS infrared image and bright Brγ emission in A1 (Cooper *et al.*, 2013) suggests that they may be HII-regions (Purser, 2017). Strong Brγ emission is expected from sources whose electron temperatures lie in the range T=8,000-10,000 K while the electron temperature of weak Brγ emitters is ∼6000 K (Tambovtseva *et al.*, 2016). A lower resolution observation of the field by Han *et al.* (2015), at 4.8 GHz, detected a single emission that encloses both A1 and A2. The spectral index of the emission can be estimated from its flux density at 4.8 GHz S_ν =1.1±0.06 mJy and the rms noise of the field at 1.4 GHz (Condon *et al.*, 1998), scaled to match the beam of the 4.8 GHz observation (Han *et al.*, 2015), setting a lower limit on the index, i.e $\alpha_\nu > 1.38$, further implying that they may be HII regions. Also, the 2.12 μm H_2 map by Ginsburg *et al.* (2009) does not show clear evidence of outflow, however, Navarete *et al.* (2015) detected a single outflow in the SE-NW direction.

While the expansion rates of HII regions can be estimated from observations of different epochs (Welter, 1980), A1 does not show any significant increase in size. Detectable displacement of a feature on the ionization front of A1 should be at least the size of the synthesised beam of the observation, ∼0.″3. The upper limit of the velocity needed to cover such a distance is $v \lesssim 46\,\mathrm{km\,s^{-1}}$, given the time difference of five and a half years and the distance of the object. Indeed, the typical velocities of ionization fronts is ∼10s km s^{-1} e.g. Butterfield *et al.* (2018) and Reynolds (1976).

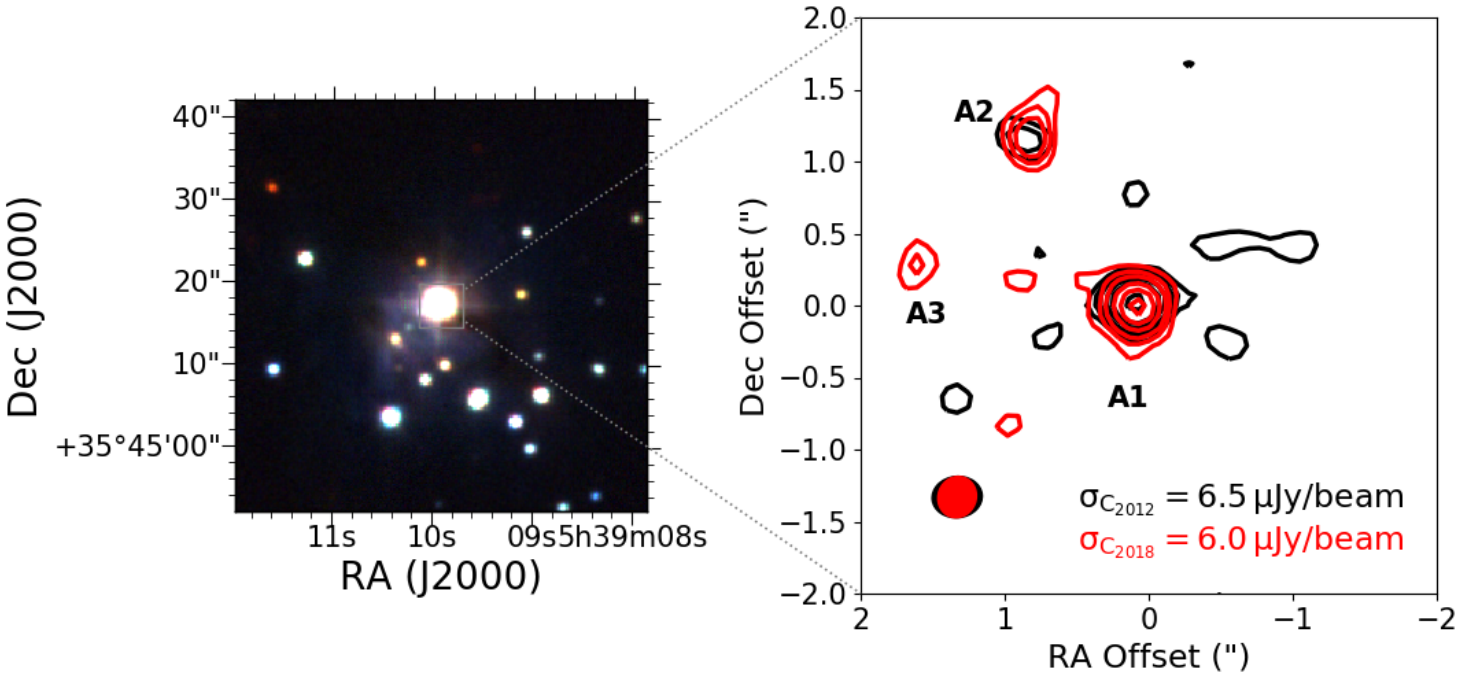

Figure 3.6: UKIDSS RGB colour (left) and C-band contour maps (right) of G173.4839+02.4317. The black and red contours correspond to observations of 2012 (Purser, 2017) and 2018 respectively. Contours levels are -3, 3, 5, 7, 9, 14, 17σ.

G173.4815+02.4459

The size of the primary beam during the observation of G173.4839+02.4317 enabled the detection of another MYSO, G173.4815+02.4459, located in the S 233 star-forming region (Ladeyschikov *et al.*, 2016) i.e $\alpha = 05^h39^m13.02''$ $\delta = +35^d45^m51.3''$. This MYSO, which is also an RMS source, was approximately $52''$ away from the phase centre of the observation. Three radio sources, E1, E3 and E4, were detected within its field unlike in Purser (2017) where six radio sources were detected. Purser (2017) identified E1, a methanol maser source (Minier *et al.*, 2000), as a core of an ionized jet while E3 and E4 were classified as lobes. Indeed the displacement of both E3 and E4 towards the west implies that they are lobes and their driving sources are located to the east. This field is known to host three mm cores (Beuther *et al.* 2002, Beuther *et al.* 2007b) and multiple outflows, identified from CO and shock excited H_2 emission (Ginsburg *et al.* 2009, Navarete *et al.* 2015, Varricatt *et al.* 2010). One of the cores is co-located with E1 (Purser, 2017), reaffirming that it is a core, however, it not clear if it is the driver of the jet that harbours lobes E3 and E4. The displacement vectors of E3 and E4, shown in Figure 3.7, suggest the presence of a precessing jet or multiple jet drivers. Magnitudes of the displacements of E3 and E4 are $0.30''$ and $0.18''$, translating to proper motions of 530 ± 50 and $320\pm30\,\mathrm{km\,s^{-1}}$ respectively, assuming that the distance of the source is 2.0 ± 0.4 kpc (Kawamura *et al.*, 1998).

Flux densities of the radio sources, derived from the 2018 observation, were found to be comparable to the 2012 fluxes (Purser, 2017) i.e 0.35 ± 0.01 mJy, 0.05 ± 0.02 mJy and 0.04 ± 0.02 mJy for E1, E3 and E4 respectively.

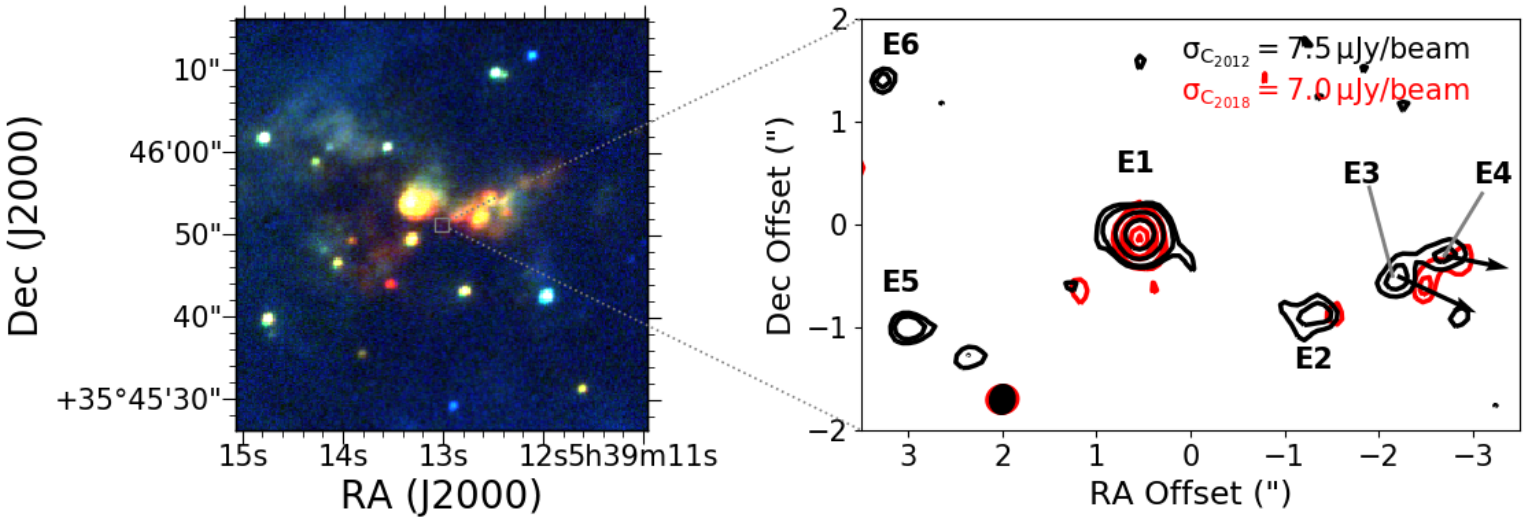

Figure 3.7: Colour map of UKIDSS RGB image of G173.4815+02.4459. Contour maps of the fields at C-band in 2012 (Purser, 2017) and 2018 observations are also shown in black and red colours respectively. Contours levels are -3, 3, 5, 7, 9, 14, 17σ.

3.3.2.3 G192.6005-00.0479

G192.6005-00.0479 is located in the S255 star-forming region. Its continuum map at both C- and K-bands exhibits the presence of a protostellar core, denoted as A (also known as S255 NIRS 3) and five jet lobes named C, D, F, G and J (see Figure 3.8 and Table 3.6). The core was resolved at both C- and K-bands, showing an elongation in a NE-SW direction at a position angle of 55°±1. Its orientation is similar to the alignment of A, C, D, F, G and J. Moreover, the infrared emission in the field has a similar orientation, further confirming the presence of a jet in the NE-SW direction. Besides the protostar, there are other radio sources in the field, i.e B, E and K that do not show any clear association with NIRS 3. B was detected at C- but not K-band indicating that it is a non-thermal lobe. Source K, on the other hand, was detected at K- and not C-band implying that it is a thermal source, perhaps an HII region. E, detected at both frequency bands has a spectral index of 1.18±0.08, another potential HII region. Only two of the radio sources in the field, A and L, have sub-millimetre counterparts (Liu *et al.*, 2018) i.e thermal cores. L whose sub-millimetre counterpart is SMA2 was weakly detected at C-band and not K-band where rms noise is 10 mJy/beam. A third sub-millimetre core, SMA3, does not have a radio counterpart at both C- and K-bands.

Previous C-band observation of the region by Purser (2017) revealed a similar distribution of the radio sources. The morphologies of the radio sources are also comparable. A and C, for example, are elongated in the NE-SW direction even-though C seems to be evolving into a new shape, perhaps due to an interaction between the fast-moving particles of the jet and its slow-moving clumpy counter-parts. Cesaroni *et al.* (2018) also detected the core, A, and its lobes but their images were more extended due to the lower resolution of their observations.

Table 3.6: Positions, flux densities and peak intensities of the radio sources that were detected in the field of G192.6005-00.047 in 2018

Object	Position		Integrated Flux (mJy)		Peak flux (mJy/Beam)		$\alpha_{_{CK}}$	Nature
	Dec	RA	C-band	K-band	C-band	K-band		
A	$06^h12'54.02''$	$+017°59'23.1''$	15.11±0.09	24.72±0.80	11.47 ± 0.04	11.28 ± 0.25	0.37±0.02	Core
B	$06^h12'54.04''$	$+017°59'24.1''$	0.13±0.03	< 0.06	0.06 ± 0.02	< 0.12	> -0.58	Lobe
D	$06^h12'53.84''$	$+017°59'21.9''$	0.55±0.03	0.27 ± 0.04	0.32±0.02	0.12 ± 0.03	-0.53 ± 0.12	Lobe
E	$06^h12'54.00''$	$+017°59'26.1''$	0.17±0.04	0.83 ± 0.07	0.15±0.02	0.84 ± 0.04	1.18 ± 0.08	HII-region
F	$06^h12'53.74''$	$+017°59'21.78''$	0.19±0.03	< 0.08	0.06±0.02	< 0.12	> -0.64	Lobe
G	$06^h12'54.33''$	$+017°59'24.5''$	0.65±0.04	0.26 ± 0.05	0.34±0.02	0.11 ± 0.03	-0.68 ± 0.15	Lobe
J	$06^h12'53.80''$	$+017°59'22.1''$	0.17±0.03	< 0.07	0.07±0.02	< 0.12	> -0.66	Lobe
K	$06^h12'54.07''$	$+017°59'23.7''$	<0.05	0.30 ± 0.06	< 0.12	0.10 ± 0.02	> 1.33	HII-region
L	$06^h12'53.85''$	$+017°59'23.5''$	0.09±0.02	<0.07	0.05±0.01	< 0.12	< 0.11	thermal core

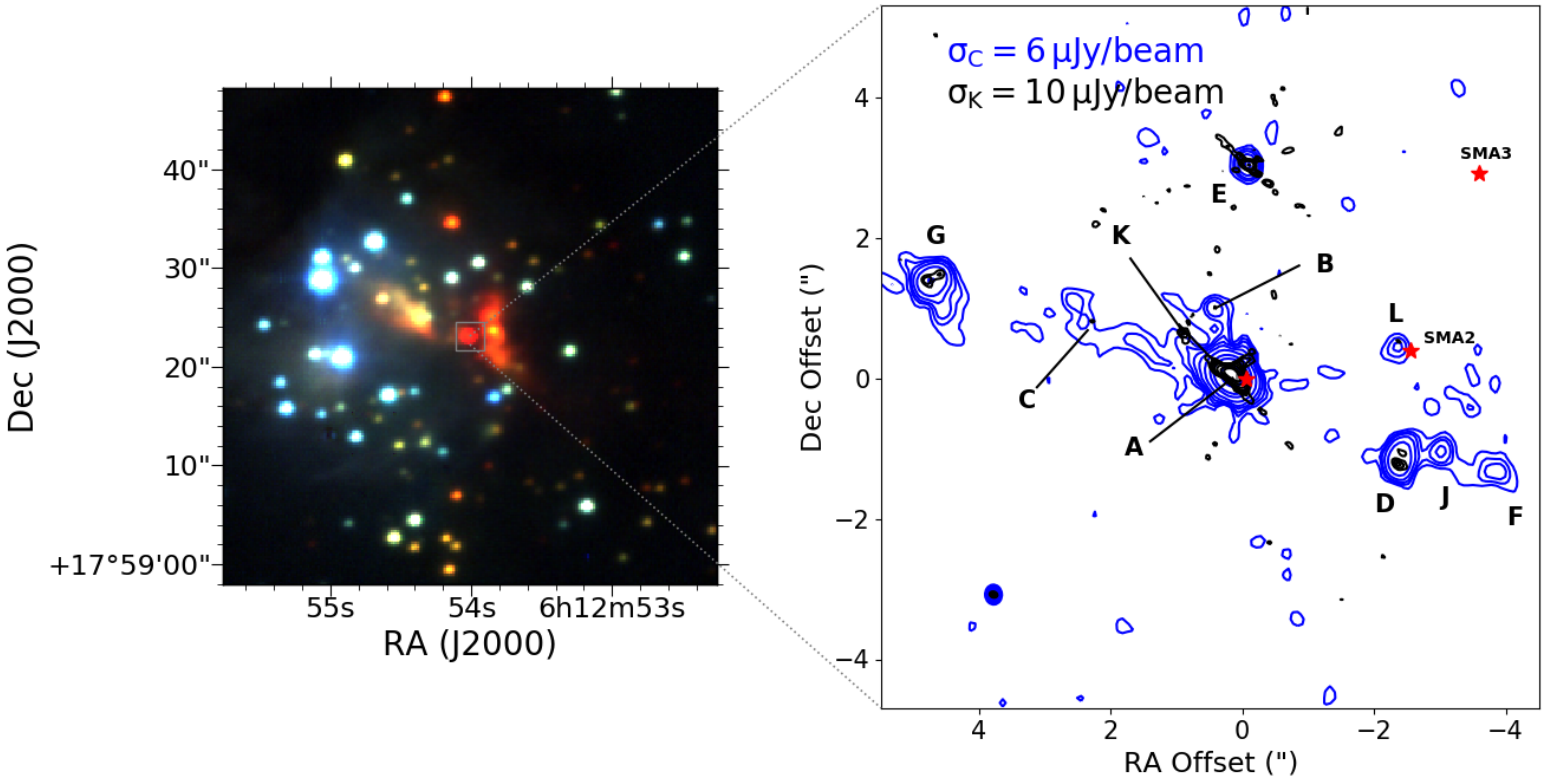

Figure 3.8: RGB colour image of G192.6005-00.0479's field made from UKIDSS J,H,K images. Contours of C- and K-band emission of the field are also shown at levels 3, 5, 7, 11, 20, 50, 150, 300 & 900σ, in blue and black colours respectively. The red asterisks represent locations of sub-millimetre cores in the field (Liu *et al.*, 2018).

Properties of S255 NIRS 3

The core of G192.6005-00.0479, also known as S255 NIRS 3, is a thermal radio source of spectral index 0.36±0.05. It displayed a significant rise in flux density after July 2016 (Cesaroni *et al.*, 2018). The flux density in 2012 was 0.79±0.02 mJy (Purser, 2017), a value comparable to Cesaroni *et al.* (2018)'s estimates of March and July 2016. Cesaroni *et al.* (2018) monitored the core from 11th March 2016 to 27th December 2016, a period totalling six epochs, following earlier reports of maser flaring (Fujisawa *et al.*, 2015) and IR brightening (Stecklum *et al.*, 2016) of the source. Their observations at both C- and K-bands manifest a clear increase in flux density of the core as shown on the right-hand panel of Figure 3.9. There is a time-gap of approximately one year between the start of the rise in the intensity of methanol masers and IR emission, and the onset of outburst in radio emission. This period may be interpreted as the time taken by the central object to accrete the material, eject part of the accreted mass, and allow for the travel of the ejected particles away from the vicinity of the central object.

The data from Cesaroni *et al.* (2018), Purser (2017) and this observation, shown in Table 3.7, were plotted to display the changes in the flux of the core for the period covering the eight epochs. As observed by Cesaroni *et al.* (2018), the core experienced an exponential rise in radio flux after July 2016. However, the observation of 2018 shows a clear deviation of the fluxes from the initial trend of the outburst. Whereas this deviation suggests that the outburst is either on a decline or plateauing, its methanol maser light curve (Szymczak *et al.*, 2018) points to a decline. More evidence of the decline was reported by Liu *et al.* (2018) after analysing the source's 900 μm continuum emission and 349.1 GHz methanol maser emission.

Predicting the nature of the outburst is not straightforward given the large

Table 3.7: Flux densities of the S255 NIRS3 at different epochs, from 2012 (Purser, 2017) to 2018. The 2016 data were taken from Cesaroni *et al.* (2018).

Date	2012	2016						2018
	Nov.	Mar.	Jul.	Aug.	Oct	Nov.	Dec.	Mar.
Wavelength	(mJy)	(mJy)	(mJy)	(mJy)	(mJy)	(mJy)	(mJy)	(mJy)
$\lambda = 1.34$ cm	–	2.7±0.3	2.2±0.2	3.1±0.3	6.6±0.7	11±1	18±2	15.11±0.09
$\lambda = 5.00$ cm	0.79±0.08	0.87±0.09	0.79±0.08	1.1±0.1	2.6±0.3	4.8±0.5	7.9±0.8	24.72±0.80

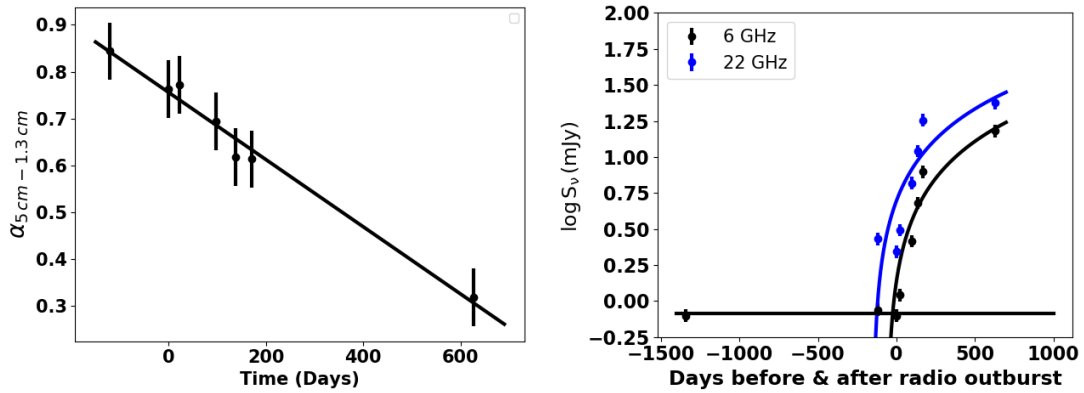

Figure 3.9: Evolution of spectral index (left) and the fluxes (right) of the outburst. Least square fits of the functions used to predict the trend of the fluxes and spectral index of the outburst are also shown in continuous lines. The horizontal line of the right panel is the approximate flux of the source at quiescence. Day zero corresponds to onset of the outburst.

time gap between data from Cesaroni *et al.* (2018) and the 2018 observation. To understand it further, the evolution of its spectral index was studied (see left panel of Figure 3.9). The spectral index of the outburst, at each of the epochs, was derived using a combination of data from 2018 observation and the C- and K-band data from Cesaroni *et al.* (2018). Uncertainties in the fluxes were all assumed to be 10% of the flux for consistency with the errors used in Cesaroni *et al.* (2018). The indices show a continuous decrease with time i.e α_ν =0.84±0.06 in March 2016, 0.76±0.06 in July 2016 during the early stages of the outburst and 0.36±0.05 on the six hundred and twenty seventh day of the outburst. Taking 10th July 2016 as the onset of the outburst i.e $t = 0$ (Cesaroni *et al.*, 2018), the spectral index α_ν of the radio emission shows a linear relation with time t i.e $\alpha_\nu = -(6.5 \pm 0.5 \times 10^{-4})t + 0.75 \pm 0.01$. If the linear trend continues, the emission from the outburst should transition into the optically thin regime ($\alpha_\nu = -0.1$) after $\sim$ 1400 days unless a restoring mechanism acts. The continued downward trend in spectral index implies a constant drop in optical depth. Some of the factors that can result in the decline of the optical depth along a line of sight through the jet are; a drop in the jet number density n, a decrease in the path length through the jet Δs, a rise in the temperature T of the jet and a drop in its ionization fraction x (Reynolds, 1986) i.e $\tau = \kappa_\nu \Delta s = a_\kappa n^2 x^2 T^{-1.35} \nu^{-2.1} \Delta s$.

Effectively, the drop in optical depth suggests a number of possibilities which may include a combination of; recombination of charged particles, a decrease in the jet density due to expansion and diffusion of jet particles. While a model of an expanding ionized gas, suggested by Cesaroni *et al.* (2018), has the potential of explaining some of the features of the outburst, the anti-correlation in the evolution of its flux and spectral index suggests the presence of non-thermal emission near the core whose intensity increases with the outburst. A similar property is seen in nova outbursts e.g Nelson *et al.* (2014).

Evolution of the spectral index during the outburst shows a well-behaved linear correlation with time, implying that the knowledge can be used to predict the flux of the source at a given frequency. The equation, $\log S_C = \log S_K + \alpha_\nu(t) \log\left(\frac{\nu_C}{\nu_K}\right)$, where $\log\left(\frac{\nu_C}{\nu_K}\right)$ is the slope and $\log S_K$ is an intercept, relates the C-band flux S_C, C- and K-band frequencies ν_C and ν_K respectively, evolving spectral index $\alpha_\nu(t)$ and evolution time of an outburst t. The collinearity between $\log S_C$ and $\alpha_\nu(t)$ implies that $\log S_C$ has a linear relation with time as well. Least-squares fitting of a logarithmic function of the form described above on the flux vs time data points displays a trend that points to a plateauing outburst.

Finally, in addition to continuum emission, S255 NIRS 3 radiates 6.7 GHz methanol maser emission and 22.2 GHz water maser emission. Contour maps of the intensities of the water and methanol maser emission for the 2018 observation are shown in Figure 3.10. The methanol maser is marginally resolved and does not show a clear morphology of its distribution, however, the water masers trace a resolved structure that is well aligned with the continuum emission. Moscadelli *et al.* (2017) compared the locations of the 6.7 GHz methanol maser, before and during the outburst, and noticed that most of the maser locations were closer to the core during the outburst, implying a change in the circumstellar environment of the source (Cesaroni *et al.*, 2018). Szymczak *et al.* (2018) analysed data, collected through long-term monitoring of 6.7 GHz methanol maser emission from S255 NIRS 3, reporting a rise in its intensity in two epochs. In the 2018 observation, the flux density of the emission is 43.4±2.7 mJy, comparable to its intensity during quiescence. The intensity map of the water masers displays three peaks which are potential locations of the jets' knots. The peaks are arranged in a linear fashion with angular separation between A, B and C displaying a quasi-regular

pattern, implying that the processes that are responsible for their formation may be semi-regular i.e periodic ejection or precession.

Radio Lobes in G192.6005-00.0479

Four radio sources, D, F, G and J, were found to have negative spectral indices, typical of non-thermal lobes. They are also aligned in a direction similar to the orientation of the radio emission of A and infrared emission in the field. This implies that they are lobes of a jet whose core is A. B and K, located to the north of A are its closest neighbours, however, the location of B and spectral index of K are inconsistent with lobes of a jet that is driven by A. K is a thermal radio source of spectral index $\alpha > 1.33$ while B is a non-thermal lobe whose index $\alpha > -0.58$.

A spectral index map of the field was generated from C- and K- band data of similar uv-coverage. The full uv-coverage of C- and K- band data are $11 - 950\,\mathrm{k}\lambda$ and $37 - 2600\,\mathrm{k}\lambda$ respectively, however, the overlap which occurs at 38-950kλ was used. The map, shown in Figure 3.11, reveals the thermal core A and two non-thermal lobes, G and D. G and D appear to be internal bow-shocks similar to the bow shocks seen in the infrared image of HH212 (Reipurth *et al.*, 2019). They are the brightest radio lobes in the field and their orientation, clearly seen in the K-band observation of 2018, is also perpendicular to the direction of the flow of jet particles i.e perpendicular to line GD. J and F, on the other hand, seem to stem out of D, perhaps due to a build-up of pressure occasioned by the accumulation of energy and materials at the bow shock. The misalignment of some of the radio lobes e.g D, J and F, also suggests precession. A precession model of precession angle $\alpha = 2°$ and period p =50 years, assuming that the jet drives out mass at a velocity v =500 $\mathrm{km\,s^{-1}}$ and is inclined at an angle of 90° seems to fit the distribution of the radio sources (see Figure 3.11).

Considering that the bow shocks, G and D, maybe internal and not terminating shocks, it is not possible to estimate the kinematic length and age of the jet with certainty. However, the angular separations of D and G from core A are $\sim 2.5''$ and $4.8''$ respectively, translating to physical distances of 0.02 pc and 0.04 pc respectively. Assuming a jet velocity of $500\,\mathrm{km\,s^{-1}}$ implies that it took 39 years and 78 years for the jet particles to travel from the core to D and G respectively. Their minimum energy and minimum magnetic field strengths, cal-

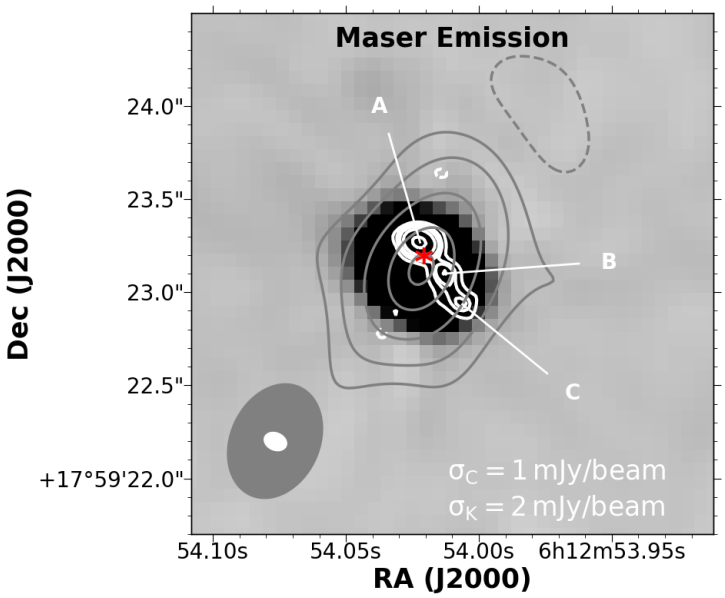

Figure 3.10: Colour map of 6 GHz continuum emission and contour maps of 6.7 GHz and 22.2 GHz maser emission are shown in gray and white colours respectively. The red asterisk represents the K-band location of the core.

culated from equipartition theorem described in section 2.5.2.3, are 4.5×10^{41} ergs and 1.1 mG respectively. In both F and J, the minimum B-field is 0.8 mG while their minimum energies are 2.3×10^{41} ergs and 2.1×10^{41} ergs respectively.

The lobes do not show any significant change in position and flux. There are, however, slight angular displacements displayed by the peak emissions of C and D. Adjacent to lobe D is a new lobe labelled J. This lobe was not detected in 2012 (Purser, 2017), perhaps a new condensation, stemming out of D (see Figure 3.12). The angular displacements of the peaks of C and D were found to be 0.2″ and 0.14″, translating to proper motions of $316\pm30\,\mathrm{km\,s^{-1}}$ and $220\pm20\,\mathrm{km\,s^{-1}}$ respectively, at the distance of the core i.e 1.8 kpc. Also, the fluxes of the lobes are relatively constant between the two epochs (see the right panel of Figure 3.12). The flux of D in 2012 was compared with the sum of the fluxes of D and J in 2018 since J may be part of D in the 2012 observation.

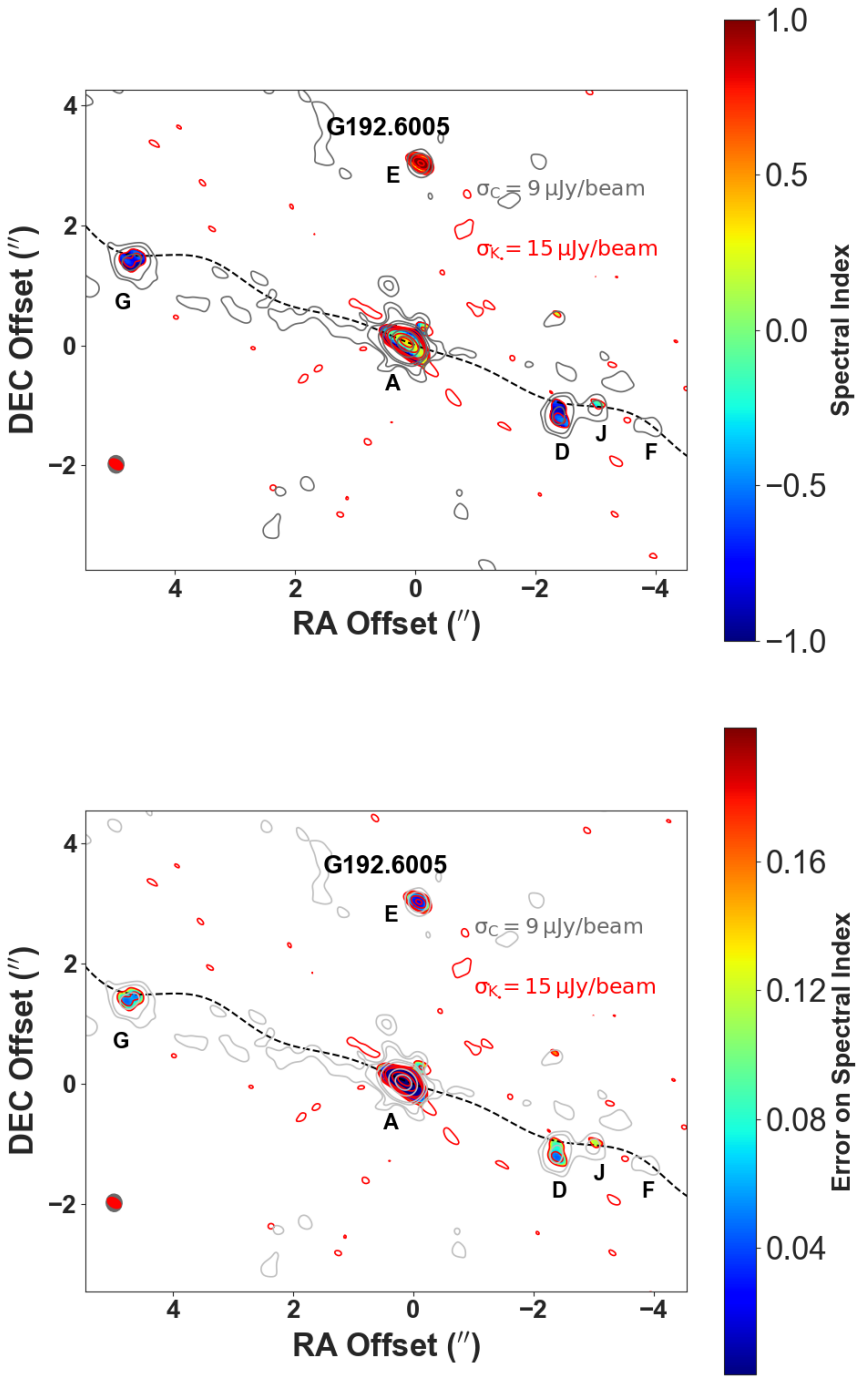

Figure 3.11: Spectral index map (top) and corresponding errors (bottom) of the field. The indices were only calculated if the flux of a pixel is higher than 3σ in both frequency bands. The dashed lines represent a precession model in which the jet is perpendicular to the line of sight.

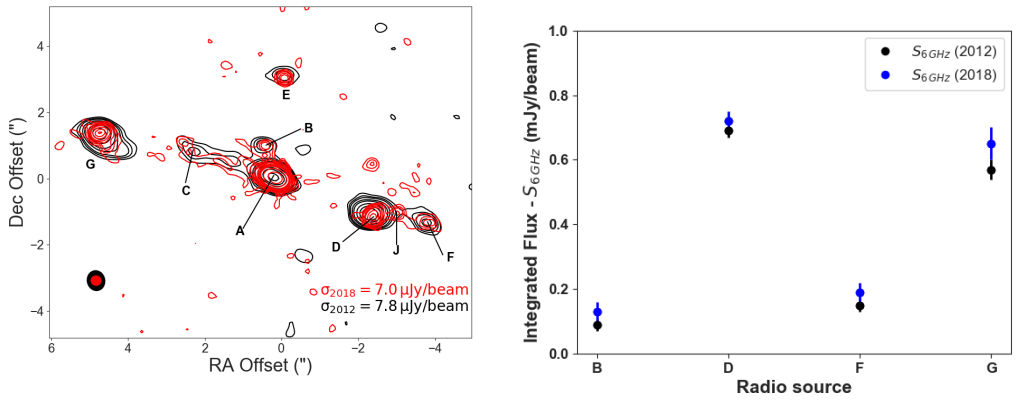

Figure 3.12: Left: Comparing the locations of the radio sources in G192.6005-00.0479. Their positions in 2012 are shown in black contours while 2018 locations are represented by the red contours. Right: Comparing the C-band fluxes of the radio lobes that are associated with core A. Blue dots represent the fluxes in 2018 while the black dots represent 2012 fluxes.

3.3.2.4 G196.4542−01.6777

The C-band map of the field, star-forming region S269 (Jiang *et al.*, 2003), manifests emission from two radio sources, an extended emission that harbours three other radio sources; A1, A2 and A3, and a point source labelled A4 (see Figure 3.13). The orientation of the C-band emission is comparable to the alignment of infrared emission in the field, suggesting that A1, A2, A3 and A4 are components of a jet aligned in the same direction. A near-infrared study of the region by Jiang *et al.* (2003) also detected H_2 emission knots that are aligned in a NE-SW direction. A2 was detected at both C- and K-bands while A1, A3 and A4 were only detected at C-band, implying that A2 is the core of the jet and A1, A3 and A4 are its non-thermal lobes. The spectral index map of the field, derived from images of similar uv-coverage, also confirms that A2 is the core while the rest are non-thermal lobes (see Figure 3.14). A list of the radio sources, their flux densities and spectral indices is given in Table 3.8. The radio sources do not show significant changes in flux and position except the flux of A1 which dropped by ∼25%.

Besides continuum emission, radiation from methanol and water masers were also detected in the field. The methanol and water masers are of frequencies

6.7 GHz and 22.2 GHz, and flux densities 6.4±0.4 mJy and 34±7 mJy respectively. Their peaks are located ∼0.3″ and 0.5″ to the SW of the core. The peak of the 6.7 GHz emission coincides with the location A3 while that of the 22.2 GHz emission manifest an elongation that spreads from A3 towards the SW (see Figure 3.15). These masers appear to be tracing the outer parts of the jet, away from the core.

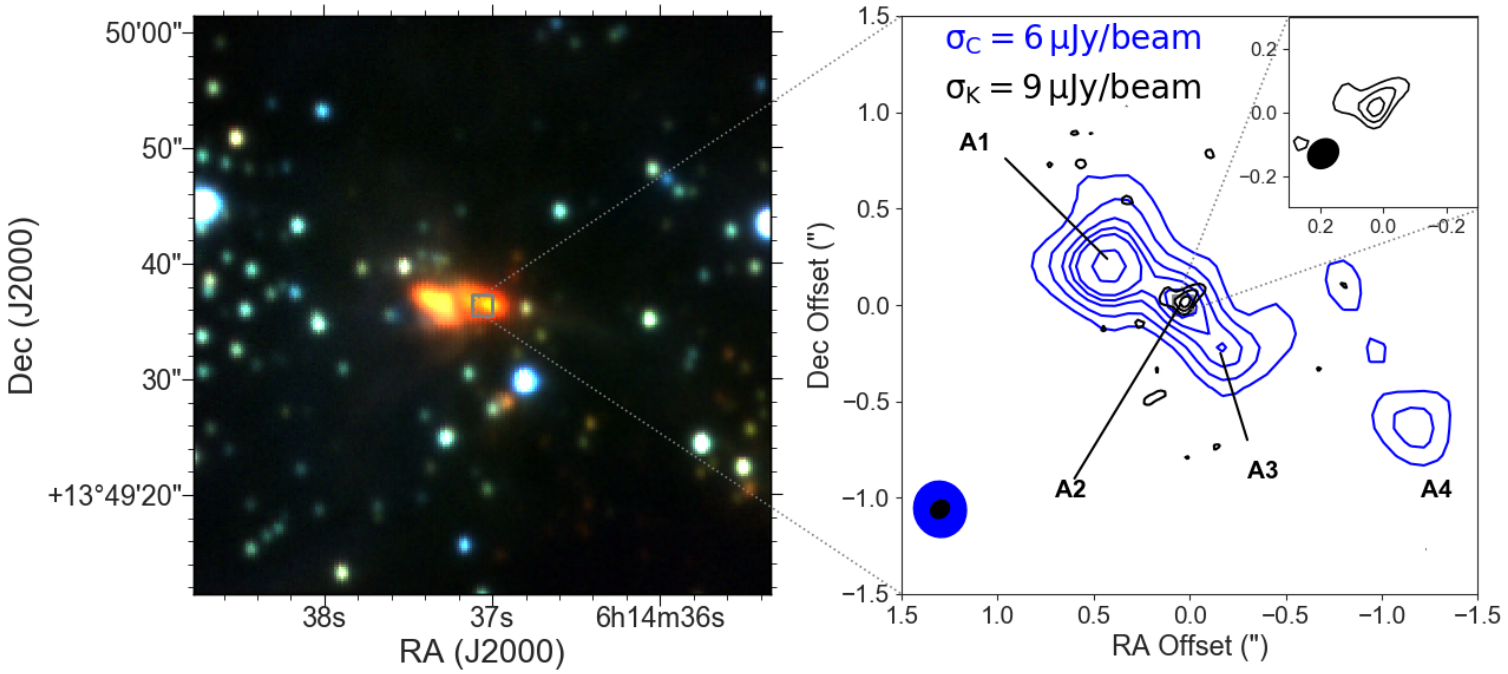

Figure 3.13: Left: RGB map of UKIDSS J, H, K images. Right: C- and K-band contours are of levels; -3, 3, 7, 11, 14, 17, 25σ and -3, 3, 6, 9σ, shown in blue and black colours respectively.

Table 3.8: C-band positions, flux densities and spectral indices of radio sources within the field of G196.4542−01.6777

Object	Position		Integrated Flux (mJy)		α_{CK}	Nature
	Dec	RA	C-band	K-band		
A1	$06^h14'37.09''$	$+013°49'36.6''$	0.30±0.02	<0.08	<-1.33	Lobe
A2	$06^h14'37.06''$	$+013°49'36.4''$	0.10±0.02	0.13±0.02	0.20 ± 0.19	Core
A3	$06^h14'37.05''$	$+013°49'36.2''$	0.09±0.02	< 0.05	< -0.44	Lobe
A4	$06^h14'36.98''$	$+013°49'35.8''$	0.07±0.02	< 0.05	< -0.25	Lobe

3.3.3 Mass Loss Rates

The morphology and spectral indices of the central MYSOs suggest that they have cores that drive out winds whose density ρ decreases with distance r as $\rho \propto r^{-2}$, except A1 in G173.4839+02.4317 which may be a HII region. The mass-loss rates of the cores were estimated by Purser (2017). However, the mass-loss rate of S255 NIRS3 was re-calculated using the C-band flux of 2018 since it was in outburst. In the calculations, the jet parameters that were adopted in Cesaroni *et al.* (2018) were used i.e a terminal velocity $v_t = 900\,\mathrm{km\,s^{-1}}$, ionisation fraction $x_o = 0.14$ and an inclination angle of 85^o, giving a comparable mass loss rate of $\dot{M} = 3.1 \pm 0.2 \times 10^{-5}\,\mathrm{M_\odot yr^{-1}}$. This rate is approximately an order of magnitude higher than its rate during quiescence i.e $2.91 \pm 2.19 \times 10^{-6}\,\mathrm{M_\odot yr^{-1}}$ (Purser, 2017). Assuming $\frac{M_{out}}{M_{acc}} \sim 0.1$ implies an accretion rate $\dot{M}_{acc} = 3.1 \times 10^{-4}\,\mathrm{M_\odot yr^{-1}}$ which is lower than the estimate from Caratti o Garatti *et al.* (2017), suggesting that the factor of 10% under-estimates accretion rates. Indeed Hartigan *et al.* (1994) finds the ratio to be ∼1% in low mass stars, a value that generates a rate that is comparable to Caratti o Garatti *et al.* (2017).

3.4 Conclusion

- Protostellar jets have cores whose positions are relatively fixed. Their lobes, however, are transitional objects that undergo noticeable positional variability. Fluxes of both cores and lobes manifest variability in some MYSOs. Flux variability in MYSO cores can be attributed to accretion activities

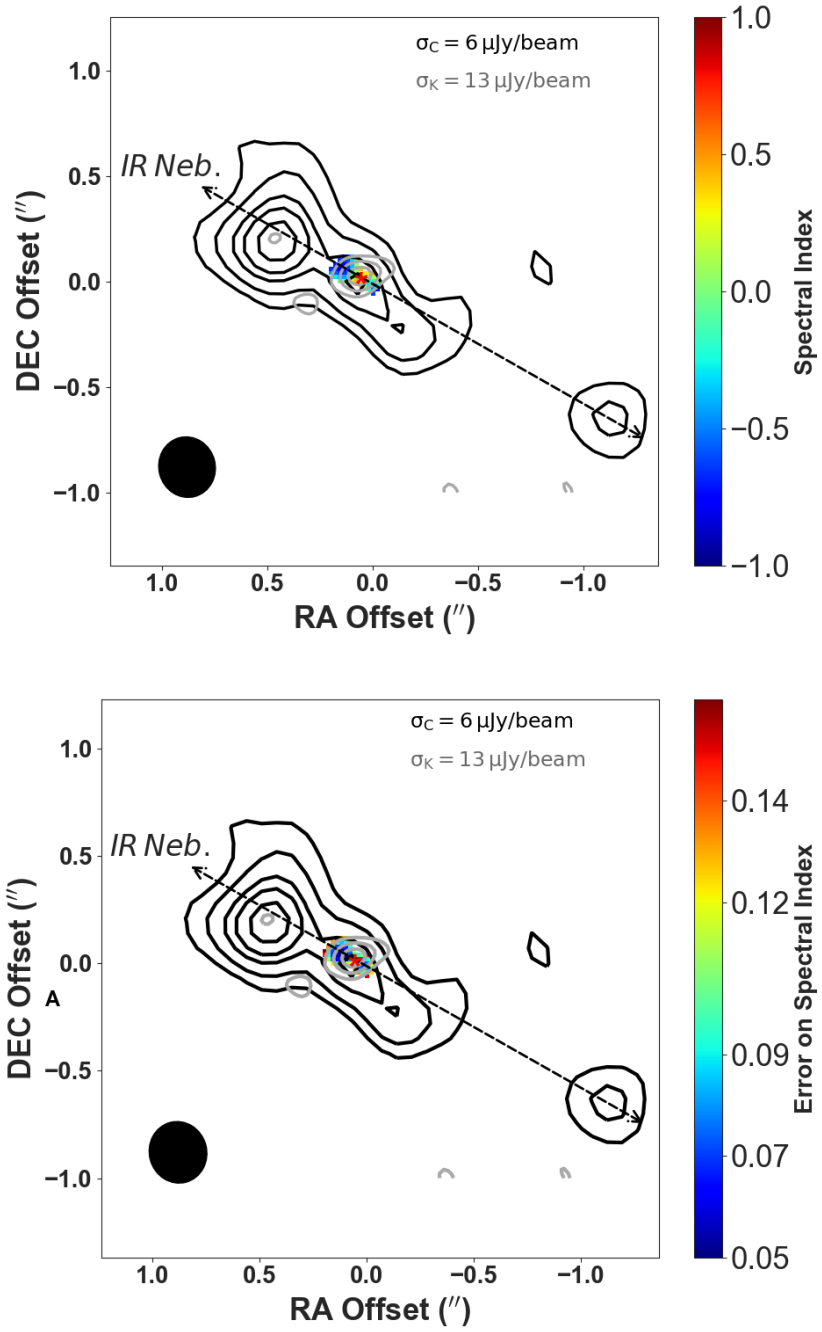

Figure 3.14: Spectral index (top) and error (bottom) maps of the field. C- and K-band contours are also shown at levels; -3, 3, 7, 13, 18, 25, 50σ and -3, 3, 5, 7, 11σ respectively.

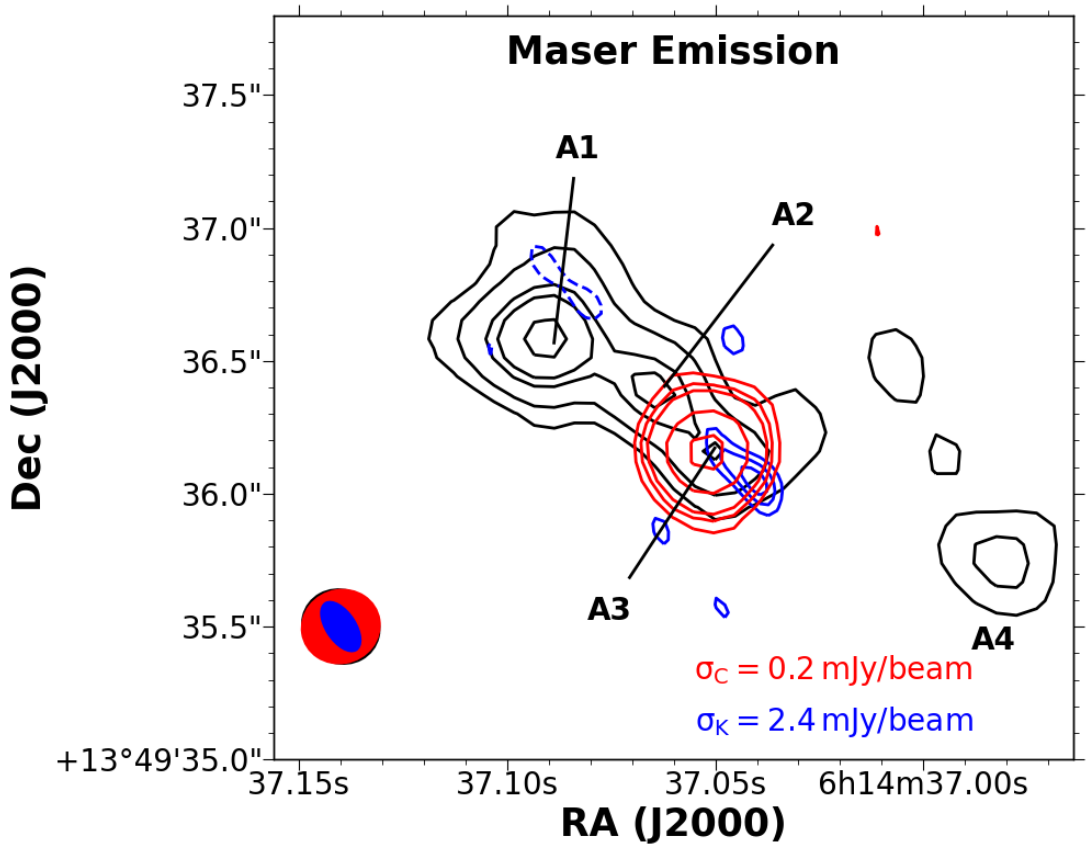

Figure 3.15: Contour maps of C-band continuum (black), 6.7 GHz methanol masers (red), and 22.2 GHz water masers (blue) emission of G196.4542 −01.6777. Their contour levels are -3, 3, 7, 14, 18 & 27σ; -3, 3, 5, 7, 15 & 25σ, and -3, 3, 5, & 7σ respectively

while in lobes, diffusion and recombination of ionized particles can result in lower fluxes. Conversely, higher magnetic flux density and energised flow can result in a higher radio flux.

- Estimates of the proper motions of the jet knots/lobes manifest a wide range of jet velocities. The minimum and maximum estimates were found to be $170\pm70\,\mathrm{km\,s^{-1}}$ and $650\pm50\,\mathrm{km\,s^{-1}}$ respectively. The spread in proper motion is evident even within a single jet, implying that the lobes undergo periods of acceleration and deceleration as they move away from the core. A keen look at the change in the position of the lobes suggests that they move both radially and tangentially manifesting precession e.g in G133.7150+01.215.

- The study of S255 NIRS3, in outburst, revealed that it emits free-free emission whose opacity reduces as the outburst evolves, consistent with a model of an expanding jet bubble or a bubble of diffusing or recombining particles. Predictions suggest that the outburst is either plateauing or declining. The mass-loss rate of S255 NIRS3 during outburst shows that massive protostars are capable of attaining the high accretion rates needed to overcome radiation pressure through accretion bursts.

Chapter 4

Radio Emission From Jets of Massive Protostars

4.1 Introduction

Cores of massive protostellar jets radiate thermal emission that are detectable as radio continuum at centimetre wavelengths (Purser *et al.* 2016, Moscadelli *et al.* 2016). To date, the model that has been used as a standard for interpreting the nature of the emission is the analytic model by Reynolds (1986). Other models, on the other hand, employ specific theories to simulate the properties of particular objects e.g Shang *et al.* (2004). Most simulations of the jets focus on their hydrodynamics properties, for example, how they are collimated (Canto *et al.*, 1988) or entrained (Lee *et al.*, 2001). Additional properties of interest include; precession (Smith & Rosen, 2005), pulsation (Stone & Norman, 1993b), and their interaction with ambient medium and disk winds (Tabone *et al.*, 2018).

Having verified the thermal nature of the cores in Chapters 2 and 3, it was imperative to simulate their continuum emission, first, to compare the results with Reynolds (1986) model, and secondly, to simulate variability properties of their emission, which cannot be explicitly inferred from the Reynolds (1986) model e.g. monitoring of flux variability. The simulation is a two-step process. It starts with modelling the hydrodynamics properties of the jets followed by calculating the intensities of their emission using a ray-tracing code. This is the first

study that involves calculations of radio emission from numerically solved hydrodynamics jets, at several epochs, comparable to long-term monitoring of a jet. The calculated spectra also cover a wide range of radio wavelengths, from 0.1 to 100 GHz.

Owing to the integral nature of the hydrodynamics segment of the simulations, a large section of this chapter is dedicated to describing the characteristics of numerical hydrodynamics simulations, and the hydrodynamics code that was used in the calculations. The nature of the hydrodynamics jets, generated during the testing of the code, are also described in detail. The second part of the chapter details how the emission was calculated and analysed.

4.2 Description of Jets

Jets, defined as narrow streams of fast-moving fluids, are ever-present in nature. Examples of jets that we interact with every day include; jets from showers, garden sprinklers and cosmetic sprays (Eggers & Villermaux, 2008). On the largest scales are the astrophysical jets. All jets, regardless of size and power, can be simulated as fast-moving particles that flowing through a stationary or slow-moving surrounding medium. Simulations of astrophysical jets assume that the jets and their ambient medium are made up of pure fluids even though they have small traces of dust, $\sim$1%. Furthermore, the inter-particle distances in the fluids are large enough to assume that the force of attraction between them is weak, and the viscous drag is negligible. The jets can thus be treated as inviscid fluids flowing through undisturbed and slowly varying ambient media of higher density.

Both pure hydrodynamics and magneto-hydrodynamics jet models can reproduce some properties of real jets. Pure hydrodynamic jets are characterised by beams of thermal matter, at supersonic speed, enveloped by working surfaces and cocoons (Norman *et al.*, 1982). These working surfaces are associated with shocks (Raga & Noriega-Crespo, 1993) whose strengths are determined by the Mach number of the beam. The shocks can emit radiation at almost all frequencies (Rodríguez *et al.* 2012a, Güdel *et al.* 2007) e.g DG Tau's HH 159. X-ray jets, for example, emit due to heating at the shocks (Takasao *et al.*, 2017) when their

fast-moving particles decelerate while radio jets emit via free-free and synchrotron processes.

An idealised stellar jet has three main parts; a jet beam, a cocoon and a bow shock at its front (Chernin *et al.*, 1994) as illustrated in Figure 4.1. Its beam is the region along the $r = 0$ axis. It has the lowest number density and contains most of the collimated and ionized particles at supersonic speeds. Most of the ejections from the core flow through this region. Jet beams are expected to take the shape of a cone of a given opening angle but the rate at which mass flows through them can be approximated assuming a cylindrical geometry i.e zero opening angle. The mass-loss rate $\dot{M}_j$ through a bipolar cylindrical jet of radius r_j, density ρ_j and velocity v_j is therefore equal to $\dot{M}_j = 2\pi r_j^2 \rho_j v_j$ (Smith, 2004). This rate is expected to reduce as a protostar evolves. Considering low mass classification of protostars, jets of Class 0 protostars of number densities n_j are expected to have a higher mass-loss rate compared to more evolved Class II objects (e.g see equations 4.1 and 4.2; Smith 2004)

$$\text{Class 0 } \dot{M}_j \approx 1.3 \times 10^{-5} \left(\frac{r_j}{500\,AU}\right)^2 \left(\frac{n_j}{10^5\,cm^{-3}}\right) \left(\frac{v_j}{100\,km\,s^{-1}}\right) \mathrm{M_\odot yr^{-1}} \quad (4.1)$$

$$\text{Class II } \dot{M}_j \approx 1.6 \times 10^{-8} \left(\frac{r_j}{100\,AU}\right)^2 \left(\frac{n_j}{10^3\,cm^{-3}}\right) \left(\frac{v_j}{300\,km\,s^{-1}}\right) \mathrm{M_\odot yr^{-1}} \quad (4.2)$$

Outside the beam is the jet cocoon which is a region of shocked ambient gas. At the boundary of a jet beam and cocoon, supersonic beam particles drag the ambient gas as they flow, causing Kelvin-Helmholtz, Rayleigh-Taylor and thermal instabilities within the jets (Micono *et al.*, 1998). The instabilities give rise to a dense shell that harbours filaments and blobs (de Gouveia dal Pino *et al.*, 1996). This region has a higher number density of particles compared to the beam. Its temperature is equally high due to collisional heating.

As the front part of the beam interacts with the subsonic ambient medium, a bow shock, commonly known as the Herbig-Haro (HH) object is formed at the

[2]Astrophysical Research With Enhanced Numerics

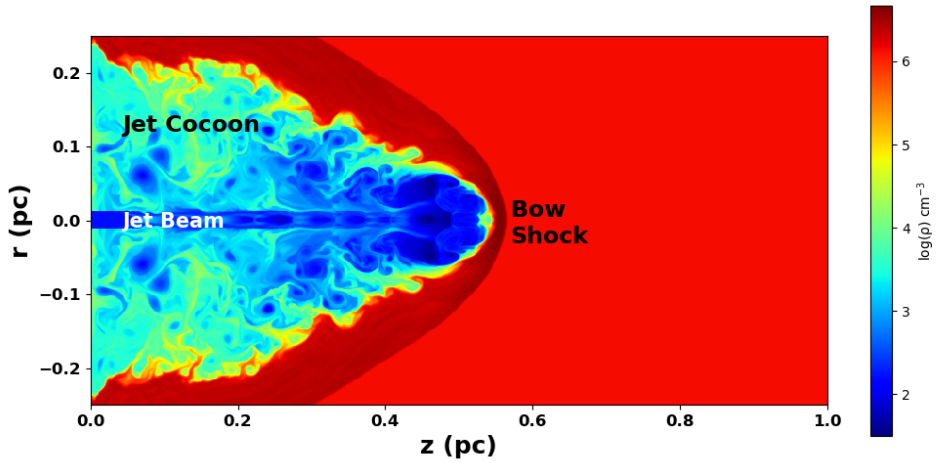

Figure 4.1: The distribution of density of particles of an adiabatic jet of mass-loss rate $\dot{M}$ =10^{-6} $M_{\odot}yr^{-1}$, velocity v=500 km s^{-1} and age t=140,000 years. The jet, generated using the ARWEN[2] code (developed by J. Pittard), was injected into an ambient medium of density ρ_a=10^6 cm^{-3} and temperature T=100 K. The jet is axisymmetric and its lower part is a reflection of the upper section about the line $r = 0.0$ pc. It was simulated on an 800 × 200 grid.

jet head. They are the most powerful and brightest shocks in a jet. Other weaker shocks, called knots, also form along the beam and perhaps the cocoon. Shock waves (or simply shocks) are formed when a wave moves faster (supersonic) than the sound speed in a medium. They are distinguished from other kinds of waves by their abrupt discontinuity in pressure, temperature and density.

4.3 Numerical Hydrodynamic Simulations

4.3.1 Introduction

The simulation of astrophysical processes and systems is a computational astrophysics technique which makes use of computing tools to imitate the astrophysical processes and systems. Numerical simulations in astrophysics can be traced back to the 1950s and 1960s (Norman, 1997), however, notable astrophysical computational hydrodynamics started in the late 1960s and early 1970s (Larson 1969, Wilson 1971). Both Larson (1969) and Wilson (1971) simulated the formation of

a star under the influence of gravity. Later, more powerful hydrodynamics codes e.g GADGET (Springel *et al.*, 2001) were developed to simulate more complex cases such as the interaction of galaxies and the formation of structures in the early universe.

Numerical simulation is a powerful tool that is used by both engineers and scientists to conduct virtual experiments. Astronomers, for example, cannot monitor the life of a star from birth to death but can reproduce such processes by numerically solving the equations of hydrodynamics that govern the processes. Through simulations, therefore, astronomers have an opportunity to emulate evolution of stars, astrophysical jets, galaxies and other objects in detail even though in reality they can only observe what nature sends to Earth (Zingale, 2014) and take snapshots of their features. Secondly, simulations provide astronomers with an opportunity to probe additional dimensions of structures (Norman, 1997).

There are various numerical techniques for fluid dynamics (Teyssier, 2015) e.g. smoothed particle hydrodynamics (SPH), grid-based hydrodynamics and moving mesh codes. Both SPH and moving mesh techniques are not discussed here. The techniques make use of equations that describe physical processes and initial conditions, normally estimated from observations, to solve the equations numerically and monitor how physical quantities such as density and temperature evolve with time. Some of the numerical hydrodynamics codes that are used in astronomy include; FLASH (Fryxell *et al.*, 2000), ZEUS-3D (Clarke, 2010), VH-1 (Hawley *et al.*, 2012), PLUTO (Mignone *et al.*, 2007), ATHENA (Stone *et al.*, 2008), RAMSES (Teyssier, 2002), ENZO (Bryan *et al.*, 2014), AREPO (Springel, 2010) and GIZMO (Hopkins, 2015).

4.3.2 Equations of Hydrodynamics

The properties of real gases can be approximated by assuming that they behave like an ideal gas. An ideal gas is one whose particles are identical, have a volume that is negligible compared to gas scales or volumes and only experience force when they undergo elastic collision within negligible time (Adkins, 1983). Real gases tend to behave like an ideal gas when their densities are low and temperatures are high e.g in various astrophysical flows. A gas can be described by

any of the following quantities; density, number density, velocity, temperature, sound speed, isothermal sound speed, pressure, internal energy, internal and total specific energies and total specific enthalpy. Three of the quantities namely density, velocity and internal specific energy are independent variables while the rest are not i.e all the other quantities are linked to these three. An equation relating pressure, P, number density, N and temperature, T, of an ideal gas is given as $P = Nk_BT = \frac{\rho k_B T}{\mu}$, where k_B and μ are Boltzmann's constant and the gas particles' mean mass respectively.

The movements of fluid particles can be described mathematically by fluid dynamics equations, derived from conservation laws of their energy, mass and momentum. The equations govern signal/fluid propagation and changes in the fluid variables with time. They can be presented as a set of partial differential or integral equations (Murawski & Lee, 2011). Solving partial differential equations (PDE), in a suitable coordinate system, can be done numerically using any of the three widely used grid-based techniques i.e finite-difference, finite-volume or finite-element methods (Guillén-González & Redondo-Neble 2014, Murawski & Lee 2011).

The flow of fluids can be described as Eulerian or Lagrangian (Rieutord, 2015). In a Lagrangian flow, a fluid element is tracked in space and time while in a Eulerian flow an element is watched as it passes through a specific location in space. The properties of a fluid element in a Lagrangian flow are estimated by following the element as it moves while in a Eulerian flow a field of the property is utilised as illustrated on Figure 4.2 (Shadloo *et al.*, 2016). PDEs of hydrodynamics processes can be written to describe either of the two forms of flow (Rieutord, 2015).

The hydrodynamic equations, also known as the Euler equations, are a set of non-linear hyperbolic PDEs derived from conservation laws of a compressible, adiabatic, inviscid fluid with zero thermal conductivity and magnetic field. The equations can be derived by considering a fluid's conserved quantities namely mass density ρ, momentum components $\rho u_{x,y,z}$ and total energy per unit mass E (Toro, 2009) as described in the next section.

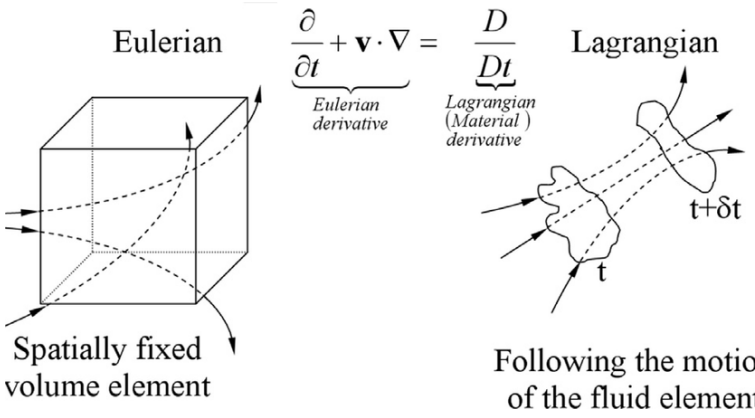

Figure 4.2: An illustration showing a Eulerian flow to the left and a Lagrangian one on the right (Shadloo *et al.*, 2016).

4.3.2.1 Conservation of Mass

This law says that mass flowing into and out of a fluid element is conserved. Consider a fluid element of volume dV and surface area dS. The total mass of fluid within the element and its time derivative are given by $\iiint_V \rho dV$ and $\frac{d}{dt}\iiint_V \rho dV$ respectively. The change in mass within the volume element with time, $\frac{d}{dt}\iiint_V \rho dV$, is equivalent to the mass flux through its surface $-\oiint_S (\rho\vec{u}).\vec{n}\, dS$. Thus $\frac{d}{dt}\iiint_V \rho dV = -\oiint_S (\rho\vec{u}).\vec{n}\, dS$; where $\vec{u}$ and $\vec{n}$ are a velocity vector and a unit vector normal to the surface of fluid element dS. Applying the Leibniz integral rule on the left hand side of the equation and the divergence theorem to its right hand side yields $\iiint_V \frac{\partial}{\partial t}\rho dV = -\iiint_V \boldsymbol{\nabla}\cdot(\rho\vec{u})dV$ which is the mass conservation equation, $\frac{\partial \rho}{\partial t} + \boldsymbol{\nabla}\cdot(\rho\vec{u}) = 0$.

4.3.2.2 Conservation of Momentum

The conservation of momentum of flowing fluids can be derived from Newton's second law of motion which states that the rate of change of momentum of a body is proportional to the total forces causing it and takes place in the direction of the forces. Some of the forces acting on a fluid element are related to its body e.g gravity while others result from the fluid element surface e.g viscosity and pressure. The rate of change in momentum within the volume element and

through its surface are equivalent to $\frac{d}{dt}\iiint_V \rho\vec{u}dV$ and $\oiint_S \rho\vec{u}\vec{u}.\vec{n}\,dS$ respectively; as a result, the linear momentum equation can be written as:

$$\sum \vec{F} = \frac{d}{dt}\iiint_V \rho\vec{u}dV + \oiint_S \rho\vec{u}\vec{u}.\vec{n}\,dS \tag{4.3}$$

Here, only the force due to pressure P exerted by particles surrounding the element is considered i.e force $F = -\oiint_S P\vec{n}dS$. This is because the flow is assumed to be non-viscous and the gravity acting on the particles is assumed to be negligible. Substituting this force with the sum of forces in equation 4.3 and writing $P\vec{n}$ in-terms of a unit tensor $\vec{I}$ as $P\vec{I}\cdot\vec{n}$ yields $\frac{d}{dt}\iiint_V \rho\vec{u}dV + \oiint_S \rho\vec{u}\vec{u}\cdot\vec{n}\,dS = -\oiint_S P\vec{n}dS = -\oiint_S P\vec{I}.\vec{n}dS$, the momentum conservation equation. Introduction of a unit tensor allows for the use of divergence theorem on the surface integrals, giving:

$$\frac{d}{dt}\iiint_V (\rho\vec{u})\,dV + \iiint_V \boldsymbol{\nabla}\cdot(\rho\vec{u}\vec{u})\,dV = -\iiint_V \boldsymbol{\nabla}\cdot\left(P\vec{I}\right)dV \tag{4.4}$$

The volume integral can then be removed because any arbitrary volume can be chosen, giving;

$$\frac{\partial}{\partial t}(\rho\vec{u}) = -\boldsymbol{\nabla}\cdot\left(\rho\vec{u}\vec{u} + P\vec{I}\right) \tag{4.5}$$

Rearranging it gives:

$$\frac{\partial}{\partial t}(\rho\vec{u}) + \boldsymbol{\nabla}\cdot(\rho\vec{u}\vec{u}) + \boldsymbol{\nabla}P = 0 \tag{4.6}$$

4.3.2.3 Conservation of Energy

Conservation of energy states that the rate of change of energy in a system is equivalent to the change in its internal heat and the work done by the system. It can be represented mathematically in a manner similar to the first law of thermodynamics as $\delta Q = dU + pdV$. The total energy density of a fluid is given by the sum of its internal energy density $\frac{U}{V} = e\rho$ and kinetic energy density $\frac{Ke}{V} = \frac{1}{2}\rho u^2$ i.e $\rho(\frac{1}{2}u^2 + e) = \rho\epsilon$, where e, ρ and ϵ are its internal specific energy,

physical density and $\frac{1}{2}u^2 + e$ respectively. The total energy of the system is thus given by $E = \int_V \rho(\frac{1}{2}u^2 + e)dV$. Clearly, part of this energy is transferred through the fluid surface S as heat while the rest does work on the surface due to pressure P that builds up as the energy increases. This relationship between the change in energy, heat transfer and work done on a system can be represented mathematically as shown below:

$$\begin{aligned} \frac{\partial}{\partial t}\int_V \rho(\frac{1}{2}u^2 + e)dV &= -\int_S \rho(\frac{1}{2}u^2 + e)\vec{u}\cdot\vec{n}dS - \int_S P\vec{u}\cdot\vec{n}dS \\ \int_V \frac{\partial}{\partial t}\rho(\frac{1}{2}u^2 + e)dV &= -\int_V \boldsymbol{\nabla}\cdot\Big(\rho(\frac{1}{2}u^2 + e)\vec{u}\Big)dV - \int_V \boldsymbol{\nabla}\cdot P\vec{u}dV \end{aligned} \tag{4.7}$$

The differential form of the equation is given as:

$$\frac{\partial \rho\epsilon}{\partial t} + \boldsymbol{\nabla}\cdot\Big(\rho(\frac{1}{2}u^2 + e)\vec{u}\Big) + \boldsymbol{\nabla}\cdot P\vec{u} = 0 \tag{4.8}$$

$$\frac{\partial \rho\epsilon}{\partial t} + \boldsymbol{\nabla}\cdot\rho\epsilon\vec{u} + \boldsymbol{\nabla}\cdot P\vec{u} = 0 \tag{4.9}$$

4.3.2.4 Material Derivatives

The material derivative is a measure of the rate at which a quantity changes with both time and position as it flows through a given gradient. It provides a means to compute the flow fields of fluids. The derivative is also known as total derivative, convective derivative, substantial derivative, substantive derivative or co-moving derivative. With the derivative, the Eulerian form of hydrodynamics equations can be transformed into Lagrangian; also known as non-conservative form of the conservation equations. Equation 4.10 illustrates how the derivative is related to the rate of change of a physical quantity $f = f(x, t)$ at a particular

point O that is fixed in space (see Figure 4.3).

$$\begin{aligned}\frac{Df}{Dt} &= \frac{d}{dt}f\Big(x(t), y(t), z(t)\Big) \\ &= \frac{\partial f}{\partial t} + \frac{dx}{dt}\frac{\partial f}{\partial x} + \frac{dy}{dt}\frac{\partial f}{\partial y} + \frac{dz}{dt}\frac{\partial f}{\partial z} \\ &= \frac{\partial f}{\partial t} + u_x\frac{\partial f}{\partial x} + u_y\frac{\partial f}{\partial y} + u_z\frac{\partial f}{\partial z} \\ &= \frac{\partial f}{\partial t} + \vec{u}\cdot\boldsymbol{\nabla} f\end{aligned} \tag{4.10}$$

In the equation, u_x, u_y, u_z and x, y, z are the fluid element's velocity and position components respectively. The equation can be written generally as $\frac{D}{Dt} = \frac{\partial}{\partial t} + \vec{u}\cdot\boldsymbol{\nabla}$. To demonstrate its need further, consider Figure 4.3. It is clear that the velocity of a fluid particle changes as it flows along a line of flow e.g through O, leading to acceleration as it passes the constriction. Such a description is plainly ignored in the conservative form where emphasis is given to a single point in space (e.g point O).

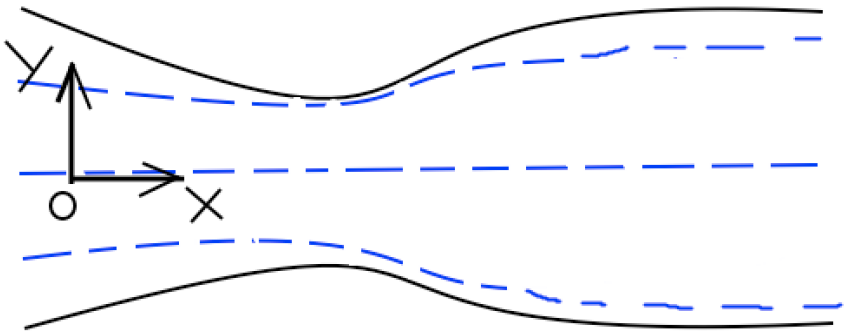

Figure 4.3: An illustration showing fluid flowing through a tube of flow.

4.3.3 The Lagrangian Forms of the Hydrodynamics Equation

4.3.3.1 Mass Conservation Equation

The mass conservation equation, $\frac{\partial \rho}{\partial t} + \boldsymbol{\nabla} \cdot (\rho \vec{u}) = 0$, also known as continuity equation can be written in Lagrangian form by writing its second term $\boldsymbol{\nabla} \cdot (\rho \vec{u})$ as $\rho \boldsymbol{\nabla} \cdot \vec{u} + \vec{u} \cdot \boldsymbol{\nabla} \rho$ (vector identity). The equation then becomes:

$$\begin{aligned} \frac{\partial \rho}{\partial t} + \rho \boldsymbol{\nabla} \cdot \vec{u} + \vec{u} \cdot \boldsymbol{\nabla} \rho = 0 \\ \frac{\partial \rho}{\partial t} + \vec{u} \cdot \boldsymbol{\nabla} \rho + \rho \boldsymbol{\nabla} \cdot \vec{u} = 0 \\ \frac{D\rho}{Dt} + \rho \boldsymbol{\nabla} \cdot \vec{u} = 0 \end{aligned} \tag{4.11}$$

4.3.3.2 The Momentum Conservation Equation

The first and second term of the momentum conservation equation (Eq 4.6) can be written as $\rho \frac{\partial \vec{u}}{\partial t} + \vec{u} \frac{\partial \rho}{\partial t}$ and $\boldsymbol{\nabla} \cdot (\rho \vec{u} \vec{u}) = \vec{u} \boldsymbol{\nabla} \cdot (\rho \vec{u}) + \rho \vec{u} \cdot \boldsymbol{\nabla} \vec{u}$ respectively resulting;

$$\rho \frac{\partial \vec{u}}{\partial t} + \vec{u} \frac{\partial \rho}{\partial t} + \vec{u} \boldsymbol{\nabla} \cdot (\rho \vec{u}) + \rho \vec{u} \cdot \boldsymbol{\nabla} \vec{u} + \boldsymbol{\nabla} P = 0. \tag{4.12}$$

This yields,

$$\rho \Big(\frac{\partial \vec{u}}{\partial t} + \vec{u} \cdot \boldsymbol{\nabla} \vec{u} \Big) + \vec{u} \Big(\frac{\partial \rho}{\partial t} + \underbrace{\boldsymbol{\nabla} \cdot (\rho \vec{u})}_{0} \Big) + \boldsymbol{\nabla} P = 0. \tag{4.13}$$

The term $\frac{\partial \rho}{\partial t} + \boldsymbol{\nabla} \cdot (\rho \vec{u})$ in equation 4.13 is the continuity equation which is equivalent to zero. Hence, the final Lagrangian form of the momentum equation is:

$$\rho \Big(\frac{\partial \vec{u}}{\partial t} + \vec{u} \cdot \boldsymbol{\nabla} \vec{u} \Big) + \boldsymbol{\nabla} P = \rho \frac{D\vec{u}}{Dt} + \boldsymbol{\nabla} P = 0 \tag{4.14}$$

4.3.3.3 The Equation of Conservation of Energy

The first and second terms in the equation of conservation of energy, equation 4.9, can also be expanded. This yields:

$$\begin{aligned} \rho\frac{\partial\epsilon}{\partial t} + \epsilon\frac{\partial\rho}{\partial t} + \epsilon\boldsymbol{\nabla}\cdot\rho\vec{u} + \rho\vec{u}\cdot\boldsymbol{\nabla}\epsilon + \boldsymbol{\nabla}\cdot P\vec{u} = 0 \\ \rho\Big(\frac{\partial\epsilon}{\partial t} + \vec{u}\cdot\boldsymbol{\nabla}\epsilon\Big) + \epsilon\underbrace{\Big(\frac{\partial\rho}{\partial t} + \boldsymbol{\nabla}\cdot\rho\vec{u}\Big)}_{0} + \boldsymbol{\nabla}\cdot P\vec{u} = 0 \end{aligned} \tag{4.15}$$

and the Lagrangian form for the conservation of energy equation:

$$\rho\frac{D\epsilon}{Dt} + P\boldsymbol{\nabla}\cdot\vec{u} = 0 \tag{4.16}$$

4.3.4 Numerical Methods

A numerical method is a technique which approximates the result of a mathematical problem whose exact solution cannot be determined. Methods used in hydrodynamic calculations are finite difference, finite volume or finite element, all of which rely on discretization.

4.3.4.1 The Finite Difference Method

In finite differencing, a continuous function, e.g the 1D advection equation shown in 4.17, is discretized along grid points. In the equation, q is the flux of the quantity being advected, u is the velocity of flow and x is the co-ordinate of flow.

$$\frac{\partial q}{\partial t} + u\frac{\partial q}{\partial x} = 0 \tag{4.17}$$

Derivatives and fluxes in the equations can be approximated by expanding the equation using the Taylor series:

$$\begin{aligned} f(x) = f(a) + f'(a)(x-a) + f''(a)\frac{(x-a)^2}{2!} + f'''(a)\frac{(x-a)^3}{3!} + ... \\ + f^n(a)\frac{(x-a)^n}{n!} + ... \end{aligned} \tag{4.18}$$

So if u_i is the velocity of the system at i^{th} location, its value at $i+1^{th}$ point, u_{i+1}, is:

$$u_{i+1} = u_i + \left(\frac{\partial u}{\partial x}\right)_i \Delta x + \left(\frac{\partial^2 u}{\partial x^2}\right)_i \frac{(\Delta x)^2}{2!} + \left(\frac{\partial^3 u}{\partial x^3}\right)_i \frac{(\Delta x)^3}{3!} + ... + \left(\frac{\partial^n u}{\partial x^n}\right)_i \frac{(\Delta x)^n}{n!} + ... \tag{4.19}$$

This equation can be rearranged to approximate the function's first derivative:

$$\left(\frac{\partial u}{\partial x}\right)_i = \frac{u_{i+1} - u_i}{\Delta x} + \left(\frac{\partial^2 u}{\partial x^2}\right)_i \frac{(\Delta x)}{2!} + \left(\frac{\partial^3 u}{\partial x^3}\right)_i \frac{(\Delta x)^2}{3!} + ... + \left(\frac{\partial^n u}{\partial x^n}\right)_i \frac{(\Delta x)^{n-1}}{n!} + ... \tag{4.20}$$

If equation 4.20 is truncated in such a manner that only the first order terms are included then it is said to be first order accurate i.e $(\frac{\partial u}{\partial x})_i = \frac{u_{i+1}-u_i}{\Delta x} + O(\Delta x)$, where $O(\Delta x)$ is the difference between the actual value of the derivative and its approximation (Zingale, 2014). A numerical equation of the form $(\frac{\partial u}{\partial x})_i = \frac{u_{i+1}-u_i}{\Delta x} + O(\Delta x)$ is said to be forward difference and first order accurate. Similarly, there is a rearward difference equation where a preceding value is used i.e $(\frac{\partial u}{\partial x})_i = \frac{u_i-u_{i-1}}{\Delta x} + O(\Delta x)$. Apart from forward and rearward differencing, there is also a central difference equation which makes use of both successive and preceding points:

$$\left(\frac{\partial u}{\partial x}\right)_i = \frac{u_{i+1} - u_{i-1}}{2\Delta x} + O\left(\Delta x^2\right) \tag{4.21}$$

This finite difference method is called a central differencing scheme and its equation is second order accurate.

4.3.4.2 The Finite Volume Method

Unlike the finite difference method where discretisation is associated with a point in space, discrete data in the finite volume method are represented by averages within assigned control volumes, also known as cells. For example, the average value of the function $f(x,t)$ at the i^{th} cell, bounded by interfaces at $i - \frac{1}{2}$ and $i + \frac{1}{2}$, can be written and illustrated as shown in equation 4.22 and Figure 4.4

respectively.

$$< f_i >= \frac{1}{\Delta x_i} \int_{x_{i-1/2}}^{x_{i+1/2}} f(x)dx \tag{4.22}$$

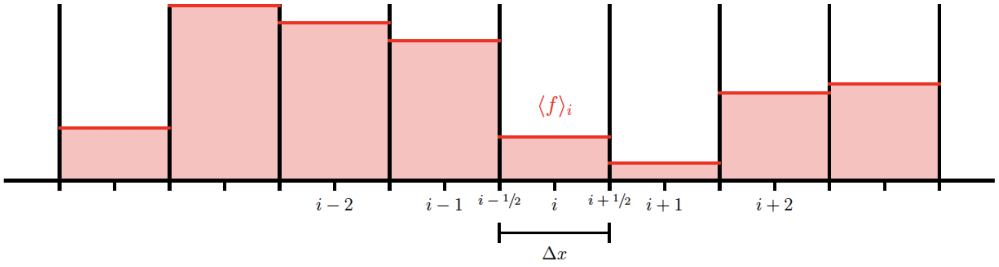

Figure 4.4: A plot illustrating how the solutions of finite volume method appear on a one dimensional grid (Zingale, 2014).

The other significant difference between the finite volume and finite difference methods is the form of the conservation laws that they solve. The finite volume method solves integral forms of partial differential equations. As an illustration, consider the 1D advection equation:

$$\frac{d}{dt}\int_{x_L}^{x_R} U dx + F(U)|_{x_R} - F(U)|_{x_L} = \int_{x_L}^{x_R} S(U,t)dx \tag{4.23}$$

where U is the conserved quantity, F is the flux and S is the source term. Setting the source term to zero yields:

$$\begin{aligned} \frac{d}{dt}\int_{x_{i-\frac{1}{2}}}^{x_{i+\frac{1}{2}}} U dx + F(U)|_{x_{i+\frac{1}{2}}} - F(U)|_{x_{i-\frac{1}{2}}} &= 0 \\ \Delta x_i \frac{dU_i}{dt} + F(U)|_{x_{i+\frac{1}{2}}} - F(U)|_{x_{i-\frac{1}{2}}} &= 0 \end{aligned} \tag{4.24}$$

This equation gives the time rate of change of the average quantity at cell i, $\frac{dU_i}{dt} = \frac{1}{\Delta x}\frac{d}{dt}\int_{x_{i-\frac{1}{2}}}^{x_{i+\frac{1}{2}}} U dx$, which is equivalent to the difference between the inward and outward fluxes flowing through $x_{i-\frac{1}{2}}$ and $x_{i+\frac{1}{2}}$ respectively. However, it does not tell us about the solutions at the cell boundaries which can only be calculated

by assuming that the solution convects with a velocity $u(t)$. The solution at $x_{i+\frac{1}{2}}$, the boundary between the quantities U_i and U_{i+1}, at time t^{n+1}, after one time step is given by:

$$U(x_{i+\frac{1}{2}}, t^n) = \begin{cases} U_i(t^n) & if\ u(t) > 0 \\ U_{i+1}(t^n) & if\ u(t) < 0, \end{cases} \tag{4.25}$$

Where t^n is the initial time. Fluxes of the quantities can also be calculated from the value of U using:

$$F(x_{i+\frac{1}{2}}, t^n) = \begin{cases} u(t)U_i(t^n) & if\ u(t) > 0 \\ u(t)U_{i+1}(t^n) & if\ u(t) < 0 \end{cases} \tag{4.26}$$

4.4 The Numerical Simulation Code - ARWEN

Finite volume methods naturally result in the Riemann problem, described as an initial value problem when the initial data consists of two constant states that are separated by a jump discontinuity, due to the discretisation of grids. Thus, the method calculates the exact solutions of the Riemann problem at each of the cell boundaries using the method of characteristics, a technique for solving partial differential equations by reducing them to systems of ordinary differential equations which can be computed from initial conditions. An average solution for a cell can then be computed and updated after a time step (see illustration in Figure 4.5). Details of the method, called the Godunov scheme (Godunov, 1959), are described in Toro (2009). The original Godunov scheme uses piecewise constant values for the cells. This has been improved in the intervening decades by calculating gradients within each cell e.g piecewise linear method (PLM) and the piecewise parabolic method (PPM; Colella & Woodward 1984). PPM is a third-order accurate solver that sharpens any discontinuities but still avoids both undershoots and overshoots (Sweby, 1999).

The numerical calculations in this thesis use the ARWEN hydrodynamics code. ARWEN is an acronym for Astrophysical Research With Enhanced Numerics and makes use of the Godunov scheme (Godunov 1959, Toro 2009). It uses the PPMLR method, a lagrangian update using PPM and then a remap

back onto the original fixed grid (Sweby, 1999).

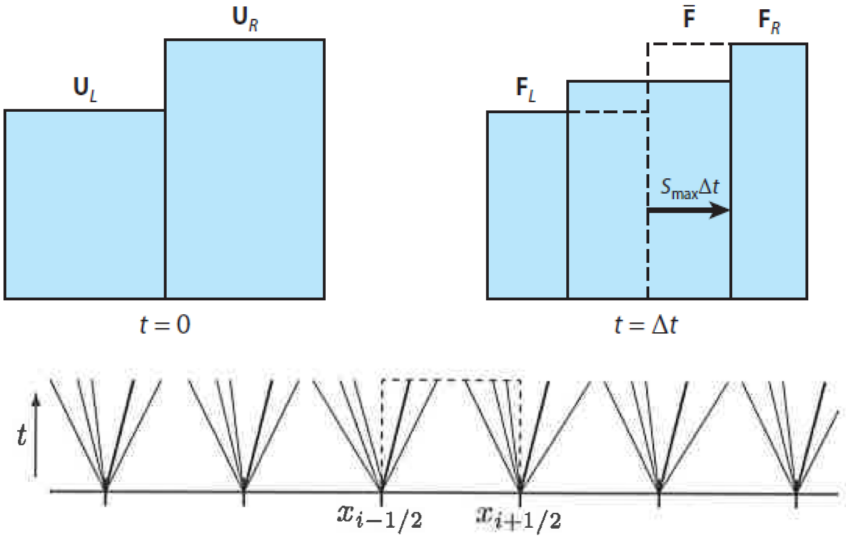

Figure 4.5: Upper panel: An illustration of a one dimensional Riemann problem and how the Godunov method can be used to update the inter-cell flux (Teyssier, 2015). The lower panel shows how the possible solutions to Riemann problems appear on a position-time plot (Sweby, 1999).

4.4.1 The Courant-Friedrichs-Lewy (CFL) Condition

Courant *et al.* (1967) noted that the distance through which a function is advected, $u\Delta t$, should be less than or equal to the grid spacing, Δx, otherwise the function is advected over a larger distance (more than a grid spacing) in a single time step, giving rise to unrealistic outcomes. The permitted time steps, set by the Courant condition, imply that $\Delta t \leq \frac{\Delta x}{u}$. This requires that $\Delta t = C\frac{\Delta x}{u}$, where C is called the Courant number. The maximum allowed value of Δt corresponds to a Courant number $C = 1$. The correct time step guarantees convergence and stability of a numerical process. In practice, C<1 is used e.g C=0.6 for a 1D PPMLR.

4.4.2 Boundary Conditions

Computational grids are populated by both active (real) zones and inactive cells called ghost zones. Ghost zones, normally located on the outer parts of active grids, are meant to store values temporarily to update neighbouring active cells at a later time. The data stored in ghost zones are largely the information about neighbouring cells, parent grid and boundary conditions which are later updated when required (Bryan *et al.*, 2014). ARWEN has three ghost zones.

The calculations in this thesis were performed on a 2-dimensional rectangular grid. Its horizontal line, labelled z-axis, represents a half of the axis of a bipolar jet while its vertical line, the r-axis, represent a half of the mid-plane of an accretion disk associated with the jet. The other two boundaries of the grid are the sides that are opposite and parallel r- and z- axes. The inner z- and r-boundaries are reflective while their outer counterparts are outflow boundaries i.e allow jet materials to flow freely (Lee *et al.*, 2001). Reflective axes may lead to unrealistic density values since particles can be trapped on the boundaries, especially along the z-axis. If the 2D jet is rotated through an angle of 360 degrees, about the z-axis, followed by a reflection on the r-axis, it outlines a bi-conical structure, similar to bipolar jets. This approximation, however, may be more accurate near the axis of the jet, unlike along the boundary of the jet and its cocoon, and the bow-shock where the effects of turbulence are maximum.

Since the jet is symmetric about the z- and r- axes, the component of velocity of the fluid that is normal to these boundaries is set to the opposite value in ghost zones. To set the jet to flow, its launch region is assigned values which are reset after every time step. The properties of particles within the launch regions are calculated from initial conditions, i.e. the simulation does not focus on the launch properties and origin of the jets.

4.4.3 Ionization, Heating and Cooling

The gas surrounding a protostellar jet is largely composed of atomic hydrogen, helium and metals in the ratio $0.7381 : 0.2485 : 0.013$ respectively (Asplund *et al.*, 2009). As jet material flows through the medium, the atomic components are ionized into energies, E^i, of different states, i, from which the ionization fraction,

$x(E^i)$, can be calculated as $x(E^i) = \frac{n(E^i)}{n(E)}$. In the equation, $n(E) = \sum_i^K n(E^i)$, is the total number density of all the atoms (Frank & Mellema, 1994).

The percentage of heavy metals in the ambient media is insignificant, in effect, minimally contributing to the mass and electron number densities of the gas. The number densities of the ambient gas can thus be approximated by equation 4.27, where m_p is the mass of a proton. With equation 4.27, it is possible to estimate the pressure P of the gas from its temperature T since they are related by the expression, $P = (n(\mathrm{H}) + n_e)k_B T$ (Rijkhorst *et al.*, 2006), where k_B is the Boltzmann constant.

$$\begin{aligned} \rho &= m_p\Big(n(\mathrm{H}) + 4n(\mathrm{He})\Big) \\ n_e &= x(\mathrm{H}^1)n(\mathrm{H}) + x(\mathrm{He}^1)n(\mathrm{He}) + 2x(\mathrm{He}^2)n(\mathrm{He}) \end{aligned} \tag{4.27}$$

Interaction between a jet and the ambient medium may occasion collisional heating and ionization. The rate of collisional ionization Γ_{coll} can be approximated by the formula $\Gamma_{coll} \approx k_{coll} n_e \rho_n$, where n_e, ρ_n and k_{coll}, given by equation 4.28, are the electron number density, mass density of neutral species and collisional ionization rate coefficient respectively (Tenorio-Tagle *et al.* 1986, Krumholz *et al.* 2007).

$$k_{coll} \approx 5.84 \times 10^{-11} \sqrt{\frac{T}{K}} e^{\frac{-13.6\,eV}{k_B T}} \ \mathrm{cm^3 s^{-1}} \tag{4.28}$$

The ionized particles can either recombine radiatively or non-radiatively. Radiative recombination results in cooling if a photon, emitted by a captured electron, escapes the jet environment without any form of interaction while non-radiative recombination results in vibration of the particles and heating of the system. The recombination rate can be estimated from the equation $\alpha_R = \alpha_R(10^4\,K)\Big(\frac{T_e}{10^4}\Big)^{-\sigma}$ by Frank & Mellema (1994) where values of α_R can be taken from Osterbrock & Ferland (2006) and σ is 0.8 for hydrogen particles. A jet undergoes both heating and cooling processes at the rate $\dot{E} = \frac{\rho}{m_H}\Big(\Gamma - \frac{\rho}{m_H}\Lambda(T)\Big)$, where $\Gamma = 2.0 \times 10^{-26}$ergs s^{-1} is the rate of radiative heating and $\Lambda(T)$ is the cooling rate. The cooling rates for $T > 10^4\,\mathrm{K}$ were calculated from the MEKAL code (see Figure 4.6), developed by Mewe *et al.* (1995). Below $10^4\,\mathrm{K}$, the cooling rates come

from the fit by Koyama & Inutsuka (2002) and corrected according to Vázquez-Semadeni *et al.* (2007).

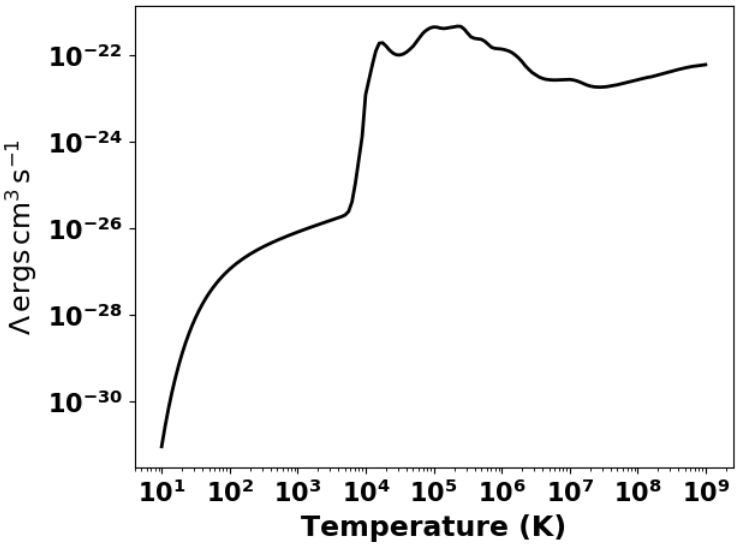

Figure 4.6: The cooling function adopted in the numerical simulation.

4.4.4 Testing ARWEN

ARWEN, like any other hydrodynamics code, solves equations of fluid motion and computes the values of the physical quantities that describe the fluid (e.g temperature, density, pressure and velocity) as it evolves. This means that the solutions from ARWEN and other codes should be comparable, however, this is not always the case as different codes use varied solvers with underlying numerical effects. There are several ways through which the accuracy of a simulation code can be verified e.g comparing results from different codes as well as making use of analytical approximations.

4.4.4.1 Analytic Approximation

The energy injected into an ambient medium by a jet is largely retained within the jet environment, building up pressure that leads to adiabatic expansion (Scheuer, 1974). Part of this pressure is released into the cocoon, collimating the jet beam

as well as advancing the cocoon towards the ambient medium. The velocity of the advance of a jet cocoon can thus be approximated analytically from its luminosity and the density of the ambient medium (de Gouveia Dal Pino, 2005) by equating the thrust that a jet exerts on its head/bow shock, $\rho_j(v_j - v_{bs})^2 A_j$, to the ram-pressure force developed by the ambient medium, $\rho_a v_{bs}^2 A_{bs}$ (Cioffi & Blondin 1992, Begelman 1996). In the equation, v_j is the jet velocity, v_{bs} is the velocity of advance of the bow shock, ρ_j is the density of the jet, ρ_a is the density of the ambient medium, A_j is the area of the jet beam of radius R_j and A_{bs} is the cross-sectional area of the jet head of radius R_h i.e $\rho_j(v_j - v_{bs})^2 R_j^2 \approx \rho_a v_{bs}^2 R_h^2$. The equation can also be written in the form $v_{bs} \approx v_j\left(1 + (\eta\alpha)^{\frac{-1}{2}}\right)^{-1}$, where $\eta = n_j/n_a$ is the ratio of jet to ambient number densities and $\alpha = (R_j/R_h)^2$. If $v_{bs} << v_j$ the equation reduces to $v_{bs} \approx v_j(\frac{\rho_j}{\rho_a}\frac{R_j}{R_h})^{\frac{1}{2}}$.

An analytic approximation of v_{bs} for a jet of velocity v_j =500 km s^{-1} and mass loss rate $\dot{M} = 10^{-6}\,\mathrm{M_\odot yr^{-1}}$ was used to test the accuracy of ARWEN. The analytic calculations of the velocities were found to be comparable with numerical estimates as seen in Figure 4.7. In the analytic calculations, the radius of the jet R_j was assumed to be equal to that of the jet head R_h i.e $R_j \sim R_h$. The average v_{bs} of the numerical estimate is v_{bs} =8.5±0.3 km s^{-1}, however, it reduces as the jet head decelerates uniformly from $v_{bs} \sim 15$ km s^{-1}, in the first few years, to ~ 2 km s^{-1}.

4.4.4.2 Comparing Outputs From ARWEN and ZEUS-2D Codes

Lee *et al.* (2001) used ZEUS-2D, a numerical hydrodynamic code (Stone & Norman, 1992), to simulate a molecular jet. They modelled a jet whose velocity $\mathrm{v_j} = 120\,\mathrm{km\,s^{-1}}$, mass-loss-rate $\dot{\mathrm{M}} = 1.2 \times 10^{-7}\,\mathrm{M_\odot yr^{-1}}$, temperature $\mathrm{T_j} = 270\,\mathrm{K}$, density $\rho_\mathrm{j} = 1.6 \times 10^{-20}\,\mathrm{g\,cm^{-3}}$ (i.e number density $\mathrm{n} = 7 \times 10^3\,\mathrm{cm^{-3}}$) and radius $\mathrm{R_j} = 2.5 \times 10^{15}\,\mathrm{cm}$. The jet was injected into a cold and uniform ambient cloud of density $\rho_\mathrm{a} = 1.6 \times 10^{-20}\,\mathrm{g\,cm^{-3}}$ and temperature $\mathrm{T} = 30\,\mathrm{K}$. It was then allowed to evolve for 650 years on a 600 by 60 grid of numerical resolution R $\sim$ 2.08×10^{14} cm. The maps of the density, temperature and pressure of their jet, after 650 years, are shown in Figure 4.8. A similar jet was simulated using ARWEN, resulting in the outputs shown in Figure 4.9.

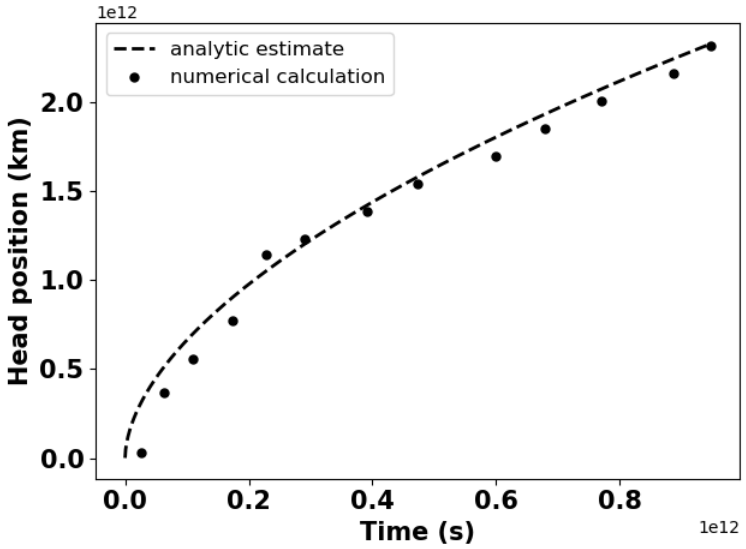

Figure 4.7: Relationship between the position of the jet head with time. The jet head has an average speed $v_{bs} = 8.5 \pm 0.3\,\mathrm{km\,s^{-1}}$.

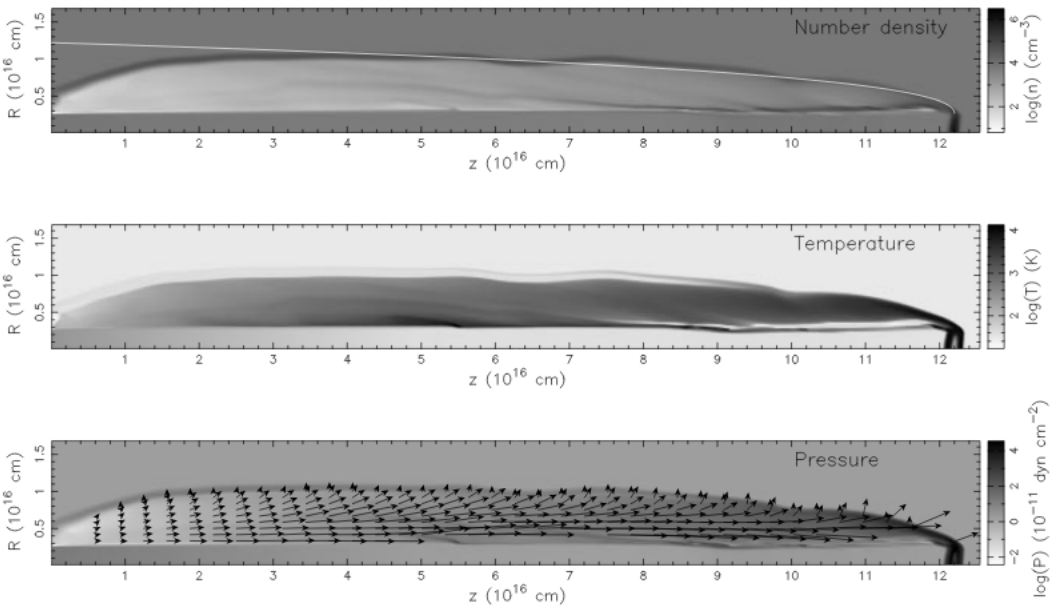

Figure 4.8: Distributions of number density, temperature, and pressure of the steady jet by Lee *et al.* (2001), at t =650 years. The vectors shown represent the velocity structure.

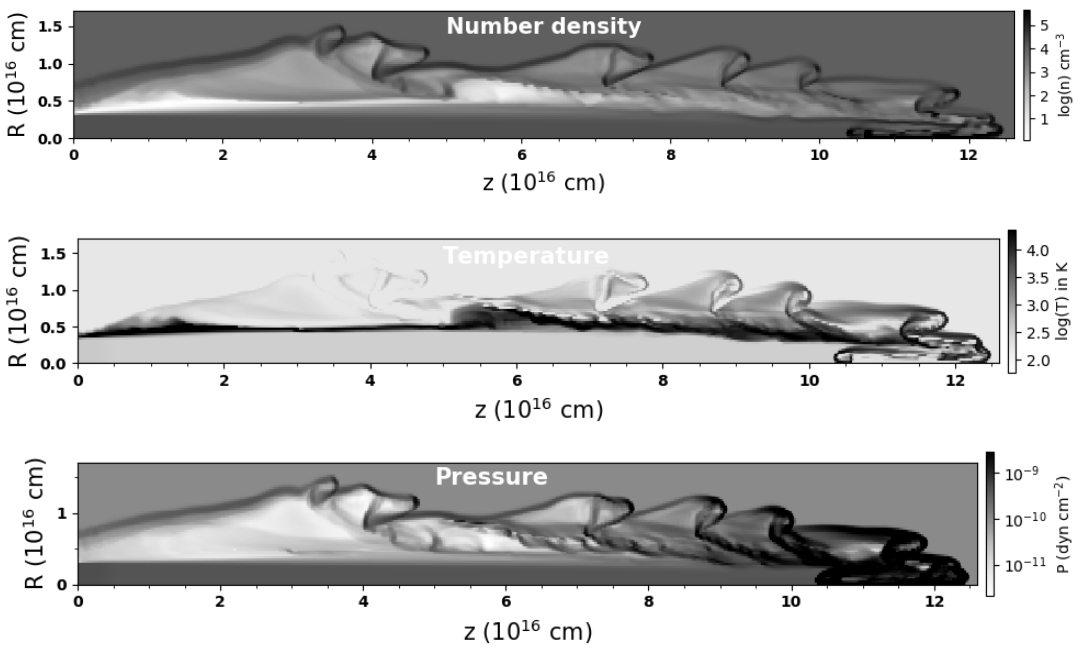

Figure 4.9: Snapshots showing the distributions of number density, temperature, and pressure of a jet simulated using ARWEN at $t = 480$ years. The jet by ARWEN flows off the grid faster, after 480 years.

Both ARWEN and ZEUS-2D generated jets of comparable number densities, temperatures and pressure. However, their morphologies and velocity of jet-heads are dissimilar. In ARWEN, for example, the average velocity of the jet-head is 80 km s^{-1}, approximately 20 km s^{-1} higher than in ZEUS-2D. The velocity, however, is in agreement with the analytic estimate which is v_{bs} ∼85 km s^{-1}, given that the average values of the ratio of the jet to ambient densities and jet to head radii are 1 and 0.5 respectively.

Cocoons of both jets also show clear differences. The jet by ARWEN shows stronger Rayleigh-Taylor and Kelvin-Helmholtz instabilities (see figures 4.8 and 4.9), perhaps due to the differences in cooling functions and numerical solvers of the codes. Use of comparable cooling curves (MacDonald & Bailey 1981, Dalgarno & McCray 1972) produce jets of similar cocoon morphologies (see Figure 4.10). Differences in viscosities have diffusive/dissipative effects (Neumann & Richtmyer, 1950) and may also contribute to the variation in instabilities. Similar instabilities were, however, present in Clarke (1996) and Stone & Norman (1993a).

4.5 Initial Conditions: Numerical Input Parameters

The relevance of simulations is connected to their ability to maintain closeness with physical systems. The initialization of such simulations should, therefore, be based on the physical properties of the objects of interest. Identifying observable quantities of the jets for initialization is thus a significant step towards simulating

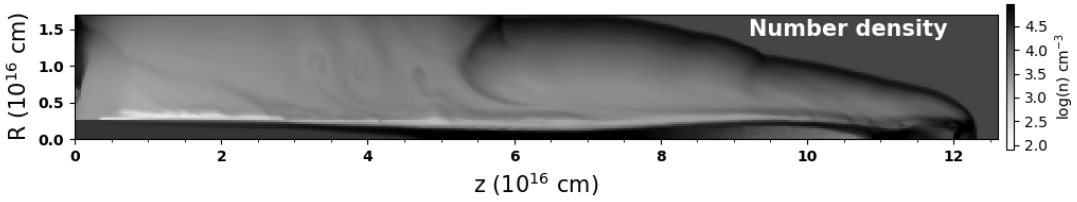

Figure 4.10: A snapshot of a 480 year old jet generated by ARWEN using cooling rates comparable to ZEUS-2D. The distribution of number density is similar to that of ZEUS-2D.

realistic jets. Some of the quantifiable properties of massive protostellar jets which can be used to initialize their models include; their velocities v_{jet}, mass loss rates $\dot{M}_{jet}$, opening angles θ_{jet} and temperatures T. Besides, one may simulate their structures may be straight, ballistic (Devine *et al.*, 1997), or even twisted (Hartigan *et al.*, 2005). Observationally, the quantities manifest a broad range of values, however, the typical values of the parameters were used in constraining and initialising the simulations. Typical values of some of the quantities are discussed in sections 4.5.1 to 4.5.5

4.5.1 Mass-Loss Rates

Radio observations show that massive protostellar jets drive out mass at rates that lie in the range 10^{-7} to $10^{-5}\,\mathrm{M_{\odot}yr^{-1}}$ (Obonyo *et al.* 2019, Purser *et al.* 2016, Bally 2016). The use of NIR emission, on the other hand, derives slightly higher rates e.g the jet driven by IRAS 13481-6124 (Fedriani *et al.*, 2018). Calculations of momentum and accretion rates of the objects also suggest that their mass loss rates are $\sim 10^{-5}\,\mathrm{M_{\odot}yr^{-1}}$. For example, momentum rates by Moscadelli *et al.* (2016) are in the range $10^{-3} - 1.0\ \mathrm{M_{\odot}yr^{-1}\,km\,s^{-1}}$, translating to mass-loss rates $\dot{\mathrm{M}}_{\mathrm{jet}} \approx 10^{-6} - 10^{-3}\,\mathrm{M_{\odot}yr^{-1}}$, assuming a jet velocity of $10^{3}\,\mathrm{km\,s^{-1}}$. Again, mass loss rates are known to be related to the accretion rates of protostars (Kurosawa *et al.*, 2006), implying that the accretion rates estimated by Pomohaci *et al.* (2017) and Haemmerlé & Peters (2016) translate to mass loss rates whose values lie in the range $\dot{\mathrm{M}}_{\mathrm{jet}} \sim 10^{-6} - 10^{-4}\,\mathrm{M_{\odot}yr^{-1}}$. Rates that lie in the range $10^{-7} - 10^{-5}\,\mathrm{M_{\odot}yr^{-1}}$, estimated from radio observations, were therefore adopted as realistic estimates for simulating jets of massive protostars, however, the modal value, $10^{-6}\,\mathrm{M_{\odot}yr^{-1}}$, was used in most of the simulations.

4.5.2 Lifespan

The jet driving phase of massive protostars is short-lived. It is the period that lies between the time when the high mass protostellar cores, hosted within the infrared dark clouds (IRDCs), collapse and the instance when the protostars are hot enough to form ultracompact HII regions (UCHII) (Zinnecker & Yorke, 2007). It is approximated to last $\approx 7 \times 10^{4}$ yrs in $\approx 10^{5}\,\mathrm{L_{\odot}}$ objects and $\approx 4 \times 10^{5}$ yrs in

$\approx 10^4\,L_\odot$ objects (Mottram *et al.*, 2011). Purser *et al.* (2016) set an upper limit on the lifespan of jets of MYSOs at 6.5×10^4 yrs. A maximum age of $2{\times}10^5$ years was adopted to cater for a wide spectrum of their masses.

4.5.3 Opening Angle

Materials flowing through a protostellar jet are normally launched at an angle to the axis of the jet. The angle, known as an opening angle, can be estimated observationally. At radio wavelengths, semi-opening angles of massive protostellar jets are approximated to lie in the range $10° - 30°$ (Moscadelli *et al.*, 2016). The angles can reduce along the jet depending on the presence and strength of the magnetic field of the jet (Ferreira, 1997). For example, in AGNs, the jet opening angles can be as wide as 60^o (Junor *et al.*, 1999) or as narrow as 12^o and still drop exponentially with distance from the black hole (Horiuchi *et al.*, 2006). Angles derived from optical jets are smaller i.e $\sim 1 - 10^o$ and yet they still show a change with distance from the protostar (Mundt, 1993). Opening angles of radio jets are generally wider near the source with typical values being several tens of degrees, perhaps an effect of poor resolution or collimation. A semi-opening angle of $10°$ was adopted to avoid a premature lateral flow of the jet away from the grid.

4.5.4 Length

The lengths of protostellar jets grow gradually, sometimes up to 10 pc (Bally *et al.*, 2007), before the formation of a terminal bow shock. Mundt (1993) compiled a list of lengths for optical jets of massive protostars. They range from $\sim 0.14 - 2.40$ pc and have an average value of 0.9 ± 0.8 pc. Radio jets, on the other hand, manifest shorter lengths since radio emission largely traces the core of the jets. For example, the average size of radio jets in Anglada *et al.* (2015) is ~ 0.003 pc. Jets of length $\lesssim$1 pc were adopted in the simulations to capture their features beyond the core.

4.5.5 Velocity

The radial velocities of jets manifest a wide range of values (Mundt, 1993). Optical jets, for example, have velocities that range from 75 to 620 $\mathrm{km\,s^{-1}}$. Radio jets also depict similar velocities (Anglada *et al.* 2015, Anglada *et al.* 2007). Typical velocities of the jets were thus taken to lie in the range $\sim$ 200-1000 $\mathrm{km\,s^{-1}}$, however, most of the calculations were performed assuming a jet velocity of 500 $\mathrm{km\,s^{-1}}$, estimated from the average proper motion of the lobes in W3 IRS5, rounded off to the nearest hundred.

Table 4.1 summarises the observational parameters and their typical values. These values were used in initialization of jet simulations by injecting jet material, at the mentioned values, into the ambient media (see illustration on the 2D grid shown in Figure 4.11). The ionised particles were introduced at an angle θ_o to the z-axis, which is also the jet axis. The first 15% of the cells of the z-axis and the injection angle were used in calculating the number of cells to populate with the energetic, hot and high-velocity particles during injection i.e cells around $z = 0, r = 0$.

4.6 Results: A Steady Jet

A jet is said to be steady if its velocity and mass loss rates are constant during the entire simulation period. Such a jet was simulated by injecting ionized particles whose average mass and temperature are $\bar{\mu}_m = 1.0{\times}10^{-24}$ g ($\sim$ 0.5 amu for pure hydrogen gas; Phillips 2001) and T =10^4 K respectively into a cold and uniform cloud of number density n_a =$1.0{\times}10^6$ $\mathrm{cm^{-3}}$ (Evans, 1999) and temperature T=100 K.

Table 4.1: Range of observation quantities that were considered in setting up the initial conditions of the simulations.

Observation quantity	Typical Values
Velocity of jet v_{jet}	$200 - 1000\,\mathrm{km\,s^{-1}}$
Mass loss rate $\dot{M}_{jet}$	$10^{-7} - 10^{-4}\,\mathrm{M_\odot yr^{-1}}$
Length	$0.01 - 1.00\,\mathrm{pc}$
Semi-opening angle θ_o	$10 - 20^\circ$

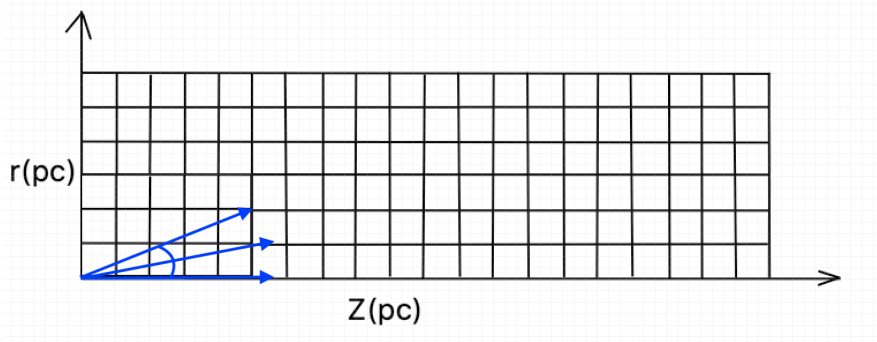

Figure 4.11: An illustration representing the 2D Eulerian grid and how jet materials are injected into an ambient medium, represented by the empty grid cells.

A steady jet whose half opening angle, velocity and mass loss rate are 10°, 500 km s^{-1} and 10^{-6} M$_{\odot}$yr^{-1} respectively was simulated (see Figure 4.12). The jet, simulated on a 2000 by 500 grid of numerical resolution 0.0001 pc ($\sim 3.1\times10^{14}$ cm), remained divergent for a short period, ∼3000 years. Thereafter, its particles were collimated and directed parallel to the jet axis by its cocoon i.e ram pressure. Its head travelled a distance of 0.125 pc in 20,000 years, translating to an average velocity of $\sim$ 6 km s^{-1} while the cocoon spread laterally to a maximum radius of 0.042 pc at a lower rate of $\sim$ 2 km s^{-1}. The analytic speed of the jet head, 6.2 km s^{-1}, is similar to the calculated average velocity of the jet head. These findings show that the velocity of a jet is almost 100 times higher than the velocity of its advance into the ambient medium.

Density, pressure and temperature plots of the steady jet do not show evidence of internal structures e.g knots, expected in protostellar jets, perhaps because the jets have a constant velocity. Radiative cooling can also result in a less collimated jet with fewer and weaker or no internal shocks (Blondin *et al.*, 1990), especially if a jet is flowing through a uniform medium. Nonetheless, some knots begin to appear within the jet beam once its head is out of the grid, and some of the gas from the cocoon begins to flow into the beam. Likewise, an initially homogeneous ambient medium becomes in-homogeneous as the jet materials interact with it, generating weaker shocks within the cocoon due to mass loading. Knots are normally more pronounced in precessing and pulsating jets (Bonito *et al.*, 2010). Jets of lower mass-loss rates and/or longer lengths also manifest shocks due to

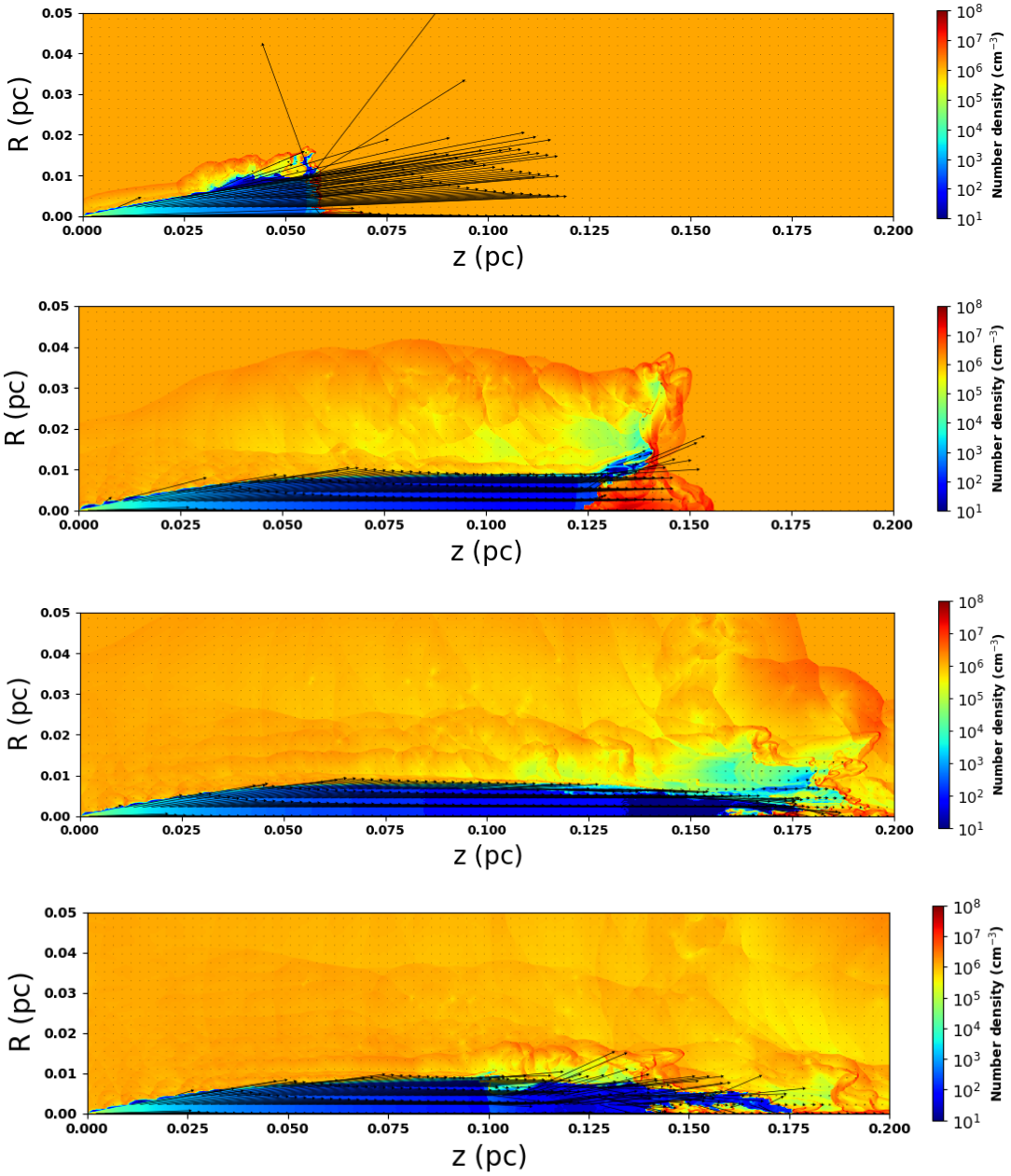

Figure 4.12: Snapshots showing the number density and direction of flow of particles across the jet at 3,000, 20,000, 40,000 and 60,000 years, displayed from the top to bottom respectively. The length and directions of the arrows represent the relative magnitudes and actual directions of the particles' velocities respectively.

mass-loading by the jet-head, followed by off-loading to the cocoons due to the longer lifespans of the jets.

The supersonic flow of the jet occasions two strong shocks; the jet shock (reverse shock) and a bow shock (forward shock), which sandwich the shocked regions. A density profile along the axis of the jet displays the four sections (see Figure 4.13). Particles of the jet beam which are located near the jet head form a thin region of hot shocked gas, the jet shock. These particles are the hottest. They get decelerated from their high velocities to lower velocities at the working surface as they interact with the slow-moving but dense jet head, giving rise to the high temperatures (Blandford & Rees, 1974). The working surface is not limited to the jet head but it surrounds the beam, occasioning a thin surface of hotter gas around the beam. This collisionally generated heat is quickly radiated away, resulting in a shocked ambient medium that is cooler ($\sim$ 100 K). The pressure along the axis of the jet also reveals a contact discontinuity between the shocked jet- and ambient- gas, a surface separating sections of different densities and temperatures but similar pressure (Marsh, 1970) i.e does not allow for the flow of mass across it. The relationship between axial number densities ρ_n of the unshocked jet particles and their distance, z, from the driving source, estimated through the method of least squares, display the characteristic property of spherical winds i.e $\left[\frac{\rho_n}{cm^{-3}}\right] = 10^{36.8} \times \left[\frac{z}{cm^2}\right]^{-2}$, where z is the distance of a particle from the source of the jet. Their temperature T and pressure p also show a decrease with distance z i.e temperature $T = 10^{17} \times z^{-0.78}$ and pressure $p = 10^{38.2} \times z^{-2.8}$. These findings suggest that as the jet spreads, its density and pressure decrease, causing the gradual cooling of the beam. Part of the injected heat may also cause adiabatic expansion of the cocoon, cooling the inner part.

Owing to the large difference between the velocities of beam particles, and the particles of the cocoon and ambient medium (see Figure 4.12), the velocities of all the particles in the field were normalized to unity, as shown in Figure 4.14, to display any patterns of evolution. Indeed, the velocity profiles of the beam, cocoon and ambient medium show significant differences. This is clearly seen at the time the jet is 20,000 years old. Within the beam, velocities of the particles are largely aligned parallel to the jet axis, while on the outer parts of the beam, the particles have velocities that are directed at a small angle to the jet-axis.

This flow is partly caused by the jet opening angle and collimation of the beam particles by the cocoon (Lee *et al.*, 2001). Particles of the cocoon, on the other hand, flow towards the beam. As the particles of the cocoon begin to interact with the supersonic particles of the beam, their flow is directed parallel to the jet axis. Lastly, the gas in the outer parts of the cocoon displays an outward motion, occasioned by the spread of an expanding cocoon. A look at the velocity distribution across the jet at different times (see Figure 4.12) displays evidence for the evolution of the jet velocity. The velocities of beam particles evolve from higher magnitudes and larger angles to lower values, implying deceleration and collimation of the beam particles. The interactions between the particles of the jet beam and the cocoon are also responsible for slowing down the beam particles, even though mass loading of the jet head may be the main cause of deceleration.

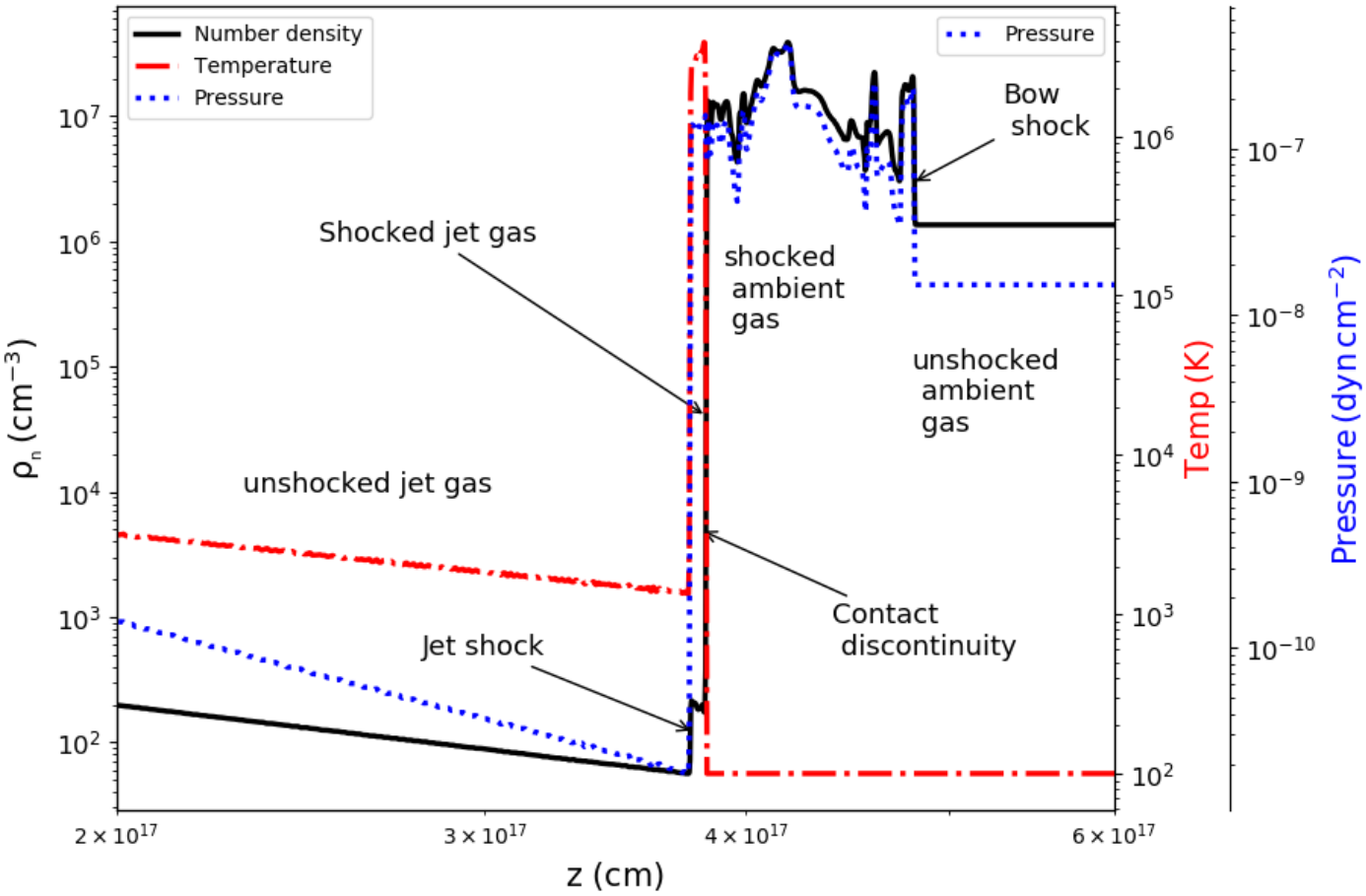

Figure 4.13: Number density, temperature and pressure along the axis of the jet at t=20,000 years.

4.7 Radio Emission From the Simulated Jets

4.7.1 Introduction

Calculation of radiative fluxes requires tracing of the radiation along a path to generate synthetic spectra (van Hoof *et al.*, 2014). The spectra of the simulated 2D jets were therefore calculated after rotating them through an angle of 360° about their $z-$axes to form conical jets. The cylindrical grid through which the ray is traced, therefore, is made up of cells which form concentric circles that are perpendicular to the jet axis. Each of the cells contains information about the density, pressure and the velocity of the hydrodynamic jet. The temperature, T, of the cells was calculated from the pressure P, density ρ and the average mass of the particles m_μ, in units of m_H, using the equation $T = \frac{Pm_\mu}{\rho k_B}$.

Information contained in each of the grid cells was read by a computation code (Pittard *et al.*, 2006) which calculates the emission and absorption coefficients of free-free emission, black body brightness B_ν(T) and brightness temperature. Kirchhoff's law of thermal radiation for a system in thermodynamic equilibrium which relates the brightness B_ν(T), emission coefficient j_ν and linear absorption coefficient α_ν of the system (Condon & Ransom, 2016) as $B_\nu(T) = \frac{j_\nu}{\alpha_\nu}$ was used to calculate $B_\nu(T)$. This is because the thermal radiation of a system in equilibrium only depends on its temperature and not its contents or the nature of its cavity walls.

The coefficient of free-free emission, j_ν, of the jets can be derived from the power of their emission per unit volume, per unit frequency and per unit solid angle, ε_ν^{ff}, by dividing it by 4π as shown in equation 4.29 in CGS units (Rybicki & Lightman, 1979). In the equation, Z is the charge number, n_e and n_i are the electron and ion number densities respectively, T is the temperature of gas, ν is the frequency, k_B is Boltzmann's constant, h is Planck's constant and g_{ff} is the free-free Gaunt factor.

$$j_\nu = \frac{\varepsilon_\nu^{ff}}{4\pi} = \frac{dW}{dV dt d\nu d\Omega} = \frac{6.8}{4\pi} \times 10^{-38} Z^2 n_e n_i T^{-\frac{1}{2}} e^{\frac{-h\nu}{k_B T}} g_{ff} \tag{4.29}$$

Non-relativistic Gaunt factors for free-free emission g_{ff} were calculated as described in Hummer (1988) to cater for any deviation of the calculated power of

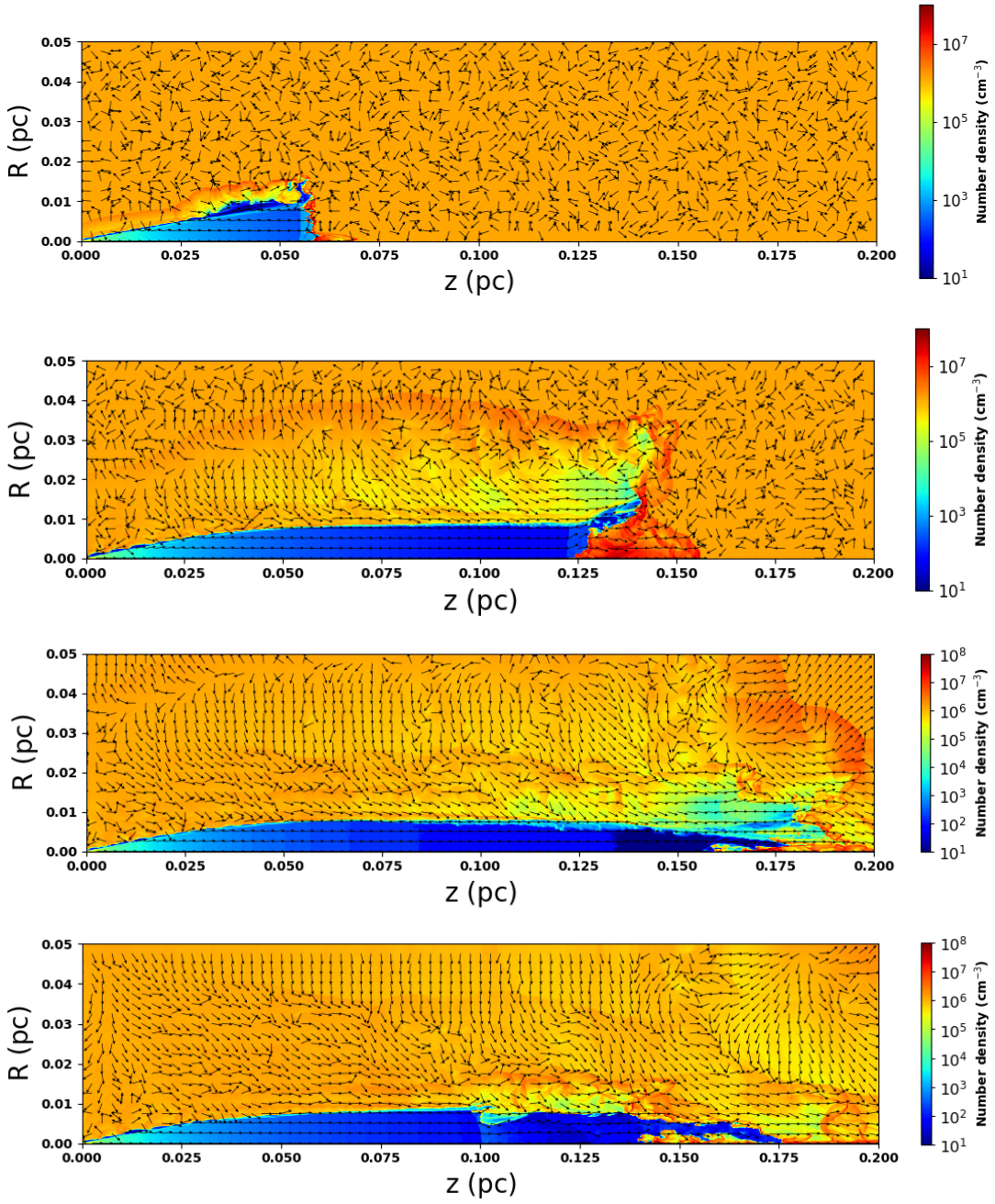

Figure 4.14: Snapshots showing the number density and direction of flow of particles across the jet at 3,000, 20,000, 40,000 and 60,000 years, displayed from the top to bottom respectively. The arrows show the directions of flow of the particles. Magnitudes of the particles' velocities are normalised to unity.

free-free emission from quantum mechanical aspects. The absorption coefficient (Rybicki & Lightman, 1979), in units of cm^{-1}, and the brightness temperature (Condon & Ransom, 2016), in Kelvin, were calculated using equations 4.30 and 4.31 respectively, in CGS units.

$$\alpha_\nu = 3.7 \times 10^8 T^{-\frac{1}{2}} Z^2 n_e n_i \nu^{-3} (1 - e^{\frac{-h\nu}{k_B T}}) g_{ff} \tag{4.30}$$

$$T_b = \frac{B_\nu(T) c^2}{2.0 \nu^2 k_B} \tag{4.31}$$

4.7.2 Radiative Transfer Scheme

Synthetic spectral maps of the simulated hydrodynamic jets were constructed on two-dimensional images of size z by $2r$ using a code that was developed by Julian Pittard (Pittard *et al.*, 2006). To construct the image, imaginary rays, parallel to the line of sight and passing through the implied cylindrical jet, were traced from the back of the jet to the image plane. The image plane is placed perpendicular to the line of sight as illustrated in Dougherty *et al.* (2003).

The intensity I_i of the radiation that emerges after crossing the i^{th} cell of length Δs in the direction along the line of sight is given by equation 4.32, where α_i and ε_i are the absorption and emission coefficients of the cell. I_{i-1}, the intensity of the $(i-1)^{th}$ cell, is attenuated as it crosses the i^{th} cell. The resultant intensity $I_{i-1} e^{-\alpha_i \Delta s}$ then combines with intensity $\frac{\varepsilon_i}{\alpha_i}$ due to the brightness of i^{th} cell, part of which is attenuated as it crosses Δs i.e $\frac{\varepsilon_i}{\alpha_i} e^{-\alpha_i \Delta s}$. The intensity I_n that emerges after crossing n cells along the line of sight is the final derived intensity along the line of sight. An image grid of intensities is then constructed from intensities of other lines of sight that pass through the cylindrical grid. The total flux at a given frequency was then calculated by summing up the intensities of all the pixels within the map.

$$\begin{aligned} I_i &= I_{i-1} e^{-\alpha_i \Delta s} + \frac{\varepsilon_i}{\alpha_i} - \frac{\varepsilon_i}{\alpha_i} e^{-\alpha_i \Delta s} \\ I_i &= I_{i-1} e^{-\alpha_i \Delta s} + \frac{\varepsilon_i}{\alpha_i} \left(1 - e^{-\alpha_i \Delta s}\right) \end{aligned} \tag{4.32}$$

4.7.3 Radio Emission and Numerical Resolution

High numerical resolution is desired in hydrodynamic simulations due to its ability to display fine structures (Nagel *et al.*, 2008), and in radiative transfer, to correctly sample the region that emits radiation. The characteristic radius of emission for spherical winds can be estimated using the equation $R(\nu) = 2.8 \times 10^{28} \gamma^{\frac{1}{3}} g_{ff}^{\frac{1}{3}} Z^{\frac{2}{3}} T^{-\frac{1}{2}} \left(\frac{\dot{M}}{\mu v \nu}\right)^{\frac{2}{3}}$ cm, where γ is the ratio of electron to ion number densities, g_{ff} is the free-free Gaunt factor, T is the temperature in K, $\dot{M}$ is the mass loss rate in $M_{\odot}\mathrm{yr}^{-1}$, μ is the mean atomic mass, ν is the frequency of emission in Hz and v is the velocity of particles in $\mathrm{km\,s^{-1}}$ (Wright & Barlow, 1975). The mass-loss rates were scaled using the equation $\dot{\mathrm{M}} \simeq \frac{2}{1-\cos\theta_o}\dot{\mathrm{M}}_{\mathrm{jet}}$ to match the rates in conical flows of opening angles θ_o. Indeed, Reynolds (1986) observed that a smaller mass loss rate in conical winds $\dot{\mathrm{M}}$ (jet) can lead to the same radio brightness as higher mass loss rates of spherical winds $\dot{\mathrm{M}}$ (spherical wind; Panagia & Felli 1975) i.e for a given mass-loss rate, jets are more opaque at smaller radii. The Gaunt factors used in the calculations were approximated using the formula given in Reynolds (1986) and Beckert *et al.* (2000).

The characteristic radii of emission for conical winds of different mass-loss rates, velocity v=500 $\mathrm{km\,s^{-1}}$ and temperature T=10,000 K are shown in Figure 4.15. At a frequency of 45 GHz, the approximate value of the turnover frequency of free-free emission from jets (Anglada *et al.*, 2018), the radii are 0.002 pc ($\simeq$ 412 AU), 0.0005 pc ($\simeq$ 103 AU) and 0.0001 pc ($\simeq$ 21 AU) for $\dot{\mathrm{M}} = 10^{-5}\mathrm{M}_{\odot}\mathrm{yr}^{-1}$, $10^{-6}\mathrm{M}_{\odot}\mathrm{yr}^{-1}$ and $10^{-7}\mathrm{M}_{\odot}\mathrm{yr}^{-1}$ respectively. Resolution for a jet of mass-loss rate $\dot{\mathrm{M}} = 10^{-6}\mathrm{M}_{\odot}\mathrm{yr}^{-1}$ was estimated by sampling its emitting radius with a minimum of ten cells, translating to a resolution R$\simeq$0.00005 pc ($\simeq 1.54 \times 10^{14}$ cm/10 AU). This resolution also allows for proper sampling of the typical launch radius of protostellar jets $r_o \lesssim 10^{15}$ cm ($\simeq$ 0.0003 pc/62 AU; Reynolds 1986, Estalella *et al.* 2012).

The effectiveness of the resolution was checked by calculating radio emission from jets of length l =0.02 pc and distance d =1.0 kpc on grids of different resolutions. An ideal jet was simulated by populating all the cells of a grid of physical size 0.02 pc by 0.005 pc with number densities that are typical of a jet of mass-loss rates $\dot{M}$ =10^{-6} $\mathrm{M}_{\odot}\mathrm{yr}^{-1}$, velocity v =500 $\mathrm{km\,s^{-1}}$, opening angle θ_o =10° and

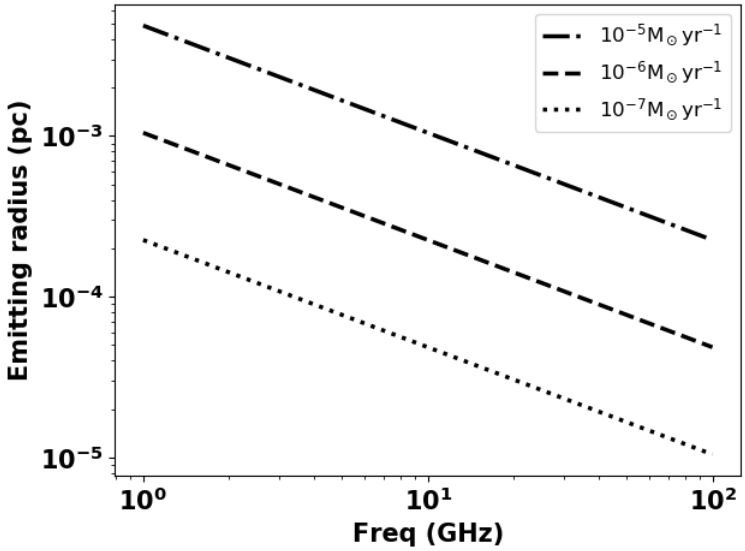

Figure 4.15: Characteristic radii of free-free emission at different frequencies of emission and mass-loss rates (Wright & Barlow, 1975).

temperature T =10^4 K (see Figure 4.16). Grids of size 200 by 50 cells, 400 by 100 cells, 800 by 200 cells and 2000 by 500 cells were used, translating to resolutions of 1×10^{-4} pc, 5×10^{-5} pc, 2.5×10^{-5} pc and 1.0×10^{-5} pc respectively (see Figure 4.17). The validity of the scheme used in generating the spectra was tested by comparing its results with calculations of Reynolds (1986).

Clearly, the turn over frequencies of the spectra change with resolution (i.e gas density), however, the slopes of their optically thick parts are relatively constant, $\sim$ 0.6, regardless of the change in resolution. Their turnover frequencies are above 40 GHz when the resolution is $\lesssim 2.5\times10^{-5}$ pc, implying that jets simulated on higher resolution grids have α $\sim$0.6 for frequencies ranging from 1.0-50 GHz, the frequency range of interest. The spectral indices, shown in Figure 4.17, were calculated using fluxes at 1.5 GHz, 6 GHz and 44 GHz to match the observations in Obonyo *et al.* (2019).

4.7.4 Radio Emission from Simulated Cores

Radio emission from a core of mass-loss rate $\dot{M}$ = 10^{-6} $M_\odot yr^{-1}$ and velocity v =500 km s^{-1} was calculated by assuming an inclination angle i = 90° and

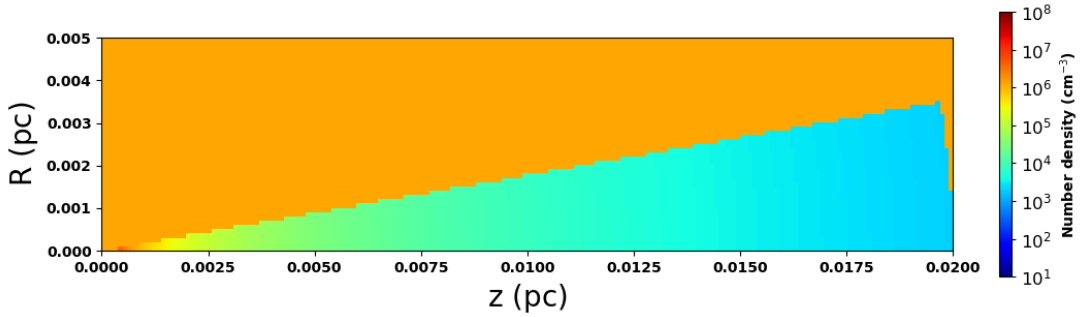

Figure 4.16: Grid of resolution 1.0×10^{-4} pc showing how the density distribution of a jet of $\dot{M}$ $=10^{-6}\,\mathrm{M_{\odot}yr^{-1}}$, velocity v $=500\,\mathrm{km\,s^{-1}}$, opening angle θ_o $=10^{\circ}$ and temperature T $=10^4\,\mathrm{K}$ appears without interacting with the ambient medium.

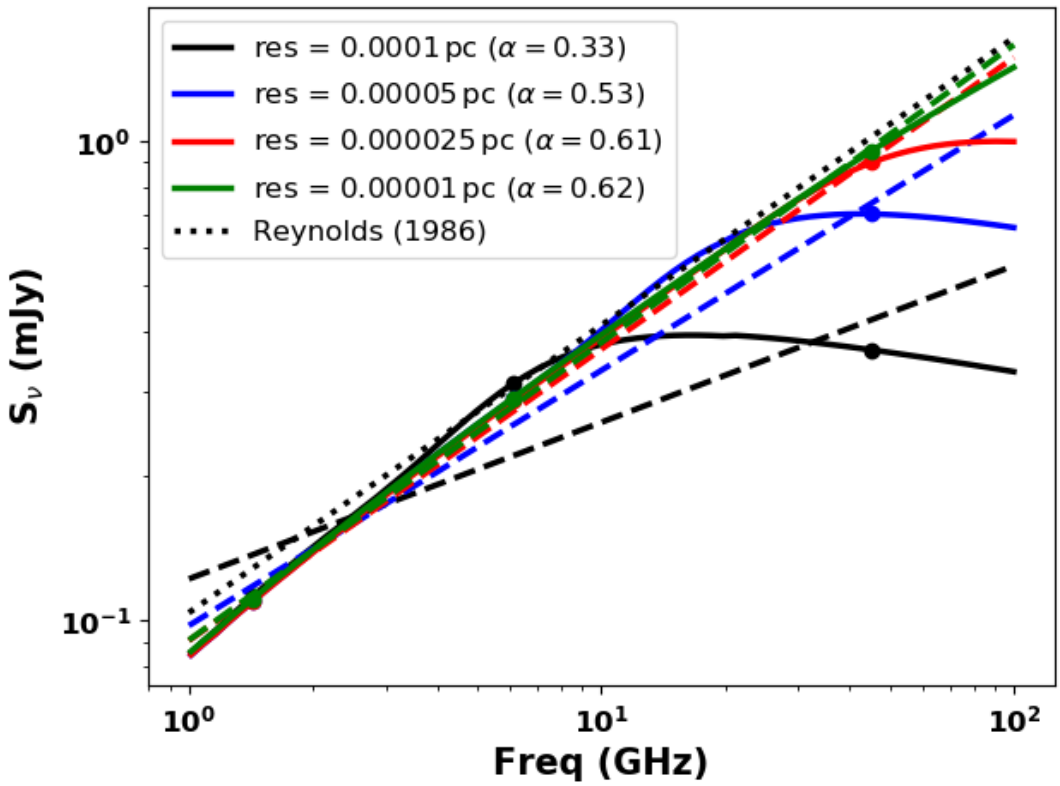

Figure 4.17: Spectra of conical winds at different resolutions are shown as solid lines. Their spectral indices were calculated using fluxes at 1.5 GHz, 6 GHz and 44 GHz to match the observations in Obonyo *et al.* (2019). The dashed lines are lines of best fit for these three frequencies while the dotted line represents the analytical result for a standard conical jet (Reynolds, 1986) of similar properties.

distance d =1.0 kpc. The radio emission from the core, simulated on a 2000 by 500 cells grid, manifests significant changes as the jet evolves. The jet has an ejection region that contains dense ionized gas of spectral index $\alpha = 1.77$. Once the jet is set to flow, its gas spreads out, lowering the opacity of the low-frequency emission significantly in about 100 years. The spectral index of the emission thus decreases to a value that is comparable to the indices of ionized winds from protostellar jets. The drop of the index continues gradually, fluctuating about $\alpha = 0.6$, the typical spectral index of ionized winds driven by jets (see Figure 4.18). This change in the nature of emission can be attributed to collisional heating and gradual expansion of the jet. Indeed, the spectrum of free-free emission radiated by a single electron as it interacts with a nearby ion is affected by its velocity and their impact parameter (Condon & Ransom, 2016), factors which are linked to temperature and density of a jet.

Intensity maps of the jet at 1.5, 5.0 and 44.0 GHz, after 200 years of evolution, shown on the upper panel of Figure 4.19 also show a reduction in the opacity of the jet at the higher frequencies. Indeed the emission is highly transparent at 44 GHz where only the mapping region and extremely hot spots are emitting, partly due to the transparent nature of the emission at 44 GHz, and perhaps an effect of the convolving beam. Convolving the emission from the mapping region with the L- and C-band beams, on the other hand, extremely weakens the emission of the region. Besides the intensity map, a spectral index map of the jet, shown on the lower panel of Figure 4.19, was also generated after convolving the intensity maps of 1.5 GHz and 6 GHz emission with a beam of 1.″0, comparable to the beam of L-band observation in Obonyo *et al.* (2019). This map clearly displays the thermal nature of the emission, with the working surfaces displaying the highest opacity. This emission though rarely detected in jets of massive protostars, compared to the strong synchrotron emission, was observed in HH 80-81 (Rodríguez-Kamenetzky *et al.*, 2017), and in some protostars in Obonyo *et al.* (2019).

The spread of the jet into the ambient medium is non-uniform. The expansion rate is higher at the early stages of evolution, however, this slows down with time due to mass loading at the jet head. This non-uniform expansion of the jet, together with the redistribution of temperature due to collisional heating,

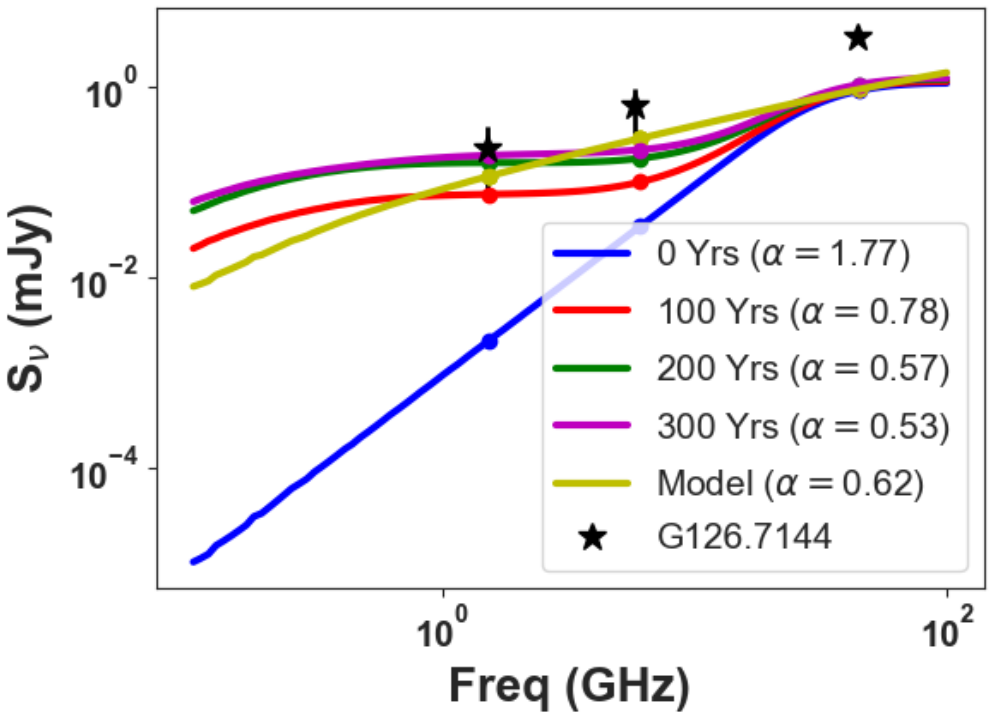

Figure 4.18: Spectra of conical winds as they interact with ambient medium are shown in red, green and magenta while the spectrum representing the analytic calculation is shown in yellow solid lines. The blue line represent the spectrum of particles within the launch region of the jet. The black asterisks represent the L-, C- and Q-band fluxes of G126.7144.

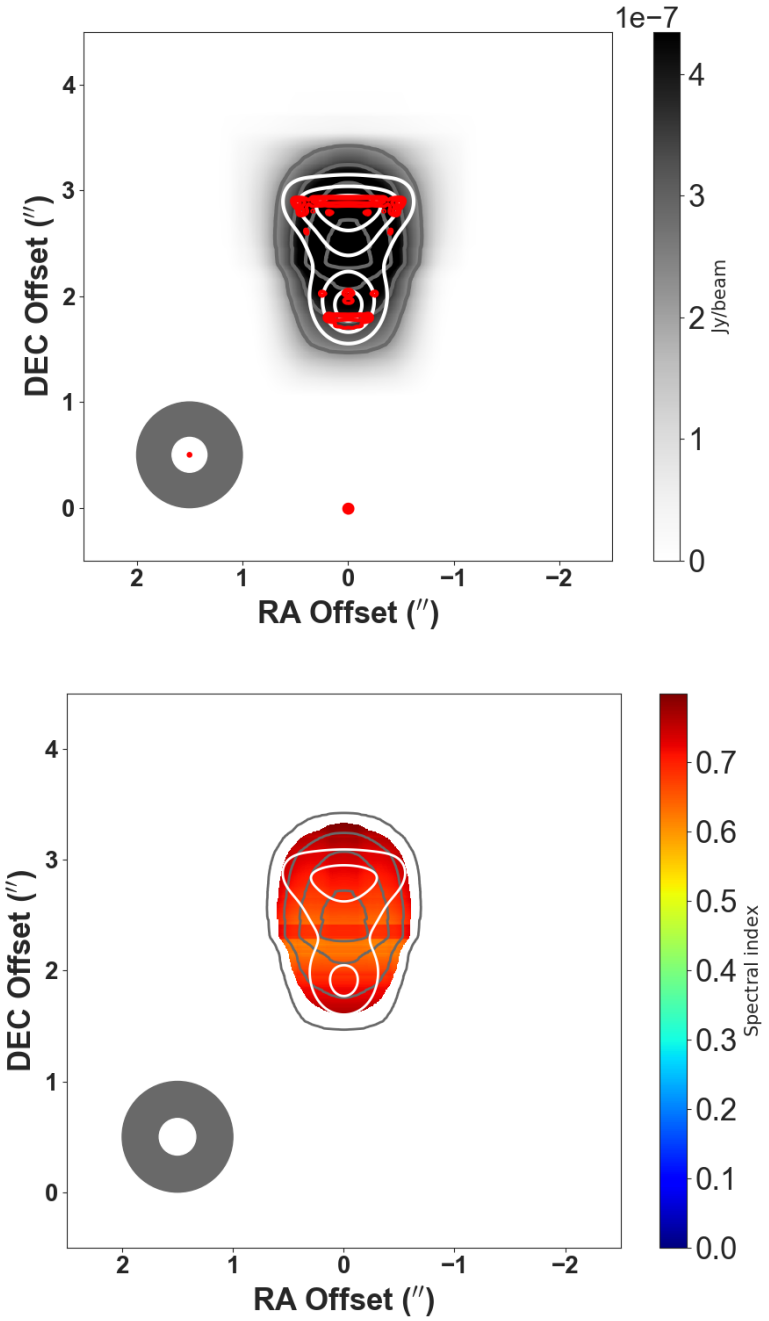

Figure 4.19: Top: Intensity maps of a 200-year-old jet at 1.5, 5.0 and 44 GHz shown in grey, white and red contour of levels 3σ,7σ,11σ,... The jet was convolved with circular beams, shown on the lower-left corner of the plot, to mimic the observations.
Bottom: Spectral index map of the jet, generated after convolving L- and C-band intensity maps of the jet with a circular beam of size $1.''0$. The bar appearing across the map seems to be an effect of the convolutions.

may be responsible for the deviation of the shape of the spectrum from that of analytic calculations (Reynolds, 1986). The spectrum of the jet manifests an S-shaped curve with a plateau at lower frequencies unlike in the analytical calculations where the slope is relatively uniform. The high-frequency plateau, however, is due to the numerical simulation as it is present at $t = 0.0$ years. Despite the variations in the spectra of an evolving jet, the average spectral index of its emission, calculated using average fluxes at L-, C- and Q-bands is 0.77±0.17, typical of the indices of ionized winds that are driven by jets. This means that the variation in the spectra does not correspond to a significant difference in the spectral index of the jet over the evolution period. The simulated fluxes were also compared with observations. The L-, C- and Q-band fluxes of G126.7144-00.8220, located at a distance of 0.7 kpc, and driving out mass at the rate $\dot{\mathrm{M}} = 1.2 \pm 0.3 \times 10^{-6}\,\mathrm{M_{\odot}yr^{-1}}$ were scaled to match the fluxes of the simulations i.e. assuming a distance of 1.0 kpc. The flux densities from the observations are higher than the simulated fluxes, especially at frequencies higher than L-band, perhaps due to the nature of the spectra of simulated jets and the higher mass-loss rate of the source. However, its L- and C-band fluxes are consistent with the simulated fluxes within the uncertainties.

The stability of the radio emission from protostellar cores was investigated further by monitoring the evolution of fluxes at certain frequencies. A core of mass-loss rate $\dot{M} = 10^{-6}\,\mathrm{M_{\odot}yr^{-1}}$ and velocity v =500 $\mathrm{km\,s^{-1}}$, simulated on a lower resolution grid of 400 by 100 cells, was used to allow for faster calculations of their fluxes. The fluxes, taken at intervals of one year for a period of 1000 years show relative stability. Emission of the jet at 6 GHz, for example, has an average flux density of 0.35±0.01 mJy, translating to an average uncertainty of 3% (see Figure 4.20). The relatively constant fluxes are accompanied by some instantaneous rise in flux with the maximum value being ∼14% above the average. Spectral indices of the jet at the different epochs are equally stable, having an average value of 0.59±0.02, throughout the evolution period.

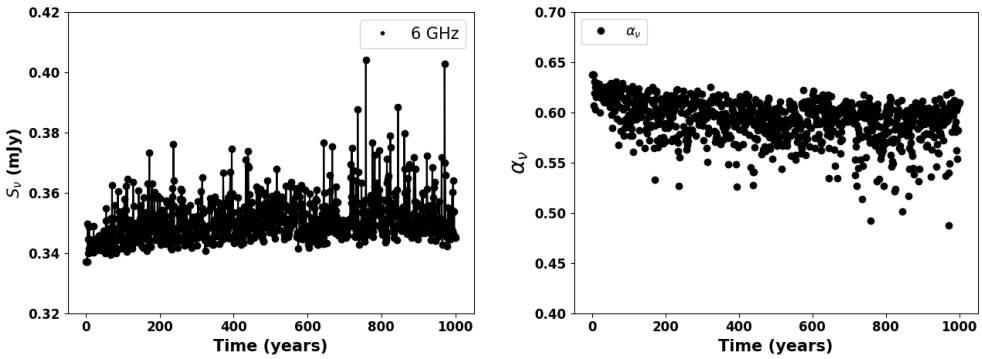

Figure 4.20: Left: Variation of 6 GHz flux of a steady jet as it interacts with the ambient medium, taken at intervals of one year for a period of 1000 years. Right: Evolution of corresponding spectral indices of its emission.

4.7.5 Variability in Jets

4.7.5.1 Variable Velocity

Protostellar jets show evidence of fluctuating velocities (Caratti o Garatti *et al.*, 2009). Evolution of radiation from a jet of variable velocity was investigated by monitoring the flux of a jet whose velocity v varies with time. The velocity was modelled to mimic a function that repeats itself after 800 years i.e $v = 400 + 100 \times \sin\frac{t\,(yrs)}{250} \times \sin\frac{t\,(yrs)}{50}\,\mathrm{km\,s^{-1}}$, setting its lowest velocity at $v \sim 320\,\mathrm{km\,s^{-1}}$ and the maximum as $500\,\mathrm{km\,s^{-1}}$, typical of jet velocities. The opening angle and mass loss rate of the jet were maintained at $\theta = 10°$ and $\dot{M} = 10^{-6}\,\mathrm{M_\odot yr^{-1}}$ respectively. The fluxes show anti-correlation with velocity i.e. $\mathrm{S}_\nu\,(\mathrm{mJy}) \propto \frac{1}{\mathrm{v}\,(1000\,\mathrm{km\,s^{-1}})}$, corresponding to the relationship between the density of a jet and the velocity of its particles. Therefore, the lower the velocity, the higher the density and flux of emission. Figure 4.21, showing the variation of fluxes at 6 GHz with time, clearly demonstrates the relation. Again, the figure shows that a drop in the velocity of the jet by 50% corresponds to a rise in its flux by 30%, implying that such changes are detectable in most observations as the typical uncertainty in observed fluxes is ∼10%.

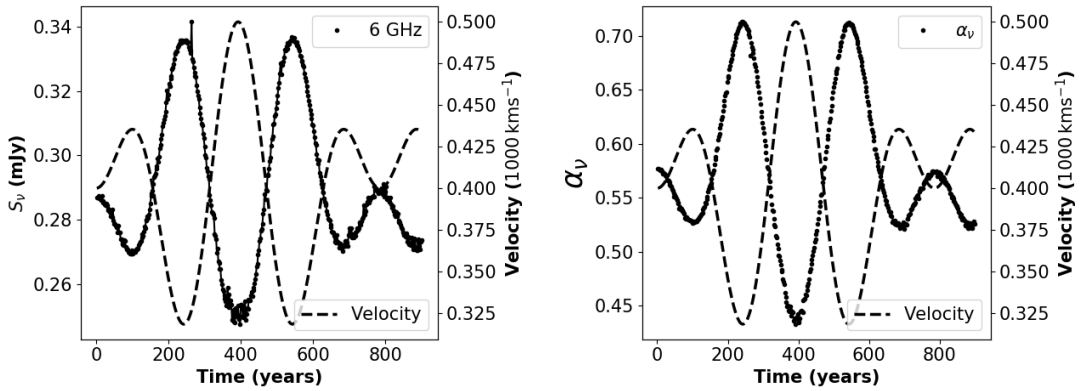

Figure 4.21: Left: Evolution of the flux of a jet flowing with a variable speed. The velocity profile of the jet is also displayed on the plot using a dashed line. Right: Evolution of the spectral indices of the jet as its velocity change with time.

4.7.5.2 Variable Mass-Loss Rate: Simulating an Outburst

The effect of varying mass-loss rate in jets was investigated by increasing the rate of a steady jet by a factor of five, from $10^{-6}\,\mathrm{M_\odot yr^{-1}}$ to $5 \times 10^{-6}\,\mathrm{M_\odot yr^{-1}}$, for a period of five years. The increase occasioned a corresponding rise in the intensity of the jet's radio emission at all frequencies with higher frequencies displaying greater increase. The uneven increase in the flux across the different frequencies also prompted a rise in the spectral index of the jet's radio emission. The flux of the jet, at a given frequency, and the spectral indices of its emission, at the different epochs, remained constant after the outburst, comparable to the light-curves of the outbursts in Bell *et al.* (1995), suggesting that the added particles did not undergo either diffusion or recombination (see Figure 4.22). Indeed, increasing the density of ionized particles in an already ionized system seems to keep the density of the system high until the added particles flow out of the system, a phenomenon whose timescales may be comparable to the lifespan of a jet. Again, the decay periods of protostellar jets are generally longer than rises (Hartmann & Kenyon, 1996)

Other than increasing the mass-loss rate to a higher constant value, it was also modelled to increase in a manner that obeys a Lorentzian function. This model that mimics a gradual increase in the rate followed by a drop, seen in some variable objects (Choi *et al.*, 2014), generated fluxes and indices that are highly

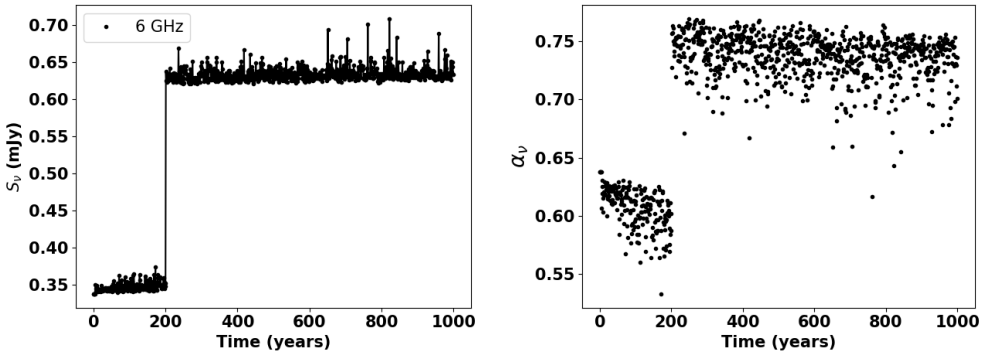

Figure 4.22: Left: Outburst of a jet, modelled as single-step increase. Right: Evolution of corresponding spectral indices of its emission.

random with no clear trend (see Figure 4.23). However, after the outburst, both the flux and spectral index of the jet stabilised at relatively constant values which are higher than their pre-outburst values.

It is clear from the simulations of variable jets that a rise in the number densities of their charged particles occasioned a corresponding rise in their fluxes and opacities. This result is inconsistent with the outburst in S255 NIRS3, where the flux rises as the opacity drops during the outburst. It is likely, therefore, that the emission from the S255 NIRS3 outburst is composed of both free-free and synchrotron radiation as suggested earlier.

4.7.5.3 Relationship Between Mass-Loss Rate and Flux Density

The relationship between mass-loss rates and flux densities of protostellar jets was explored by simulating fully ionized and steady jets of different mass-loss rates on grids of resolution $2{\times}10^{-5}$ pc. Their opening angles, sizes, and velocities were fixed, i.e $\theta = 10°$, z =0.02 pc and v =500 km s^{-1} respectively, as mass-loss rates were increased by an order of magnitude in subsequent simulations, generating jets whose rates are 10^{-9}, 10^{-8}, 10^{-7}, 10^{-6} and 10^{-5} M$_\odot$yr^{-1}. Varying the mass-loss rate of the jets affects the nature of their emission spectra. Jets of higher mass-loss rates radiate optically thick emission of higher intensities and turn-over frequencies while their counterparts of lower mass-loss rates e.g $\dot{M} \leq 10^{-8}$ M$_\odot$yr^{-1} are optically thin at all frequencies.

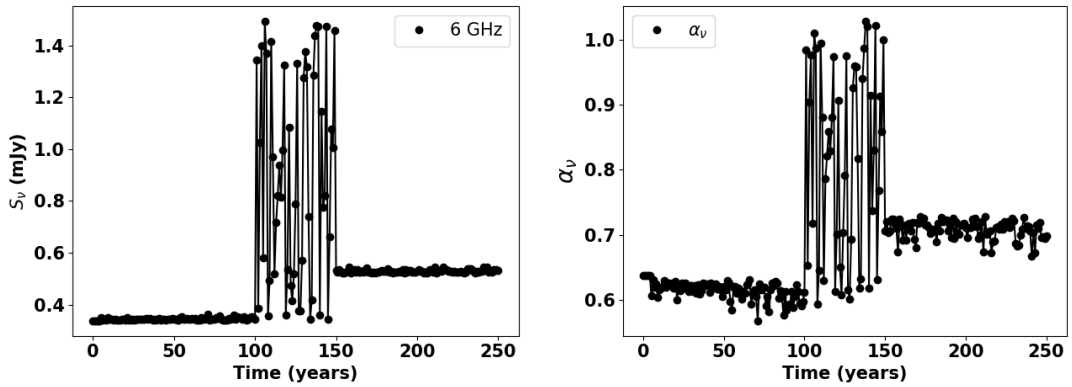

Figure 4.23: Left: Variation of 6 and 22 GHz fluxes of the simulated jets with age. The time gap between the fluxes is 100 years. Right: Evolution of corresponding spectral indices.

To compare fluxes from jets of similar opacities, four jets of mass-loss rates 10^{-8}, 10^{-7}, 10^{-6} and $10^{-5}\,M_\odot yr^{-1}$ were simulated on grids of different physical sizes. Their spectral indices lie in the range 0.5-1.0 (see Figure 4.24). It is clear from Figure 4.24 that increasing the mass-loss rates leads to higher flux densities, largely due to the increase in the number densities of the charged particles in the system. At 45.0 GHz, for example, the mass-loss rates and the flux densities of the jets are related according to equation 4.33.

$$\frac{S_\nu}{[mJy]} = 10^{8.8\pm0.4} \times \left[\frac{\dot{M}}{M_\odot yr^{-1}}\right]^{1.4\pm0.2} \tag{4.33}$$

The relation was also calculated for all the frequencies, estimating the average value for the power of $\left[\frac{\dot{M}}{M_\odot yr^{-1}}\right]$ as 1.3±0.1 and that of its coefficients as $10^{8\pm1}$. The power of $\dot{M}$, derived from the simulations, is consistent with the analytic calculations by Wright & Barlow (1975) and Reynolds (1986) i.e $S_\nu \propto \dot{M}^{\frac{4}{3}}$.

4.8 Conclusion

Hydrodynamics simulations of the jets show that particles of their cocoons tend to flow towards their beams, in effect, aiding their collimation. Studies by Mellema & Frank (1997) and Lee *et al.* (2001) also revealed that these jets have the potential

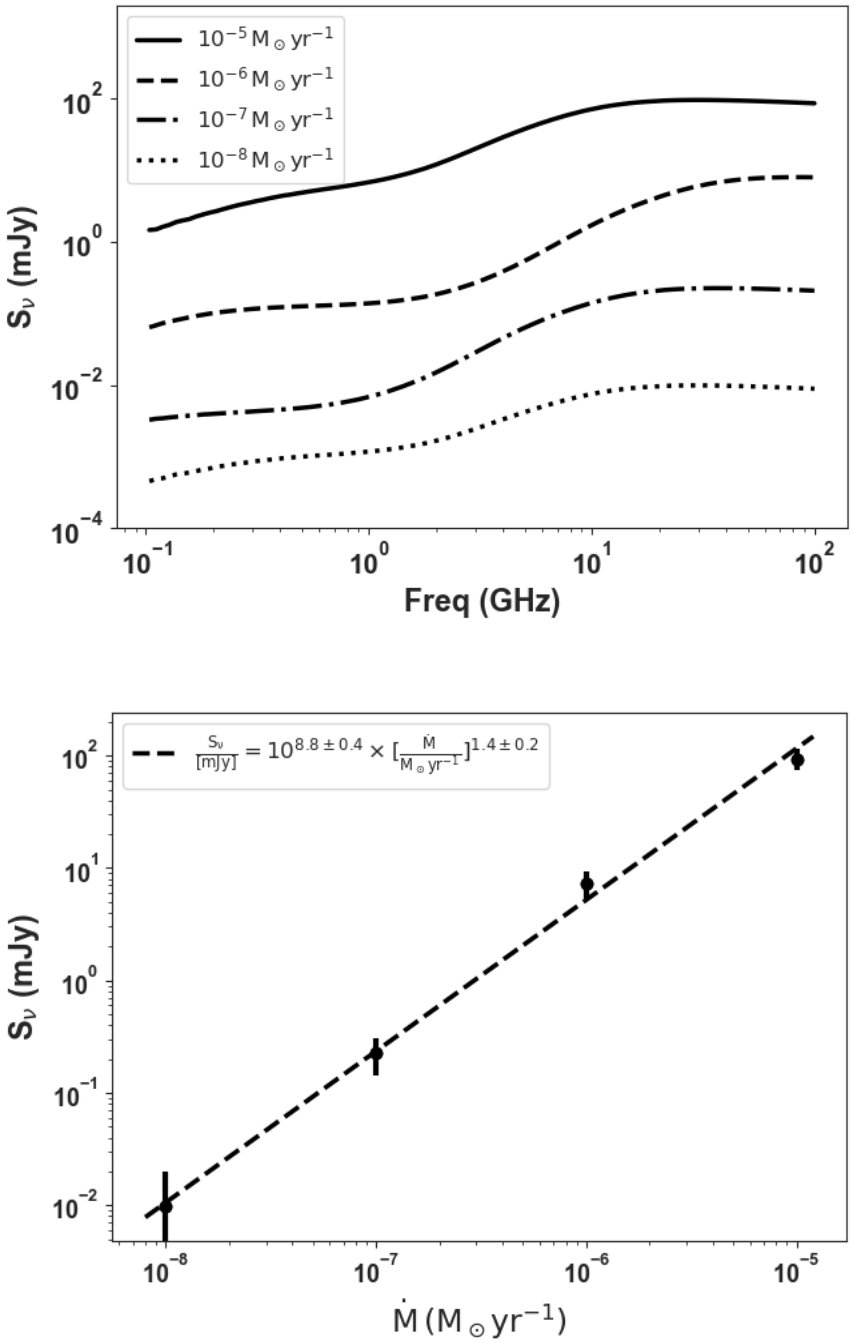

Figure 4.24: Top: Spectra of optically thick jets of varied mass-loss rates and sizes. Bottom: A plot showing how mass-loss rates of the ionized jet vary with flux density at 45 GHz.

to collimate as their particles flow away from the central object. In Mellema & Frank (1997), for example, spherically flowing protostellar winds are collimated as they interact with the material of its disk. The observation of W75N (B; Carrasco-González *et al.* 2015), in 2015, was a confirmation that some massive protostellar jets are hydrodynamically collimated. The collimation of the jets is largely due to the interaction between the jet particles and particles of the ambient medium. As the jet particles collide with ambient gas, they generate heat, making the interface between the jet beam and its cocoon, normally called a working surface, the hottest region. These working surfaces have been reported in both computational (Raga *et al.* 2000, Rubini *et al.* 2007) and observational (Purser *et al.*, 2016) studies of protostellar jets.

In addition to studying the hydrodynamics properties of protostellar jets, the nature of their emission were also explored. The study clearly shows, for the first time, that the fluxes and spectral indices of steady jets are relatively constant and stable during the entire evolution period of the jets. It was also shown that varying the mass-loss rates and velocities of the jets led to corresponding changes in their fluxes and spectral indices. Their velocities, for example, showed anti-correlation with flux densities and spectral indices. Changes in mass-loss rates, however, did not show a predictable trend but altered their fluxes and spectral indices randomly before settling at higher values. Such variabilities have been observed in massive protostars (Anglada *et al.* 2018, Cesaroni *et al.* 2018), however, it is not clear whether the changes are due to variation in velocity, mass-loss rates or both.

While many factors, e.g. the opening angle and the angle of inclination of a protostellar jet, can affect their flux densities, the significant factor is the number density of charged particles. The two factors that highly affect the number densities of charged particles in jets are their velocities and mass-loss rates. The relationship between the mass-loss rates and flux densities of the objects was thus explored, and found to be given by the equation, $\left[\frac{S_\nu}{\mathrm{mJy}}\right] \propto \left[\frac{\dot{M}}{M_\odot \mathrm{yr}^{-1}}\right]^{1.4\pm0.2}$, in optically thick jets. This relation is similar to the analytical calculations by both Wright & Barlow (1975) and Reynolds (1986).

Chapter 5

Conclusion and Future Work

5.1 Conclusion

This research aimed to establish the prevalence of non-thermal/synchrotron emission in massive protostars. The emission is expected from magnetically driven jets (Shu *et al.* 1994a, Blandford & Payne 1982) which are indirect indicators of disk-fed accretion. The recent discovery of polarised sychrotron emission in HH80-81 (Carrasco-González *et al.*, 2010), a massive protostar, showed that some of these objects harbour magnetic jets. Subsequent observations of large samples of massive protostars at frequencies $\nu \gtrsim 6\,\mathrm{GHz}$ e.g Purser *et al.* (2016), Rosero *et al.* (2016) and Moscadelli *et al.* (2016) also established that some of the massive protostars drive out jets with non-thermal lobes.

The findings in Purser *et al.* (2016) were followed up by selecting a sample of fifteen massive protostars from Purser (2017) to systematically search for evidence of non-thermal emission. The objects were observed at a lower frequency, 1.5 GHz, where synchrotron emission is brighter. Analysis of the fifteen objects showed that 40% have non-thermal lobes, especially sources of higher bolometric luminosity. Even though a non-thermal lobe may be generated when the particles of a jet interact with the magnetic field of its ambient medium, the alignment of lobes with the infrared emission from reflection nebula shows that the magnetic fields may be associated with the jets.

The fraction of non-thermal lobes detected in the sample is comparable to

Purser *et al.* (2016) and Moscadelli *et al.* (2016), however, the preferential detection of non-thermal lobes in objects of higher bolometric luminosities, and the increase of mass-loss rates with the luminosities suggests that low luminosity objects may have weaker jets and fainter lobes. Also, lobes of protostellar jets have been shown to manifest intrinsic variability (Vig *et al.*, 2018) which may make it difficult to detect them. The energies and magnetic field strengths of the lobes were estimated using a minimum energy requirement. Their typical values were found to lie in the range 10^{40} - 10^{42} ergs and 0.4-1.1 mG respectively, comparable to the estimates in HH 80-81 (Carrasco-González *et al.*, 2010). Analysis of the extent of Zeeman splitting of OH maser emission from a large sample of massive star-forming regions (Fish *et al.*, 2003) also derived magnetic field strengths, $0.1 \leq B \leq 10$ mG, that agree with the B-fields of the lobes. The atomic component of the interstellar medium, however, has weaker magnetic field strengths, typically a few μG (Ferrière, 2011). Ferrière (2011) also found out that the fields in the atomic clouds increase with density.

While the lobes of massive protostellar jets may be thermal or non-thermal (Rodríguez-Kamenetzky *et al.*, 2017), all their cores were found to be thermal with an average spectral index of 0.42 ± 0.27. Massive stars have radiative envelopes that emit far UV radiation. The UV radiation can ionize their surroundings which then emit free-free radiation, however, a simulation by Hosokawa *et al.* (2010) showed that at the protostellar stage, their envelopes go through a convective phase where they can generate magnetic fields via the dynamo effect like low mass stars (White *et al.*, 1992). The difficulty in detecting synchrotron emission from the objects may be occasioned by the presence of dusty envelopes which are capable of absorbing energetic electrons that are responsible for generating the emission. Likewise, there was no detection of synchrotron emission from the cores in Obonyo *et al.* (2019), however, the nature of emission from S255 NIRS3, which was in outburst, may be an indicator of the presence of synchrotron emission. It displayed a rise in flux and a corresponding drop in the spectral index. It may, therefore, be interpreted as emission comparable to radiation from an expanding ionized bubble or an object that emits a combination of synchrotron and free-free emission.

The relationship between radio and bolometric luminosities of the cores, at

L-band, was also explored. The trend was found to be comparable with results from other frequencies (Anglada *et al.*, 2018), confirming collisional ionization of jets. Use of Reynolds (1986)'s model in estimating the mass-loss rates of the cores put the rates at 3×10^{-7} to $7\times10^{-6}\,M_{\odot}yr^{-1}$, approximately two orders of magnitude higher than low mass stars (Hartigan *et al.*, 1995b). Such high mass-loss rates correspond to higher accretion rates which are necessary for overcoming the strong radiation pressure from accreting high mass protostars (Hosokawa & Omukai, 2008).

The technique used in determining the nature of emission from massive protostars, spectral indexing, revealed that some of the sources are variable and could introduce uncertainties associated with their variability. A new set of data was therefore selected from a previous observation and re-observed in 2018, at the same frequency, to search for evidence for both positional and flux variability. A total of four objects were observed. In all the cases, the cores did not show any change in position, however, some lobes displayed proper motion. Two of the sources, S255 NIR3 and W3 IRS5, displayed significant evidence of flux and positional variabilities respectively. Indeed S255 NIR3 was in outburst showing that these objects undergo radio bursts whose spectral indices fall with time. The radio burst was considered a manifestation of an accretion burst, a likely solution to the high accretion rates expected in massive star formation. W3 IRS5, on the other hand, displayed precession and proper motion. The proper motions of the lobes were found to lie in the range $80\,km\,s^{-1}$ to $600\,km\,s^{-1}$, showing similarity with the previous estimates i.e 100 to $1000\,km\,s^{-1}$ (Anglada *et al.*, 2018). These lobes also displayed evidence of acceleration followed by deceleration, farther away from the core, perhaps due to their interaction with the ambient medium. Similar properties were seen by Marti *et al.* (1995) in HH80-81.

This observational study of the jets was finally complemented with hydrodynamics and ray-tracing simulations. The observable properties of the jets were simulated. It was clear from the simulations that the interaction between jets and the ambient medium can collimate the jets. Radio emission from the jets was calculated and found to be relatively constant during their entire evolution periods unless the mass-loss rates or velocities of the jets were varied. The velocities of the jets showed anti-correlation with fluxes and spectral indices, however,

an increase in their mass-loss rates results in a corresponding rise in flux and spectral indices.

Overall, therefore, massive protostellar jets have properties that are comparable to those of low mass counterparts, except in some features e.g the magnitude of mass-loss rates, suggesting that massive star formation is a scaled-up version of low mass star formation. However, there are several unresolved questions. Unlike in low mass stars where the accretion luminosity can be estimated and used in calculating the accretion rates directly, in massive star formation the ratio, $\frac{\dot{M}_{jet}}{\dot{M}_{acc}}$, from low and intermediate mass stars has been used. This implies that the rates derived in massive protostars may have large uncertainties if the mechanisms that are responsible for accretion and outflow in low and high mass star formation are different. Indeed the accretion rates that are derived from the observation of massive protostars, for example, are lower than the rates needed to overcome the strong radiation pressure for an O-star to form i.e. $\sim 10^{-4}\,\mathrm{M_{\odot}yr^{-1}}$ (Krumholz *et al.*, 2009). Moreover, only a handful of MYSOs are known to harbour accretion disks which are essential in driving protostellar jets, the objects needed to release part of the radiation pressure in massive protostars through their cavities. Also, only forty per cent of the MYSOs displayed the presence of non-thermal lobes which is a strong pointer to the existence of magnetic jets and disk-fed accretion. The sources of the lobes are equally not clear. Whether they result from the interaction between the jets and the ambient gas or intrinsically connected with the central object is yet to be established. Finally, the driving mechanism for the jets which lack non-thermal lobes is also unclear.

The jets driven by massive protostars also play significant roles in star formation in general. The presence of shocks and the proper motions derived confirm that the jets are energetic enough to destroy their natal molecular clouds, hindering the formation of new stars (Arce, 2003). Precession of the jets further aids the disruption of the clouds and redistribution of their materials which may contain metals to the outer regions of the cloud. There, they are cooled and compressed by shock waves of the jets awaiting the formation of future generations of stars (Lee *et al.*, 2005). The metals are equally necessary for the formation of planets and life (Heger *et al.*, 2003).

5.2 Future Work

There is the potential for studying a larger sample of MYSOs in the southern hemisphere with MeerKAT, a radio telescope consisting of 64 antennas in the Northern Cape of South Africa. MeerKAT whose longest baseline is 8 km conducted an L-band survey of the Galactic plane at a resolution of $\sim 6''$ and a sensitivity, $\sim 6\,\mu Jy$, favourable for studying the extended emission of a jet. These observations can be cross-matched with the RMS catalogue to identify and characterise the sources. Once the Square Kilometre Array telescope (the SKA) whose baseline is projected to be 3,000 km will be fully operational, deeper and high resolution (∼13 mas at L-band) observations will be conducted to study any diffuse non-thermal emission and the ejection radii of the jets. The origin of the jet lobes will also be identified. Polarization and radio recombination lines of the jets will also be explored in the future observations of higher sensitivity. With the detection of fainter cores, it will be possible to explore the low radio luminosity regime of the radio vs bolometric luminosity plot. It is not yet clear if the correlation is affected by limits on sensitivity or a physical property of the protostellar jets.

Estimating the brightness temperatures of the cores of massive protostars has remained elusive due to their large distances. With eMerlin (enhanced Multi-Element Radio Linked Interferometer Network), the actual sizes of the objects can be resolved at C-band given its high resolution i.e $\sim$ 40 mas at C-band. This, coupled with observing the non-thermal lobes, at higher resolution, for more accurate proper motions can be explored with eMerlin. In addition, a search for discs from objects whose jets are well studied can be done at higher frequencies, ∼30-1000 GHz, using ALMA (Atacama Large Millimeter Array) to complement the studies. A search for binaries in hosts of precessing jets can also be carried out using the ALMA observations.

One of the difficulties encountered while studying jets of massive protostars is estimating their launching radii. This radius is approximated to be $\lesssim 10^{15}$ cm (∼67 AU; Reynolds 1986) even though there is evidence that jets are collimated at smaller radii (Mundt, 1985). Recent estimate, in a low mass star, puts it at 0.5 AU (Anglada *et al.* 2018, Estalella *et al.* 2012). These revised radii will

require a telescope of high resolution like the SKA, at full operation, and the next generation VLA, ng−VLA, to observe. In addition, the high-resolution observations will enable astronomers to distinguish between the two competing models (Shu *et al.* 1994a, Blandford & Payne 1982) that were proposed to explain the driving mechanisms of magnetic jets. Finally, simulations of the protostars can be done in three dimensions, at higher resolutions, using a high-performance supercomputer. Other properties of jets, e.g precession and ionization fraction can be modelled using better launching radii.

Bibliography

Adkins, C.J. (1983). *Equilibrium Thermodynamics*. Cambridge University Press, 3rd edn. 129

Ainsworth, R. (2016). Morphology and time evolution of thermal jets associated with low-mass young stars. *PhD Thesis*, 104. 58

Ainsworth, R.E., Scaife, A.M.M., Ray, T.P., Taylor, A.M., Green, D.A. & Buckle, J.V. (2014). Tentative Evidence for Relativistic Electrons Generated by the Jet of the Young Sun-like Star DG Tau. ApJ, **792**, L18. 67

Alves, J., Lombardi, M. & Lada, C.J. (2007). The mass function of dense molecular cores and the origin of the IMF. A&A, **462**, L17–L21. 16

André, P., Könyves, V., Arzoumanian, D., Palmeirim, P. & Peretto, N. (2013). Star Formation as Revealed by Herschel. In R. Kawabe, N. Kuno & S. Yamamoto, eds., *New Trends in Radio Astronomy in the ALMA Era: The 30th Anniversary of Nobeyama Radio Observatory*, vol. 476 of *Astronomical Society of the Pacific Conference Series*, 95. vi, 8

Anglada, G. (1995). Centimeter Continuum Emission from Outflow Sources. In S. Lizano & J.M. Torrelles, eds., *Revista Mexicana de Astronomia y Astrofisica Conference Series*, vol. 1 of *Revista Mexicana de Astronomia y Astrofisica Conference Series*, 67. ix, 21, 68, 71

Anglada, G., López, R., Estalella, R., Masegosa, J., Riera, A. & Raga, A.C. (2007). Proper Motions of the Jets in the Region of HH 30 and HL/XZ Tau: Evidence for a Binary Exciting Source of the HH 30 Jet. AJ, **133**, 2799–2814. 150

Anglada, G., Rodríguez, L.F. & Carrasco-Gonzalez, C. (2015). Radio Jets in Young Stellar Objects with the SKA. *Proceedings of science*, 121. 68, 72, 149, 150

Anglada, G., Rodríguez, L.F. & Carrasco-González, C. (2018). Radio jets from young stellar objects. A&A Rev., **26**, 3. vii, ix, 20, 23, 25, 28, 70, 71, 73, 159, 171, 174, 176

Arce, H.G. (2003). The Impact of Giant Stellar Outflows on their Clouds. In J. Arthur & W.J. Henney, eds., *Revista Mexicana de Astronomia y Astrofisica Conference Series*, vol. 15 of *Revista Mexicana de Astronomia y Astrofisica Conference Series*, 123–125. 175

Arce, H.G., Shepherd, D., Gueth, F., Lee, C.F., Bachiller, R., Rosen, A. & Beuther, H. (2007). Molecular Outflows in Low- and High-Mass Star-forming Regions. In B. Reipurth, D. Jewitt & K. Keil, eds., *Protostars and Planets V*, 245. 22

Armitage, P.J., Livio, M. & Pringle, J.E. (2001). Episodic accretion in magnetically layered protoplanetary discs. MNRAS, **324**, 705–711. 26

Asplund, M., Grevesse, N., Sauval, A.J. & Scott, P. (2009). The Chemical Composition of the Sun. ARA&A, **47**, 481–522. 141

Bacciotti, F. (2002). Diagnostic Determination of Ionization and Density in Stellar Jets from Line Ratios. In W.J. Henney, W. Steffen, L. Binette & A. Raga, eds., *Revista Mexicana de Astronomia y Astrofisica Conference Series*, vol. 13 of *Revista Mexicana de Astronomia y Astrofisica Conference Series*, 8–15. 72

Bacciotti, F. & Eislöffel, J. (1999). Ionization and density along the beams of Herbig-Haro jets. A&A, **342**, 717–735. 72

Bacciotti, F., Chiuderi, C. & Oliva, E. (1995). The structure of optical stellar jets: a phenomenological analysis. A&A, **296**, 185. 24

Bachiller, R. & Tafalla, M. (1999). Bipolar Molecular Outflows. In C.J. Lada & N.D. Kylafis, eds., *NATO Advanced Science Institutes (ASI) Series C*, vol. 540 of *NATO Advanced Science Institutes (ASI) Series C*, 227. 21

Ballesteros-Paredes, J., Klessen, R.S., Mac Low, M.M. & Vazquez-Semadeni, E. (2007). Molecular Cloud Turbulence and Star Formation. *Protostars and Planets V*, 63–80. 15

Bally, J. (2016). Protostellar Outflows. ARA&A, **54**, 491–528. 19, 21, 148

Bally, J., Reipurth, B. & Davis, C.J. (2007). Observations of Jets and Outflows from Young Stars. *Protostars and Planets V*, 215–230. 22, 149

Banerjee, R. & Pudritz, R.E. (2007). Massive Star Formation via High Accretion Rates and Early Disk-driven Outflows. ApJ, **660**, 479–488. 13, 20

Bastian, U. & Mundt, R. (1985). FU Orionis star winds. A&A, **144**, 57–63. 26

Battersby, C., Bally, J. & Svoboda, B. (2017). The Lifetimes of Phases in High-mass Star-forming Regions. ApJ, **835**, 263. 18

Beck, R. & Krause, M. (2005). Revised equipartition and minimum energy formula for magnetic field strength estimates from radio synchrotron observations. *Astronomische Nachrichten*, **326**, 414–427. 58

Beckert, T., Duschl, W.J. & Mezger, P.G. (2000). Free-free and recombination radiation from massive star-forming regions. A&A, **356**, 1149–1156. 159

Begelman, M.C. (1996). *Baby Cygnus A's*, 209. Cambridge University Press. 144

Bell, A.R. (1978). The acceleration of cosmic rays in shock fronts. I. MNRAS, **182**, 147–156. 38

Bell, K.R. & Lin, D.N.C. (1994). Using FU Orionis outbursts to constrain self-regulated protostellar disk models. ApJ, **427**, 987–1004. 26

Bell, K.R., Lin, D.N.C., Hartmann, L.W. & Kenyon, S.J. (1995). The FU Orionis Outburst as a Thermal Accretion Event: Observational Constraints for Protostellar Disk Models. ApJ, **444**, 376. 167

Beuther, H. & Shepherd, D. (2005). Precursors of UchII Regions and the Evolution of Massive Outflows. In *Astrophysics and Space Science Library*, vol. 324 of *Astrophysics and Space Science Library*, 105. 20

Beuther, H., Schilke, P., Gueth, F., McCaughrean, M., Andersen, M., Sridharan, T.K. & Menten, K.M. (2002). IRAS 05358+3543: Multiple outflows at the earliest stages of massive star formation. A&A, **387**, 931–943. 107

Beuther, H., Churchwell, E.B., McKee, C.F. & Tan, J.C. (2007a). The Formation of Massive Stars. *Protostars and Planets V*, 165–180. 2

Beuther, H., Leurini, S., Schilke, P., Wyrowski, F., Menten, K.M. & Zhang, Q. (2007b). Interferometric multi-wavelength (sub)millimeter continuum study of the young high-mass protocluster IRAS 05358+3543. A&A, **466**, 1065–1076. 107

Beuther, H., Zhang, Q., Hunter, T.R., Sridharan, T.K. & Bergin, E.A. (2007c). The 10^5 L high-mass protostellar object IRAS 23151+5912. A&A, **473**, 493–500. 18

Bhandare, A., Kuiper, R., Henning, T., Fendt, C., Marleau, G.D. & Kölligan, A. (2018). First core properties: from low- to high-mass star formation. A&A, **618**, A95. 9

Blandford, R. & Eichler, D. (1987). Particle acceleration at astrophysical shocks: A theory of cosmic ray origin. Phys. Rep., **154**, 1–75. 38

Blandford, R.D. & Payne, D.G. (1982). Hydromagnetic flows from accretion discs and the production of radio jets. MNRAS, **199**, 883–903. 21, 30, 89, 172, 177

Blandford, R.D. & Rees, M.J. (1974). A 'twin-exhaust' model for double radio sources. MNRAS, **169**, 395–415. 153

Blitz, L. (1979). *A study of the molecular complexes accompanying MON OB1 MON OB2 and CMA OB1*. Ph.D. thesis, Columbia Univ., New York, NY. 6

Blitz, L. & Shu, F.H. (1980). The origin and lifetime of giant molecular cloud complexes. ApJ, **238**, 148–157. 4, 5

Blitz, L. & Williams, J.P. (1999). Molecular Clouds. In C.J. Lada & N.D. Kylafis, eds., *NATO Advanced Science Institutes (ASI) Series C*, vol. 540 of *NATO Advanced Science Institutes (ASI) Series C*, 3. 2, 4

Blondin, J.M., Fryxell, B.A. & Konigl, A. (1990). The structure and evolution of radiatively cooling jets. ApJ, **360**, 370–386. 151

Bonito, R., Orlando, S., Peres, G., Eislöffel, J., Miceli, M. & Favata, F. (2010). Generation of radiative knots in a randomly pulsed protostellar jet. I. Dynamics and energetics. A&A, **511**, A42. 151

Bonnell, I.A. & Bate, M.R. (2002). Accretion in stellar clusters and the collisional formation of massive stars. MNRAS, **336**, 659–669. vii, 17, 19

Bonnell, I.A. & Bate, M.R. (2005). Binary systems and stellar mergers in massive star formation. MNRAS, **362**, 915–920. 17

Bonnell, I.A., Bate, M.R., Clarke, C.J. & Pringle, J.E. (1997). Accretion and the stellar mass spectrum in small clusters. MNRAS, **285**, 201–208. 16

Bonnell, I.A., Clarke, C.J., Bate, M.R. & Pringle, J.E. (2001). Accretion in stellar clusters and the initial mass function. MNRAS, **324**, 573–579. 16

Bonnor, W.B. (1956). Boyle's Law and gravitational instability. MNRAS, **116**, 351. 9

Briggs, D.S. (1995). High Fidelity Interferometric Imaging: Robust Weighting and NNLS Deconvolution. In *American Astronomical Society Meeting Abstracts*, vol. 27 of *Bulletin of the American Astronomical Society*, 1444. 45, 93

Brogan, C.L., Hunter, T.R. & Fomalont, E.B. (2018). Advanced Gain Calibration Techniques in Radio Interferometry. *arXiv e-prints*, arXiv:1805.05266. 45

Brooks, K.J., Garay, G., Voronkov, M. & Rodríguez, L.F. (2007). Continuum Observations at 3 and 12 mm of the High-Mass Protostellar Jet IRAS 16547-4247. ApJ, **669**, 459–463. 39

Bryan, G.L., Norman, M.L., O'Shea, B.W., Abel, T., Wise, J.H., Turk, M.J., Reynolds, D.R., Collins, D.C., Wang, P., Skillman, S.W., Smith, B., Harkness, R.P., Bordner, J., Kim, J.h., Kuhlen, M., Xu, H., Goldbaum, N., Hummels, C., Kritsuk, A.G., Tasker, E., Skory, S., Simpson, C.M., Hahn, O., Oishi, J.S., So, G.C., Zhao, F., Cen, R., Li, Y. & Enzo Collaboration (2014). ENZO: An Adaptive Mesh Refinement Code for Astrophysics. ApJS, **211**, 19. 129, 141

Burns, R.A. (2018). Water masers in bowshocks: Addressing the radiation pressure problem of massive star formation. In A. Tarchi, M.J. Reid & P. Castangia, eds., *Astrophysical Masers: Unlocking the Mysteries of the Universe*, vol. 336 of *IAU Symposium*, 263–266. 27

Burns, R.A., Handa, T., Nagayama, T., Sunada, K. & Omodaka, T. (2016). H_2O masers in a jet-driven bow shock: episodic ejection from a massive young stellar object. MNRAS, **460**, 283–290. 93

Butterfield, N., Lang, C.C., Morris, M., Mills, E.A.C. & Ott, J. (2018). M0.20-0.033: An Expanding Molecular Shell in the Galactic Center Radio Arc. ApJ, **852**, 11. 105

Cabrit, S. (2002). Constraints on accretion-ejection structures in young stars. In J. Bouvier & J.P. Zahn, eds., *EAS Publications Series*, vol. 3 of *EAS Publications Series*, 147–182. 21

Cabrit, S. (2007). The accretion-ejection connexion in T Tauri stars: jet models vs. observations. In J. Bouvier & I. Appenzeller, eds., *Star-Disk Interaction in Young Stars*, vol. 243 of *IAU Symposium*, 203–214. 22

Cabrit, S. & Bertout, C. (1992). CO line formation in bipolar flows. III - The energetics of molecular flows and ionized winds. A&A, **261**, 274–284. 68

Cabrit, S., Ferreira, J. & Dougados, C. (2011). Molecular and atomic jets in young low-mass stars: Properties and origin. In G.E. Romero, R.A. Sunyaev & T. Belloni, eds., *Jets at All Scales*, vol. 275 of *IAU Symposium*, 374–382. 21

Canto, J., Tenorio-Tagle, G. & Rozyczka, M. (1988). The formation of interstellar jets by the convergence of supersonic conical flows. A&A, **192**, 287–294. 29, 125

Caratti o Garatti, A., Eislöffel, J., Froebrich, D., Nisini, B., Giannini, T. & Calzoletti, L. (2009). First detection of acceleration and deceleration in protostellar jets? Time variability in the Chamaeleontis II outflows. A&A, **502**, 579–597. 91, 166

Caratti o Garatti, A., Stecklum, B., Garcia Lopez, R., Eislöffel, J., Ray, T.P., Sanna, A., Cesaroni, R., Walmsley, C.M., Oudmaijer, R.D., de Wit, W.J., Moscadelli, L., Greiner, J., Krabbe, A., Fischer, C., Klein, R. & Ibañez, J.M. (2017). Disk-mediated accretion burst in a high-mass young stellar object. *Nature Physics*, **13**, 276–279. 1, 27, 92, 121

Carral, P., Kurtz, S., Rodríguez, L.F., Martí, J., Lizano, S. & Osorio, M. (1999). VLA Continuum Observations of Suspected Massive Hot Cores. RMxAA, **35**, 97–108. 54, 86

Carrasco-González, C., Rodríguez, L.F., Anglada, G., Martí, J., Torrelles, J.M. & Osorio, M. (2010). A Magnetized Jet from a Massive Protostar. *Science*, **330**, 1209. vii, 28, 38, 39, 40, 68, 172, 173

Carrasco-González, C., Galván-Madrid, R., Anglada, G., Osorio, M., D'Alessio, P., Hofner, P., Rodríguez, L.F., Linz, H. & Araya, E.D. (2012). Resolving the Circumstellar Disk around the Massive Protostar Driving the HH 80-81 Jet. ApJ, **752**, L29. 16

Carrasco-González, C., Rodríguez, L.F., Anglada, G., Martí, J., Torrelles, J.M. & Osorio, M. (2013). Discovery of synchrotron emission from a YSO jet. In *European Physical Journal Web of Conferences*, vol. 61 of *European Physical Journal Web of Conferences*, 03003. 39

Carrasco-González, C., Torrelles, J.M., Cantó, J., Curiel, S., Surcis, G., Vlemmings, W.H.T., van Langevelde, H.J., Goddi, C., Anglada, G., Kim, S.W., Kim, J.S. & Gómez, J.F. (2015). Observing the onset of outflow collimation in a massive protostar. *Science*, **348**, 114–117. 28, 91, 171

Carroll, B.W. & Ostlie, D.A. (2006). *An introduction to modern astrophysics and cosmology*. San Francisco: Pearson, Addison-Wesley, 2nd edn. 1

Casali, M., Adamson, A., Alves de Oliveira, C., Almaini, O., Burch, K., Chuter, T., Elliot, J., Folger, M., Foucaud, S., Hambly, N., Hastie, M., Henry, D., Hirst, P., Irwin, M., Ives, D., Lawrence, A., Laidlaw, K., Lee, D., Lewis, J., Lunney, D., McLay, S., Montgomery, D., Pickup, A., Read, M., Rees, N., Robson, I., Sekiguchi, K., Vick, A., Warren, S. & Woodward, B. (2007). The UKIRT wide-field camera. A&A, **467**, 777–784. 47

Ceccarelli, C., Haas, M.R., Hollenbach, D.J. & Rudolph, A.L. (1997). O I 63 Micron-determined Mass-Loss Rates in Young Stellar Objects. ApJ, **476**, 771–780. 73

Cesaroni, R., Moscadelli, L., Neri, R., Sanna, A., Caratti o Garatti, A., Eisloffel, J., Stecklum, B., Ray, T. & Walmsley, C.M. (2018). Radio outburst from a massive (proto)star. When accretion turns into ejection. A&A, **612**, A103. 24, 55, 109, 112, 113, 114, 121, 171

Chambers, E.T., Jackson, J.M., Rathborne, J.M. & Simon, R. (2009). Star Formation Activity of Cores within Infrared Dark Clouds. ApJS, **181**, 360–390. 18

Chernin, L., Masson, C., Gouveia dal Pino, E.M. & Benz, W. (1994). Momentum transfer by astrophysical jets. ApJ, **426**, 204–214. 127

Choi, M., Lee, J.E. & Kang, M. (2014). Radio Variability Survey of Very Low Luminosity Protostars. ApJ, **789**, 9. 24, 91, 167

Chrysostomou, A., Bacciotti, F., Nisini, B., Ray, T.P., Eislöffel, J., Davis, C.J. & Takami, M. (2008). Investigating the transport of angular momentum from young stellar objects. Do H2 jets from class I YSOs rotate? A&A, **482**, 575–583. 24

Cioffi, D.F. & Blondin, J.M. (1992). The evolution of cocoons surrounding light, extragalactic jets. ApJ, **392**, 458–464. 144

Clarke, A.J., Lumsden, S.L., Oudmaijer, R.D., Busfield, A.L., Hoare, M.G., Moore, T.J.T., Sheret, T.L. & Urquhart, J.S. (2006). Evidence for variable outflows in the young stellar object V645 Cygni. A&A, **457**, 183–188. 27, 78, 92

Clarke, D.A. (1996). The Standard Model Revisited: Propagation of a 3D Jet. In P.E. Hardee, A.H. Bridle & J.A. Zensus, eds., *Energy Transport in Radio Galaxies and Quasars*, vol. 100 of *Astronomical Society of the Pacific Conference Series*, 311. 147

Clarke, D.A. (2010). On the Reliability of ZEUS-3D. ApJS, **187**, 119–134. 129

Clayton, D.D. (1983). *Principles of Stellar Evolution and Nucleosynthesis*. University of Chicago Press. 1

Clemens, D.P. & Barvainis, R. (1988). A catalog of small, optically selected molecular clouds - Optical, infrared, and millimeter properties. ApJS, **68**, 257–286. 4

Cohen, M. (1977). The nature of V645 Cygni = CRL 2789. ApJ, **215**, 533–535. 78

Colella, P. & Woodward, P.R. (1984). The Piecewise Parabolic Method (PPM) for Gas-Dynamical Simulations. *Journal of Computational Physics*, **54**, 174–201. 139

Condon, J.J. & Ransom, S.M. (2016). *Essential Radio Astronomy*. Princeton University Press. 32, 37, 156, 158, 162

Condon, J.J., Cotton, W.D., Greisen, E.W., Yin, Q.F., Perley, R.A., Taylor, G.B. & Broderick, J.J. (1998). The NRAO VLA Sky Survey. AJ, **115**, 1693–1716. 105

Contreras Peña, C., Lucas, P.W., Minniti, D., Kurtev, R., Stimson, W., Navarro Molina, C., Borissova, J., Kumar, M.S.N., Thompson, M.A., Gledhill, T., Terzi, R., Froebrich, D. & Caratti o Garatti, A. (2017). A population of eruptive variable protostars in VVV. MNRAS, **465**, 3011–3038. 91

Cooper, H.D.B., Lumsden, S.L., Oudmaijer, R.D., Hoare, M.G., Clarke, A.J., Urquhart, J.S., Mottram, J.C., Moore, T.J.T. & Davies, B. (2013). The RMS survey: near-IR spectroscopy of massive young stellar objects. MNRAS, **430**, 1125–1157. 105

Coughlan, C.P., Ainsworth, R.E., Eislöffel, J., Hoeft, M., Drabent, A., Scaife, A.M.M., Ray, T.P., Bell, M.E., Broderick, J.W., Corbel, S., Griessmeier, J.M., van der Horst, A.J., van Leeuwen, J., Markoff, S., Pietka, M., Stewart, A.J., Wijers, R.A.M.J. & Zarka, P. (2017). A LOFAR Detection of the Low-mass Young Star T Tau at 149 MHz. ApJ, **834**, 206. 22

Courant, R., Friedrichs, K. & Lewy, H. (1967). On the Partial Difference Equations of Mathematical Physics. *IBM Journal of Research and Development*, **11**, 215–234. 140

Cragg, D.M., Johns, K.P., Godfrey, P.D. & Brown, R.D. (1992). Pumping the interstellar methanol masers. MNRAS, **259**, 203–208. 6

Crowther, P.A., Caballero-Nieves, S.M., Bostroem, K.A., Maíz Apellániz, J., Schneider, F.R.N., Walborn, N.R., Angus, C.R., Brott, I., Bonanos, A., de Koter, A., de Mink, S.E., Evans, C.J., Gräfener, G., Herrero, A., Howarth, I.D., Langer, N., Lennon,

D.J., Puls, J., Sana, H. & Vink, J.S. (2016). The R136 star cluster dissected with Hubble Space Telescope/STIS. I. Far-ultraviolet spectroscopic census and the origin of He II λ1640 in young star clusters. MNRAS, **458**, 624–659. 7, 18

Curiel, S., Ho, P.T.P., Patel, N.A., Torrelles, J.M., Rodríguez, L.F., Trinidad, M.A., Cantó, J., Hernández, L., Gómez, J.F. & Garay, G. (2006). Large Proper Motions in the Jet of the High-Mass YSO Cepheus A HW2. ApJ, **638**, 878–886. 92

Cyganowski, C.J., Whitney, B.A., Holden, E., Braden, E., Brogan, C.L., Churchwell, E., Indebetouw, R., Watson, D.F., Babler, B.L., Benjamin, R., Gomez, M., Meade, M.R., Povich, M.S., Robitaille, T.P. & Watson, C. (2008). A Catalog of Extended Green Objects in the GLIMPSE Survey: A New Sample of Massive Young Stellar Object Outflow Candidates. AJ, **136**, 2391–2412. 18, 47, 48

D'Addario, L. (1982). Digital Processing and Spectral Correlators. In A.R. Thompson & L.R. D'Addario, eds., *Synthesis Mapping*. 32

Dalgarno, A. & McCray, R.A. (1972). Heating and Ionization of HI Regions. ARA&A, **10**, 375. 147

Davis, C.J., Moriarty-Schieven, G., Eislöffel, J., Hoare, M.G. & Ray, T.P. (1998). Observations of Shocked H_2 and Entrained CO in Outflows from Luminous Young Stars. AJ, **115**, 1118–1134. 47, 83, 87

Davis, C.J., Gell, R., Khanzadyan, T., Smith, M.D. & Jenness, T. (2010). A general catalogue of molecular hydrogen emission-line objects (MHOs) in outflows from young stars. A&A, **511**, A24. 21

De Buizer, J.M., Radomski, J.T., Telesco, C.M. & Piña, R.K. (2005). Observations of Massive Star-Forming Regions with Water Masers: Mid-Infrared Imaging. ApJS, **156**, 179–215. 82

de Gouveia Dal Pino, E.M. (2005). Astrophysical jets and outflows. *Advances in Space Research*, **35**, 908–924. 144

de Gouveia dal Pino, E.M., Birkinshaw, M. & Benz, W. (1996). A Possible Mechanism for Wiggling Protostellar Jets from Three-dimensional Simulations in a Stratified Ambient Medium. ApJ, **460**, L111. 127

de Pree, C.G., Rodriguez, L.F. & Goss, W.M. (1995). Ultracompact H II regions: are their lifetimes extended by dense, warm environments? RMxAA, **31**, 39–44. 19

de Wit, W.J., Hoare, M.G., Fujiyoshi, T., Oudmaijer, R.D., Honda, M., Kataza, H., Miyata, T., Okamoto, Y.K., Onaka, T., Sako, S. & Yamashita, T. (2009). Resolved 24.5 micron emission from massive young stellar objects. A&A, **494**, 157–178. 87

del Valle, M.V. & Romero, G.E. (2011). Non thermal emission from T Tauri stars. In G.E. Romero, R.A. Sunyaev & T. Belloni, eds., *Jets at All Scales*, vol. 275 of *IAU Symposium*, 404–405. 28

Devine, D., Bally, J., Reipurth, B. & Heathcote, S. (1997). Kinematics and Evolution of the Giant HH34 Complex. AJ, **114**, 2095. 148

Di Francesco, J., Evans, N.J., II, Harvey, P.M., Mundy, L.G., Guilloteau, S. & Chandler, C.J. (1997). Millimeter and Radio Interferometry of Herbig Ae/Be Stars. ApJ, **482**, 433–441. 54, 78

Dionatos, O. & Güdel, M. (2017). Feedback of atomic jets from embedded protostars in NGC 1333. A&A, **597**, A64. 22

Dobashi, K. & Uehara, H. (2001). A CO Outflow and a Molecular Cloud Core Associated with a Young Massive Star IRAS 22134+5834. PASJ, **53**, 799–809. 80

Dougherty, S.M., Pittard, J.M., Kasian, L., Coker, R.F., Williams, P.M. & Lloyd, H.M. (2003). Radio emission models of colliding-wind binary systems. A&A, **409**, 217–233. 158

Drass, H., Haas, M., Chini, R., Bayo, A., Hackstein, M., Hoffmeister, V., Godoy, N. & Vogt, N. (2016). The bimodal initial mass function in the Orion nebula cloud. MNRAS, **461**, 1734–1744. 7

Dunham, M.M., Evans, N.J., II, Terebey, S., Dullemond, C.P. & Young, C.H. (2010). Evolutionary Signatures in the Formation of Low-Mass Protostars. II. Toward Reconciling Models and Observations. ApJ, **710**, 470–502. vi, 12

Ebert, R. (1955). The Influence of Dust on the Equation of State of a contracting Cloud and the Formation of Stars. In *Liege International Astrophysical Colloquia*, vol. 6 of *Liege International Astrophysical Colloquia*, 666–672. 9

Eggers, J. & Villermaux, E. (2008). Physics of liquid jets. *Reports on Progress in Physics*, **71**, 036601. 126

Eisloffel, J., Smith, M.D., Davis, C.J. & Ray, T.P. (1996). Molecular Hydrogen in the Outflow From CEP E. AJ, **112**, 2086. 99, 100

Eisloffel, J., Mundt, R., Ray, T.P. & Rodriguez, L.F. (2000). Collimation and Propagation of Stellar Jets. *Protostars and Planets IV*, 815. 72

Eisner, J.A., Rieke, G.H., Rieke, M.J., Flaherty, K.M., Stone, J.M., Arnold, T.J., Cortes, S.R., Cox, E., Hawkins, C., Cole, A., Zajac, S. & Rudolph, A.L. (2015). Time-monitoring observations of Brγ emission from young stars. MNRAS, **447**, 202–217. 78

Estalella, R., López, R., Anglada, G., Gómez, G., Riera, A. & Carrasco-González, C. (2012). The Counterjet of HH 30: New Light on Its Binary Driving Source. AJ, **144**, 61. 159, 176

Evans, I., Neal J. (1999). Physical Conditions in Regions of Star Formation. ARA&A, **37**, 311–362. 150

Fallscheer, C., Beuther, H., Zhang, Q., Keto, E. & Sridharan, T.K. (2009). Rotational structure and outflow in the infrared dark cloud 18223-3. A&A, **504**, 127–137. 18

Favata, F., Fridlund, C.V.M., Micela, G., Sciortino, S. & Kaas, A.A. (2002). Discovery of X-ray emission from the protostellar jet L1551 IRS5 (HH 154). A&A, **386**, 204–210. 20

Fedriani, R., Caratti o Garatti, A., Coffey, D., Garcia Lopez, R., Kraus, S., Weigelt, G., Stecklum, B., Ray, T.P. & Walmsley, C.M. (2018). Parsec-scale jets driven by high-mass young stellar objects. Connecting the au- and the parsec-scale jet in IRAS 13481-6124. A&A, **616**, A126. 148

Feigelson, E.D., Carkner, L. & Wilking, B.A. (1998). Circularly Polarized Radio Emission from an X-Ray Protostar. ApJ, **494**, L215–L218. 28

Ferreira, J. (1997). Magnetically-driven jets from Keplerian accretion discs. A&A, **319**, 340–359. 149

Ferrière, K. (2011). Interstellar magnetic fields. Mem. Soc. Astron. Italiana, **82**, 824. 173

Fish, V.L., Reid, M.J., Argon, A.L. & Menten, K.M. (2003). Interstellar Hydroxyl Masers in the Galaxy. II. Zeeman Pairs and the Galactic Magnetic Field. ApJ, **596**, 328–343. 68, 173

Fontani, F., Cesaroni, R., Testi, L., Molinari, S., Zhang, Q., Brand, J. & Walmsley, C.M. (2004). Nature of two massive protostellar candidates: IRAS 21307+5049 and IRAS 22172+5549. A&A, **424**, 179–195. 75

Fontani, F., Cesaroni, R. & Furuya, R.S. (2010). Class I and Class II methanol masers in high-mass star-forming regions. A&A, **517**, A56. 6

Forbrich, J., Lada, C.J., Muench, A.A., Alves, J. & Lombardi, M. (2009). A Spitzer Census of Star Formation Activity in the Pipe Nebula. ApJ, **704**, 292–305. 2

Frank, A. & Mellema, G. (1994). A radiation-gasdynamical method for numerical simulations of ionized nebulae: Radiation-gasdynamics of PNe I. A&A, **289**, 937–945. 142

Frank, A. & Mellema, G. (1996). Hydrodynamical Models of Outflow Collimation in Young Stellar Objects. ApJ, **472**, 684. 22, 28, 29

Frank, A., Ray, T.P., Cabrit, S., Hartigan, P., Arce, H.G., Bacciotti, F., Bally, J., Benisty, M., Eislöffel, J., Güdel, M., Lebedev, S., Nisini, B. & Raga, A. (2014). Jets and Outflows from Star to Cloud: Observations Confront Theory. *Protostars and Planets VI*, 451–474. 20, 22

Fryxell, B., Olson, K., Ricker, P., Timmes, F.X., Zingale, M., Lamb, D.Q., MacNeice, P., Rosner, R., Truran, J.W. & Tufo, H. (2000). FLASH: An Adaptive Mesh Hydrodynamics Code for Modeling Astrophysical Thermonuclear Flashes. ApJS, **131**, 273–334. 129

Fujisawa, K., Yonekura, Y., Sugiyama, K., Horiuchi, H., Hayashi, T., Hachisuka, K., Matsumoto, N. & Niinuma, K. (2015). A flare of methanol maser in S255. *The Astronomer's Telegram*, **8286**, 1. 112

Gao, Y. & Lou, Y.Q. (2017). Variable protostellar mass accretion rates in cloud cores. MNRAS, **466**, L53–L57. 11

Gaustad, J.E. (1963). The Opacity of Diffuse Cosmic Matter and the Early Stages of Star Formation. ApJ, **138**, 1050. 9

Gieseking, F. (1973). Photographic Observations of V1057 Cyg. *Information Bulletin on Variable Stars*, **806**. 26

Gillmon, K. & Shull, J.M. (2006). Molecular Hydrogen in Infrared Cirrus. ApJ, **636**, 908–915. 4

Ginsburg, A.G., Bally, J., Yan, C.H. & Williams, J.P. (2009). Outflows and Massive Stars in the Protocluster IRAS 05358+3543. ApJ, **707**, 310–327. 105, 107

Girart, J.M., Beltrán, M.T., Zhang, Q., Rao, R. & Estalella, R. (2009). Magnetic Fields in the Formation of Massive Stars. *Science*, **324**, 1408. 37, 38

Godunov, S.K. (1959). Finite Difference Scheme for Numerical Solution of Discontinuous Solution of Hydrodynamic Equations. *Mat. Sb.*, **47**, 271–306. 139

Gomez, J.F., Torrelles, J.M., Estalella, R., Anglada, G., Verdes-Montenegro, L. & Ho, P.T.P. (1992). On the nature of the bipolar molecular outflow in AFGL 437. ApJ, **397**, 492–499. 87

Goodman, A.A., Benson, P.J., Fuller, G.A. & Myers, P.C. (1993). Dense cores in dark clouds. VIII - Velocity gradients. ApJ, **406**, 528–547. 3

Gramajo, L.V., Rodón, J.A. & Gómez, M. (2014). Spectral Energy Distribution Analysis of Class I and Class II FU Orionis Stars. AJ, **147**, 140. 12

Güdel, M., Telleschi, A., Audard, M., Skinner, S.L., Briggs, K.R., Palla, F. & Dougados, C. (2007). X-rays from jet-driving protostars and T Tauri stars. A&A, **468**, 515–528. 126

Gueth, F. & Guilloteau, S. (1999). The jet-driven molecular outflow of HH 211. A&A, **343**, 571–584. 21

Guillén-González, F. & Redondo-Neble, M.V. (2014). Convergence and error estimates of a viscosity-splitting finite-element scheme for the Primitive Equations. *ArXiv e-prints, 1411.5400*. 130

Hachisuka, K., Brunthaler, A., Menten, K.M., Reid, M.J., Imai, H., Hagiwara, Y., Miyoshi, M., Horiuchi, S. & Sasao, T. (2006). Water Maser Motions in W3(OH) and a Determination of Its Distance. ApJ, **645**, 337–344. 93

Haemmerlé, L. & Peters, T. (2016). Impact of initial models and variable accretion rates on the pre-main-sequence evolution of massive and intermediate-mass stars and the early evolution of H II regions. MNRAS, **458**, 3299–3313. 148

Hamann, F. & Persson, S.E. (1989). High-resolution spectra of the luminous young stellar object V645 Cygni. ApJ, **339**, 1078–1088. 78

Han, X.H., Zhou, J.J., Wang, J.Z., Esimbek, J., Zhang, J.S. & Wang, N. (2015). Combination of CN(1-0), HCN(1-0), and HNC(1-0): A possible

indicator for a high-mass star formation sequence in the Milky Way. A&A, **576**, A131. 105

Hartigan, P., Morse, J.A. & Raymond, J. (1994). Mass-loss rates, ionization fractions, shock velocities, and magnetic fields of stellar jets. ApJ, **436**, 125–143. 24, 72, 121

Hartigan, P., Edwards, S. & Ghandour, L. (1995a). Accretion and Outflow from Young Stars. In M. Pena & S. Kurtz, eds., *Revista Mexicana de Astronomia y Astrofisica Conference Series*, vol. 3 of *Revista Mexicana de Astronomia y Astrofisica, vol. 27*, 93. 73

Hartigan, P., Edwards, S. & Ghandour, L. (1995b). Disk Accretion and Mass Loss from Young Stars. ApJ, **452**, 736. 20, 73, 74, 174

Hartigan, P., Heathcote, S., Morse, J.A., Reipurth, B. & Bally, J. (2005). Proper Motions of the HH 47 Jet Observed with the Hubble Space Telescope. AJ, **130**, 2197–2205. 148

Hartmann, L. & Kenyon, S.J. (1985). On the nature of FU Orionis objects. ApJ, **299**, 462–478. 26

Hartmann, L. & Kenyon, S.J. (1996). The FU Orionis Phenomenon. ARA&A, **34**, 207–240. 26, 167

Hartmann, L., Calvet, N. & Boss, A. (1996). Sheet Models of Protostellar Collapse. ApJ, **464**, 387. 11

Hawley, J., Blondin, J., Lindahl, G. & Lufkin, E. (2012). VH-1: Multidimensional ideal compressible hydrodynamics code. 129

Hayashi, C. & Nakano, T. (1963). Evolution of Stars of Small Masses in the Pre-Main-Sequence Stages. *Progress of Theoretical Physics*, **30**, 460–474. 7

He, Y.X., Zhou, J.J., Esimbek, J., Ji, W.G., Wu, G., Tang, X.D., Komesh, T., Yuan, Y., Li, D.L. & Baan, W.A. (2016). Properties of massive star-forming clumps with infall motions. MNRAS. 15, 16

Heathcote, S., Reipurth, B. & Raga, A.C. (1998). Structure, Excitation, and Kinematics of the Luminous Herbig-Haro Objects 80/81. AJ, **116**, 1940–1960. 23

Heger, A., Fryer, C.L., Woosley, S.E., Langer, N. & Hartmann, D.H. (2003). How Massive Single Stars End Their Life. ApJ, **591**, 288–300. 175

Heitsch, F., Burkert, A., Hartmann, L.W., Slyz, A.D. & Devriendt, J.E.G. (2005). Formation of Structure in Molecular Clouds: A Case Study. ApJ, **633**, L113–L116. 5

Herbig, G.H. (1966). On the interpretation of FU orionis. *Vistas in Astronomy*, **8**, 109–125. 24

Herbig, G.H. (1977). Eruptive phenomena in early stellar evolution. ApJ, **217**, 693–715. 26

Herbig, G.H. & Jones, B.F. (1981). Large proper motions of the Herbig-Haro objects HH 1 and HH 2. AJ, **86**, 1232–1244. vii, 21

Hewett, P.C., Warren, S.J., Leggett, S.K. & Hodgkin, S.T. (2006). The UKIRT Infrared Deep Sky Survey ZY JHK photometric system: passbands and synthetic colours. MNRAS, **367**, 454–468. 47

Hindson, L., Thompson, M.A., Urquhart, J.S., Faimali, A., Johnston-Hollitt, M., Clark, J.S. & Davies, B. (2013). The G305 star-forming complex: radio continuum and molecular line observations. MNRAS, **435**, 2003–2022. vi, 2, 3

Hoare, M.G. (2015). How young stars grow and become focused. *Science*, **348**, 44–45. vii, 29, 38

Hoffleit, D. (1939). Wachmann's Nova-Like Star: A Comparison with Other Peculiar Objects. *Harvard College Observatory Bulletin*, **911**, 41–48. 26

Hogerheijde, M. (1998). *The molecular environment of low-mass protostars*. Ph.D. thesis, Leiden University. vi, 12

Honma, M., Bushimata, T., Choi, Y.K., Hirota, T., Imai, H., Iwadate, K., Jike, T., Kameya, O., Kamohara, R., Kan-Ya, Y., Kawaguchi, N., Kijima, M., Kobayashi, H., Kuji, S., Kurayama, T., Manabe, S., Miyaji, T., Nagayama, T., Nakagawa, A., Oh, C.S., Omodaka, T., Oyama, T., Sakai, S., Sato, K., Sasao, T., Shibata, K.M., Shintani, M., Suda, H., Tamura, Y., Tsushima, M. & Yamashita Kazuyoshi (2007). Astrometry of Galactic Star-Forming Region Sharpless 269 with VERA: Parallax Measurements and Constraint on Outer Rotation Curve. PASJ, **59**, 889. 93

Hopkins, P.F. (2015). A new class of accurate, mesh-free hydrodynamic simulation methods. MNRAS, **450**, 53–110. 129

Horiuchi, S., Meier, D.L., Preston, R.A. & Tingay, S.J. (2006). Ten Milliparsec-Scale Structure of the Nucleus Region in Centaurus A. PASJ, **58**, 211–216. 149

Hosokawa, T. & Omukai, K. (2008). Evolution of Massive Protostars with High Accretion Rates. In H. Beuther, H. Linz & T. Henning, eds., *Massive Star Formation: Observations Confront Theory*, vol. 387 of *Astronomical Society of the Pacific Conference Series*, 255. 7, 174

Hosokawa, T. & Omukai, K. (2009). Evolution of Massive Protostars with High Accretion Rates. ApJ, **691**, 823–846. 28, 38

Hosokawa, T., Yorke, H.W. & Omukai, K. (2010). Evolution of Massive Protostars Via Disk Accretion. ApJ, **721**, 478–492. vi, 10, 16, 173

Huang, S.S. (1957). Star Formation. *Leaflet of the Astronomical Society of the Pacific*, **7**, 321. 20

Hummer, D.G. (1988). A fast and accurate method for evaluating the nonrelativistic free-free Gaunt factor for hydrogenic ions. ApJ, **327**, 477–484. 156

Hunter, T.R., Brogan, C.L., MacLeod, G., Cyganowski, C.J., Chandler, C.J., Chibueze, J.O., Friesen, R., Indebetouw, R., Thesner,

C. & Young, K.H. (2017). An Extraordinary Outburst in the Massive Protostellar System NGC6334I-MM1: Quadrupling of the Millimeter Continuum. ApJ, **837**, L29. 27, 92

Jansky, K.G. (1933). Radio Waves from Outside the Solar System. Nature, **132**, 66. 31

Ji, S., Oh, S.P., Ruszkowski, M. & Markevitch, M. (2016). The efficiency of magnetic field amplification at shocks by turbulence. MNRAS, **463**, 3989–4003. 38

Jiang, Z., Yao, Y., Yang, J., Ishii, M., Nagata, T., Nakaya, H. & Sato, S. (2001). K'-Band Polarimetric Imaging of S187 IR and S233. AJ, **122**, 313–321. 85

Jiang, Z., Yao, Y., Yang, J., Baba, D., Kato, D., Kurita, M., Nagashima, C., Nagata, T., Nagayama, T., Nakajima, Y., Ishii, M., Tamura, M. & Sugitani, K. (2003). A Near-Infrared Study of the Star-forming Region S269. ApJ, **596**, 1064–1079. 118

Jiménez-Serra, I., Martín-Pintado, J., Báez-Rubio, A., Patel, N. & Thum, C. (2011). Extremely Broad Radio Recombination Maser Lines Toward the High-velocity Ionized Jet in Cepheus A HW2. ApJ, **732**, L27. 27, 72

Jin, M., Lee, J.E., Kim, K.T. & Evans, N.J., II (2016). The Inflow Signature toward Different Evolutionary Phases of Massive Star Formation. ApJS, **225**, 21. 18

Junor, W., Biretta, J.A. & Livio, M. (1999). Formation of the radio jet in M87 at 100 Schwarzschild radii from the central black hole. Nature, **401**, 891–892. 149

Kahn, F.D. (1974). Cocoons around early-type stars. A&A, **37**, 149–162. 13

Kawamura, A., Onishi, T., Yonekura, Y., Dobashi, K., Mizuno, A., Ogawa, H. & Fukui, Y. (1998). A ^{13}CO Survey of Molecular Clouds in Gemini and Auriga. ApJS, **117**, 387–425. 107

Keane, E.F. (2018). Pulsar Science with the SKA. In P. Weltevrede, B.B.P. Perera, L.L. Preston & S. Sanidas, eds., *Pulsar Astrophysics the Next Fifty Years*, vol. 337 of *IAU Symposium*, 158–164. 31

Kennicutt, R.C. (2005). The role of massive stars in astrophysics. In R. Cesaroni, M. Felli, E. Churchwell & M. Walmsley, eds., *Massive Star Birth: A Crossroads of Astrophysics*, vol. 227 of *IAU Symposium*, 3–11. 1

Klaassen, P.D., Galván-Madrid, R., Peters, T., Longmore, S.N. & Maercker, M. (2013). Ionization driven molecular outflow in K3-50A. A&A, **556**, A107. 22

Knez, C., Shirley, Y.L., Evans, N.J., II & Mueller, K.E. (2002). CS J=7-6 Mapping of Massive Star Formation Regions Associated with Water Masers. In P. Crowther, ed., *Hot Star Workshop III: The Earliest Phases of Massive Star Birth*, vol. 267 of *Astronomical Society of the Pacific Conference Series*, 375. 6

Kollmann, P., Roussos, E., Paranicas, C., Woodfield, E.E., Mauk, B.H., Clark, G., Smith, D.C. & Vandegriff, J. (2018). Electron Acceleration to MeV Energies at Jupiter and Saturn. *Journal of Geophysical Research (Space Physics)*, **123**, 9110–9129. 38

Konigl, A. (1982). On the nature of bipolar sources in dense molecular clouds. ApJ, **261**, 115–134. 29

Konigl, A. & Pudritz, R.E. (2000). Disk Winds and the Accretion-Outflow Connection. *Protostars and Planets IV*, 759. 24, 26, 73

Koo, B.C. & McKee, C.F. (1992). Dynamics of wind bubbles and superbubbles. I - Slow winds and fast winds. II - Analytic theory. ApJ, **388**, 93–126. 29

Koyama, H. & Inutsuka, S.i. (2002). An Origin of Supersonic Motions in Interstellar Clouds. ApJ, **564**, L97–L100. 143

Kraus, S., Hofmann, K.H., Menten, K.M., Schertl, D., Weigelt, G., Wyrowski, F., Meilland, A., Perraut, K., Petrov, R., Robbe-Dubois, S., Schilke, P. & Testi, L. (2010). A hot compact dust disk around a massive young stellar object. Nature, **466**, 339–342. 13

Krumholz, M.R. (2015). The Formation of Very Massive Stars. In J.S. Vink, ed., *Very Massive Stars in the Local Universe*, vol. 412 of *Astrophysics and Space Science Library*, 43. 13, 14

Krumholz, M.R. & Bonnell, I.A. (2009). *Models for the formation of massive stars*, 288. Cambridge University Press. vi, 17

Krumholz, M.R., Klein, R.I. & McKee, C.F. (2005). Radiation pressure in massive star formation. In R. Cesaroni, M. Felli, E. Churchwell & M. Walmsley, eds., *Massive Star Birth: A Crossroads of Astrophysics*, vol. 227 of *IAU Symposium*, 231–236. 14

Krumholz, M.R., Stone, J.M. & Gardiner, T.A. (2007). Magnetohydrodynamic Evolution of H II Regions in Molecular Clouds: Simulation Methodology, Tests, and Uniform Media. ApJ, **671**, 518–535. 142

Krumholz, M.R., Klein, R.I., McKee, C.F., Offner, S.S.R. & Cunningham, A.J. (2009). The Formation of Massive Star Systems by Accretion. *Science*, **323**, 754. 92, 175

Kuiper, R., Klahr, H., Beuther, H. & Henning, T. (2010). Circumventing the Radiation Pressure Barrier in the Formation of Massive Stars via Disk Accretion. ApJ, **722**, 1556–1576. 13, 14, 15

Kuiper, R., Klahr, H., Beuther, H. & Henning, T. (2014). A Solution to the Radiation Pressure Problem in the Formation of Massive Stars. In D. Stamatellos, S. Goodwin & D. Ward-Thompson, eds., *The Labyrinth of Star Formation*, vol. 36 of *Astrophysics and Space Science Proceedings*, 379. 13, 20

Kuiper, R., Yorke, H.W. & Turner, N.J. (2015). Protostellar Outflows and Radiative Feedback from Massive Stars. ApJ, **800**, 86. 20

Kumar, M.S.N., Bachiller, R. & Davis, C.J. (2002). H_2 Emission around Massive Young Stellar Objects with Outflows. ApJ, **576**, 313–322. 80

Kumar Dewangan, L. & Anandarao, B.G. (2010). Spitzer IRAC imaging photometric study of the massive star-forming region AFGL 437. MNRAS, **402**, 2583–2590. 87

Kurosawa, R., Harries, T.J. & Symington, N.H. (2006). On the formation of Hα line emission around classical T Tauri stars. MNRAS, **370**, 580–596. 148

Kurtz, S., Churchwell, E. & Wood, D.O.S. (1994). Ultracompact H II regions. 2: New high-resolution radio images. ApJS, **91**, 659–712. 86

Kwan, J. (1979). The mass spectrum of interstellar clouds. ApJ, **229**, 567–577. 4

Lada, C.J. & Kylafis, N.D. (1991). Book-Review - the Physics of Star Formation and Early Stellar Evolution. *Journal of the British Astronomical Association*, **101**, 35. 3

Ladeyschikov, D.A., Kirsanova, M.S., Tsivilev, A.P. & Sobolev, A.M. (2016). Molecular emission in dense massive clumps from the star-forming regions S231-S235. *Astrophysical Bulletin*, **71**, 208–224. 107

Larson, R.B. (1969). Numerical calculations of the dynamics of collapsing proto-star. MNRAS, **145**, 271. vi, 7, 9, 10, 128

Larson, R.B. (1978). The stellar state - Formation of solar-type stars. In T. Gehrels, ed., *IAU Colloq. 52: Protostars and Planets*, 43–57. 15

Larson, R.B. (1981). Turbulence and star formation in molecular clouds. MNRAS, **194**, 809–826. vi, 3, 4, 5

Larson, R.B. (1994). The Evolution of Molecular Clouds. In T.L. Wilson & K.J. Johnston, eds., *The Structure and Content of Molecular Clouds*, vol. 439 of *Lecture Notes in Physics, Berlin Springer Verlag*, 13. 2, 3

Latif, M.A. & Schleicher, D.R.G. (2016). Magnetic fields in primordial accretion disks. A&A, **585**, A151. 38

Launhardt, R., Pavlyuchenkov, Y., Gueth, F., Chen, X., Dutrey, A., Guilloteau, S., Henning, T., Piétu, V., Schreyer, K. & Semenov, D. (2009). Rotating molecular outflows: the young T Tauri star in CB 26. A&A, **494**, 147–156. 24

Lawrence, A., Warren, S.J., Almaini, O., Edge, A.C., Hambly, N.C., Jameson, R.F., Lucas, P., Casali, M., Adamson, A., Dye, S., Emerson, J.P., Foucaud, S., Hewett, P., Hirst, P., Hodgkin, S.T., Irwin, M.J., Lodieu, N., McMahon, R.G., Simpson, C., Smail, I., Mortlock, D. & Folger, M. (2007). The UKIRT Infrared Deep Sky Survey (UKIDSS). MNRAS, **379**, 1599–1617. 47

Lee, C.F., Stone, J.M., Ostriker, E.C. & Mundy, L.G. (2001). Hydrodynamic Simulations of Jet- and Wind-driven Protostellar Outflows. ApJ, **557**, 429–442. xiii, 125, 141, 144, 145, 154, 169

Lee, C.F., Hwang, H.C., Ching, T.C., Hirano, N., Lai, S.P., Rao, R. & Ho, P.T.P. (2018). Unveiling a magnetized jet from a low-mass protostar. *Nature Communications*, **9**, 4636. 38

Lee, H.T., Chen, W.P., Zhang, Z.W. & Hu, J.Y. (2005). Triggered Star Formation in the Orion Bright-rimmed Clouds. ApJ, **624**, 808–820. 175

Levshakov, S.A., Henkel, C., Reimers, D., Wang, M., Mao, R., Wang, H. & Xu, Y. (2013). Star-forming regions of the Aquila rift cloud complex. I. NH_3 tracers of dense molecular cores. A&A, **553**, A58. 82

Liu, H.B., Takami, M., Kudo, T., Hashimoto, J., Dong, R., Vorobyov, E.I., Pyo, T.S., Fukagawa, M., Tamura, M., Henning, T., Dunham, M.M., Karr, J.L., Kusakabe, N. & Tsuribe, T. (2016). Circumstellar disks of the most vigorously accreting young stars. *Science Advances*, **2**, e1500875. 26

Liu, S.Y., Su, Y.N., Zinchenko, I., Wang, K.S. & Wang, Y. (2018). A Submillimeter Burst of S255IR SMA1: The Rise and Fall of Its Luminosity. ApJ, **863**, L12. xi, 109, 111, 112

Longair, M.S. (2011). *High Energy Astrophysics*. Cambridge University Press. 58

López-Cámara, D. & Raga, A.C. (2010). Side Entrainment in a Jet Embedded in a Sidewind. ApJ, **723**, 449–456. 39

Lu, X., Zhang, Q., Liu, H.B., Wang, J. & Gu, Q. (2014). Very Large Array Observations of Ammonia in High-mass Star Formation Regions. ApJ, **790**, 84. 82

Lucas, P.W., Hoare, M.G., Longmore, A., Schröder, A.C., Davis, C.J., Adamson, A., Bandyopadhyay, R.M., de Grijs, R., Smith, M., Gosling, A., Mitchison, S., Gáspár, A., Coe, M., Tamura, M., Parker, Q., Irwin, M., Hambly, N., Bryant, J., Collins, R.S., Cross, N., Evans, D.W., Gonzalez-Solares, E., Hodgkin, S., Lewis, J., Read, M., Riello, M., Sutorius, E.T.W., Lawrence, A., Drew, J.E., Dye, S. & Thompson, M.A. (2008). The UKIDSS Galactic Plane Survey. MNRAS, **391**, 136–163. 47

Lumsden, S.L., Hoare, M.G., Urquhart, J.S., Oudmaijer, R.D., Davies, B., Mottram, J.C., Cooper, H.D.B. & Moore, T.J.T. (2013). The Red MSX Source Survey: The Massive Young Stellar Population of Our Galaxy. ApJS, **208**, 11. 40

MacDonald, J. & Bailey, M.E. (1981). The evolution of flows of stellar mass loss in active galaxies. MNRAS, **197**, 995–1019. 147

Manjarrez, G., Gómez, J.F. & de Gregorio-Monsalvo, I. (2012). Dense gas and exciting sources of the molecular outflow in the AFGL 437 star-forming region. MNRAS, **419**, 3338–3345. 87

Mannings, V., Boss, A. & Russell, S. (2000). Protostars and Planets IV. *icarus - Elsevier*, **143**, 1–1. 17

Marsh, M.C. (1970). Ionization front interactions in interstellar gas. MNRAS, **147**, 95. 153

Marti, J., Rodriguez, L.F. & Reipurth, B. (1995). Large Proper Motions and Ejection of New Condensations in the HH 80-81 Thermal Radio Jet. ApJ, **449**, 184. 23, 91, 92, 174

Martí, J., Rodríguez, L.F. & Reipurth, B. (1998). Proper Motions of the Inner Condensations in the HH 80-81 Thermal Radio Jet. ApJ, **502**, 337–341. 23, 24, 73

Massey, P. (2003). MASSIVE STARS IN THE LOCAL GROUP: Implications for Stellar Evolution and Star Formation. ARA&A, **41**, 15–56. 2

Matt, S. & Pudritz, R.E. (2005). The spin of accreting stars: dependence on magnetic coupling to the disc. MNRAS, **356**, 167–182. 73

McKee, C.F. & Chakrabarti, S. (2005). SEDs of massive protostars. In R. Cesaroni, M. Felli, E. Churchwell & M. Walmsley, eds., *Massive Star Birth: A Crossroads of Astrophysics*, vol. 227 of *IAU Symposium*, 276–281. 39

McKee, C.F. & Ostriker, E.C. (2007). Theory of Star Formation. ARA&A, **45**, 565–687. 4, 5

McKee, C.F. & Tan, J.C. (2002). Massive star formation in 100,000 years from turbulent and pressurized molecular clouds. Nature, **416**, 59–61. 74

McKee, C.F. & Tan, J.C. (2003). The Formation of Massive Stars from Turbulent Cores. ApJ, **585**, 850–871. 16

McKinnon, M., Beasley, A., Murphy, E., Selina, R., Farnsworth, R. & Walter, A. (2019). ngVLA: The Next Generation Very Large Array. In BAAS, vol. 51, 81. 31

McMullin, J.P., Waters, B., Schiebel, D., Young, W. & Golap, K. (2007). CASA Architecture and Applications. In R.A. Shaw, F. Hill & D.J. Bell, eds., *Astronomical Data Analysis Software and Systems XVI*, vol. 376 of *Astronomical Society of the Pacific Conference Series*, 127. 43, 93

Megeath, S.T., Wilson, T.L. & Corbin, M.R. (2005). Hubble Space Telescope NICMOS Imaging of W3 IRS 5: A Trapezium in the Making? ApJ, **622**, L141–L144. 17

Mellema, G. & Frank, A. (1997). Outflow collimation in young stellar objects. MNRAS, **292**, 795–807. 169, 171

Mewe, R., Kaastra, J.S. & Liedahl, D.A. (1995). MEKAL cooling curves. *Legacy*, **6**, 16. 142

Micono, M., Massaglia, S., Bodo, G., Rossi, P. & Ferrari, A. (1998). Kelvin-Helmholtz instabilities in stellar jets. IV. On the origin of the emission knots. A&A, **333**, 1001–1006. 127

Mignone, A., Bodo, G., Massaglia, S., Matsakos, T., Tesileanu, O., Zanni, C. & Ferrari, A. (2007). PLUTO: A Numerical Code for Computational Astrophysics. ApJS, **170**, 228–242. 129

Millar, T.J. & Hatchell, J. (1997). Models and Observations of Hot Molecular Cores. *Commmunications of the Konkoly Observatory Hungary*, **100**, 207–222. 19

Minier, V., Booth, R.S. & Conway, J.E. (2000). VLBI observations of 6.7 and 12.2 GHz methanol masers toward high mass star-forming regions. I. Observational results: protostellar disks or outflows? A&A, **362**, 1093–1108. 107

Mitchell, G.F. & Hasegawa, T.I. (1991). An extremely high velocity CO outflow from NGC 7538 IRS 9. ApJ, **371**, L33–L36. 82, 83

Mitchell, G.F., Lee, S.W., Maillard, J.P., Matthews, H., Hasegawa, T.I. & Harris, A.I. (1995). A multitransition CO study of GL 490. ApJ, **438**, 794–812. 87

Miura, R.E., Kohno, K., Tosaki, T., Espada, D., Hwang, N., Kuno, N., Okumura, S.K., Hirota, A., Muraoka, K., Onodera, S., Minamidani, T., Komugi, S., Nakanishi, K., Sawada, T., Kaneko, H. &

Kawabe, R. (2012). Giant Molecular Cloud Evolutions in the Nearby Spiral Galaxy M33. ApJ, **761**, 37. 4

Molinari, S., Pezzuto, S., Cesaroni, R., Brand, J., Faustini, F. & Testi, L. (2008). The evolution of the spectral energy distribution in massive young stellar objects. A&A, **481**, 345–365. 41

Monet, D.G., Jenkins, J.M., Dunham, E.W., Bryson, S.T., Gilliland, R.L., Latham, D.W., Borucki, W.J. & Koch, D.G. (2010). Preliminary Astrometric Results from Kepler. *arXiv e-prints*, arXiv:1001.0305. 93

Moscadelli, L., Sánchez-Monge, Á., Goddi, C., Li, J.J., Sanna, A., Cesaroni, R., Pestalozzi, M., Molinari, S. & Reid, M.J. (2016). Outflow structure within 1000 au of high-mass YSOs. I. First results from a combined study of maser and radio continuum emission. A&A, **585**, A71. 23, 73, 125, 148, 149, 172, 173

Moscadelli, L., Sanna, A., Goddi, C., Walmsley, M.C., Cesaroni, R., Caratti o Garatti, A., Stecklum, B., Menten, K.M. & Kraus, A. (2017). Extended CH_3OH maser flare excited by a bursting massive YSO. A&A, **600**, L8. 114

Motte, F., Andre, P. & Neri, R. (1998). The initial conditions of star formation in the rho Ophiuchi main cloud: wide-field millimeter continuum mapping. A&A, **336**, 150–172. 7

Mottram, J.C., Hoare, M.G., Davies, B., Lumsden, S.L., Oudmaijer, R.D., Urquhart, J.S., Moore, T.J.T., Cooper, H.D.B. & Stead, J.J. (2011). The RMS Survey: The Luminosity Functions and Timescales of Massive Young Stellar Objects and Compact H II Regions. ApJ, **730**, L33. 149

Mundt, R. (1985). Highly collimated mass outflows from young stars. In D.C. Black & M.S. Matthews, eds., *Protostars and Planets II*, 414–433. 176

Mundt, R. (1993). Observational Properties of Jets from Young Stars. In L. Errico & A.A. Vittone, eds., *Stellar Jets and Bipolar Outflows*, vol. 186 of *Astrophysics and Space Science Library*, 91. 149, 150

Mundt, R. & Ray, T.P. (1994). Optical outflows from Herbig Ae/Be stars and other high luminosity young stellar objects. In P.S. The, M.R. Perez & E.P.J. van den Heuvel, eds., *The Nature and Evolutionary Status of Herbig Ae/Be Stars*, vol. 62 of *Astronomical Society of the Pacific Conference Series*, 237. 23, 41, 72, 73

Murawski, K. & Lee, D. (2011). Numerical methods of solving equations of hydrodynamics from perspectives of the code FLASH. *The Journal of Polish Academy of Sciences*, **59**, 1. 130

Murray, N. (2011). Star Formation Efficiencies and Lifetimes of Giant Molecular Clouds in the Milky Way. ApJ, **729**, 133. 3

Nagel, W.E., Krner, D.B. & Resch, M.M. (2008). *High Performance Computing in Science and Engineering ' 08*. Springer. 159

Navarete, F., Damineli, A., Barbosa, C.L. & Blum, R.D. (2015). A survey of extended H_2 emission from massive YSOs. MNRAS, **450**, 4364–4398. 47, 77, 82, 83, 85, 86, 87, 105, 107

Navarete, F., Galli, P.A.B. & Damineli, A. (2019). Gaia-DR2 distance to the W3 Complex in the Perseus Arm. MNRAS, **487**, 2771–2784. 99

Nelson, T., Chomiuk, L., Roy, N., Sokoloski, J.L., Mukai, K., Krauss, M.I., Mioduszewski, A.J., Rupen, M.P. & Weston, J. (2014). The 2011 Outburst of Recurrent Nova T Pyx: Radio Observations Reveal the Ejecta Mass and Hint at Complex Mass Loss. ApJ, **785**, 78. 114

Neumann, J. & Richtmyer, R. (1950). A Method for the Numerical Calculation of Hydrodynamic Shocks. *Journ. Appl Physics*, **21**, 232–237. 147

Norman, M.L. (1997). Computational Astrophysics: The "New Astronomy" for the 21st Century. In D.A. Clarke & M.J. West, eds., *Computational Astrophysics; 12th Kingston Meeting on Theoretical Astrophysics*, vol. 123 of *Astronomical Society of the Pacific Conference Series*, 3. 128, 129

Norman, M.L., Winkler, K.H.A., Smarr, L. & Smith, M.D. (1982). Structure and dynamics of supersonic jets. A&A, **113**, 285–302. 126

Obonyo, W.O., Lumsden, S.L., Hoare, M.G., Purser, S.J.D., Kurtz, S.E. & Johnston, K.G. (2019). A search for non-thermal radio emission from jets of massive young stellar objects. MNRAS, **486**, 3664–3684. xiv, 148, 160, 161, 162, 173

Oey, M.S. & Clarke, C.J. (2009). *Massive stars: Feedback effects in the local universe:*, 74–92. Cambridge University Press. 1

Osterbrock, D.E. & Ferland, G.J. (2006). *Astrophysics of gaseous nebulae and active galactic nuclei*. CA: University Science Books. 142

Panagia, N. & Felli, M. (1975). The spectrum of the free-free radiation from extended envelopes. A&A, **39**, 1–5. 159

Panoglou, D., Cabrit, S., Pineau Des Forêts, G., Garcia, P.J.V., Ferreira, J. & Casse, F. (2012). Molecule survival in magnetized protostellar disk winds. I. Chemical model and first results. A&A, **538**, A2. 23

Paron, S., Fariña, C. & Ortega, M.E. (2016). Near-IR imaging toward a puzzling young stellar object precessing jet. A&A, **593**, A132. 91

Pearson, T.J. & Readhead, A.C.S. (1984). Image Formation by Self-Calibration in Radio Astronomy. ARA&A, **22**, 97–130. 45

Peretto, N. & Fuller, G.A. (2010). A Statistical Study of the Mass and Density Structure of Infrared Dark Clouds. ApJ, **723**, 555–562. vii, 20

Perley, R.A., Chandler, C.J., Butler, B.J. & Wrobel, J.M. (2011). The Expanded Very Large Array: A New Telescope for New Science. ApJ, **739**, L1. 32

Phillips, A. (2001). *The physics of stars*. John Wiley and sons, 2nd edn. 150

Pittard, J.M., Dougherty, S.M., Coker, R.F., O'Connor, E. & Bolingbroke, N.J. (2006). Radio emission models of colliding-wind binary systems. Inclusion of IC cooling. A&A, **446**, 1001–1019. 156, 158

Poetzel, R., Mundt, R. & Ray, T.P. (1993). Herbig-Haro Outflows and Jets from High-Luminosity Young Stellar Objects. In L. Errico & A.A. Vittone, eds., *Stellar Jets and Bipolar Outflows*, vol. 186 of *Astrophysics and Space Science Library*, 231. 73

Pomohaci, R., Oudmaijer, R.D., Lumsden, S.L., Hoare, M.G. & Mendigutía, I. (2017). Medium-resolution near-infrared spectroscopy of massive young stellar objects. MNRAS, **472**, 3624–3636. 74, 148

Pravdo, S.H., Rodriguez, L.F., Curiel, S., Canto, J., Torrelles, J.M., Becker, R.H. & Sellgren, K. (1985). Detection of radio continuum emission from Herbig-Haro objects 1 and 2 and from their central exciting source. ApJ, **293**, L35–L38. vii, 21

Prialnik, D. (2000). *An Introduction to the Theory of Stellar Structure and Evolution*. Cambridge University Press. 2

Pudritz, R.E. & Norman, C.A. (1983). Centrifugally driven winds from contracting molecular disks. ApJ, **274**, 677–697. 28, 30

Pudritz, R.E., Ouyed, R., Fendt, C. & Brandenburg, A. (2007). Disk Winds, Jets, and Outflows: Theoretical and Computational Foundations. *Protostars and Planets V*, 277–294. 20, 22, 73

Purser, S.J.D. (2017). *Ionised Jets Associated With Massive Young Stellar Objects*. Ph.D. thesis, University of Leeds. xi, 39, 40, 41, 55, 57, 77, 80, 92, 93, 97, 99, 100, 101, 103, 105, 106, 107, 108, 109, 112, 116, 121, 172

Purser, S.J.D., Lumsden, S.L., Hoare, M.G., Urquhart, J.S., Cunningham, N., Purcell, C.R., Brooks, K.J., Garay, G., Gúzman, A.E. & Voronkov, M.A. (2016). A search for ionized jets towards massive young stellar objects. MNRAS, **460**, 1039–1053. 24, 73, 89, 92, 125, 148, 149, 171, 172, 173

Purser, S.J.D., Lumsden, S.L., Hoare, M.G. & Cunningham, N. (2018). Investigating the temporal domain of massive ionized jets - I. A pilot study. MNRAS, **475**, 2–19. 24

Raga, A.C. & Noriega-Crespo, A. (1993). The jet/environment density ratio of stellar jets. RMxAA, **25**, 149–153. 126

Raga, A.C., Cantó, J. & D'Alessio, P. (2000). The Dynamics of Stellar Jets. Ap&SS, **272**, 135–143. 171

Rathborne, J.M., Jackson, J.M., Chambers, E.T., Stojimirovic, I., Simon, R., Shipman, R. & Frieswijk, W. (2010). The Early Stages of Star Formation in Infrared Dark Clouds: Characterizing the Core Dust Properties. ApJ, **715**, 310–322. 18

Ray, T.P., Poetzel, R., Solf, J. & Mundt, R. (1990). Optical jets from the high-luminosity young stars LkH-alpha 234 and AFGL 4029. ApJ, **357**, L45–L48. 85, 86

Reid, M.J., Menten, K.M., Zheng, X.W., Brunthaler, A., Moscadelli, L., Xu, Y., Zhang, B., Sato, M., Honma, M., Hirota, T., Hachisuka, K., Choi, Y.K., Moellenbrock, G.A. & Bartkiewicz, A. (2009). Trigonometric Parallaxes of Massive Star-Forming Regions. VI. Galactic Structure, Fundamental Parameters, and Noncircular Motions. ApJ, **700**, 137–148. 4

Reipurth, B. (1990). FU Orionis eruptions and early stellar evolution. In L.V. Mirzoian, B.R. Pettersen & M.K. Tsvetkov, eds., *Flare Stars in Star Clusters, Associations and the Solar Vicinity*, vol. 137 of *IAU Symposium*, 229–251. 24

Reipurth, B. & Bally, J. (2001). Herbig-Haro Flows: Probes of Early Stellar Evolution. ARA&A, **39**, 403–455. 20

Reipurth, B. & Heathcote, S. (1997). 50 Years of Herbig-Haro Research. From discovery to HST. In B. Reipurth & C. Bertout, eds., *Herbig-Haro Flows and the Birth of Stars*, vol. 182 of *IAU Symposium*, 3–18. 21

Reipurth, B., Davis, C.J., Bally, J., Raga, A.C., Bowler, B.P., Geballe, T.R., Aspin, C. & Chiang, H.F. (2019). The Giant HerbigHaro Flow HH 212 and Associated Star Formation. AJ, **158**, 107. 115

Rengarajan, T.N. & Ho, P.T.P. (1996). Search for Optically Thick H II Regions and Ionized Stellar Wind from Luminous Embedded Infrared Sources. ApJ, **465**, 363. 83

Reynolds, R.J. (1976). Observations of the Gum nebula with a Fabry-Perot spectrometer. ApJ, **203**, 151–153. 105

Reynolds, S.P. (1986). Continuum spectra of collimated, ionized stellar winds. ApJ, **304**, 713–720. xiv, 23, 27, 28, 39, 70, 72, 74, 113, 125, 159, 160, 161, 165, 169, 171, 174, 176

Rieutord, M. (2015). *Fluid Dynamics: An Introduction*. Springer. 130

Rijkhorst, E.J., Plewa, T., Dubey, A. & Mellema, G. (2006). Hybrid characteristics: 3D radiative transfer for parallel adaptive mesh refinement hydrodynamics. A&A, **452**, 907–920. 142

Rodriguez, L.F., Ho, P.T.P. & Moran, J.M. (1980). Anisotropic mass outflow in Cepheus A. ApJ, **240**, L149–L152. 20

Rodríguez, L.F., Moran, J.M., Franco-Hernández, R., Garay, G., Brooks, K.J. & Mardones, D. (2008). The Collimated Jet Source in IRAS 16547-4247: Time Variation, Possible Precession, and Upper Limits to the Proper Motions Along the Jet Axis. AJ, **135**, 2370–2379. vii, 24, 25

Rodríguez, L.F., Gómez, Y., Loinard, L. & Mioduszewski, A.J. (2010). On the Size of the Non-Thermal Component in the Radio Emission from Cyg OB2 #5. RMxAA, **46**, 215–219. 22

Rodríguez, L.F., Dzib, S.A., Loinard, L., Zapata, L.A., Raga, A.C., Cantó, J. & Riera, A. (2012a). Radio and Optical Observations of DG Tau B. RMxAA, **48**, 243–249. 126

Rodríguez, T., Trinidad, M.A. & Migenes, V. (2012b). Search for Circumstellar Disks and Radio Jets in the Massive Star-formation Region IRAS 23033+5951. ApJ, **755**, 100. 54, 80

Rodríguez-Kamenetzky, A., Carrasco-González, C., Araudo, A., Torrelles, J.M., Anglada, G., Martí, J., Rodríguez, L.F. & Valotto, C. (2016). Investigating Particle Acceleration in Protostellar Jets: The Triple Radio Continuum Source in Serpens. ApJ, **818**, 27. 39, 89

Rodríguez-Kamenetzky, A., Carrasco-González, C., Araudo, A., Romero, G.E., Torrelles, J.M., Rodríguez, L.F., Anglada, G., Martí, J., Perucho, M. & Valotto, C. (2017). The Highly Collimated Radio Jet of HH 80-81: Structure and Nonthermal Emission. ApJ, **851**, 16. 39, 55, 162, 173

Rosero, V., Hofner, P., Claussen, M., Kurtz, S., Cesaroni, R., Araya, E.D., Carrasco-González, C., Rodríguez, L.F., Menten, K.M., Wyrowski, F., Loinard, L. & Ellingsen, S.P. (2016). Weak and Compact Radio Emission in Early High-mass Star-forming Regions. I. VLA Observations. ApJS, **227**, 25. 27, 28, 172

Rubini, F., Lorusso, S., Del Zanna, L. & Bacciotti, F. (2007). Proper motions of radiative knots in simulations of stellar jets. An alternative to pulsating inflow conditions. A&A, **472**, 855–865. 171

Russell, C.T. (1993). Planetary magnetospheres. *Reports on Progress in Physics*, **56**, 687–732. 38

Rybicki, G.B. & Lightman, A.P. (1979). *Radiative processes in astrophysics*. A Wiley-Interscience publication. 27, 37, 156, 158

Sánchez-Monge, Á., Palau, A., Estalella, R., Beltrán, M.T. & Girart, J.M. (2008). Survey of intermediate/high mass star-forming regions at centimeter and millimeter wavelengths. A&A, **485**, 497–515. 83

Sandell, G., Goss, W.M. & Wright, M. (2005). Protostars and Outflows in the NGC 7538 IRS 9 Cloud Core. ApJ, **621**, 839–852. 54, 83

Scheuer, P.A.G. (1974). Models of extragalactic radio sources with a continuous energy supply from a central object. MNRAS, **166**, 513–528. 143

Schreyer, K., Henning, T., van der Tak, F.F.S., Boonman, A.M.S. & van Dishoeck, E.F. (2002). The young intermediate-mass stellar object AFGL 490 - A disk surrounded by a cold envelope. A&A, **394**, 561–583. 87

Schulz, A., Black, J.H., Lada, C.J., Ulich, B.L., Martin, R.N., Snell, R.L. & Erickson, N.J. (1989). The bipolar molecular outflow of V645 Cygni. ApJ, **341**, 288–292. 78

Schulz, N.S. (2012). *The Formation and Early Evolution of Stars: From Dust to Stars and Planets*. Springer-Verlag Berlin Heidelberg, 2nd edn. 11

Scoville, N.Z. & Solomon, P.M. (1975). Molecular clouds in the Galaxy. ApJ, **199**, L105–L109. 2

Shadloo, M., Oger, G. & Le Touzé, D. (2016). Smoothed particle hydrodynamics method for fluid flows, towards industrial applications: Motivations, current state, and challenges. *Elsevier: Computers and Fluids*, **136**, 11–36. xiii, 130, 131

Shang, H., Lizano, S., Glassgold, A. & Shu, F. (2004). Free-free Radio Emission from Young Stellar Objects. ApJ, **612**, L69–L72. 125

Sheikhnezami, S. & Fendt, C. (2015). Wobbling and Precessing Jets from Warped Disks in Binary Systems. ApJ, **814**, 113. 24

Shimonishi, T., Onaka, T., Kawamura, A. & Aikawa, Y. (2016). The Detection of a Hot Molecular Core in the Large Magellanic Cloud with ALMA. ApJ, **827**, 72. 18

Shirley, Y.L., Claussen, M.J., Bourke, T.L., Young, C.H. & Blake, G.A. (2007). The Detection and Characterization of Centimeter Radio Continuum Emission from the Low-Mass Protostar L1014-IRS. ApJ, **667**, 329–339. 70

Shu, F., Najita, J., Ostriker, E., Wilkin, F., Ruden, S. & Lizano, S. (1994a). Magnetocentrifugally driven flows from young stars and disks. 1: A generalized model. ApJ, **429**, 781–796. vii, 21, 28, 30, 31, 172, 177

Shu, F.H. (1977). Self-similar collapse of isothermal spheres and star formation. ApJ, **214**, 488–497. 9, 11

Shu, F.H., Adams, F.C. & Lizano, S. (1987). Star formation in molecular clouds - Observation and theory. ARA&A, **25**, 23–81. vi, 6, 7, 11, 12

Shu, F.H., Najita, J., Ruden, S.P. & Lizano, S. (1994b). Magnetocentrifugally driven flows from young stars and disks. 2: Formulation of the dynamical problem. ApJ, **429**, 797–807. 89

Shultz, M., Wade, G.A., Alecian, E. & BinaMIcS Collaboration (2015). Detection of magnetic fields in both B-type components of the ϵ Lupi system: a new constraint on the origin of fossil fields? MNRAS, **454**, L1–L5. 28

Sicilia-Aguilar, A., Kim, J.S., Sobolev, A., Getman, K., Henning, T. & Fang, M. (2013). The low-mass stellar population in the young cluster Tr 37. Disk evolution, accretion, and environment. A&A, **559**, A3. 15

Skrutskie, M.F., Cutri, R.M., Stiening, R., Weinberg, M.D., Schneider, S., Carpenter, J.M., Beichman, C., Capps, R., Chester, T., Elias, J., Huchra, J., Liebert, J., Lonsdale, C., Monet, D.G., Price, S., Seitzer, P., Jarrett, T., Kirkpatrick, J.D., Gizis, J.E., Howard, E., Evans, T., Fowler, J., Fullmer, L., Hurt, R., Light, R., Kopan, E.L., Marsh, K.A., McCallon, H.L., Tam, R., Van Dyk, S. & Wheelock, S. (2006). The Two Micron All Sky Survey (2MASS). AJ, **131**, 1163–1183. 47, 83, 85

Smith, H.A. & Fischer, J. (1992). Multiple jets from the young star IRAS 21334 + 5039. ApJ, **398**, L99–L102. 77

Smith, M.D. (2004). *The origin of stars*. Imperial College Press. 4, 6, 19, 22, 30, 127

Smith, M.D. & Rosen, A. (2005). Hydrodynamic simulations of molecular outflows driven by slow-precessing protostellar jets. MNRAS, **357**, 579–589. 125

Snell, R.L., Loren, R.B. & Plambeck, R.L. (1980). Observations of CO in L1551 - Evidence for stellar wind driven shocks. ApJ, **239**, L17–L22. 20

Snell, R.L., Dickman, R.L. & Huang, Y.L. (1990). Molecular Outflows Associated with a Flux-limited Sample of Bright Far-Infrared Sources. ApJ, **352**, 139. 93

Solomon, P.M., Sanders, D.B. & Rivolo, A.R. (1985). The Massachusetts Stony Brook galactic plane CO survey - Disk and spiral arm molecular cloud populations. ApJ, **292**, L19–L24. 7

Solomon, P.M., Rivolo, A.R., Barrett, J. & Yahil, A. (1987). Mass, luminosity, and line width relations of Galactic molecular clouds. ApJ, **319**, 730–741. 3

Springel, V. (2010). E pur si muove: Galilean-invariant cosmological hydrodynamical simulations on a moving mesh. MNRAS, **401**, 791–851. 129

Springel, V., Yoshida, N. & White, S.D.M. (2001). GADGET: a code for collisionless and gasdynamical cosmological simulations. *New Astronomy*, **6**, 79–117. 129

Stecklum, B., Caratti o Garatti, A., Cardenas, M.C., Greiner, J., Kruehler, T., Klose, S. & Eisloeffel, J. (2016). The methanol maser flare of S255IR and an outburst from the high-mass YSO S255IR-NIRS3 - more than a coincidence? *The Astronomer's Telegram*, **8732**, 1. 112

Stepanovs, D. & Fendt, C. (2016). An Extensive Numerical Survey of the Correlation Between Outflow Dynamics and Accretion Disk Magnetization. ApJ, **825**, 14. 26

Stone, J.M. & Norman, M.L. (1992). ZEUS-2D: A radiation magnetohydrodynamics code for astrophysical flows in two space dimensions. I - The hydrodynamic algorithms and tests. ApJS, **80**, 753–790. 144

Stone, J.M. & Norman, M.L. (1993a). Numerical simulations of protostellar jets with nonequilibrium cooling. I - Method and two-dimensional results. II - Models of pulsed jets. ApJ, **413**, 198–220. 147

Stone, J.M. & Norman, M.L. (1993b). Numerical Simulations of Protostellar Jets with Nonequilibrium Cooling. II. Models of Pulsed Jets. ApJ, **413**, 210. 125

Stone, J.M., Gardiner, T.A., Teuben, P., Hawley, J.F. & Simon, J.B. (2008). Athena: A New Code for Astrophysical MHD. ApJS, **178**, 137–177. 129

Sweby, P.K. (1999). Godunov Methods. In E.F. Toro, ed., *Godunov Methods: Theory and applications*, vol. 121, 879. xiii, 139, 140

Szymczak, M., Olech, M., Wolak, P., Gérard, E. & Bartkiewicz, A. (2018). Giant burst of methanol maser in S255IR-NIRS3. A&A, **617**, A80. 112, 114

Tabone, B., Raga, A., Cabrit, S. & Pineau des Forêts, G. (2018). Interaction between a pulsating jet and a surrounding disk wind. A hydrodynamical perspective. A&A, **614**, A119. 125

Takasao, S., Suzuki, T.K. & Shibata, K. (2017). A Theoretical Model of X-Ray Jets from Young Stellar Objects. ApJ, **847**, 46. 126

Tambovtseva, L.V., Grinin, V.P. & Weigelt, G. (2016). Brackett γ radiation from the inner gaseous accretion disk, magnetosphere, and disk wind region of Herbig AeBe stars. A&A, **590**, A97. 105

Tan, J.C., Beltrán, M.T., Caselli, P., Fontani, F., Fuente, A., Krumholz, M.R., McKee, C.F. & Stolte, A. (2014). Massive Star Formation. In H. Beuther, R.S. Klessen, C.P. Dullemond & T. Henning, eds., *Protostars and Planets VI*, 149. 6

Tapia, M., Roth, M. & Persi, P. (2015). The massive Class I eruptive variable V723 Carinae and its neighbour Car I-125. MNRAS, **446**, 4088–4097. 27, 92

Teixeira, G.D.C., Kumar, M.S.N., Smith, L., Lucas, P.W., Morris, C., Borissova, J., Monteiro, M.J.P.F.G., Caratti o Garatti, A.,

Contreras Peña, C., Froebrich, D. & Gameiro, J.F. (2018). Photometric variability of massive young stellar objects. A&A, **619**, A41. 92

Tenorio-Tagle, G., Bodenheimer, P., Lin, D.N.C. & Noriega-Crespo, A. (1986). On star formation in stellar systems. I - Photoionization effects in protoglobular clusters. MNRAS, **221**, 635–658. 142

Teyssier, R. (2002). Cosmological hydrodynamics with adaptive mesh refinement. A new high resolution code called RAMSES. A&A, **385**, 337–364. 129

Teyssier, R. (2015). Grid-Based Hydrodynamics in Astrophysical Fluid Flows. ARA&A, **53**, 325–364. xiii, 129, 140

Thomas, N.H., Hora, J.L. & Smith, H.A. (2013). Variability of Massive Young Stellar Objects in Cygnus-X. In *American Astronomical Society Meeting Abstracts #221*, vol. 221 of *American Astronomical Society Meeting Abstracts*, 256.26. 92

Thompson, A.R., Moran, J.M. & Swenson, G.W. (1986). *Interferometry and synthesis in radio astronomy*. New York, Wiley-Interscience, 1986, 554 p. vii, 32, 33

Thompson, A.R., Moran, J.M. & Swenson, J., George W. (2001). *Interferometry and Synthesis in Radio Astronomy, 2nd Edition*. Wiley-VCH Verlag GmbH. 31

Tieftrunk, A.R., Gaume, R.A., Claussen, M.J., Wilson, T.L. & Johnston, K.J. (1997). The H II/molecular cloud complex W3 revisited: imaging the radio continuum sources using multi-configuration, multi-frequency observations with the VLA. A&A, **318**, 931–946. 101

Tofani, G., Felli, M., Taylor, G.B. & Hunter, T.R. (1995). Exploring the engines of molecular outflows. Radio continuum and water maser observations. A&AS, **112**, 299. 82

Tomisaka, K. (2002). Collapse of Rotating Magnetized Molecular Cloud Cores and Mass Outflows. ApJ, **575**, 306–326. 11

Toro, E.F. (2009). *Riemann Solvers and Numerical Methods for Fluid Dynamics*. Springer, 3rd edn. 130, 139

Trinidad, M.A., Curiel, S., Torrelles, J.M., Rodríguez, L.F., Migenes, V. & Patel, N. (2006). Interferometric Observations toward the High-Mass Young Stellar Object IRAS 23139+5939: Radio Continuum and Water Maser Emission. AJ, **132**, 1918–1922. 54, 82

Turner, N.J.J., Bodenheimer, P. & Bell, K.R. (1997). Models of the Spectral Energy Distributions of FU Orionis Stars. ApJ, **480**, 754–766. 26

Urquhart, J.S., Morgan, L.K., Figura, C.C., Moore, T.J.T., Lumsden, S.L., Hoare, M.G., Oudmaijer, R.D., Mottram, J.C., Davies, B. & Dunham, M.K. (2011). The Red MSX Source survey: ammonia and water maser analysis of massive star-forming regions. MNRAS, **418**, 1689–1706. 42

van der Tak, F.F.S. (2004). Hot Molecular Cores and High Mass Star Formation. In M.G. Burton, R. Jayawardhana & T.L. Bourke, eds., *Star Formation at High Angular Resolution*, vol. 221 of *IAU Symposium*, 59. 18

van der Tak, F.F.S. & Menten, K.M. (2005). Very compact radio emission from high-mass protostars. II. Dust disks and ionized accretion flows. A&A, **437**, 947–956. 55, 83

van der Tak, F.F.S., Tuthill, P.G. & Danchi, W.C. (2005). Subarcsecond mid-infrared and radio observations of the W3 IRS5 protocluster. A&A, **431**, 993–1005. 97, 99, 101

van Hoof, P.A.M., Williams, R.J.R., Volk, K., Chatzikos, M., Ferland, G.J., Lykins, M., Porter, R.L. & Wang, Y. (2014). Accurate determination of the free-free Gaunt factor - I. Non-relativistic Gaunt factors. MNRAS, **444**, 420–428. 156

Varricatt, W.P., Davis, C.J., Ramsay, S. & Todd, S.P. (2010). A near-IR imaging survey of intermediate- and high-mass young stellar outflow candidates. MNRAS, **404**, 661–720. 47, 75, 107

Vázquez-Semadeni, E., Gómez, G.C., Jappsen, A.K., Ballesteros-Paredes, J., González, R.F. & Klessen, R.S. (2007). Molecular Cloud Evolution. II. From Cloud Formation to the Early Stages of Star Formation in Decaying Conditions. ApJ, **657**, 870–883. 143

Velusamy, T., Langer, W.D. & Marsh, K.A. (2007). Highly Collimated Jets and Wide-Angle Outflows in HH 46/47: New Evidence from Spitzer Infrared Images. ApJ, **668**, L159–L162. 39

Vig, S., Veena, V.S., Mandal, S., Tej, A. & Ghosh, S.K. (2018). Detection of non-thermal emission from the massive protostellar jet HH80-81 at low radio frequencies using GMRT. MNRAS, **474**, 3808–3816. 39, 55, 173

Vorobyov, E.I. & Basu, S. (2005). The Origin of Episodic Accretion Bursts in the Early Stages of Star Formation. ApJ, **633**, L137–L140. 26

Vorobyov, E.I. & Basu, S. (2006). The Burst Mode of Protostellar Accretion. ApJ, **650**, 956–969. 92

Walker, R.C. (1997). Kiloparsec-Scale Motions in 3C 120–Revisited. ApJ, **488**, 675–681. 93

Walter, F.M., Stringfellow, G.S., Sherry, W.H. & Field-Pollatou, A. (2004). V1647 Orionis (IRAS 05436-0007) in Outburst: The First Three Months. AJ, **128**, 1872–1879. 26

Wang, P., Li, Z.Y., Abel, T. & Nakamura, F. (2010). Outflow Feedback Regulated Massive Star Formation in Parsec-Scale Cluster-Forming Clumps. ApJ, **709**, 27–41. 23

Wang, Y., Audard, M., Fontani, F., Sánchez-Monge, Á., Busquet, G., Palau, A., Beuther, H., Tan, J.C., Estalella, R., Isella, A., Gueth, F. & Jiménez-Serra, I. (2016). Ongoing star formation in the protocluster IRAS 22134+5834. A&A, **587**, A69. 54, 79

Welter, G.L. (1980). The structure and dynamics of H II regions. ApJ, **240**, 514–523. 105

White, S.M., Pallavicini, R. & Kundu, M.R. (1992). Radio flares and magnetic fields on weak-line T Tauri stars. A&A, **259**, 149–154. 39, 173

Wilson, J.R. (1971). A Numerical Study of Gravitational Stellar Collapse. ApJ, **163**, 209. 128

Wilson, T.L. (2011). Techniques of Radio Astronomy. *arXiv e-prints*, arXiv:1111.1183. 31

Wilson, T.L., Boboltz, D.A., Gaume, R.A. & Megeath, S.T. (2003). High-Resolution Continuum Imaging at 1.3 and 0.7 Centimeters of the W3 IRS 5 Region. ApJ, **597**, 434–442. 97

Winick, H. & Doniach, S., eds. (1980). *Synchrotron Radiation Research*. 37

Wolf-Chase, G., Arvidsson, K. & Smutko, M. (2017). MHOs toward HMOs: A Search for Molecular Hydrogen Emission-Line Objects toward High-mass Outflows. ApJ, **844**, 38. 21, 47, 75, 80

Wouterloot, J.G.A., Henkel, C. & Walmsley, C.M. (1989). CO observations of IRAS sources in Orion and Cepheus. A&A, **215**, 131–146. 82

Wright, A.E. & Barlow, M.J. (1975). The radio and infrared spectrum of early-type stars undergoing mass loss. MNRAS, **170**, 41–51. xiv, 27, 28, 159, 160, 169, 171

Wright, M. (2001). PROBING THE STAR-FORMING REGION W3(OH) WITH GROUND-STATE HYDROXYL MASERS. *PhD Thesis, University of Bristol*, 7. 41

Wu, Y.W., Xu, Y., Yang, J. & Li, J.J. (2009). A multiwavelength study of the massive star-forming region IRAS 22506+5944. *Research in Astronomy and Astrophysics*, **9**, 1343–1350. 80

Xu, J.L. & Wang, J.J. (2010). Submillimeter/millimeter observations of the high-mass star forming region IRAS 22506+5944. *Research in Astronomy and Astrophysics*, **10**, 151–158. 80

Xu, J.L., Zavagno, A., Yu, N., Liu, X.L., Xu, Y., Yuan, J., Zhang, C.P., Zhang, S.J., Zhang, G.Y., Ning, C.C. & Ju, B.G. (2019). The effects of ionization feedback on star formation: a case study of the M 16 H II region. A&A, **627**, A27. 14

Yorke, H.W. & Sonnhalter, C. (2002). On the Formation of Massive Stars. ApJ, **569**, 846–862. 13

Zhu, Z., Hartmann, L. & Gammie, C. (2009). Nonsteady Accretion in Protostars. ApJ, **694**, 1045–1055. 92

Zingale, M. (2014). *Introduction to Computational Astrophysical Hydrodynamics*. Open-Astrophysics-Bookshelf. xiii, 129, 137, 138

Zinnecker, H. & McCaughrean, M.J. (1997). Infrared Jets from Protostars: The case of HH212. In D.T. Wickramasinghe, G.V. Bicknell & L. Ferrario, eds., *IAU Colloq. 163: Accretion Phenomena and Related Outflows*, vol. 121 of *Astronomical Society of the Pacific Conference Series*, 531. 20

Zinnecker, H. & Yorke, H.W. (2007). Toward Understanding Massive Star Formation. ARA&A, **45**, 481–563. 2, 4, 6, 14, 148

Zwintz, K. (2008). Comparing the Observational Instability Regions for Pulsating Pre-Main-Sequence and Classical δ Scuti Stars. ApJ, **673**, 1088–1092. 91